Cape Peninsula
University of Technology

DESIGN AND IMPLEMNTATION OF POWER CONVERTER MINIGRIDS FOR EMBEDDED GENERATION

by

MOHAMED ALMIHAT

A thesis submitted in fulfilment of the requirements for the degree

Doctor of Engineering: Electrical Engineering

in the Faculty of Engineering and the Built Environment

at the Cape Peninsula University of Technology

Supervisor: Prof MTE Kahn

Bellville

September 2023

DECLARATION

I, Mohamed Almihat, declare that the contents of this dissertation/thesis represent my own unaided work, and that the dissertation/thesis has not previously been submitted for academic examination towards any qualification. Furthermore, it represents my own opinions and not necessarily those of the Cape Peninsula University of Technology.

1/9/2023

Signed **Date**

ABSTRACT

Supplying energy to off-grid and remote areas has always been a challenge despite the penetration of micro and minigrids in those areas. Challenges include the implantation costs of minigrids compared to the community low-income, the scarcity of skilled workers required to operate the plants, as well as issues pertaining to the reliability of solar and wind sources that are dependent on the time of the day, the weather, and the annual season. . As such, the operation of these minigrids not only requires a meticulous design but also autonomous management and control to ensure continuous service to the community in an operation mode known as an islanded mode.

The literature survey conducted on the management and control of the energy in an islanded minigrid highlighted the need for further study to contribute to this area. Therefore, the focus of this study was on energy management and control systems for a multivariable energy system consisting of solar and wind plants backed up with a diesel generator and battery storage. The proposed algorithm referred to possible scenarios relating to the behaviour of the major energy sources when either one or more are at their lowest levels, as well as the variable levels of the load demand to establish the rules that will govern the response of the minigrid.

In addition, the study worked on addressing issues related to the quality of power received by the variable or nonlinear load by designing a control system aiming at eliminating the harmonic distortions resulting from the presence of reactance in the load together with the presence of a voltage source inverter to process the power coming to the photovoltaic (PV) plant. Through meticulous modelling of the output network consisting of an LC filter and an RL load, a proportional–integral control was designed and tuned to ensure that the variable load would receive a harmonic-free output voltage and current.

Finally, the study implemented the energy management strategy incorporating the power quality aspect to supply electricity in a rural area. This was completed using real-time software such as Typhoon HIL (Hardware In the Loop) to illustrate the functionality of an islanded minigrid where worst-case levels for the solar and wind plants were catered for. Overall, the aim of this study, which was to bring about a solution to control multivariable sources and make them successfully operate in an islanded mode, was achieved.

ACKNOWLEDGEMENTS

All glory be to ALLAH, who directed me to be who I am, and all gratitude to HIM for HIS guidance and kindness that HE bestowed upon me, giving me the strength to successfully finish my studies.

To Professor Mohamed Tariq Kahn,the Reseach Chair in Energy and my doctoral advisor, who has provided me with direction, passionate assistance, and persistent encouragement over the entirety of this research endeavour. Particularly grateful for his insightful advice, encouragement, support, and effort invested in ensuring the success of this project.

Many thanks to Dr Ali Almaktoof for his support and advice, to all my colleagues and friends at the Department of Electrical Electronic and Computer Engineering, particularly the Centre for Distributed Power and Electronic Systems (CDPES), for their intellectual interaction, encouragement, and motivation during my studies.

MGM ALMIHAT

DEDICATION

This thesis is dedicated to my mother and father, and to my brothers and sisters; and for my daughter Rawand may they see their love and support reflected in this work.

TABLE OF CONTENTS

LIST OF FIGURES

LIST OF TABLES

APPENDICES

GLOSSARY

ABBREVIATIONS & ACRONYMS

AC	Alternating current
AM	Air mass
ASPDs	Adjustable speed drives
CAES	Compressed air energy storage
CPU	Central processing unit
DC	Direct current
DER	Distributed energy resources
DFIG	Doubly-fed induction generator
DOD	Depth of discharge
EMI	Electromagnetic interference
ESS	Energy storage systems
EVs	Electric vehicles
FACTS	Flexible AC transmission systems
FB-ZVR	Full-Bridge Zero-Voltage-Rectifier
FETs	Field effect transistors
FETs	Field effect transistors
HAWT	Horizontal axis wind turbine
HERIC	Highly Efficient and Reliable Inverter concept
HVG	High voltage generator
IEA	International Energy Agency
IGBT	Insulated gate bipolar transistor
MG	Minigrid
MIMO	Multiple-input-multiple-output
MMCs	Modular multilevel converters

MPP	Maximum power point
MPPT	Maximum power point tracking
NPC	Neutral point clamping
P	Active power
P	Proportional
PCC	Point common coupling
PI	Proportional integral
PMSG	Permanent Magnet Synchronous Generator
PSH	Pumped storage hydropower
PV	Photovoltaic
PVs	Photovoltaic systems
Q	Reactive power
RESs	Renewable energy systems
SCIG	Squirrel cage induction generator
SMs	Submodules
SOC	State of charge
TEWAC	Totally enclosed water to air cooled
TFG	Transverse flux generator
THDs	Total harmonic distortions
TSR	Tip speed ratio
UPS	Uninterruptible power supply
VAWT	Vertical axis wind turbine
VSI	Voltage source inverter
WPP	Wind power plants
WRSG	Wound rotor synchronous generator
WT	Wind turbine

CHAPTER ONE

RESEARCH OVERVIEW

1.1 Introduction

Rural and off-grid areas in the Sub-Saharan region suffer from the lack of electricity, while power interruptions for a long period of time prevail in grid-connected areas despite the abundance of natural and renewable energy sources readily available. Numerous studies were conducted in this area, including a study by (Micangeli et al., 2017) concerning the statistics about the electrification rates. According to the statistics released by the International Energy Agency (IEA) and the World Energy Outlook (WEO) in 2017, an estimation of 14% of the total population of the world, which is around 1.1 billion people, have no access to electricity, with 95% of them located in developing Asia and Sub-Saharan Africa (Emmanuel et al., 2020).

Africa still depends on wood, charcoal, and diesel to generate energy for cooking and lighting purposes, while electricity availability is falling short in Sub-Saharan Africa with a rapidly increasing population. The situation is critical given that the 84% living without electricity come from that region. Predictions go on to indicate that there will still be about 655 million people living without electricity in SSA with no electricity by the year 2030.

This study aims to find a solution to the limited electricity accessibility in rural areas by providing these areas with a renewable energy system in another minigrid system to ensure the availability of daily power.

1.2 Background

Electricity can be generated in different forms and ways, for instance using diesel generators and gas turbines to supply customers through transmission lines or networks. The cost of these distribution lines is usually high when it comes to reaching and providing rural areas with needed power due to the long distances. Such costs are not worth it given who benefits from it, especially since the residents of the rural areas are fewer compared to the city population. Therefore, power electronics play an important key in resolving this issue by reducing the cost of generated energy and transferring the power to the consumers. Minigrids can be viewed as one of the best solutions, especially when installed in an area abundant in renewable energy resources such as sunlight and wind. As such, power can be generated and supplied to the local communities at an affordable cost and without harm to the environment.

According to (Longe et al., 2019) stated in their research that in South Africa, the rate of electrification in urban areas is higher than in rural areas, and this is due to the higher demand for power in the cities, which makes it complicated to supply the rural areas with electricity from the national grid because of many reasons, such as the distance and geographical aspects of the area, and the high cost of power generated compared with the low demand in rural areas.

According to (Mbinkar et al., 2021) a minigrid system consists of an electricity generation system that may be accompanied by a storage system for the power generated and a distribution system that delivers electricity to isolated loads that are not covered or connected with the national electricity grid system. The steps for creating a minigrid system consist of determining the elements, including the configuration for every sub-system that will provide a reliable and safe service that covers the consumers' needs.

1.2 Overview of multivariable controller

The term multivariable control does not refer to a specific control strategy but rather a description of a wide family of control tactics. This gives the designers a wide range of choices to design and choose a suitable control method based on their needs and uses, which is an advantage for the system to work properly by minimizing the risk and errors during the control period by flexibly shifting from one power input to another to sustain the system and decrease the fault within the optimal control system (Bordons et al., 2020).

In this regard, micro and minigrid control architectures through centralized and decentralized schemes were found to be suitable to manage the energy transactions within an islanded minigrid to ensure an uninterrupted power supply to the load. On the other hand, there is a pressing need to take care of the power quality at the output, especially when the load is nonlinear and a voltage source inverter is involved in the DC conversion into AC power.

There are two kinds of controllers commonly used in the energy and industrial sector: the Proportional integral (PI) and the Proportional-Integral-Derivative (PID), each with its own features In this study, the focus will be on PI incorporated with minigrid.

1.3 Statement of the research problem

As a renewable energy-based resource, micro or minigrid proves to be suitable for sustainable electricity supply to rural communities. However, some of the critical challenges encountered in the operation of minigrids pertain to the higher cost involved in their implantation in relation to low-income communities, as well as bill payment issues and finding skilled people to run the minigrid (Peters et al., 2019). Moreover, (Gerlach et al.,

2013) further explained that the risk of investing in the minigrid in rural areas is that there are no laws or regulations to protect investors.

From an energy management and power quality perspective, the minigrid has challenges related to the nature of the plants making it. Both PV and wind plants are known for their non-reliability due to the intermittent nature of sunlight and wind. This has led to the need for backup energy systems, mainly generators and storage systems. In this sense, there is plenty of free-of-charge energy with issues and backup energy systems that are reliable but costly, such as diesel plants and battery storage systems.

The main issue with such plants lies in the management of the energy in an efficient way in terms of ensuring that the load demand is satisfied at any time of the day and the excess is stored for future use. Intensive research on finding a system that could make the decision to connect this plant, reconnect this other, send the excess power into a storage system or recall it back for use by the load, reveals/indicates that there is still room for improvement.. The second issue pertains to the quality of power delivered to the load, which may be linear or nonlinear, on top of the presence of a voltage source inverter (VSI), which is the source of harmonic distortions.

The focus of this research is to devise an energy management system for a a multivariable controller minigrid consisting of the following four types of power sources, namely wind turbine, solar photovoltaic, battery, and diesel generator. In addition, the research has worked on ensuring power quality by eliminating distortions in the load power.

1.4 Research objectives

The main objective of this research is to explore existing methods and develop a better controlling system of islanded minigrid, and to ensure that the power supplied is stable to feed the required demand load in the rural areas. The work offers a simple and efficient multivariable PI controller strategy for improved output voltage control of the three-phase voltage source inverter (VSI) used for islanded minigrid systems. The three-phase VSI with output LC filter will be used to provide a sinusoidal output voltage, regardless of the arbitrary consumer load profiles.

The second research objective is to check the robustness of the proposed control under variable loads, in terms of the total harmonic distortions (THDs) in the output stage of the inverters to ensure the power supply quality, The second research objective is to check the robustness of the proposed control under variable loads, in terms of the total harmonic distortions (THDs) in the output stage of the inverters to ensure the power supply quality. To

be more specific, THD explains the measure of the harmonic complex, the current, and voltage waveforms comprehend.

1.5 Methodology

To achieve the objectives stated above, the following approach has been considered:

- Literature study on distributed energy systems, behaviour of renewable energy sources, voltage source inverters (VSI), total harmonic distortions (THDs), energy management architectures, and linear control methods for minigrid systems.
- An algorithm for a RE model was developed and implemented to simulate possible effects of naturally unstable energy sources such as solar and wind energy as well as the battery storage, of which the performance depends on the level of charge at a point in time of the day. Matrix Laboratory Release 2018B (MATLAB R2018B) integrated development environment was used to test the functionality of the algorithm and produce the instantaneous power profiles for each source and the load.
- A linear control system of the proportional (P) and proportional integral (PI) was developed, and performance evaluation of a multivariable voltage and current control for a three-phase voltage source inverter was completed in terms of eliminating THDs in the output stage of the LC filter. Mathematical models for the variable load, the combo LC filter, and RL load were modeled both in time and s-domain for the open-loop and closed transfer functions.
- Multivariable energy control was implemented using a real-time software based on the needs of the rural area where PV, wind, diesel, generator, storage batteries formed the plant making the islanded minigrid. The performance and efficiency of the minigrid supplying the arbitrary consumer load was completed using Typhoon HIL, which is a real-time hardware in the loop development environment.

  In the following figure 1.1 shows the proposed system and its compounds.

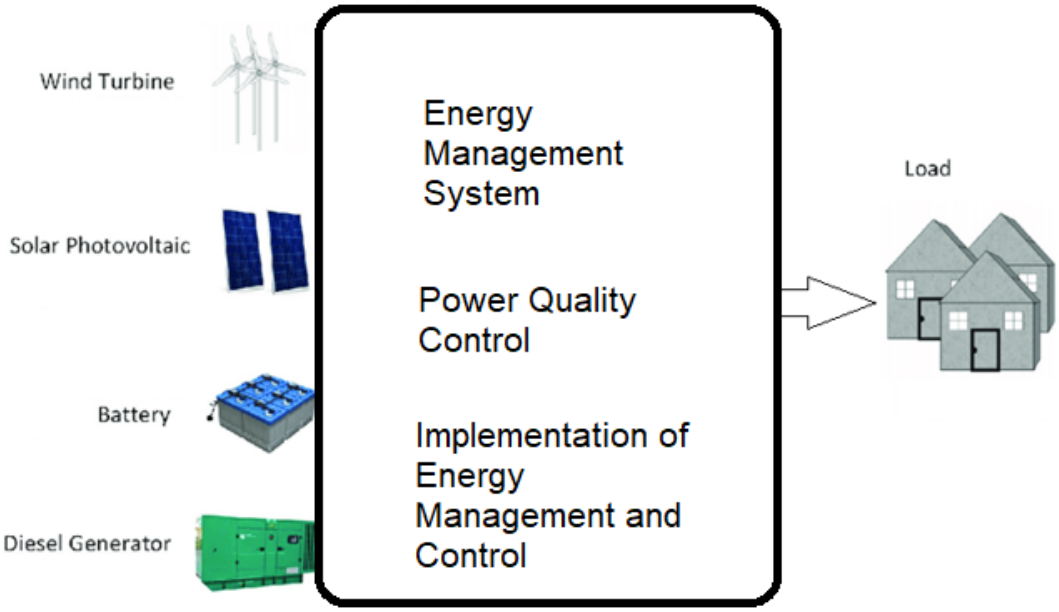

Figure 1. 1: Modelling of the hybrid minigrid with PV, wind, diesel and battery generating system with a variable load

1.6 Research deliverables

The deliverables of this research consist of a novel energy management algorithm for a RE minigrid, a model of P and PI control system to deal with total harmonic distortions present in the variable, and the implementation of an islanded minigrid for rural area energy supply. All these findings were compiled in the form of a thesis and yielded journal articles and conference papers.

1.7 Publications

1.7.1 Published papers

1. Almihat, M.G.M., Kahn, M.T.E., Aboalez, K. and Almaktoof, A.M., 2022. Energy and Sustainable Development in Smart Cities: An Overview. Smart Cities, 5(4), pp.1389-1408.
2. Almihat, M.G.M. and Kahn, M.T., 2022. Wind Turbines Control Trends and Challenges: An Overview. International Journal of Innovative Research and Scientific Studies, 5(4), pp.378-390.
3. Microgrid for rural communities under review in solar energy and sustainable development journal.
4. PV stand-alone system for remote areas published in ICEESEN 2022 Turkey.
5. Almihat, M.G.M., Kahn, M.T. and Almaktoof, A.M., 2022. African Journal of Advanced Pure and Applied Sciences (AJAPAS). Applied Sciences (AJAPAS), 1(3).

6. Alsharif, A., Jomah, R.Y., Alshareef, A., Almihat, M., Salah, A. and Al Smin, A., 2022. Hybrid Systems Renewable Energy Based Street Lighting Planning: A Case Study. African Journal of Advanced Pure and Applied Sciences (AJAPAS), pp.31-40.
7. Khonani, Davhana M. and Almaktoof, A M and Almihat, Mohamed, Optimal Sizing of Stand-Alone Photovoltaic Systems for Rural Electrification (July 26, 2021). AIUE Proceedings of the 2nd Energy and Human Habitat Conference 2021, Available at SSRN: https://ssrn.com/abstract=3901360 or http://dx.doi.org/10.2139/ssrn.3901360
8. Altayef, E., Fatih, A., Adel, A.J., Shaima, D., Ehada, H., ABDUL SAMAD, B.D.E.R.E.D.D.I.N., Almihat, M.G.M. and Almaktoof, A.M., 2020, November. Design for a Standalone Wind-Hydrogen Plant A novel in Tripoli-Libya. In AIUE Proceedings of the 18th Industrial and Commercial Use of Energy Conference

1.7.2 Submitted papers

9. An overview of the microgrid system and its structures and compounds submitted to EAI Endorsed Transactions on Energy Web under review
10. Solar system and its control strategies: An overview submitted to frontiers in energy research journal.
11. A Review of AC and DC Microgrid Energy Management Systems submitted to IEEE Access
12. Centralized control system for a multivariable islanded minigrid submitted to AIMS energy.

1.8 Chapters outline

Chapter Two: Literature review

Chapter two discusses distributed generation technologies, the modelling and behaviour of renewable energy sources, namely solar and wind-based, along with generators and energy storage systems. It also goes into detail about power converters and the voltage source inverter (VSI) with its mathematical representation, and lastly, investigates harmonic distortions. Models and performance profiles of REs and components such as the VSI are also developed.

Chapter Three: Minigrid control strategies

Chapter Three focuses on control strategies for micro and minigrids, including centralized, decentralized, and minigrid operation modes, along with power quality control techniques.

Chapter Four: Design and implementation of an algorithm for energy transaction management

Chapter Four consists of the development of an algorithm to control the islanded minigrid. The algorithm, which was simulated using MATLAB IDE, took into account possible scenarios that may take place in an islanded grid where solar and wind plants, known for unpredictability and unreliability, are the major energy sources.

Chapter Five: Control of the output voltage with variable load connected to an lc filter

Chapter Five's topics aimed at eliminating harmonic distortions which may result from the presence of a nonlinear load and VSI. Mathematical model for the LC filter, the RL load, and of the transfer function for the current and voltage in t and s-domains, as well as the study of the system stability, the open and closed loop responses, and the implementation of the P and I controller are the main topics in this chapter.

Chapter Six: Implementation and control of distributed energy systems using Typhoon HIL: rural area case study

Chapter Six consists of the implementation of the islanded minigrid applied to rural areas using real-time software. It investigates possible scenarios related to the behaviour of solar and wind sources to control the rest of the plants (i.e., diesel generator and storage battery) and ensure that the minigrid's operation is not affected.

Chapter Seven: Conclusion

Chapter Seven consists of the overall findings of this thesis.

CHAPTER TWO

LITERATURE REVIEW

2.1 Introduction

This chapter covers in detail topics ranging from distributed generation and the performance and behaviour of renewable energy resources. In addition to solar energy, energy converters and the voltage source inverter are discussed. Wind turbines and their different classifications and modelling are thoroughly explored. Furthermore, the voltage source inverter and harmonic distortions are other topics investigated in this chapter.

2.1.1 Distributed generation technologies

Vaguely known as small-scale generation, the distributed power system may appear to be a new concept, but such is not the case. In the early years of power generation and utilization, focus and planning used to be made with regard to satisfying the needs of a locality close to the generation plant. This imperative was due to the fact that the power system was direct current (DC) and, as such, was not suitable for long-distance transmission due to power losses. Supply and demand as regard the consumer could be balanced via the use of energy backup and storage systems such as batteries that could be connected to the grid.

The distributed energy systems as we know them now are a result of technological advances that came with the emergence of alternating current (AC) systems, which allowed energy transmission over much longer distances and energy economics that lowered the per-unit cost. This has led to the construction of huge, interconnected grids and the connection of a multitude of time-varying loads. In case of a failure of a plant in a grid, other plants with distributed power will compensate for the loss, bringing a feature of security in terms of the operation of the grid.

Interest in distributed generation became acute following technological innovations, economics, and environmental regulations pertaining to the energy sector. The international energy agency (IEA) had to define some priorities around those imperatives, including the development of distributed generation technologies in relation to constraints in the construction of transmission lines, reliability in matching consumer demand, liberalization of the energy market, and concerns about climate change.

Electrical power suppliers find distributed generation a suitable platform to reach out to many customers and meet their demands. Depending on features of interest, customers have the flexibility to choose from which supplier they will buy electricity. The flexibility of distributed generators is further enhanced by their ease in construction and the lead time associated

with their small sizes, small costs, and completion time. Distributed generators are found to be useful in the peak period when the grid electricity tariff goes high. These generators may therefore be used as a hedge against price fluctuations. This has led to the introduction of renewable energy sources, heat applications in power generation, and the potential to improve efficiency.

Reliability and power quality are other features that can be fulfilled through distributed generation. There is always a problem when there is power intermittence in the discontinuity of services and the risks which may be caused by the power instability in connected appliances. However, some services in the production industry, as well as chemicals and hospitals, to name a few, can be severely affected in case of power intermittence. Technologies that have been looked at to address issues of supply intermittence include the uninterruptible power supply (UPS), gas and diesel standby generators, etc.

Microgrids (MGs) are a critical component of the electrical network due to their capacity to mitigate issues resulting from rapid energy demand growth. Therefore, the proper design of MGs has been one of the primary concerns of academics and engineers(Salehi & , Herminio Martínez-García, 2022). Human population growth is responsible for the daily rise in energy use. In addition, industrialization makes energy the fundamental factor in improving the lives of urban and rural residents, given the depletion of fossil fuel reserves and the escalating cost of these resources. The increased energy demand in urban and rural regions pushes for the adoption of renewable energy sources, also known as alternative energy sources, including solar and wind, which are the most often utilized. These sources are combined into a hybrid system with two or more generation units and an energy storage system or fossil fuel generator for backup during peak demand hours (Frederiks et al., 2015).The concept of the microgrid is described by (Lasseter, 2001)as a single system with various power sources combined as a single source to serve the consumer's energy needs. It is anticipated that an increase in the use of small-scale energy-producing devices would increase global power capacity and facilitate the integration of renewables into the power grid. Microgrid offers a natural platform for addressing the challenges of combining renewables by offering a small electric grid with decentralized energy generation and energy storage systems (Buraimoh et al., 2022). Several nations throughout the globe have examined the construction of renewable-energy-based microgrids for rural electrification and procedures under implementation to support the formation of local energy communities. For example, Poland decided to establish an energy cooperative to bridge the gap in the development of the civil dimension of energy on a local level, enhancing the efficiency of using renewable energy sources in rural areas and reducing the electrification issue following the European Union's energy development strategy (Jasiński et al., 2021). A MG provides electricity to remote

towns, islands, or for customized demand purposes, thereby decreasing power loss. Incorporating RESs with varying power ratings into a distribution network is crucial. Because of this, operating microgrids is difficult, especially when it comes to ensuring reliable power distribution in DG units and maintaining consistent network power quality. Therefore, innovative approaches to control (such as AI, predictive control, and multi-agent systems) must be developed and put into place in order to address both power quality and distribution problems in the long term. In addition, microgrids often use renewable energy sources for most of their DG units, as these sources have very low inertia. However, there may be significant voltage and frequency variations in these low-inertia DG units due to sudden disruptions (Hossain et al., 2017). Hence, the microgrid can reduce the total cost of generated electricity by developing systems and replacing diesel generators to provide the community with a clean and sustainable power supply to cover their daily power needs. As single microgrids provide community demands, and individual microgrids also provide backup generation for other microgrids in the community, the community microgrid structure would improve the reliability and affordability of the community's power supply. In addition, individual microgrids could lower their installed capacity requirements with optimal power sharing, which might be necessary for crowded urban populations (Che et al., 2015).

2.2 Renewable energy resources and drawbacks

The rationale behind this chapter pertains to the existing drawbacks of RE sources in terms of providing primary energy. Three sources of energy considered for this study are solar, wind, and generator types of energy. Solar power plants receive primary energy from the sun’s radiation, which depends on the weather and time of the day, as well as the clarity between the photovoltaic device and the sunbeam. As for wind power plants, their performance depends on the speed of the wind as well as the mechanisms involved in the operation of the turbine. Among the three RE systems of interest, generators are the only ones with a relatively stable energy source as their performance depends on the fuel supply and the condition of the generator’s essentials.

2.3 Solar energy sources

Solar energy is the most viable alternative energy source. It is clean and is meant to be on as long as the sun keeps shining. The following section discusses some performance of solar energy with emphasis on the issues that may adversely affect power generation through photovoltaic systems (PVs.

Photovoltaic systems for general and rural applications operate in networked and island modes. The benefit of mobile systems is their ability to track the sun and maximize solar

energy during the day. In grid-connected mode, the solar system's electrical energy is injected into the primary grid using inverters, which alter the shape and match the voltage level and frequency of the photovoltaic system's electrical energy. Due to the injection of voltage and current, the use of photovoltaic power plants connected to the primary grid in a centralized or decentralized way (while amplifying the current energy in the distribution network) prevents the voltage drop of the distribution network (Ranjbaran et al., 2019).

Maximum power point tracking (MPPT) is an optimization method that makes small but consistent adjustments to the modules' electrical working points. As a result, PV modules can produce as much energy as possible (Ibrahim et al., 2021).The MPPT coupled system allows for a much more flexible connection between the PV panel and the customer than the direct-connected technique. Moreover, the MPPT tracker may guarantee that the PV panel operates at its Maximum Power Point (MPP) while the converter fulfills the operational requirements of the load. However, without storage, the consumer must operate at variable power and quickly use the whole solar panel's output.

2.3.1 Photovoltaic effect

Photovoltaic energy is based on the photoelectric effect. This photovoltaic cells transforms electromagnetic radiation into electrical energy . The sun emits this kind of radiation, which has the advantage of being limitless and applicable everywhere in an area. Additionally, it is a clean energy source since PV modules generate power without generating greenhouse gases (Choudhary & Srivastava, 2019).However, this resource has two downsides: its production is fundamentally dependent on climatic conditions, and a large surface area is needed to create significant amounts of energy owing to PV cells' relatively low efficiency (Azizi et al., 2018). The performance of PV cells is defined by the efficiency with which they convert energy from the sun. Usually, sunlight with a modest amount of energy may successfully create electricity, and most of this sunlight will be reflected or absorbed by the cell's composition. The maximum power point is the optimal operating temperature and light intensity for each photovoltaic cell. Thus, it represents a typical current-voltage curve illustrating the output characteristics of a PV cell at a particular cell temperature and solar irradiance level (Nieto-Nieto et al., 2020).Hence, the following mathematical equations can be used to calculate the output power (Equations 2.1 and 2.2).

$$I_{ph} = \frac{G}{G_{ref}} [\, I_{ph}, ref + \mu_{sc} \left(T_{cell} - T_{cell)}\right] \qquad \text{Equation 2.1}$$

$$I = I_{ph} - I_0 \left[e \frac{(V + R_s I) q}{nkT} - 1 \right] - \frac{(V + R_s I)}{R_{sh}} \qquad \text{Equation 2.2}$$

Where I_{ph} is short-circuit current (A), $G_{ref} = 1000\,W/m^2$ reference solar irradiation at 25^0, and $G\left(\frac{W}{m^2}\right)$ is the solar irradiation.

$\mu_{sc}(A/K)$ refers to temperature coefficient, while $T_{cell}(K)$ is the actual cell temperature, $I(A)$ is the PV output current, $I_0(A)$is the reverse saturation current, $q(C)$ is the electron charge, $K(J/K)$ is Boltzmann's constant, $V(V)$ refers to PV output voltage, $R_S(\Omega)$ is a series resistance, and finally, $R_P(\Omega)$ refers to parallel resistance.

2.3.2 Solar energy behaviour modelling

The performance of PV plants depends on multiple factors, of which the most determining are the intensity of the sun's radiation, the area of the PV array, the conversion efficiency of PV cell as well as the temperature in the environment of the PV arrays. The intensity of the sun's radiation, also referred to as irradiance, is itself a function of the time of the day and the sky condition of the day. The peak value of the irradiance depends on the geographical position where the plant is located on the globe.Mathematically, the instantaneous value of the Photovoltaic system's(PV's) output power is provided by Equation 2. 3, while the profile of the irradiance can be expressed as per Equation 2.4.

$$P_{PV} = f(I, A, \eta) \qquad \text{Equation 2.3}$$

$$I = f(S_c, t_d, I_m, G_l) \qquad \text{Equation 2.4}$$

Where P_{PV} stands for the PV output power,I stands for the instantaneous irradiance, A stands for the area of the PV arrays, η stands for the efficiency of the PV cell, S_c stands for the sky conditions, t_d stands for the time of the day, I_m is the peak value of the irradiance, and G_l stands for the geographical position where the plant is installed on the globe. Altogether, the above-mentioned variables play a role in the performance of PV arrays.

2.3.3 Instantaneous irradiance

The irradiance or sun's radiation, which is the power received per unit area, is qualified as instantaneous due to the variation of its intensity during the course of the daytime. The intensity of the irradiance is at its minimum at sunrise since the sunbeams are parallel to the PV arrays and thus have no incidence. The intensity gradually increases to reach its peak at noon when the sunbeams directly strike the PV arrays, then decreases during the afternoon and reaches its lowest value once again at sunset. In normal conditions, the standard value of peak irradiance is 1000 W/m^2, that is, the intensity of the sun's radiation on the day of clear sky air mass (AM) of 1.5 and an incident angle normal to the PV arrays. This, in fact, corresponds to the peak value of the irradiance occurring at noon.

2.3.4 Area

Along with instantaneous irradiance, area is another determining variable of the output power of the PV arrays. The larger the area, the more input power is received by PV arrays. Equation 2.5 is a mathematical expression of the power received by PV arrays:

$$P_R = I * A \qquad \text{Equation 2.5}$$

Where P_R stands for the power received by the PV arrays.

Due to the low efficiency of the PV cells in the plant, a relatively large area of PV panels is required for energy productionBut with PV production costs decreasing to make them affordable, PV plants are becoming more and more mainstream as a means of power production.

2.3.5 Time of the day

Due to a rotary motion around itself, a location experiences different irradiances during the daytime, thus, different energies at various times of the day. Generally, on a day in which the duration of daytime equals that of night time, the sun rises at 6 AM and sets at 6 PM. In between those time points, a location will experience different levels of irradiance and, therefore, power. In other words, the time of the day correlates with the incident angle by which the sunbeam strikes the PV arrays. The time of the day influences the amount of irradiance an area on the globe receives, along with all the components and variables of solar energy, such as temperature and heat. While the revolutionary movement of the earth is done in a full cycle of 360^0 (24 hours), an area of the globe can only see the sun for half a cycle of 180^0 (12 hours). In other words, the irradiance is directly proportional to the cosine of the angle the sunbeam forms with the vector normal to an area of the globe. The mathematical expression of the variation of the irradiance during the course of a day is given by Equation 2.6.

$$I_d \approx \begin{Bmatrix} I_m \cos(\theta) \\ \theta \epsilon [-90,90] \end{Bmatrix} \qquad \text{Equation 2.6}$$

Where I_d and θ are, respectively, the irradiance dynamics over a day, and the angle formed between the sun rays and the vector normal to the area surface. I_m is the peak value of the irradiance

As shown in Figure 2.1, the change in irradiance with respect to the daily time progression may be understood. The abscissa of the graph shows the course of the day in terms of hours, while the ordinate of the graph shows the intensity of the irradiation, expressed in watts per square meter (W/m^2).

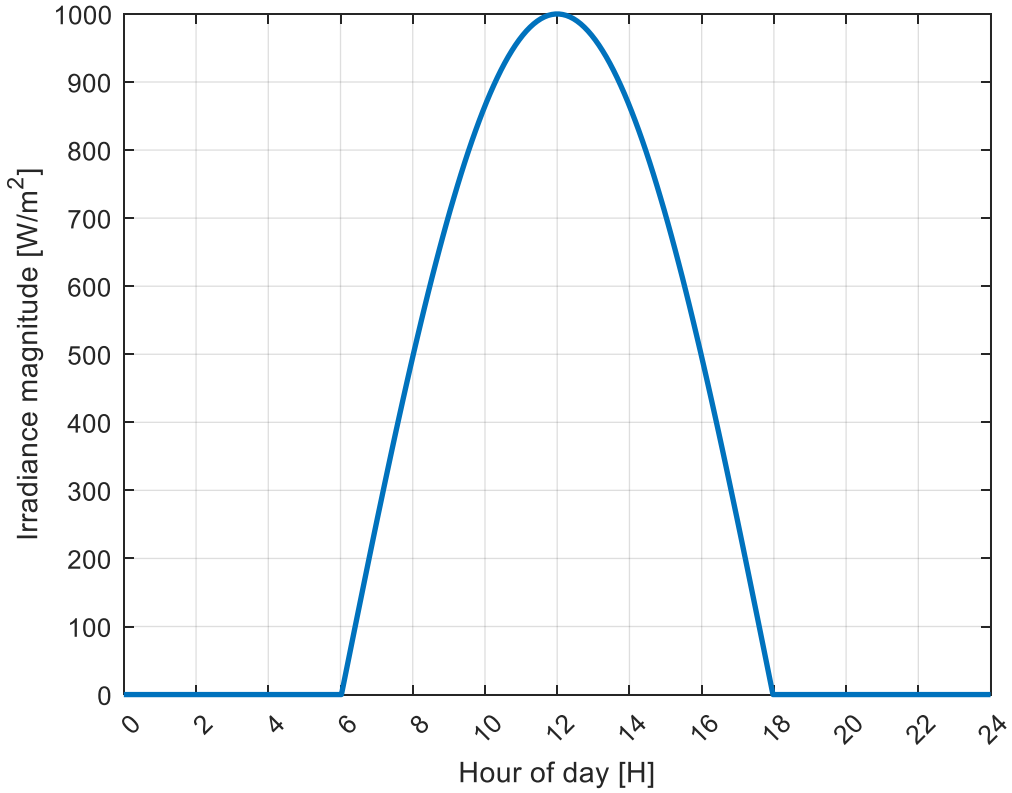

Figure 2. 1: Solar energy daily profile

2.3.6 Seasons and geographical position

Season and geographical position are two other interrelated factors that dictate the performance of a PV system. Seasons depends on the latitude where a region is located on the globe. Depending on the season, the intensity of the irradiance that an area experiences will vary according to the sun's apparent position at a point in time. During summer, the sun will be in an area providing its highest levels of irradiance, but will gradually withdraw during autumn, providing fair levels of irradiance. The sun will end up providing its lowest radiation levels during winter, while such levels will begin to rise during spring. As the season is defined by the position of the sun between the tropic of Cancer and the tropic of Capricorn, which are located at 23^0 and -23^0, respectively, the effect of the season on the performance of PV arrays will also depend on the location of an area and that of the sun at a point in time of the year. Seasons are closely related to atmospheric conditions that manifest in ambient temperatures and humidity, rainfalls, wind movements, and dust that, in turn, decrease the intensity of the light received (Tanesab et al., 2018).

On the other hand, the geographical position where PVs are planted will also determine the amount of irradiance that is received. In a sense, the geographical position of an area determines how far the area is relative to the sun and how long it could take the light to reach the area. Areas around the equator will have better experiences regarding the weather

balance, while those in the intertropical zone experience significant weather changes as a result of changes in season (Shravanth Vasisht et al., 2016).

Therefore, the expression of solar radiation can be expressed as per Equation 2.7.

$$I \approx I_d \sin(\varphi), \varphi \epsilon [-23^0, 23^0] \quad \text{Equation 2.7}$$

Expanding the expression of I_d in Equation 2.7 yields Equation 2.8 as follows:

$$I_d \approx I_m \sin(\theta) \sin(\varphi), \begin{Bmatrix} \varphi \epsilon [-23^0, 23^0] \\ \theta \epsilon [-90^0, 90^0] \end{Bmatrix} \quad \text{Equation 2.8}$$

Where I_s and φ are, respectively, seasonal irradiance and the angle corresponding to the apparent motion of the sun between the tropics. I_m is the peak value of the irradiance.

The following diagram illustrates how the occurrence in issue may be academically explained by visual representation within a three-dimensional (3D) framework. Appendix 2.1 contains the computational guidelines used to create the visual depiction of this phenomena. This is relevant to the daily fluctuation in solar energy levels in the area of the Earth bordered by the tropics.

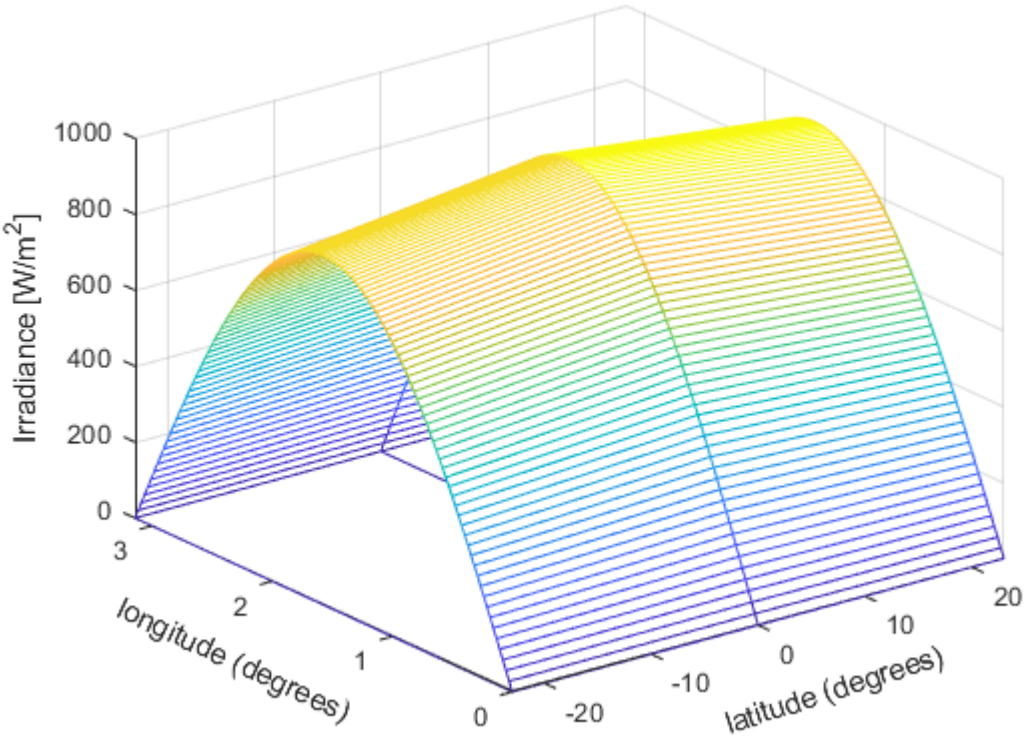

Figure 2. 2: Solar energy daily profile between the tropics

The mathematical expressions developed considered a fully illuminated day. However, further effects on the output includes the attenuation caused the atmospheric conditions and possible shading.

2.3.7 Atmospheric conditions and shading objects

On the one hand, atmospheric conditions in the form of clouds and precipitations also attenuate the levels of irradiance or block the sun's radiation either partially or fully. On days of such conditions, PV plants may be out of service or perform poorly. On the other hand, objects can obstruct the path of sunbeams to PV arrays. These obstructions may be shadows of objects interfering with the flow of current within the cells, thus attenuating the level of current and power produced by the PV system. These objects include but are not limited to tall buildings, trees, towers, raindrops, and bird droppings, to name but a few. The effects of shading and non-uniform atmospheric conditions in the environment of the PV system is a cause of non-uniform luminescence of the PV cells. As a result, the maximum power point tracker becomes inefficient because it will detect multiple local maxima power points, of which only one is a global power point. Besides this, the resulting mismatch of PV output power forms another shortfall in terms of the effective exploitation of PV power systems (Bidram et al., 2012)

As for the mathematical expression of the irradiance in these conditions, a brightness factor shall be introduced in the equation to describe the uniform brightness of the irradiance (Equation 2.9).

$$I = \alpha I_s \qquad \text{Equation 2.9}$$

Where α is the sky clarity that can take values ranging from 0 and 1.

The expansion of the expression of the irradiance yields Equation 2.10:

$$I = \alpha I_m \sin(\theta)\sin(\varphi), \begin{Bmatrix} \varphi\boldsymbol{\epsilon}\,[-23^0, 23^0] \\ \theta\epsilon[-0, 180^0] \\ \alpha\epsilon[0,1] \end{Bmatrix} \qquad \text{Equation 2.10}$$

φ is the angle corresponding to the apparent motion of the sun between the tropics, I_m is the peak value of the irradiance.

The daily solar energy pattern at tropical latitudes is shown in Figure 2.3, which also depicts the subtle variations in solar irradiance caused by air conditions and shading effects. Due to Earth's axial tilt, the picture shows how sun intensity changes throughout the day, peaking around solar noon. This representation extends beyond irradiance distribution by include atmospheric factors that affect observed departures from ideal circumstances, such air mass and cloud cover. The requirement for careful placement of solar equipment is further

emphasized by the consideration of shadowing from terrain and buildings. In essence, Figure 2.3 emphasizes the complexity of tropical solar energy dynamics, which is essential for developing an all-encompassing energy plan.

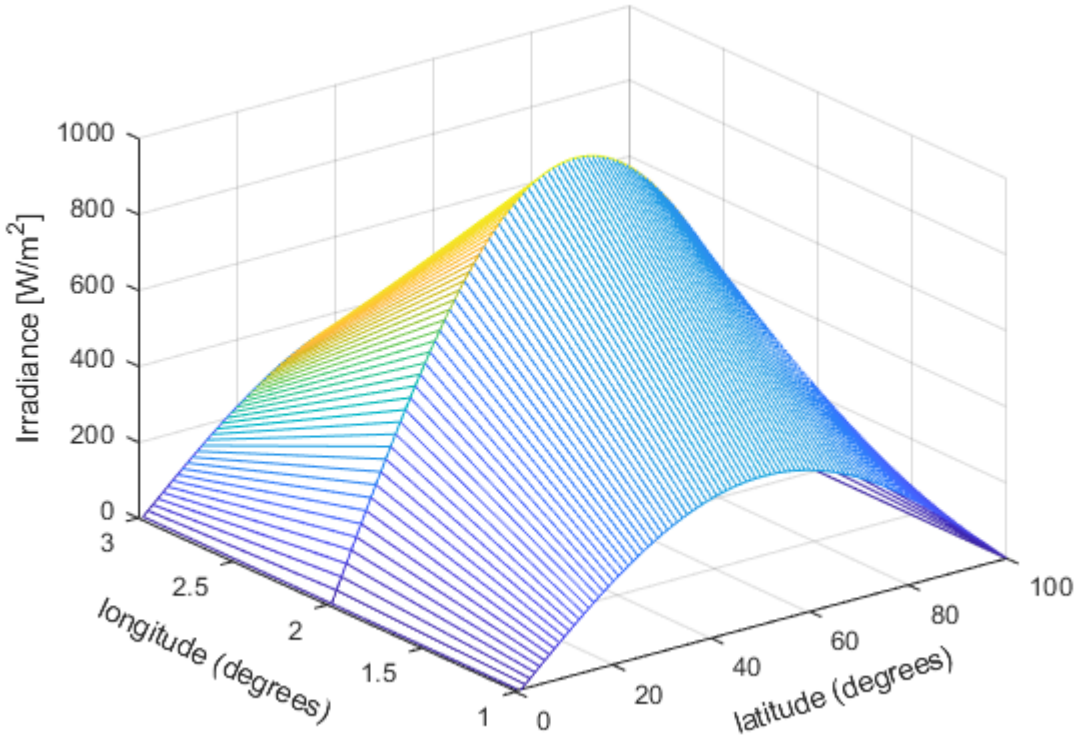

Figure 2.3 : Solar energy daily profile between tropics including atmospheric conditions and shading

Where I and α are, respectively, the irradiance and the sky clarity rate.

In the case in which the attenuation is non-uniform due to the irradiance received by a PV array when partially shaded, the mathematical representation becomes complicated, thus making maximum power point tracking techniques inefficient due to the emergence of multiple maxima power points.

2.3.8 PV power converters

Power converters depend on the primary power harvested by PV arrays. Their efficiency is around as high as 98.8%. There are three possibilities to process primary solar power into end-usable power: module converters, string inverters, and central inverters. The latter two power converters (string and central inverters) dominate the market in terms of solar energy processing, while the use of module converters is yet to expand.

Central inverters are highly involved in the commercial sector and utility-scale PV systems with a power rating of at least 100 $kW_{p,}$ as well as small-scale power systems. String converters find applications in power ratings ranging between 1 kW_p and 100 kW_p while in the residential and small-scale commercial sectors at 98.5% maximum efficiency. As for lower power applications such as rooftop PV units and off-grid power systems, power optimizers (98.8% maximum efficiency) and micro-inverters (90-95% efficiency) are preferable due to their power and efficiency, where the MPPT is performed on a panel level. However, the converters' and inverters' outputs often present characteristic mismatches in terms of the amplitude in current, voltage, and frequency, requiring further electronic circuitry interface.

2.4 Module converters

Microinverters and power optimizers are major converters utilized at a module level and can be DC-DC or DC-AC and may have a DC or AC load with an operational voltage ranging between 30 and 60 V (Arbetter et al., 1995).They can be connected in cascade to match the power requirements of microgrids or nanogrids. Power optimizers are preferable as they lead other technologies with regard to the best conversion efficiency. However, even in a distributed power system, the MPPT process is performed at a panel level to avoid the effect of a faulty panel on the entire power system. However, the system design is complex due to the number of electronics involved in the construction of all the optimizers.

2.4.1 Buck converter

The buck converter steps down the voltage coming from the PV cells and presumed to be higher than the incoming voltage. The output will be proportional to the duty cycle of which the value ranges between 0 and 1, exclusive of the interval limits or extrema (Equation 2.11).

The schematic representation of a buck converter, a crucial part of power electronics and voltage control, is shown in Figure 2.4. The buck converter, sometimes referred to as a step-down converter, is a crucial component for effectively converting a greater input voltage to a lower output voltage.

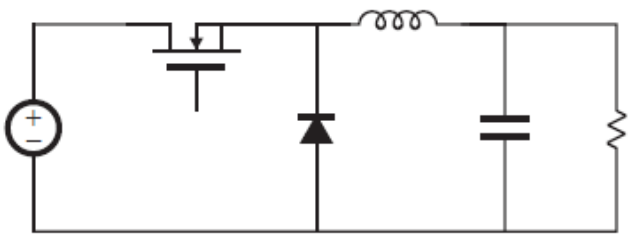

Figure 2. 4: Schematic diagram of a buck converter

The graphical depiction highlights the complex arrangement and connections that are part of the operating architecture of the buck converter. An input voltage source, an inductor, a switching device (commonly implemented as a transistor), a diode, an output load, and control circuitry are generally included in this arrangement. The conversion of electrical energy from the input source into a regulated and lowered output voltage across the load is the main goal of the buck converter.

$$V_{out} = DV_{pv}$$ Equation 2.11

Where V_{out} and V_{pv} are the DC voltage and the PV voltage, respectively, while D is the duty cycle.

2.4.2 Boost converter

The boost converter is a particular kind of DC-DC power converter used to raise the source voltage. In photovoltaic (PV) systems, where the output voltage from solar panels may not always match the appropriate voltage level for the intended use, this is very helpful. It is suggested from Figure 2.5 that the PV voltage is substantially lower than the desired output voltage. An inductor, a diode, a capacitor, and a switch (usually a transistor) are used in a boost converter's basic function in a particular arrangement. Current passes through the inductor when the switch is closed, storing energy in its magnetic field. The inductor then releases this accumulated energy when the switch is opened by generating a voltage across its terminals, leading to an output voltage that is greater than the input voltage.

The relationship between the input and the output is given by Equation 2.12.

$$V_{out} = \frac{V_{pv}}{1-D}$$ Equation 2.12

V_{out} and V_{pv} are the DC voltage, and D is the duty cycle.

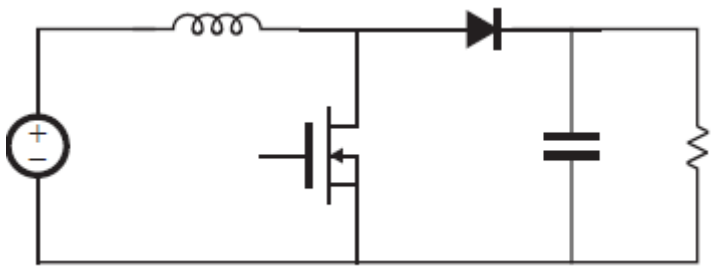

Figure 2.5: Schematic diagram of a boost converter

Where D is less strictly greater than 0 and less than 1.

2.4.3 Buck-boost converter

A flexible electrical device known as a buck-boost converter is capable of modifying the input voltage to produce a certain direct current (DC) output level. This capability is achieved by enacting voltage amplification or attenuation (as shown in Figure 2.6). The operating characteristics of a boost converter and a buck converter are combined in this converter. It is notable, however, that the polarity of the output voltage that results from the execution of voltage augmentation or reduction procedures undergoes inversion. The buck-boost converter, which may be used for both voltage control and power electronics applications, basically achieves its functionality by cleverly managing the voltage connection.

. This feature of versatility makes this type of converter preferable over those reviewed above (Equation 2.13).

$$V_{out} = V_{pv} * \frac{-D}{1-D}$$ Equation 2.13

V_{out} and V_{pv} are the DC voltage, and D is the duty cycle.

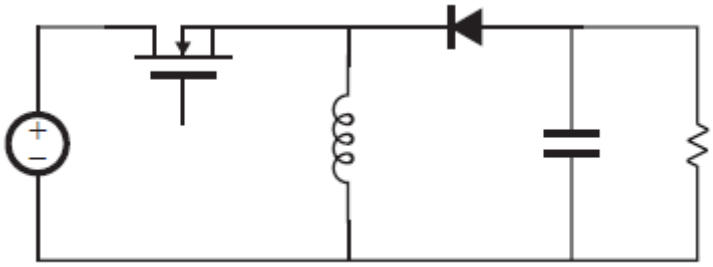

Figure 2. 6:Schematic diagram of a buck-boost converter

The buck-boost converter is a stunning example of engineering creativity, effortlessly combining voltage amplification and attenuation functions inside a single framework. It plays a crucial role in many applications, from renewable energy systems to portable electronic devices, because to its versatility in meeting various voltage regulation demands while controlling polarity. The buck-boost converter's adaptive abilities are positioned to continue playing a crucial role in reshaping the field of modern power electronics as technology develops.

2.4.4 Cuk converter

The distinction between this particular variant of converter, Elboarte, and those appraised earlier, resides predominantly in the count of constituents. In lieu of a singular configuration, the Cuk converter adopts a setup comprising of dual inductors and dual capacitors, all orchestrating an analogous operation to that of a buck-boost converter. Refer to Figure 2.7

for an illustrative representation of the schematic diagram delineating the structural layout of the Cuk converter.

i.e., it increases or decreases the input with inverted polarity according to the load needs (Figure 2.7).

$$\frac{V_{out}}{V_{in}} = \frac{D}{(1-D)}$$ Equation 2.14

V_{out} and V_{pv} are the DC voltage, and D is the duty cycle.

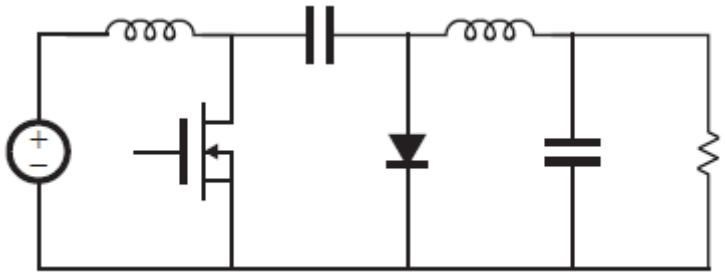

Figure 2. 7: Schematic diagram of a Cuk converter

The Cuk converter deviates from the conventional single inductor or capacitor design seen in other converters by using two inductors and two capacitors. The Cuk converter can successfully carry out its duty thanks to this dual-inductor, dual-capacitor configuration, much like a buck-boost converter.

2.4.5 SEPIC

The SEPIC converter has a slightly different configuration with two inductors and two capacitors, a switching device, and a diode, as shown in Figure 2.8. It works by increasing or decreasing the input voltage and keeping the polarity (Equation 2.15).

$$V_{out} = V_{pv} * \frac{D}{1-D}$$ Equation 2.15

V_{out} and V_{pv} are the DC voltage, and D is the duty cycle

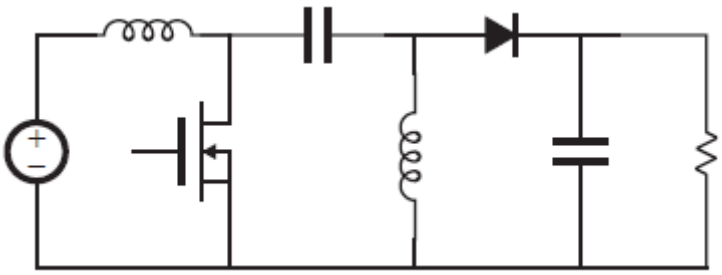

Figure 2. 8: Schematic diagram of a SEPIC

As shown in Figure 2.8, the SEPIC (Single-Ended Primary-Inductor Converter) has a marginally unique configuration that includes two inductors, two capacitors, a switching mechanism, and a diode. The SEPIC converter's operating concept is based on modulating the input voltage's magnitude to produce either amplification or attenuation while simultaneously preserving the input voltage's original polarity. Please refer to Figure 2.8, which shows the complete schematic depiction of a SEPIC converter, for an illustrative visual reference.

The converters reviewed so far are seen as ideal. For non-ideal converters, the internal resistance of the inductor is also considered. This significantly changes the expression of the conversion ratio of the converters. Equation 2.11 shows the conversion ratio of a buck converter, Equation 2.12 shows the conversion ratio of a boost converter, Equation 2.13 shows the conversion ratio of a buck-boost converter, Equation 2.14 presents the conversion ratio of a Cuk converter, and lastly, Equation 2.15 shows the conversion ratio of a SEPIC converter.

These converters (the buck, boost, buck-boost, cuk, and SEPI) can only offer low conversion rates. Stepping up the module level voltage to the voltage required at the inverter level, especially for grid-connected PV applications, might be problematic. In the design of power optimizers for such applications, there is a need to reduce or avoid the complexity that may be due to the need for a large number of power optimizers to achieve a large conversion ratio. This would require having multiple power optimizers in parallel, which will result in efficiency reduction.

2.5 Wind energy

2.5.1 Background

Wind power integration has been a topic of interest circa the late 1970s to early 1980s, which has seen wind power deployment growing exponentially (Hernández-Escobedo et al., 2014).In the United States, the contribution of wind power plants (WPPs) to the grid has been forecast to hit the 20% mark by the year 2030 (Singh & Santoso, 2012).The exploitation of wind energy began slowly with turbines of a generation capacity of about 10 kW in the 1970s, but quickly picked up, and now 5 MW wind turbines are commonplace (Singh & Santoso, 2012)

Microturbines are small turbines that generate power from wind, water, and other fuels, including natural gas. Microturbines provide more benefits than other small-scale technologies, including fewer moving parts, smaller size, lightweight, improved efficiency, reduced emissions, lower power prices, and the ability to utilize wasted energy (Fershalov et

al., 2021). Hence, the need for renewable energy sources has expanded dramatically in recent years. Wind energy represents one of the most cost-effective and non-polluting means of generating electricity from renewable sources. Wind generators are used in grid-connected and stand-alone systems for remote power loads. The wind energy conversion system collects wind energy from the wind turbine and transforms it into electrical energy by employing a generator in fixed-speed and variable-speed configurations. Due to low energy production, the strain on mechanical parts, and poor power quality, fixed-speed wind energy conversion systems have been replaced by variable-speed systems to minimize compressive damage and aerodynamic noise.

These mechanisms may be regulated to allow the turbine to function at its most significant power factor and receive the most energy from the wind under varying wind conditions (Igwemezie et al., 2019).

Even though wind technology was consistently becoming fruitful, with its level of penetration in the domain of energy deepening, integration of wind power plants (WPP) in large-scale utility has remained an unsolved issue. Literature has highlighted the challenges and impacts that integrating WPPs into the large-scale grid could pose, thus making this topic a focal point of research in the area of energy generation as early as the 1970s (Igwemezie et al., 2019). Issues pertaining to the intermittent aspect and the reliance on an induction asynchronous generator were found to be the most critical. The prospect of viewing wind technology as a potential alternative to conventional power generators would come at the cost of grid stability (Slootweg et al., 2003).

Literature about integrating WPP into the large-scale grid has been produced in several countries, including Denmark, Sweden, Germany, California, India, and the US, among others. However, it remains a priority to establish a dynamic model of wind generators with a collaboration of key stakeholders in the energy domain at all levels, such as power systems experts, planners and operators, energy consultants, and WPP developers themselves.

2.5.2 Wind turbine technology

Wind turbine (WT) technology consists of horizontal technology and vertical technology. Horizontal technology is the most dominant of modern utility-scales, with power ratings ranging between 500 kW and 5 MW. The output of the WT is expected to handle the fluctuation of wind power resulting from the inherent variation of wind speed. Major components of a WT comprise:

- Rotor with blades and hub
- Drive train (shaft, gearbox, mechanical brake, and electrical generator)

- Nacelle and main frame
- Tower and foundation

Electrical system (cables, switchgear, transformer, power electronic components)

A visual depiction of a wind turbine (WT) is shown in Figure 2.30, along with a caption that lists each of its individual parts. The picture serves as a graphic representation of the main essential components that make up the wind turbine system.

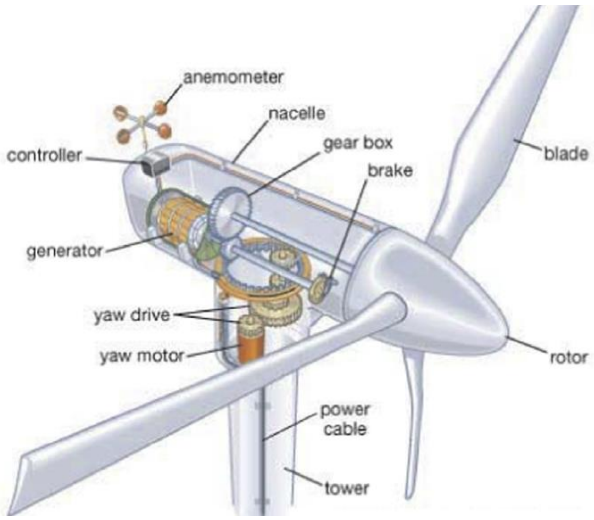

Figure 2.9: Wind turbine components

2.5.3 Wind turbines classification

To implement a wind plant, one needs hundreds of wind turbines (WTs) of the same type or technology. Parameters such as cost, complexity, structural design, efficiency, and wind power extraction are elements referred to when designing wind turbines. Wind turbines can be classified in two ways: firstly, according to the orientation of the rotation axis and, secondly, according to the speed and power control methods (Sánchez & Rios, 2016).

According to the orientation of the rotation axis of the turbine, there is a horizontal axis wind turbine (HAWT) and a vertical axis wind turbine (VAWT). The requirements of the power to be extracted and the performance of the WT type will determine which type suits land or sea applications (Johari et al., 2018). HAWTs are known for high conversion efficiencies that are associated with the blade design and their orientation that favour access to strong winds. However, HAWTs require a strong tower capable of supporting the usually heavyweight nacelle in addition to strong wind forces. This type of WT also involves a high installation cost to ensure a robust and durable structure is in place. On the other hand, VAWTs provide the advantage of requiring low installation costs. However, their conversion efficiencies are lower due to the fact that winds that reach the lower part of the blades are weaker, while the aerodynamic orientation limits the performance (Pagnini et al., 2015).

2.5.3.1 Classification according to the speed

According to the rotor speed control, there are four major types of wind turbines: fixed-speed WT, variable slip WT, doubly-fed induction generator WT, and full-converter WT(Ruiz et al., 2018).

2.5.3.2 Classification according to the type of generator

A WT can be configured to run on any three-phase generator. The generator's frequency of operation can be adapted to the frequency of the grid with the help of electrical converters. Synchronous and asynchronous generators are mostly used in the operation of WTs. Generators are classified as follows:

Type 1: Asynchronous induction generators such as the Squirrel Cage Induction Generator (SCIG) and the Wound Rotor Induction Generator (WRIG) (Wu et al., 2008).

Type 2: Synchronous generators, such as Permanent Magnet Synchronous Generator (PMSG) (Badrzadeh & Kingdom, 2004). and the Wound Rotor Synchronous Generator (WRSG) (Orlando et al., 2013).

Other types include the high voltage generator (HVG) and transverse flux generator (TFG).

Moreover, WTs can also be classified according to the wind speed control.

2.5.4 Classification according to the speed control

2.5.4.1 Fixed speed control

The SCIG WT is a basic, low-cost but robust and reliable wind generator. It represents most of the wind power plants installed so far. It operates at a more or less constant speed determined by a fixed gear ratio, thus allowing only little fluctuation in the rotor speed (1%), and runs on a squirrel cage induction machine directly connected to the grid. The speed must also be aligned with the frequency of the grid and the number of poles of the generator. In most cases, the WT does not have blade pitching capability. In terms of wind power control, control schemes available for FSWTs (fixed-speed wind turbines) are passive control, encompassing pitch control, and active stall control as shown below.

a) Passive control

Pitch control: In pitch control, blades are not rigidly attached to the hub and can be reoriented in or out of the direction of the wind at convenience to increase the wind extracted power. The pitch control accommodates the power control as it allows for start-up control and emergency stop of the generator. A critical drawback of pitch control is that small changes in the wind speed may result in huge disturbances in output power, given that pitch control cannot respond fast enough to address the fluctuations in the output power.

b) Active stall control

This preserves all the features of power quality parameters through the flexible mounting of the blades to the hub. It also caters for start-ups and emergency stops. The only issue with this control technology is that it is pricy.

On the other hand, the blades are fixed to the hub and designed in a way such that the flow of the air over the blades flexes the latter to ensure that maximum power is extracted. However, at high-speed wind power, the laminar flow of the air becomes turbulent. To limit overloads to the induction machines, the blades were designed to extract a limited power. Consequently, fixed-speed WTs operation is sub-optimal regarding the exploitation of the wind as well as the reactive power compensation. With FSWTs, maximum efficiencies can only be achieved at a specific speed of the wind, while it decreases at different speeds.

An illustration of the spatial layout and configuration of a wind turbine with a fixed operational velocity is shown in Figure 2.10. The figure is essential for communicating a visual representation of the precise configuration and layout relevant to the production of wind energy, with an emphasis on wind turbines that rotate at a constant speed. The graphic clarifies the placement and relationships of the individual parts that make up the wind turbine system by using schematic illustration. Understanding the relative placement of parts like the rotor, nacelle, tower, and fundamental support structures is made easier with the help of this graphic. The illustration provides a clear understanding of the physical characteristics and connections found in a wind turbine that operates with a constant rotational speed.

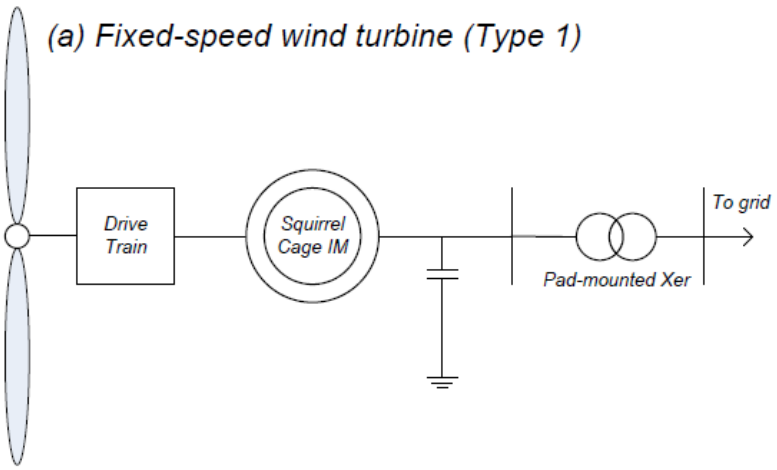

Figure 2.10: Layout for fixed-speed WT

2.5.4.2 Variable speed WTs (VWTs)

Variable speed is a phrase that regroups the remaining types of WTs. They are designed to operate at a certain range of rotor speeds and allow blade-pitching. Blade-pitching is a

feature that helps extract more power from wind energy. VWTs have a special ability to adjust the rotor speed depending on the wind speed to meet the grid's power and frequency requirements. To make this happen, the ratio of the tip speed to that of the wind must be kept optimum to record maximum efficiencies at different speeds. Figure 2.11 shows the layout of a variable speed WT.

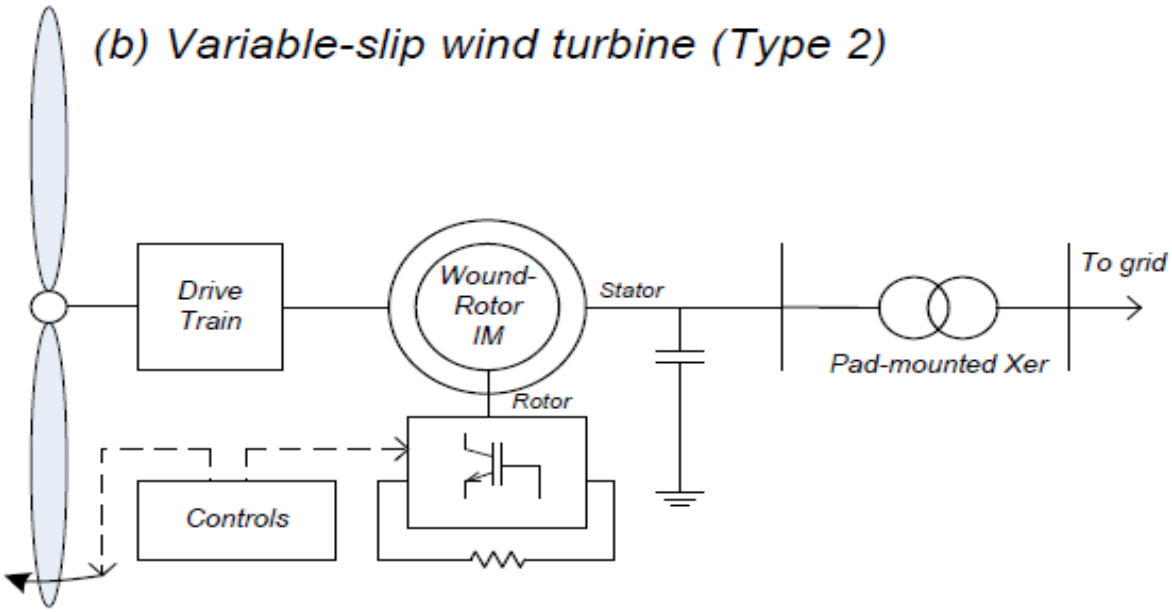

Figure 2.1: Layout for a variable speed WT

An illustration of the design and functioning components of a variable-speed wind turbine are shown in Figure 2.11. It provides a thorough visual grasp of how structural components interact with the dynamic operational processes that are unique to this technology, which helps people comprehend its operational dynamics in relation to renewable energy systems.

2.5.4.3 Limited variable slip (VS) or dynamic rotor resistance (DRR) WTs

The variation of the speed in the VS/DRR WTs occurs by varying the value of the electrical resistance in the rotor circuit of the induction machine thus producing slip or speed variation of up to 10%. The drawback of this type of WT manifests in power losses that occur in the form of heat dissipated at the level of the rotor resistance. Figure 2.12 shows a diagram of a VS WT. A restricted variable speed wind turbine's operational dynamics are illustrated in Figure 2.12. With regard to wind energy conversion, this illustration helps to clarify the complex relationship between energy optimization and system dependability.

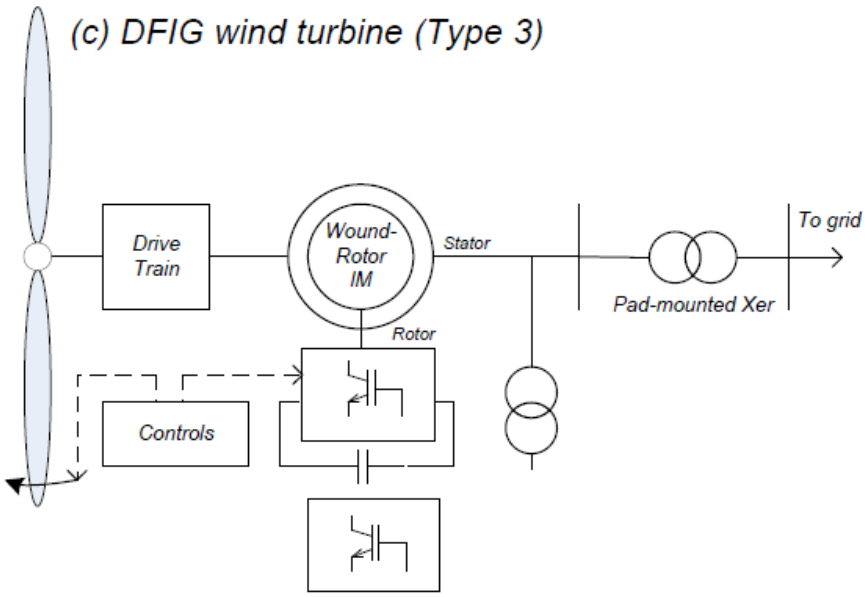

Figure 2. 22: Limited variable speed WT

2.5.4.4 Variable speed with partial-scale frequency converter

This control technology typically applies to the doubly-fed induction generator (DFIG) WTs.

The design of the DFIG WT derives from the limited-speed WRIG with a partial-scale frequency converter at the rotor level. The presence of these converters is to recover the power loss that might have occurred in the rotor resistance during the slip process. An approach of flux vector control decouples active power from the reactive. Thus, DFIG turbines maximize power extraction while reducing mechanical stresses.

2.5.4.5 Variable-speed with full-frequency converter

In full-frequency converter WTs, the AC-DC-AC converter is the only path of electrical power from the turbine to the grid. These WTs may employ synchronous or induction generators while offering the advantage of control independency between the active and reactive power. This control scheme caters for the variations of the WT speed in full, and the generator is connected to the grid through the full-scale frequency converter that also performs the compensation of the reactive power and allows a smooth connection to the grid. The generators of WRSG, WRIG, and PMSG can be excited electrically.

One of the major drawbacks observed relate to the speed control, especially at start-ups and emergency stops of generators. To address this shortfall, a soft-starter technology was referred to. Figure 2.13 shows a full-converter WT.

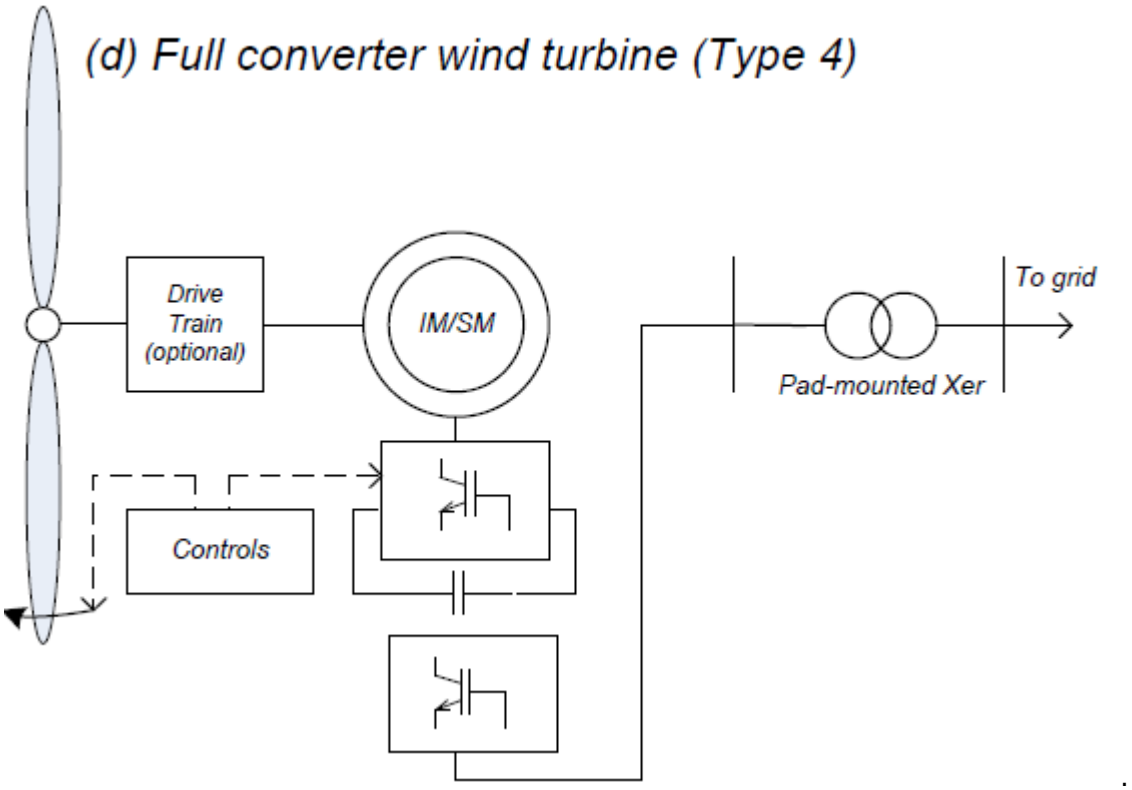

Figure 2. 33: Full-converter WT layout

The complex interaction between a full-converter wind turbine, the related generator, and the utility grid is shown in Figure 2.13. This depiction accurately captures the underlying technological sophistication needed to best harvest wind energy while meeting the requirements of contemporary power distribution networks.

2.6 Wind turbine modelling

Modelling the performance of the WT depends primarily on the rotor torque that drives an electrical generator. The rotor torque is a direct product of the wind speed or flow rate. Since the wind speed is often much lower than the required speed or frequency of the generator, the wind plant comprises a gear system that converts the rotor speed to match the grid frequency. This is why modelling the performance of a WT can be broken down into a) aerodynamic block, b) mechanical block, and c) electrical block.

2.6.1 Aerodynamic block

The aerodynamic block of a WT plays a role in collecting the primary power that runs a wind plant. The degree of alignment of the incident wind to the rotation axis of the WT and rotor blade determines the amount of wind power received by the WT. Relevant forces, speed types, and angles involved in the performance of a WT are explored in the section below.

2.6.2 Lift force

To understand how power is collected by the rotor blade, it is important to understand how the wind speed leads to the rotation of the rotor blades. The wind is meant to be normal to the rotation axis of the rotor to allow the lift force of the blades. A quick observation of the blade design can make the lifting phenomenon simple to understand. Figure 2.14 depicts a WT, and by looking at one specific marked blade, one can notice cross sections. Figure 2.35 shows the blade cross-section in detail with relevant angles. The blade of a WT is designed in such a way that the bottom surface of the blade is relatively flatter compared to the top surface. When the wind flows, it embraces both surfaces, thus creating a pressure difference between the two surfaces, resulting in a lift force.

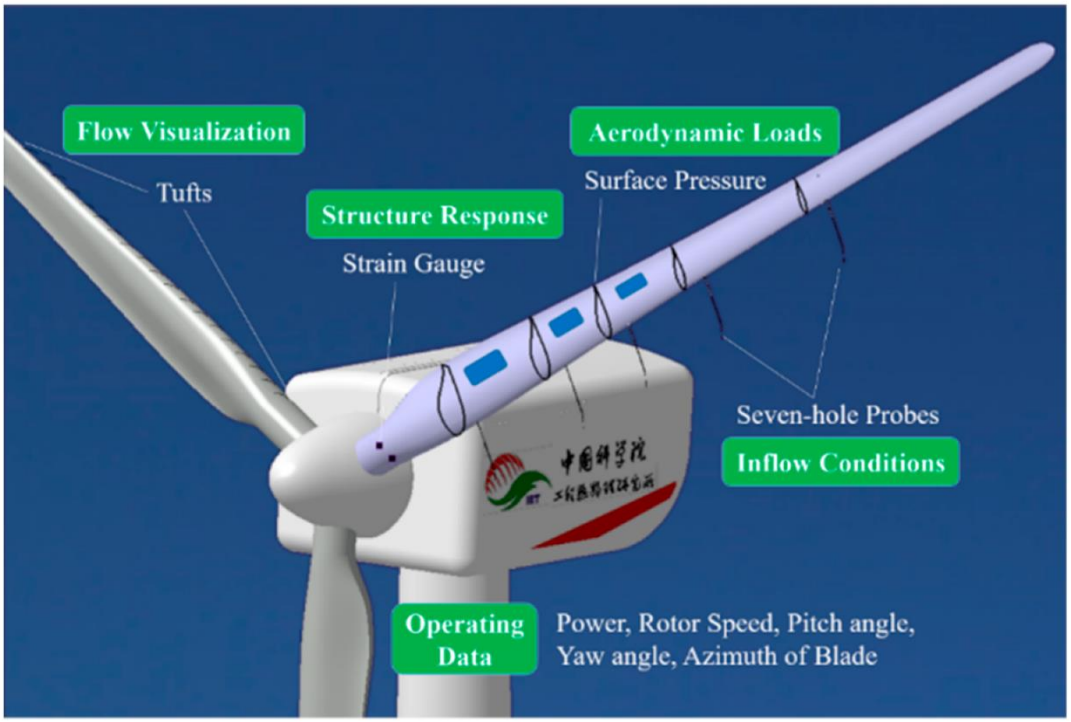

Figure 2. 44: Illustration of the WT aerodynamics

Figure 2.14 perfectly captures the intricate interactions seen in wind tunnel aerodynamics, making it easier to understand the underlying ideas behind the evaluation and improvement of aerodynamic performance. Its thorough explanation of streamline patterns, velocity vectors, and pressure distributions successfully adds to the general academic conversation in the field of fluid dynamics and aerodynamic testing.

2.6.3 Attack angle and pitch angle

The directness of the incident wind reaching the wind blade determines the wind power the turbine receives. Firstly, the incident wind should face the rotation axis of the turbine to ensure that the incoming wind flow is swept to the maximum. In other words, the wind

incident line must make zero degrees with the rotor's rotating line. Any angle between the rotation of the line and the incident wind is called the attack angle. However, the attack angle is not the same along a blade; it depends on the position of the blade. Figure 2.15 and 2.16 illustrates the influence of the position (shown by the cross-section) on a blade on the lift angle produced.regarding the lift angle produced. The lift force increases as one moves away from the root to the tip. Figure 2.15 is a crucial educational tool that clarifies the complex anatomy of a wind blade and highlights its significance in the field of renewable energy conversion.

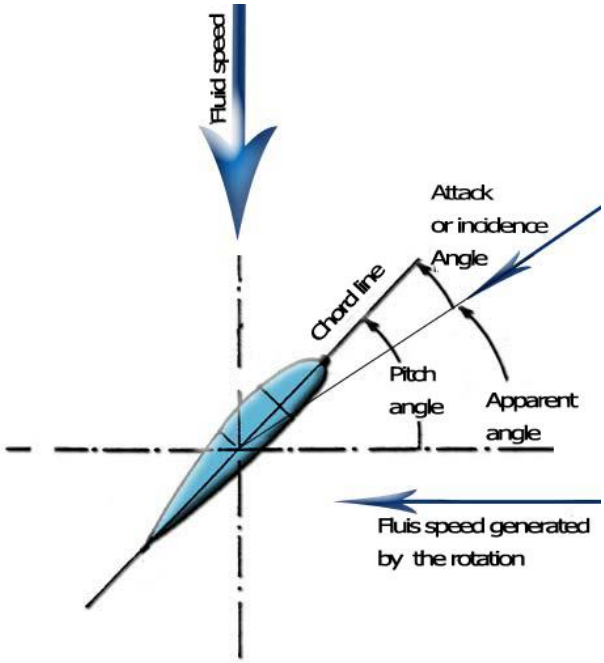

Figure 2.55: Cross-section of a wind blade

The picture highlights the complex interaction between these individual components, illuminating how they cooperatively contribute to the overall performance of the wind blade. By illuminating the complex technical issues that underlie the blade's design and operating efficacy, this thorough representation improves our comprehension of the internal dynamics of the blade.

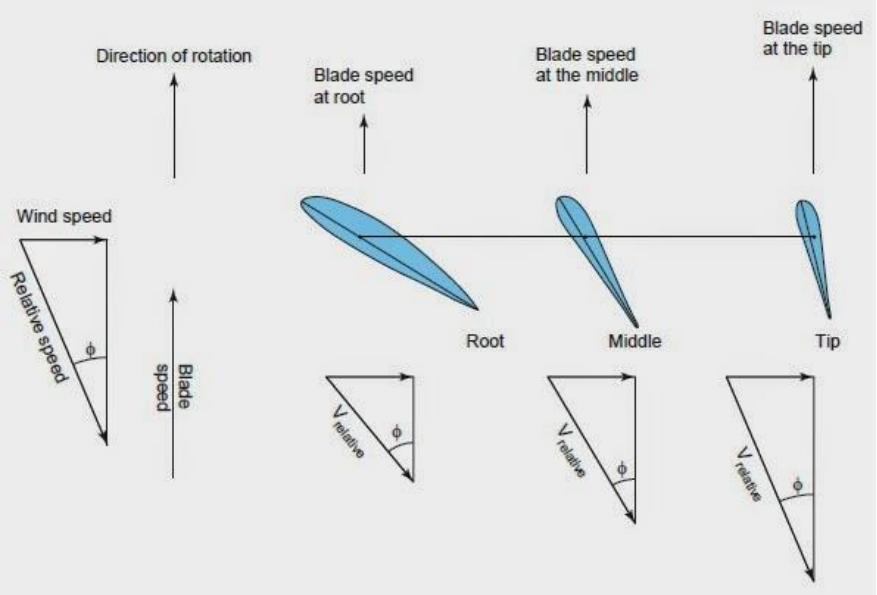

Figure 2.66: Cross-sections at various positions on the blade

The precise details of the blade's shape and manufacture are crucially illuminated by Figure 2.16. The blade's geometrical and structural characteristics are made easier to understand thanks to the showing of cross-sectional views at certain points, which encourages a thorough evaluation of the blade's overall functioning and behavior.

2.7 Wind energy modelling

In a wind plant, the blade plays an important role as the wind power collector, determining the speed and wind power that the turbine receives. The kinetic energy generated is expressed as follows (Equation 2.17):

$$E = \frac{1}{2} m V_{wind}^2 \qquad \text{Equation 2.17}$$

Where m is the mass of the air around the blades and V_{wind} is the wind speed.

Considering the fact that the energy received by the rotor is proportional to the flow of the air, the mathematical representation can be (Equation 2.18):

$$\dot{m} = \rho A W_{ind} \qquad \text{Equation 2.18}$$

Where $\dot{m}$ is the air mass flow, ρ is the air density, and A is the area swept by the blades of the WT.

By substituting Equation 2.18 into Equation 2.17, we obtain Equation 2.19:

$$E = \frac{1}{2} \rho A V_{wind}^3 \qquad \text{Equation 2.19}$$

Given that the rotor has a coefficient of performance (Cp) that is less than or equal to 0.59, the power that can be delivered by a rotor can be expressed as per Equation 2.20:

$$P_{rotor} = \frac{1}{2} C_p \rho \pi R_{rotor}^2 V_{wind}^3 \quad \text{Equation 2.20}$$

Where P_{rotor} is the power deliverable by the rotor and R_{rotor} is the radius of the area swept by the blades.

It is important to note that the coefficient of performance of a WT depends on the blade tip speed ratio (TSR), denoted by λ. The TSR is the ratio between the wind speed over the wind speed, as well as the blade pitch angle. Figure 2.37 shows how the directions of speed and relevant angles are involved in the wind power collection. Equation 2.21 describes how the TSR is calculated.

$$\lambda = \frac{\omega_{rotor} * R_{rotor}}{V_{wind}} \quad \text{Equation 2.21}$$

Where ω_{rotor} is the rotor angular velocity.

On the other hand, the pitch angle of the blade is the angle formed between the chord line and the tangential line to the blade's surface.

2.7.1 Rotor power coefficient

The rotor power coefficient is the ratio of the rotor power over the incident wind power. This coefficient relates to the TSR, which at a constant value, determines the rotor power. The formula for the wind power can be presented as per Equation 2.22.

$$C_p = \frac{Rotor_{power}}{Wind_{power}} \quad \text{Equation 2.22}$$

2.7.2 Mechanical drive train

The second stage of wind power generation consists of the mechanical train or gearbox. The wind power is conveyed to the gearbox through a shaft. One disk of the gearbox is connected to the second disk that is, in turn, connected to an inductor machine as shown in Figure 2.17 (a). Figure 2.17 (b) shows the simplified and equivalent system of the mechanical system.

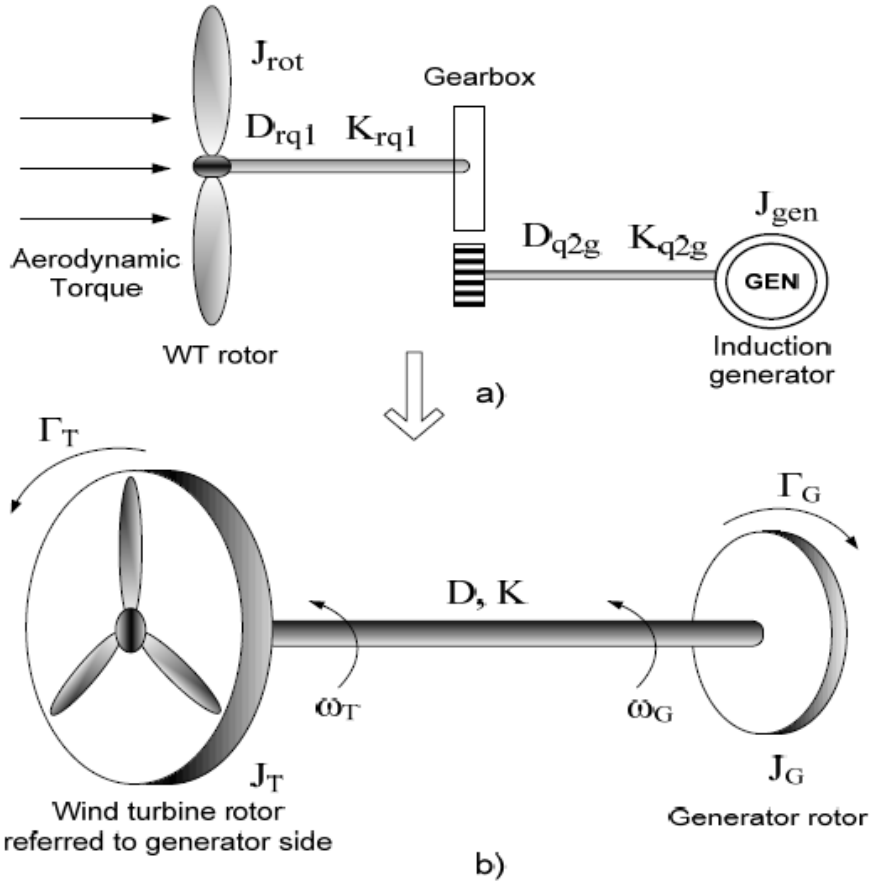

Figure 2.77: WT drivetrain model

It is important to first comprehend the model of a disk linked to a shaft to gain a full understanding of the model of the whole drivetrain. Figure 2.18 depicts the mechanical model of such a system and the components of the Equation of the torque. The equation of the torque considers the stiffness coefficient of the shaft K, the viscous damping coefficient D, and the disk inertia J.

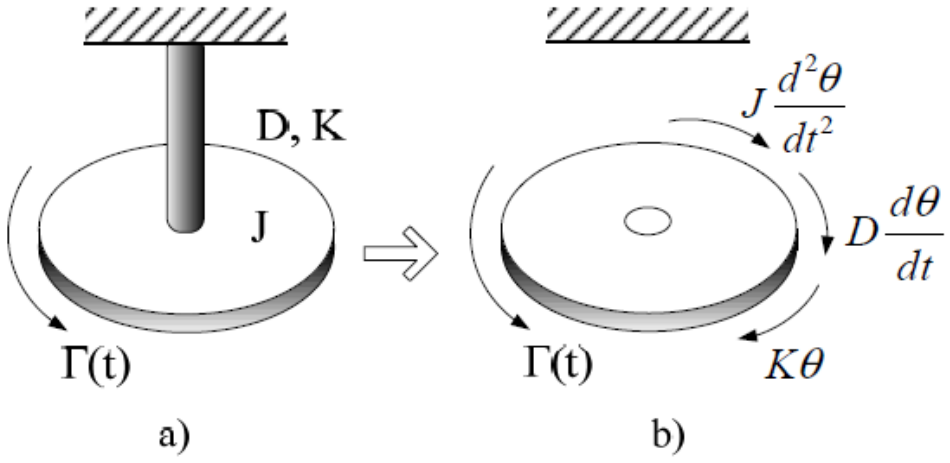

Figure 2. 88: Drivetrain mechanical model

Equation 2.23 gives the formulation of the torque as follows:

$$T = J\frac{d^2\theta}{dt^2} + D\frac{d\theta}{dt} + K\theta \qquad \text{Equation 2.23}$$

T represents the torque acting on the system, and J represents the moment of inertia of the system, and θ the angular displacement of the system. And $d^2\theta\ /dt^2$ It represents the angular acceleration of the system. Angular acceleration measures how quickly the angular velocity is changing over time. It is measured in radians per second squared (rad/s²). And K This symbol represents the spring constant or stiffness coefficient. To account for the system stiffness' impact on the torque, it is multiplied by the angular displacement (θ). Depending on the equation's context, the spring constant is expressed in units of torque per radian (Nm/rad) or an equivalent quantity.

Therefore, this equation applies for either of the disk-shaft systems, yielding Equations 2.24and 2.25. Moreover, considers the moment of inertia, angular acceleration, damping, angular velocity, and stiffness of the initial part of a mechanical system to calculate the torque applied to that part. It illustrates the contribution of these elements to the rotational dynamics of the first component.

$$T_1 = J_1\frac{d^2\theta_1}{dt^2} + D_1\frac{d\theta_1}{dt} + K_1\theta_1 \qquad \text{Equation 2.25}$$

T_1 Torque acting on the first component, J_1 Moment of inertia of the first component, θ_1 Angular displacement of the first component, $d^2\theta_1/dt^2$ Second derivative of the angular displacement of the first component with respect to time. It represents the angular acceleration of the first component. D_1 Damping coefficient associated with the first component. Damping opposes the motion of the first component's rotation. $d\theta_1/dt$ First derivative of the angular displacement of the first component with respect to time. It represents the angular velocity of the first component. K_1 Spring constant or stiffness coefficient of the first component. It quantifies how stiff the first component's rotational motion is in response to an applied torque.

$$T_2 = J_2\frac{d^2\theta_2}{dt^2} + D_2\frac{d\theta_2}{dt} + K_2\theta_2 \qquad \text{Equation 2.26}$$

Also bearing in mind the relationship between the number of teeth on rotor disk $N_1$to the generator disk N_2, $T_1 = \frac{N_1}{N_2}T_2$ and $\theta_2 = \frac{N_1}{N_2}\theta_1$, Equation 2.25 can be rewritten as Equation 2.27:

$$T_1 = \frac{N_1}{N_2}\left(J_2 \frac{N_1}{N_2}\frac{d^2\theta_1}{dt^2} + D_2 \frac{N_1}{N_2}\frac{d\theta_1}{dt} + K_2 \frac{N_1}{N_2}\theta_1\right)$$ Equation 2.27

T_1 Torque applied to Gear One, $\frac{N_1}{N_2}$: Ratio of the number of teeth on rotor disk to generator disk, J_2 Inertia coefficient at Gear Two, $\frac{d^2\theta_1}{dt^2}$ Second derivative of the angular displacement θ_1 with respect to time. D_2 Damping coefficient at Gear Two, $\frac{d\theta_1}{dt}$ First derivative of the angular displacement θ_1 with respect to time, K_2 Spring constant at Gear Two, θ_1 Angular displacement of Gear One.

Equation 2.26 can also be rewritten as per Equation 2.28:

$$T_1 = \frac{N_1}{N_2}\left(J_{refl} \frac{d^2\theta_1}{dt^2} + D_{refl} \frac{d\theta_1}{dt} + K_{refl}\theta_1\right)$$ Equation 2.28

T_1 Torque applied to Gear One, $\frac{N_1}{N_2}$: Ratio of the number of teeth on rotor disk to generator disk, J_{refl} Reflected inertia coefficient at Gear One, D_{refl} Reflected damping coefficient at Gear One, K_{refl} Reflected spring constant at Gear One.

Where $J_{refl} = \frac{N_1}{N_2}J_2,\ D_{refl} = \frac{N_1}{N_2}D_2,\ K_{refl} = \frac{N_1}{N_2}K_2$ are coefficients reflected at Gear One and Gear Two. Therefore, the system torque can be expressed as per Equation 2.29.

$$T = J_{equiv}\frac{d^2\theta}{dt^2} + D_{equiv}\frac{d\theta}{dt} + K_{equiv}\theta$$ Equation 2.29

Where $J_{equiv} = J_1 + J_{refl}$, $D_{equiv} = D_1 + D_{refl}$, $K_{equiv} = K_1 + K_{refl}$

T Total system torque, J_{equiv} Equivalent inertia coefficient of the system, D_{equiv}Equivalent damping coefficient of the system, K_{equiv} Equivalent spring constant of the system.

Referring to Figure (2.38)., the torque applied to the turbine wind torque and the electromechanical torque from the direct-connect to the induction motor generator act in opposition. The equations describing the system represented in that figure are as per Equations 2.30 and 2.31.

$$T_T = J_T\ddot{\theta}_T + D_T\left(\dot{\theta}_T - \dot{\theta}_G\right) + K_T(\theta_T - \theta_G)$$ Equation 2.30

T_T Torque applied to the turbine, J_T Inertia coefficient of the turbine, $\ddot{\theta}_T$ Second derivative of the turbine's angular displacement with respect to time, D_T Damping coefficient of the turbine, $\dot{\theta}_T$ First derivative of the turbine's angular displacement with respect to time, $\dot{\theta}_G$ Angular displacement rate of the generator.

$$-T_G = J_G\ddot{\theta}_G + D_G\left(\dot{\theta}_G - \dot{\theta}_T\right) + K_G(\theta_G - \theta_T)$$ Equation 2.31

Where the quantities with T and G subscripts, respectively, associate with the turbine and the generator, $-T_G$ Negative of the torque applied to the generator, J_G Inertia coefficient of the generator, $\ddot{\theta}_G$ Second derivative of the generator's angular displacement with respect to time, D_G Damping coefficient of the generator, $\dot{\theta}_G$ First derivative of the generator's angular displacement with respect to time, θ_G Angular displacement of the generator, θ_T Angular displacement of the turbine.

Since $\frac{d(\theta_T-\theta_G)}{dt} = \omega_T - \omega_G$, the rotor equation can be represented in terms of the rotor speed as follows (Equation 2.32):

$$\dot{\omega}_T = \frac{1}{J_T}(T_T - D_T(\omega_T - \omega_G) - K_T(\theta_T - \theta_G)) \quad \text{Equation 2.32}$$

ω_T Acceleration of turbine rotor speed, $\frac{1}{J_T}$ Reciprocal of the inertia coefficient of the turbine, T_T Torque applied to the turbine, D_T Damping coefficient of the turbine, ω_T Turbine rotor speed, ω_G Generator rotor speed, K_T Spring constant associated with the turbine.

Conversely, the generator speed can be represented as per Equation 2.33 as follows:

$$\dot{\omega}_G = \frac{1}{J_G}(-T_G + D_G(\omega_T - \omega_G) + K_G(\theta_T - \theta_G)) \quad \text{Equation 2.33}$$

$\dot{\omega}_G$ Acceleration of generator rotor speed, $\frac{1}{J_G}$ Reciprocal of the inertia coefficient of the generator, $-T_G$ Negative of the torque applied to the generator, D_G Damping coefficient of the generator, ω_T Turbine rotor speed, ω_G Generator rotor speed, K_G Spring constant associated with the generator.

After modelling the torque and speed of the generator, respectively, the next part of the wind plant to be modelled is the induction motor.

2.7.3 Electrical block

The electrical block mainly consists of a three-phase generator and the connection to the grid, which can be a delta or star configuration. The generators can be explored by looking at conventional generators.

To sum up the modelling section, one can refer to the block diagram in Figure 2.19. The input parameters in the WT model is the wind speed V_{wind}. Based on the resulting rotor speed and pitch angle, one can calculate the TSR, denoted λ, and then the coefficient of performance of the rotor, thus its torque. Based on the teeth ratio in the gearbox, the generator torque and speed can be calculated. Then, a second order transfer function is derived to allow the control of the WT.

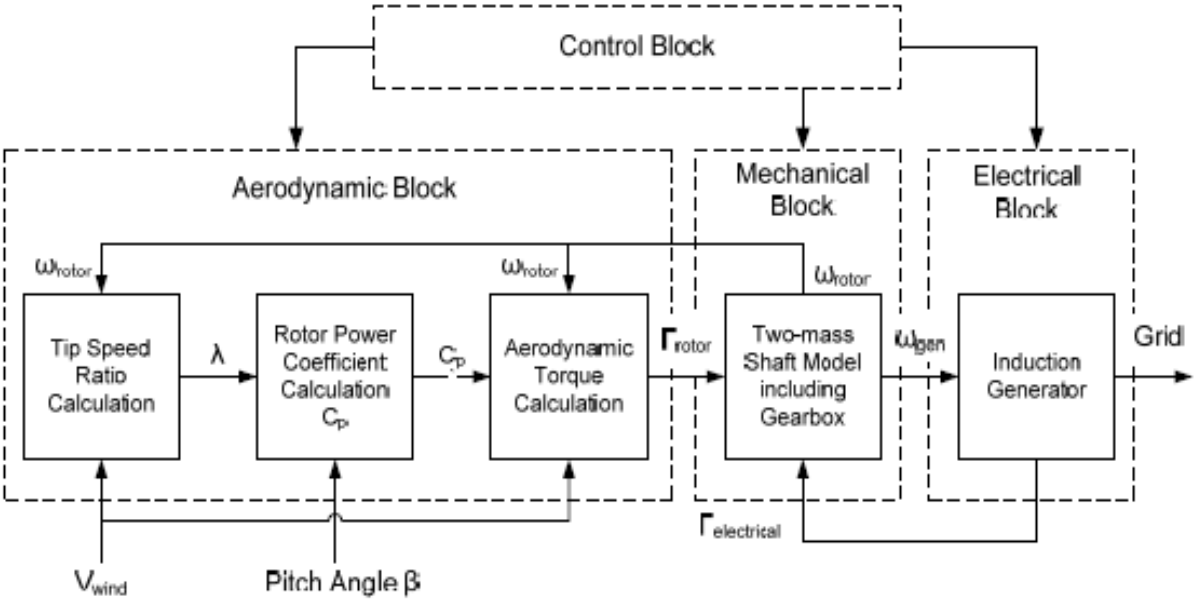

Figure 2.99: Electrical block

The schematic depiction of the electrical block, a crucial part of the system under examination, is shown in Figure 2.19. This block's main components are a trinary-phase generator connected to a grid infrastructure that may be set up in either a delta or star configuration. This architecture warrants research into the generators included inside it using a lens resembling traditional generator analysis.

From the relationship between the angular velocity of the rotor speed and the generator speed, considering that the speed of Gear Two is proportional to the teeth number relationship, the speed of the second gear is expected to be higher than that of the first gear. Figure 2.20 depicts the output response with $\frac{N_1}{N_1} = 10$.

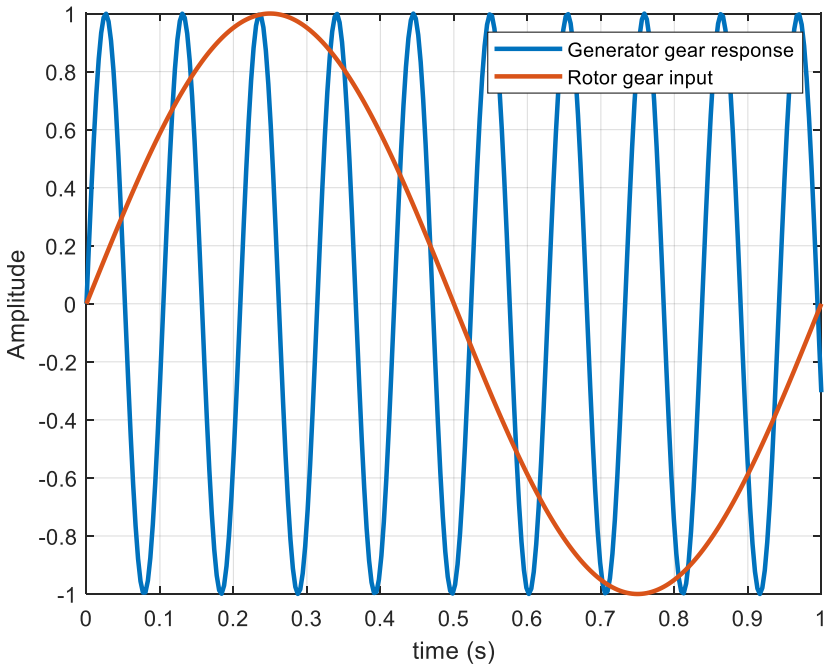

Figure 2.20: Comparing rotor input and generator response

Figure 2.21 depicts the expected output of a three-phase squirrel cage generator subdivided by a phase angle of 1200 degrees.

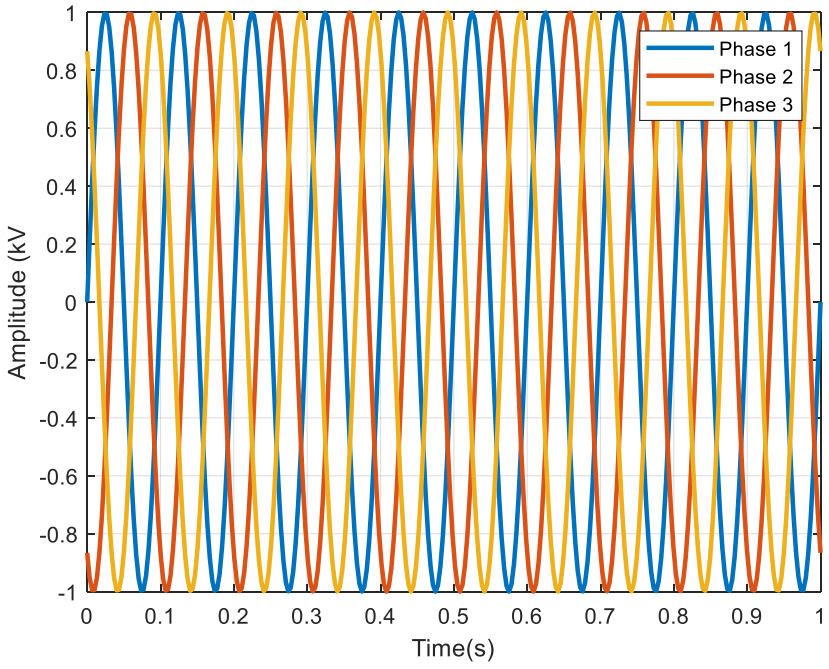

Figure 2.101: Illustration of three-phase generator response

In which Figure 2.21 is magnified to improve visibility, the output can be shown in line with the presentation shown in Figure 2.22.

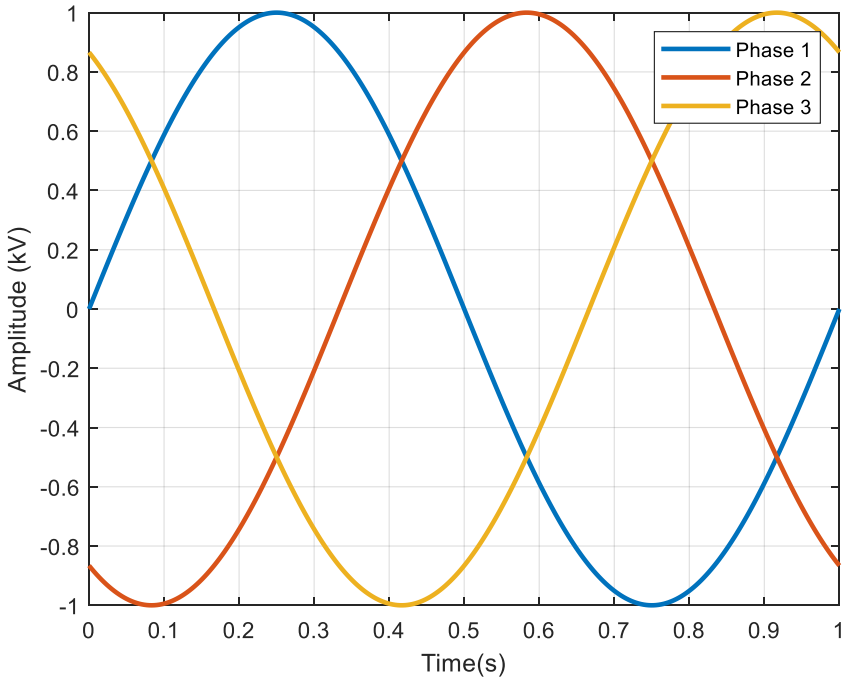

Figure 2.112: Close-up of Figure 2.21

2.7.4 Conclusion on wind energy

The need to have WTs in the pool of renewable energy sources has been motivated in this section. The non-reliability of solar energy, which has become mainstream in alternative energy sources, coupled with economics and climate issues associated with fossil fuels opens a room to look for more possibilities of energy generation. WTs classifications were discussed according to several factors. In terms of the rotational axis of the turbine, there are horizontal axis WTs (HAWTs) and vertical axis WTs (VAWTs).

In terms of speed control possibilities, there are fixed-speed WTs and variable-speed WTs. Furthermore, in terms of the type of generator technology, there are asynchronous induction generator WTs such as squirrel cage induction generator (SCIG) and wound rotor induction generator (WRIG) on the one hand, and synchronous generator WTs like the permanent magnet synchronous generator (PMSG) and wound rotor synchronous generator (WRSG) on the other hand.

As for modelling the WTs' performance, three major blocks of the system were established, namely the aerodynamic block, the mechanical train, and the electrical block. In the aerodynamic block, it was established that the rotor power obeys the law of kinetic energy, which directly depends on the wind mass and velocity. But as applied to the wind domain specifically, the wind flow rate and the area swept by the rotor were considered. It was also established that given the structure of the wind blade, the WTs have a coefficient of

performance limit that they can go beyond depending on the tip-speed ratio and the pitch angle.

A full mathematical model of the torque of the mechanical train, which is actually a gearbox, proves to be a second-order transfer function in relation to the angular velocity and displacement. The ratio of the number of teeth in the gears allows for the increase or adjust the torque and speed of the generator. A control system to monitor and adjust the speed needs to be designed and customized according to the needs of a generator. In this regard, knowledge about generators and their applications in the domain of wind energy generation and power generation is needed.

2.8 Generators

Therefore, generators have become necessary to kick in when other energy sources are out of operation. Though they are an expensive option in terms of running costs, backup generators are reliable, and their end-product is ready for use without further processes.

A diesel generator consists of a diesel engine, a generator, and numerous accessories, such as the chassis, control systems, emergency circuit breakers, heat-generating systems, and automated start systems that create power. Small turbines have higher startup costs, more complicated maintenance, and longer rotation durations than diesel generators. In addition, a diesel generator's output is solely dependent on the quantity of fuel. Therefore, the link between diesel generator output power and fuel content is a linear relationship (Alzahrani et al., 2021).

Generators have been traditionally used as backup systems for mainstream energy generation. But as time goes on with the industrial, commercial and residential development, demands in electrical energy consumption have increased to the point where the supply does not match the demand anymore. Resorting to alternative sources in solar and wind has not been met with full success due to the drawbacks related to reliability, namely the dependence on the weather and seasons, which leads to generation intermittence (Abualigah et al., 2022).

Therefore, generators have become necessary to kick in when other energy sources are out of operation. Though they are an expensive option in terms of running costs, backup generators are reliable, and their end-product is ready for use without further processes in the upcoming section, concepts and principles of a generator are briefly reviewed.

2.8.1 Faraday's law

The law of Faraday is key to understanding the operation of generators. When a magnetic flux in a coil keeps changing continually, it yields a voltage. This is the principle of electromagnetism. Generators, transformers, motors and solenoids use this principle to generate the voltage. In other words, changing the magnetic flux around the coil creates the current flow in that coil. Mathematically, this can be represented as per Equation 2.34:

$$emf = -L\frac{d\varphi}{dt} \qquad \text{Equation 2.34}$$

Where emf is the induced voltage, φ is the magnetic flux, L is the inductance, and t is the time.

A reverse effect also exists in that passing a changing current through a coil creates a magnetic field around that coil. In both scenarios, what is required is a magnetic flux or current and movement.

To better understand the principle of Faraday's law, one can take a permanent magnet and a winding. A permanent magnet bar has flux lines going from one end to the other or from one pole to the other in the same way it is for the earth. The earth is itself a magnet with flux lines that flow from North to South. The magnetic field is strong when the flux lines are close to the winding but is weak otherwise, and so is the current produced. Figure 2.23 illustrates a winding in the vicinity of a magnet.

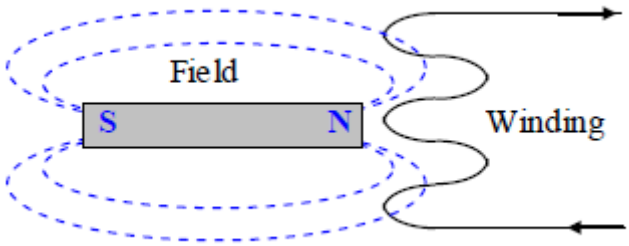

Figure 2. 123: Faraday's law illustration of magnet and winding

When the magnet changes position, such as being rotated, and the North Pole moves away from the winding followed by the magnetic lines, the induced current changes or reduces accordingly and becomes null when no flux lines cross the winding (Figure 2.23).

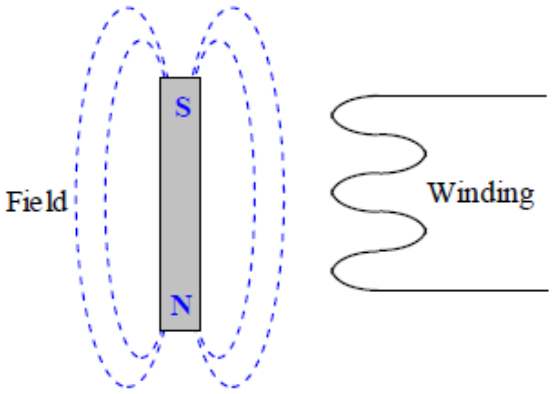

Figure 2.134: Magnet in parallel with the winding

As the magnet continues to rotate, the North Pole moves away while the South Pole moves closer to the winding. This changes the direction of the current flow and the intensity reaches the maximum when the South Pole gets the closest to the winding (Figure 2.24). Then the cycle restarts.

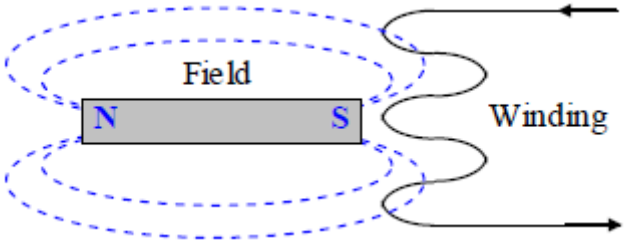

Figure 2.145: South pole facing the winding

As the magnet rotates in a circular movement, the strength of the magnetic flux describes a sinusoidal function and increases the intensity of the induced current (Equation 25). The induced current is null when the magnetic bar is parallel to the winding axis. It reaches an absolute peak value when the magnet bar is perpendicular to the axis of the winding (Figure 2.25).

$$\varphi(t) = \varphi_M \sin(\omega t)$$ Equation 2.35

Where φ_M is the magnetic flux's peak value and ω is the angular velocity of the magnetic rotary movement.

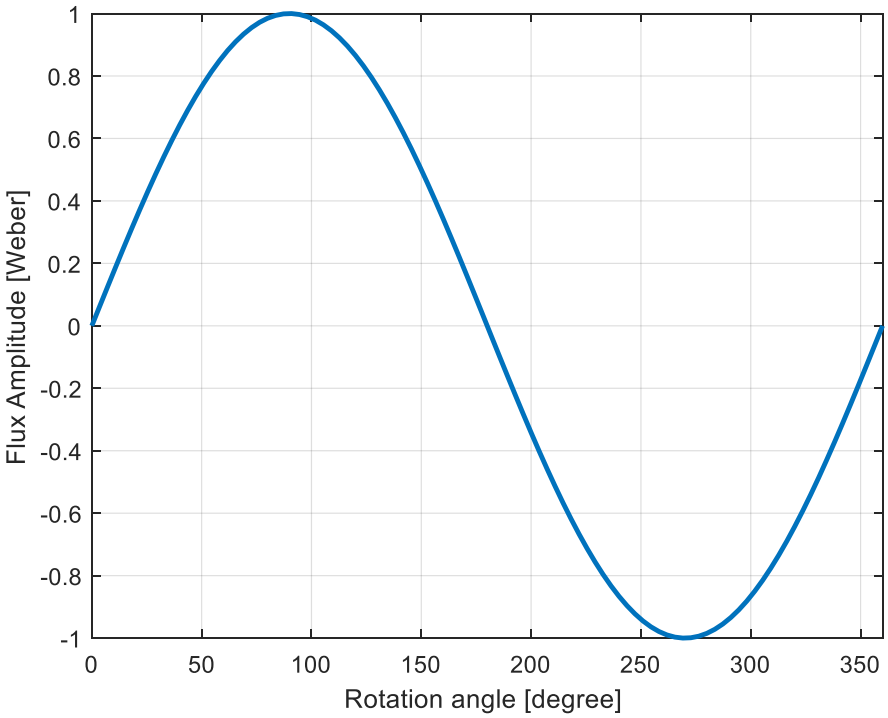

Figure 2.156: Magnetic flux variation as the magnet rotates

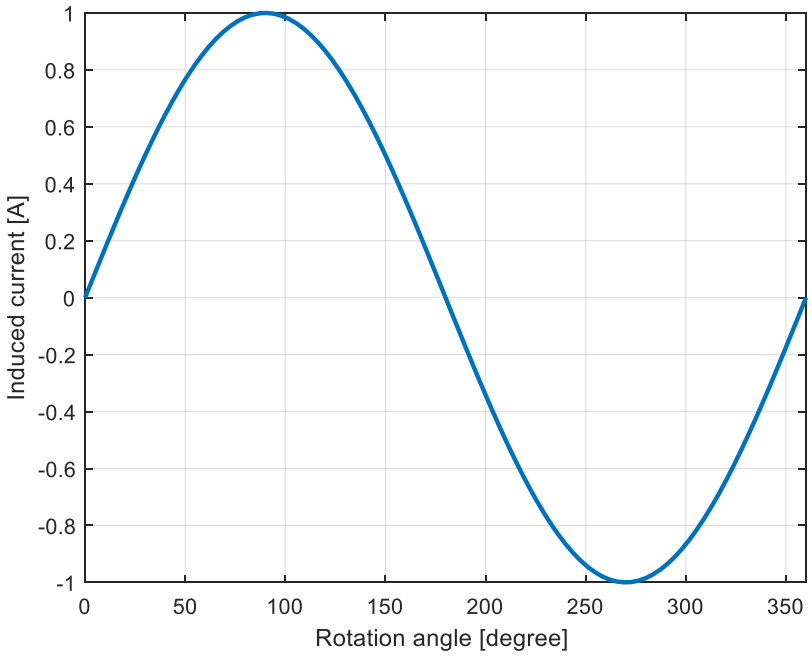

Figure 2.167: Induced current as the magnet rotates

However, it is found that currents produced by such a magnet rotating in the vicinity of a winding are not strong. To achieve stronger currents, the electromagnetic theory is applied. An electromagnet is achieved by winding a conductor around a metal bar. When a current is supplied in the coil winding, a magnetic field is created in the metal bar, giving it North and

South poles. Therefore, an electromagnet with a stronger field can be achieved by putting together many electromagnets (Figure 2.28).

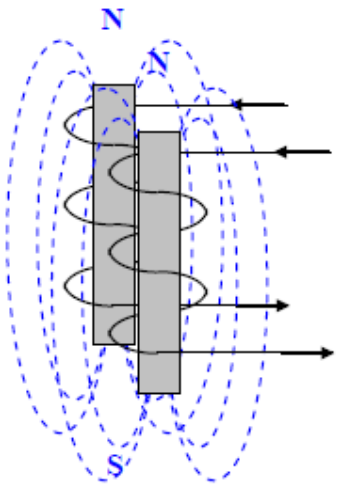

Figure 2.178: Combining electromagnet for more strength

The amount of magnetic field depends on the amount of current that passes through the winding. Conversely, the amount of current depends on the amount of magnetic field passing a winding. There are different ways to achieve alternating current, which yields types of AC generators, as explored in the following section.

2.8.2 Rotating armature generator

In a rotating armature AC generator, the magnetic field provided by a stator is cut by a rotor to produce an AC voltage as per Faraday's law. The produced voltage is collected and becomes available for use through two slip rings equipped with brushes connected to either rotor (rotating loop) terminals (Figure 2.29).

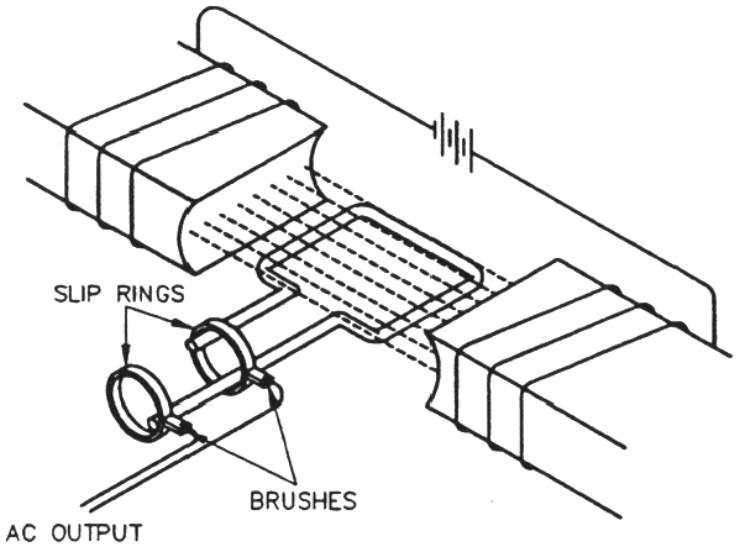

Figure 2.189: Rotating armature AC generator

Given the difficulties observed in having slip rings and brushes that can carry large amounts of current, rotating armature AC generators suit small power applications. The implication of this is that rotating magnetic field AC generators are the most suitable in terms of high power generation.

2.8.3 Rotating field AC generators

The most widely used in power generation are the rotating field AC generators, which operate in a reverse way compared to armature rotating AC generators. A fixed DC excitation voltage is supplied to a rotary loop through brushes and slip rings, thus creating an electromagnet of fixed polarity. The rotation of such an electromagnet in the vicinity of a winding will result in an AC output current that can be used to supply the load (Figure 2.30). In this type of generator, the excitation voltage can be handled easily by the slip rings and brushes as the DC voltage is fixed and reasonably small. Also, since the output terminals are connected to a stationary electromagnet, large amounts of output currents can be handled easily.

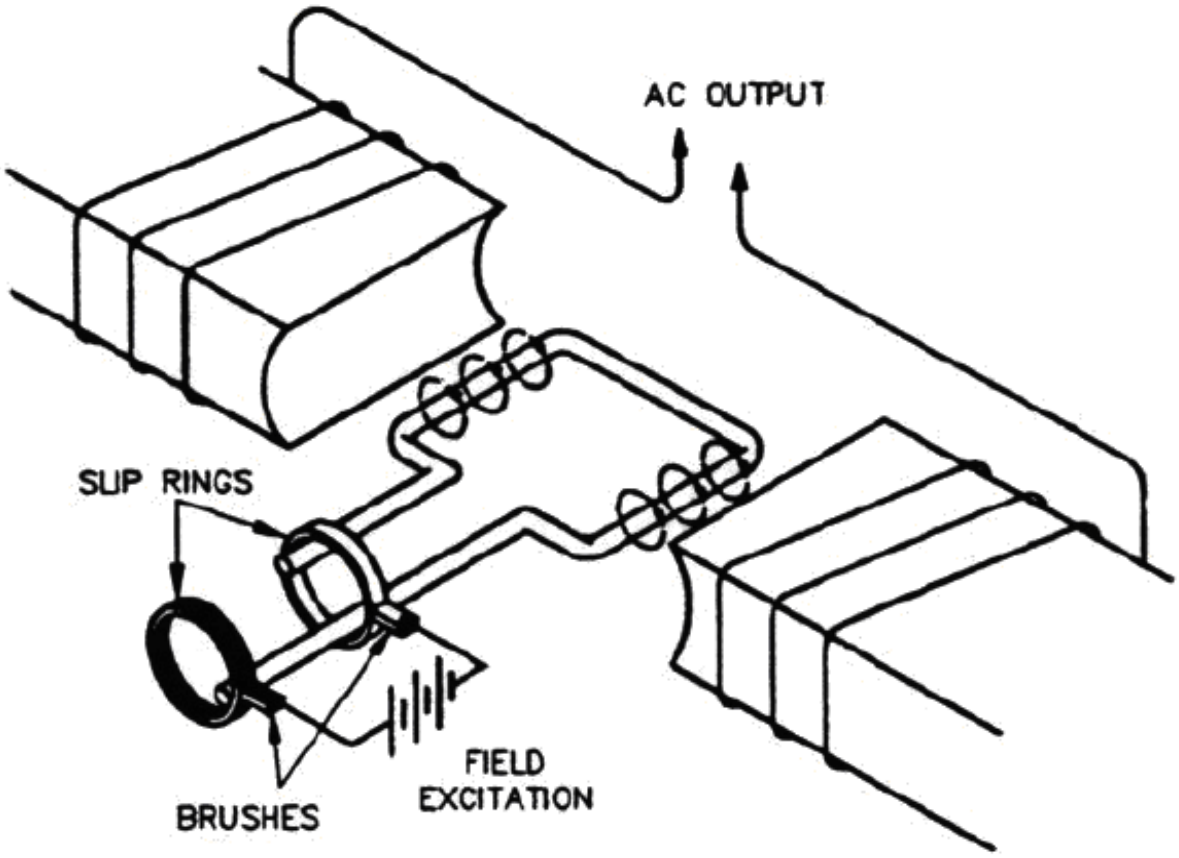

Figure 2.30: Illustration of a rotary winding magnet generator

2.8.4 Polyphase generators

The polyphase generator is the way to go to fulfil high power generation as single-phase generators have limited applications, for example, they cannot supply power to three-phase motors and other machinery. Compared to single-phase, three-phase generators offer the advantages of transmitting more power at less cost, producing about double the power of a single-phase generator of the same physical size and fulfilling the functionalities of a single-phase generator.

The working principle of a three-phase generator is similar to that of a single one; it suffices to add two more coils and arrange them in a balanced way. Since a complete rotation of a rotary bipolar electromagnet is 360^0, three coils would be spaced with 120^0 (360^0 / 3) (Figure 2.31).

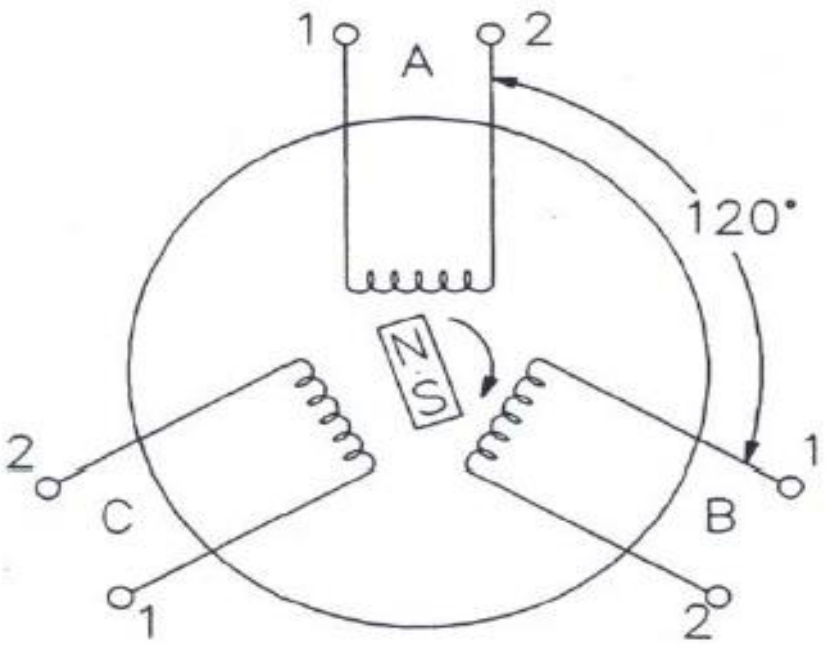

Figure 2.191: Three-phase magnet coil configuration

In this setup, the North Pole of the magnet will start its cycle and complete one full rotation around coil number 2 after passing coil number 1 by an angle of 120^0 degrees. Similarly, coil number 3 will experience the same after passing coil number 2 by an angle of 120^0 degrees, which is equivalent to passing coil number 1 by an angle of 240^0 degrees. The resulting voltages are illustrated in Figure 2.32.

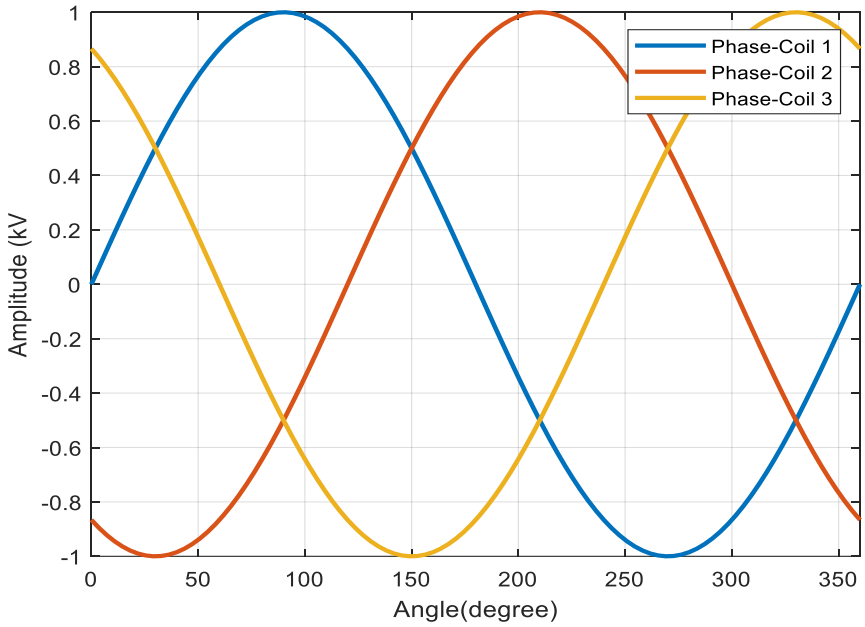

Figure 2.202: Three-phase output voltage versus the rotational angle

2.8.5 Classification based on the coolant

The most imperative need when it comes to high-power generators is cooling due to temperature rises that can compromise the functioning and safety of the generator. Fluids used in the cooling of power generators include air, Hydrogen 30 PSIG, Hydrogen 45 PSIG, and water. All these fluids depend on several parameters, including their relative specific heat, density, practical volume flow, and approximate removal ability. Water has proven to be the best performer in terms of removing heat in terms of the cooling efficient.

Hydrogen has been recommended for generators of power ratings below 300 MVA, while water was advised for generators above 250 MVA. The limitation of water as a coolant comes simply from the fact that it complexity of the generator's design in terms of additional piping and de-ionizing kits, thus making it costly. That is why it has been recommended for applications where the ratio performance cost is good.

2.8.6 Air-cooled generators

In this category of generators, there are open-ventilated (OV) and totally-enclosed-water-to-air-cooled (TEWAC) generators. In the OV generators, the air is directly drawn from outside into the generator through a filter from one end and exits from the other end. In the TEWAC system, the air is circulated inside the generator, passing through heat exchangers mounted on the frame of the generator.

2.8.7 Classification according to generator's rotor

There are two types of generators from the rotor's perspective: salient pole generators and cylindrical rotor generators.

2.8.7.1 Salient pole rotor generators

Salient pole rotor generators have large diameters, large mass, and large inertia, making them suitable and ideal for slow-moving generators such as hydroelectric generators. Their large size helps maintain constant frequency in a power system. Salient pole rotors have a field pole that runs along the cylinder-shaped rotor. The pole is wrapped in insulated copper windings along its length, thus forming a pole. A field winding is formed by connecting in series the pole winding to the adjacent pole winding (Figure 2.33).

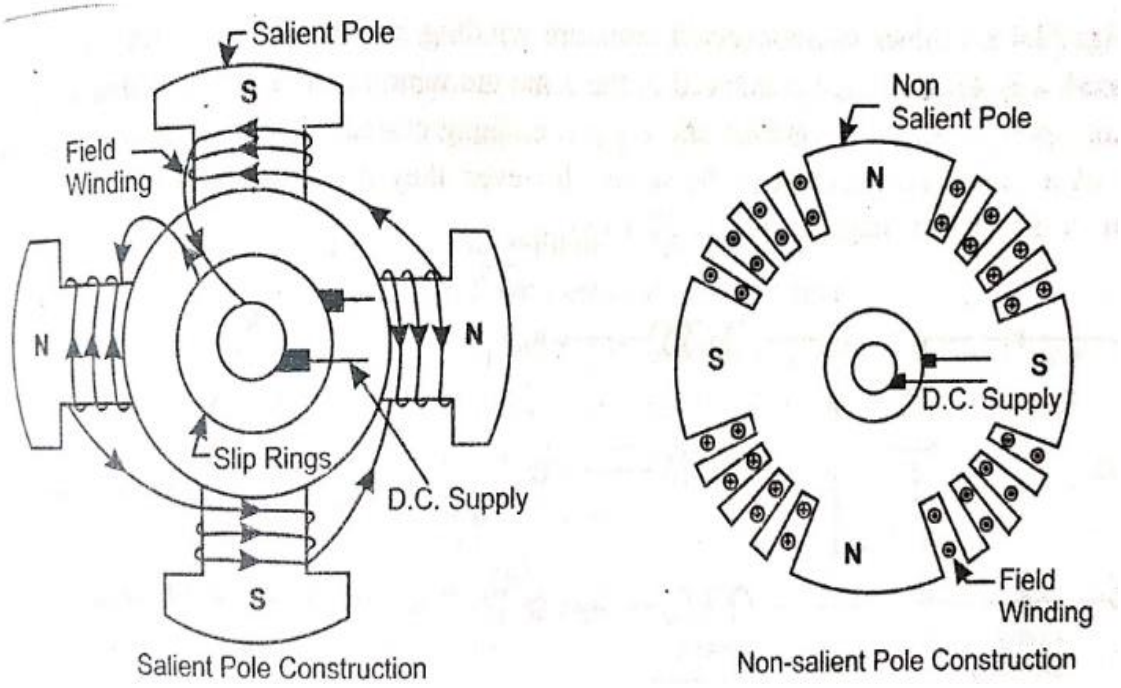

Figure 2.213: Salient pole rotor and cylindrical rotor

2.8.7.2 Cylindrical rotor generators

Cylindrical generators are used in high-speed generators such as steam generators, given their fast speed. A great amount of inertia is still achieved due to their fast rotational speed. The cylindrical rotor is a solid steel shaft with slots in the lengthwise direction outside its shape. Laminated copper bars are laid in the slots and kept stationary with the help of wedges, thus forming the field winding of the cylindrical rotor. As such, the rotor becomes a strong electromagnet which induces voltage and current in the stator winding.

2.9 Energy storage systems

2.9.1 Introduction

Energy storage systems are becoming more relevant and can be utilized to keep energy that is not needed at a point in time. The same or part of the stored energy can be reinjected into the energy supply system and fed into the grid system. Energy storage systems have found more applications following the trend to reduce fossil fuel-driven power plants for their liability in global warming and climate change.

With the advent of renewable energy systems (RESs) spearheaded by solar and wind, storage energy systems are necessary to cover or back up the intermittence natural to those RESs. Energy storage systems can also boost the effectiveness of the grid when it comes to responding to fluctuations in energy demands. The performance of an energy storage system can be measured based on how quickly it can respond to demand and how fast it can recharge. The relevance of a storage system lies in the fact that it may suppress the need and the cost required to build a backup plant.

2.9.2 Background

Energy storage offers a range of benefits, including balancing output and demand, improving power quality, smoothing the intermittency of renewable resources, and providing auxiliary services like frequency and voltage management in minigrid (MG) operations. The intermittent nature of renewable energy sources poses a challenge for consistent and uninterrupted power supply to consumers, and it endangers grid operations from various operational and technical perspectives. To overcome this challenge, minigrids consisting of loads and distributed generation (DG) are proposed to maximize the use of renewable energy sources (RES) that can operate in standalone and grid-connected modes. Energy storage systems (ESS) can aid the integration of RES into the MG by smoothing fluctuations, improving power quality, contributing to frequency regulation, and providing other ancillary services (Palizban & Kauhaniemi, 2016).

Energy storage is critical for achieving efficient and sustainable energy systems. It requires diverting all or a portion of energy flows to a suitable storage system, then utilizing the stored energy when required. Without storage, energy services rely on a just-in-time commodity where generation follows demand, including energy losses. However, storage installation at various levels can affect the network's energy exchanges by shifting from a just-in-time commodity to a time-adjustable commodity. This shift moves towards load following generation, and storage can smooth out the variability of energy supply. This expanded range of applications enables customers who are also local energy producers (prosumers) to

supply energy services to various energy markets, including new forms of local energy markets and energy communities

2.9.3 Overview on Energy storage technologies

Several technologies are used to store energy and are all compared based on their strength and weaknesses. Those that can at least accommodate a capacity of 20 MW are considered, including pumped storage hydropower, compressed air, molten salt, Li-ion battery, lead acid battery, flow battery, hydrogen, and flywheel (Bagheri-Sanjareh et al., 2021).

As for storing electrical energy, electrochemical cells like rechargeable batteries can achieve this. Hence, the fact that secondary cells undergo reversible electrochemical processes gives them that name. Many rechargeable batteries are available, from tiny button cells to massive megawatt-hour banks connected to the power grid. Several chemical compounds make rechargeable batteries, including lead-acid, nickel-cadmium, nickel-metal, lithium-ion, and lithium-ion-polymer. As a result, rechargeable batteries are more cost-effective and less hazardous to the environment than standard disposable batteries. While, in some cases, rechargeable batteries are manufactured and distributed in the exact sizes as standard batteries, the only difference is that they may be recharged and used multiple times. Rechargeable batteries feed electrical energy into the grid for consumption during high-demand periods, balancing the grid's demand. For example, new power systems like solar power use rechargeable batteries to store energy during the day and draw it down at night (Al-Salloomee et al., 2022).

2.9.3.1 Pumped storage hydropower

Pumped storage hydropower (PSH) facilities can store large amounts of energy by elevating water to a higher storage reservoir during energy low-cost periods and releasing it to run hydropower turbines during peak-cost periods. Recent advances have seen PSH technologies with adjustable speeds to respond efficiently to the demands as well as operating in a closed loop regarding the flow of water to avoid water wastage.

PSH offers the advantage of being cheaper compared to other counterparts, especially when it comes to large hydropower capacity that can be easily achieved. When compared to Li-ion batteries, for instance, the cost is lower for PSH, and the duration of service delivery is higher with the same capacity. Whereas a Li-ion battery can supply energy for 6 hours, PSH can go as much as 10 hours and is 80% efficient (Y. Yang et al., 2018). However, the construction of a PSH plant may take between 3 to 5 years which can turn off investors who have lined up for short-term projects.

2.9.3.2 Compressed air energy storage

Compressed air energy storage (CAES) operates by having the air compressed and stored underground during the period when the cost of electricity is low. The stored air is then released and heated. The resulting heat turn turbines on during peak periods when the electricity cost is high. CAES uses natural gases, meaning that it releases carbon and triples the energy generated. When the pressure in the air is retained, CAES delivers with an efficiency of 70%. Otherwise, its efficiency ranges between 42% and 55%. According to (Wang et al., 2017) there were only three CAES plants by the time their research paper was written. Where, the authors highlight compressed air energy storage (CAES) as a potential option and present an outline of its current stage of technological development as well as an analysis of its most significant technological limitations and drawbacks. They plan for this study to act as a guide for future research and development in this subject.

2.9.3.3 Thermal storage

Thermal storage uses temperature to store heat energy. The energy is stored by heating rocks, salts, water or other relevant materials that are kept in an insulated environment. The energy can be released when needed by pumping cold water into the hot rock, salt, or water, which releases steam that is, in turn, used to turn electric generators on. The same technology can be used to cool or heat the environment in place of electricity (Tooryan et al., 2020).

Thermal storage can deliver at an efficiency ranging between 50% and 90%, depending on the material.

2.9.3.4 Lithium-ion battery

The lithium-ion battery became commercial as early as the 90s, targeting small-scale consumers such as cell phones. After upgrading, it found more applications in electric vehicles (EVs) around 2017, with a cost of about $210/kWh. Predictions indicate that the cost of this type of battery would drop to $100/kWh by 2025. Lithium-ion battery technology has occupied the grid energy storage market at 90%, given its light weight and high energy (Rivera-Barrera et al., 2017).

Lithium-ion batteries have found applications in the electrification of small businesses and households. It has penetrated rural areas, where it is paired with PVs for households and commercial applications. The lithium-ion battery has helped solve problems encountered in the use of air-polluting diesel generators and risky natural gas. General Electric has manufactured a lithium-ion battery of 1 MW capacity, releasing it for market in 2019 (Vins & Sirovy, 2019),in order to ease energy compaction, transportation, and flexibility.

2.9.3.5 Lead acid battery

The lead acid battery was among the earliest energy storage technology used. They were popular in powering EVs (Sanguesa et al., 2021).Due to its low power density and short life cycle, the lead acid battery has been replaced by the long-lasting lithium-ion battery.

2.9.3.6 Flow battery

The flow battery is another type of battery that can rival the lithium-ion battery. Despite holding less than 5% of the grid energy storage market and having a lower power density, the flow battery suits continuous power supplies over a longer duration (Sanguesa et al., 2021).

2.9.3.7 Solid state battery

The solid-state battery finds applications in large grids, where it beats the lithium-ion battery on several fronts, given its small size and high safety. The solid-state battery offers the major advantage of not being prone to possible fire outbreaks associated with liquid electrolytes found in other battery types, such as the lithium-ion battery (C. Li et al., 2021).However, the solid-state battery cannot quite beat to beat the lithium-ion battery due to its high cost and the fact that it is far less manufactured.

2.9.3.8 Hydrogen

The hydrogen gas (H2) generates electricity through the combination of hydrogen and oxygen. This technology offers the advantage of being reliable, having a high energy density, and not releasing dangerous emissions. When using hydrogen pure water is the only by-product. Therefore, when the electricity cost is low, hydrogen can be produced and stored through electrolysis of water. During periods when the electricity price goes high or the demand increases, hydrogen can then be utilized. Cheaper options of hydrogen generation can be found via reforming gases, ethanol, and hydrocarbons that are carbon emissive. Fuel cell facilities are quite expensive due to the use of platinum and expensive metal. Nevertheless, they are mostly used as a backup for emergency loads such as telecom relays, data centres, etc (Mohseni et al., 2020).

2.9.3.9 Flywheels

Motors store energy by spinning their rotors at a very high speed e.g., 50,000 rpm. This happens during periods of cheaper electricity costs. The electric energy can be obtained by a reverse process where the motor acts as a generator spinning via the kinetic energy stored in the flywheel. Flywheels are usually kept in a vacuum environment to avoid friction and energy losses. Though flywheels do not suit long-term energy storage, they are effective in load levelling and shifting.

Table 2.1: A recapitulative table of the data on energy storage systems

	Max Power rating (MW)	Typical discharge time	Max cycles or lifetime	Energy density (Watt-hour per litre)	Efficiency (%)
Pumped hydro	3000	4-16 h	30-60	0.2	70-85
Compressed air	1000	2-30 h	20-40 years	2-6	40-70
Molten salt	150	Hours	30 years	7-210	80-90
Li-ion battery	100	1 min-8 h	1000-10000	200-400	85-95
Lead acid battery	100	1 min-8 h	6-40 years	50-80	80-90
Flow battery	100	Hours	12,000-18,000	20-70	60-85
Hydrogen	100	Min - week	5-30 years	600 @ 200 bars	25-45
Flywheel	20	Sec – min	20000-100000	20-80	70-95

2.10 Voltage source inverter

A voltage source inverter is a power electronic component that plays the role of converting the DC voltage into AC voltage. It actually fulfils the reverse role played by the AC to DC converters, of which the aim is to obtain a DC voltage from an AC voltage. Depending on which parameter one wishes to control, there are voltage source inverters and current source inverters (CSI). With voltage source inverters, one has control over the voltage, while in the case of current source inverters, one has control over the current (Rodriguez et al., 2020).The output of the VSI or the CSI is a signal of a different frequency, which may be of the same or different amplitude.

Ideally, the shape of a VSI should not be affected by the variation of the load connected to the inverter. The applications of VSIs include adjustable speed drives (ASDs), uninterruptible power supply (UPS), voltage compensators, flexible AC transmission systems (FACTS), and photovoltaic generators. In this study, the VSIs are expected to play a massive role as photovoltaic sources are part of the distributed energy generation system proposed.

VSIs fulfil their functions in both single and three-phase applications by using half or full-bridge switching configurations. The switching devices are mostly transistors such as bipolar junction transistors (BJTs), field effect transistors (FETs), and insulated gate transistors (IGBTS). These switching devices are usually driven by a step signal (square wave) or a pulse width modulation (PWM) signal. The output can be kept constant by keeping the switching signal constant if the input signal is constant for varying output voltage, which may

be required by the non-fixed load, which is often the case, the switching PWM signal needs to be adjusted accordingly. In other words, the duty cycle of the PWM signal is varied to match the voltage needs of the load. The PWM signal has proven to offer better quality than the square wave signal. At times, VSIs can only provide a signal with stiff characteristics, hence this type of VSI is referred to as stiff. The concept of AC to DC conversion is explained in the upcoming section (Zhou et al., 2020).

2.10.1 Basic concept of VSI

The operation of VSIs can be understood by considering the circuit in Figure 2.55. The configuration consists of two transistors, an NPN and a PNP. The base is shorted, and from the shorting point, an AC voltage source is connected to a resistive load. The emitter of the NPN transistor is biased with appositive DC voltage +E, while the emitter of a PNP transistor is biased using a negative DC voltage –E. At the positive swing of the input signal, the NPN diode will conduct, while for the negative swing of the input signal, the PNP conducts in a negative direction. The currents flowing in the resistive load change directions according to whether the incoming signal is positive or negative.

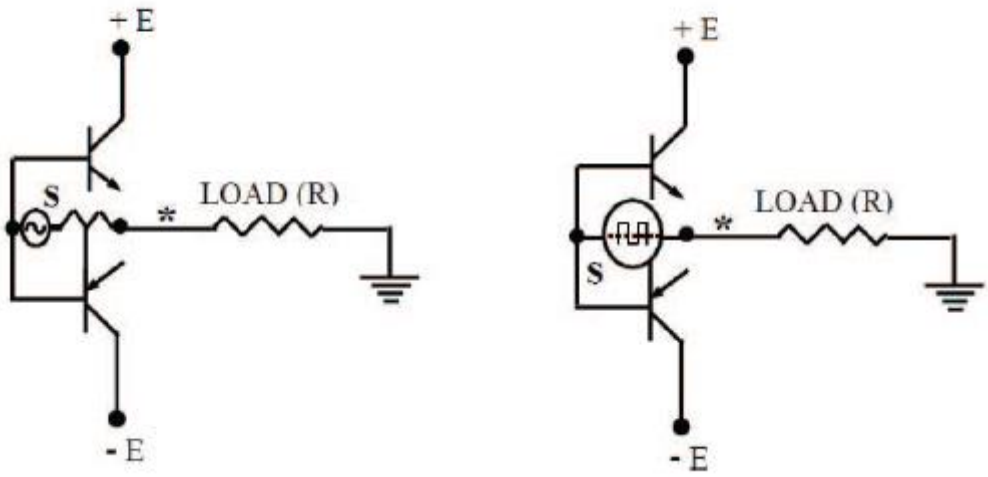

Figure 2.224: Transistorized VSI

Three major types of VSIs are single-phase half bridge, single-phase full bridge, and three-phase VSI. Each of these configurations has unique operational and topological traits, which have a significant impact on their effectiveness and application in a variety of power conversion scenarios. The clarification of these VSI categories aids in a thorough knowledge of their functional distinctions and the importance of those distinctions in modern power electronic systems.

2.10.2 Single-phase half bridge VSI

The VSI illustration in Figure 2.35 is that of a half bridge single-phase VSI. It is meant to show the basic concept and presents some fundamental disadvantages. The fact that it consists of two types of voltage sources and two different switching devices that may have different switching frequencies is a shortfall. Single-phase half bridge configuration, one voltage source only, and the type of transistor are therefore considered. Two switching devices like IGBTs and MOSFETs using one DC voltage source suit the application.

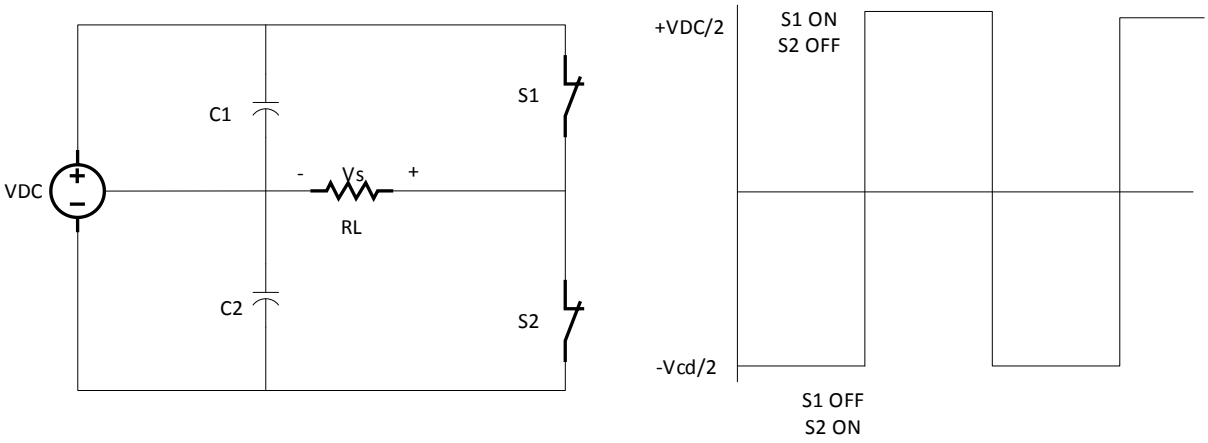

Figure 2. 235: Half bridge single-phase VSI illustration

When switch 1 is on and switch 2 is off, the voltage across the load resistor is positive and equal to the charge of the capacitor, of which the voltage is half of the source voltage. Otherwise, in a scenario when switch 1 is off and switch 2 is on, the voltage across the load resistor has inverted polarities with half of the input voltage. The inconvenience resulting from a single-phase half-bridge Voltage Source Inverter (VSI) arrangement, in which the output magnitude is only half of the input voltage, can be successfully alleviated by using a full-bridge VSI setup.

2.10.3 Single-phase full bridge VSI

The operating setup of a single-phase full bridge Voltage Source Inverter (VSI) includes the use of four separate switching devices. The amplitude of the output voltage swing is proportional to the magnitude of the input voltage source. Figure 2.36 depicts the operating dynamics of the entire bridge VSI.

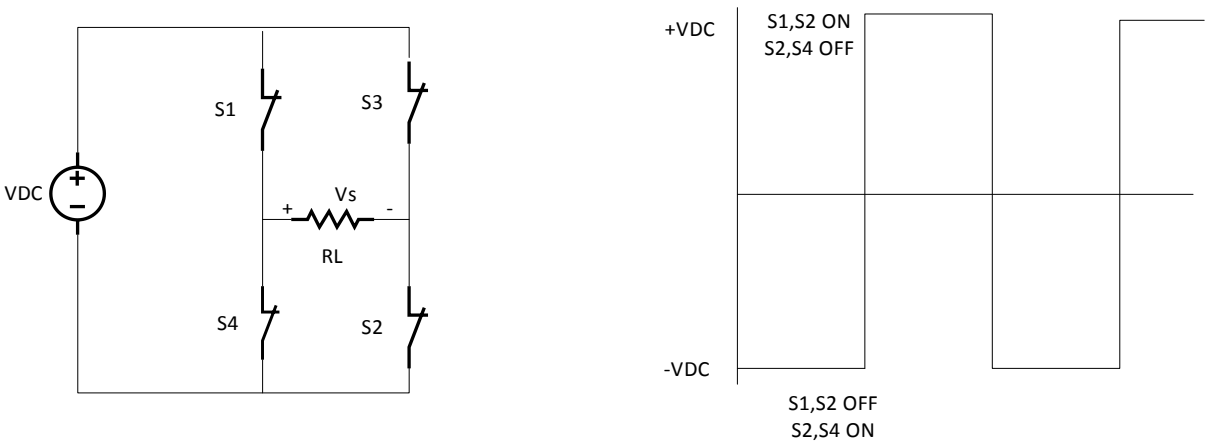

Figure 2.246: Single-phase full bridge VSI diagram and output

When both switches 1 and 2 are turned on, the output of the Voltage Source Inverter (VSI) equals the magnitude of the source voltage. This event demonstrates that the output of the VSI aligns with the amplitude of the voltage source, as seen in Figure 2.36.

2.10.4 Three-phase VSI

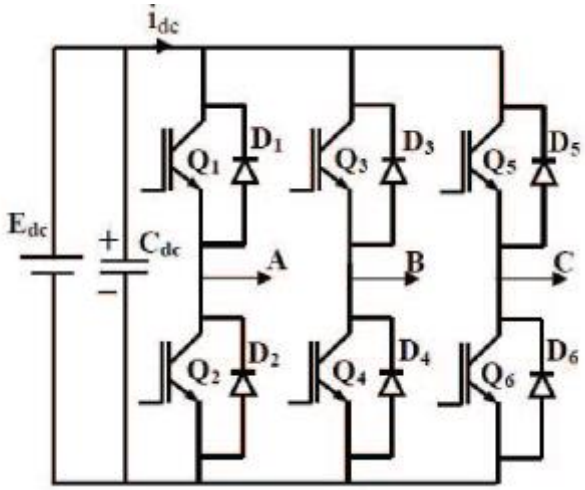

Figure 2. 257: Three-phase VSI circuit diagram

In the three-phase inverter depicted in Figure 2.37, phase A is associated with transistors Q1 and Q2, phase B is associated with transistors Q3 and Q4, while phase C is associated with transistors Q5 and Q6. How the number of switching devices is determined is discussed in upcoming sections. Phases A, B, and C are delayed or advanced and have a duration time of 120^0 in order to have a balanced output voltage. Also, having switching devices, the three phases will be separated by a 60^0 advance or delay. Each switching device's voltage output amplitude must include either the positive peak magnitude of the DC input voltage or its equivalent negative peak magnitude.

The calculation of the line-to-line or phase-to-phase voltage requires recognition of the limitation that only a pair of switches may be turned on at the same time.

2.10.5 Switching functions

In order to understand the functionality of an inverter, one should first understand how many switching devices are needed by an inverter (Yu et al., 2012).This depends on the relationship between the amounts of input lines and output lines. If the input has *m* lines and the output has *n* lines, the number of switches needed is m x n. For instance, if we have two input lines and three output lines, the amount of switching devices is 2 x 3, which is 6. There are direct and indirect switching functions. The relationship between the switching devices can be represented as per Figure 2.38.

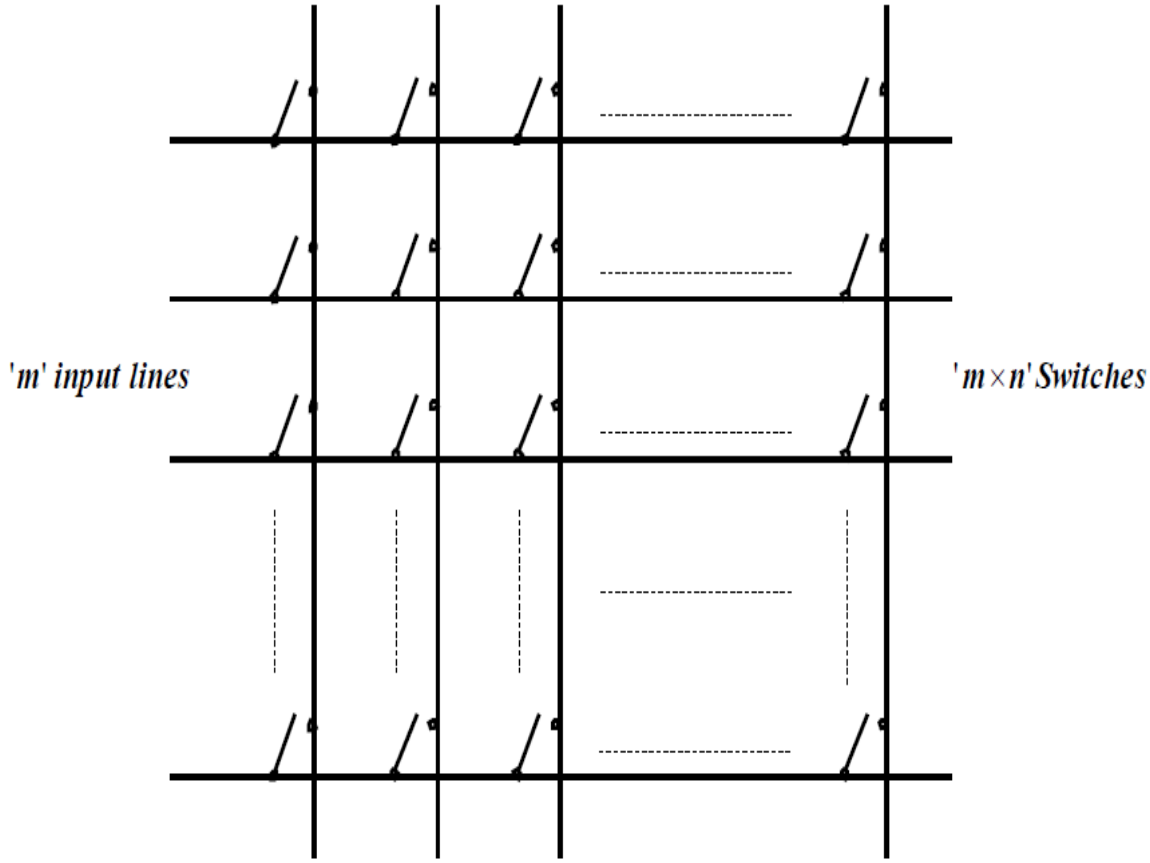

Figure 2.268: Switching matrix

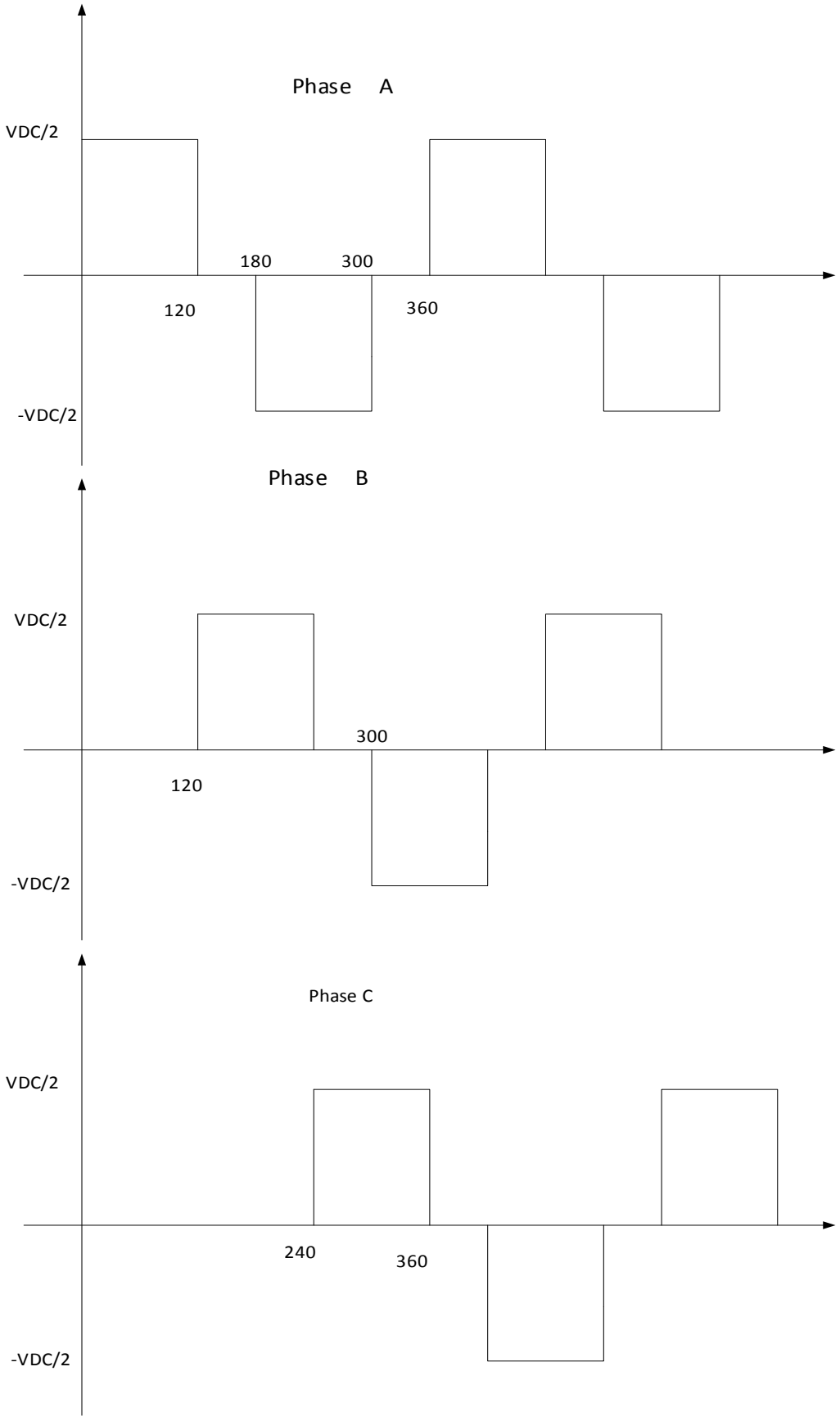

Figure 2.279: Switching output

There are two options for actuating device transitions: direct and indirect switching functions. In the context of the direct switch matrix, energy accumulation is only connected to the input and output lines, resulting in the energy storage components assimilating into circuit load elements. In the case of indirect switch converters, also known as integrated converters, the energy storage parts are tightly interconnected inside the matrix's architecture. In the indirect operating mode, this setup uses a small number of switch components. The switch matrix provides the benefit of organizing the switching mechanisms in accordance with individual applications.

2.10.6 Switch states and switching functions

The fact that each switch can be either turned ON or OFF presents the opportunity to show these functions mathematically. A function related to the switches normally designed *Q* can be derived and denoted $Q(t)$, which yields a circuit of a matrix of m rows and n columns. Representing each element of the switching matrix as $qij(t)$, such element is HIGH or 1 when the corresponding switch is ON or OFF. Therefore, the elements of matrix *Q(t),* also denoted *q(t),* are termed switching functions (Equations 2.35).

$$q_{ij} = \begin{cases} 1, switch\ at\ i,j\ is\ ON \\ 0, switch\ at\ i,j\ is\ OFF \end{cases} \qquad \text{Equation 2.35}$$

This implies that at a specific time, *Q(t)* will be a matrix of zeros and ones.

2.10.7 Mathematical representation of switching functions

Given the periodic aspect of the switching devices used in converters and inverters, the Fourier series is suitable to represent the switching functions (reference). With devices switching at a frequency f, the switching period is represented by $T = 1/f\ \omega = 2\pi f$.

Let the angular duration of the unit-value period be $\frac{2\pi}{A}$ with $A \geq 1$; the boundaries around the zero reference can be $-\frac{\pi}{A}$ and $\frac{\pi}{A}$. The Fourier series of such a signal can be represented by Equation 2.36.

$$H(\omega t) = \sum_{n=0}^{\infty}[C_n \cos(n\omega t) + S_n \sin(n\omega t)] \qquad \text{Equation 2.36}$$

$H(\omega t)$ represents a periodic function in terms of angular frequency ωt, C_n and S_n are coefficients of the Fourier series expansion,

The coefficients of this Fourier series are determined using Equations 2.37 and 2.38.

$$S_n = \frac{2}{T}\int_{-\frac{T}{2}}^{\frac{T}{2}} Hsin(\omega t)dt \qquad \text{Equation 2.37}$$

$$S_n = \frac{1}{\pi}\int_{-\frac{\pi}{A}}^{\frac{\pi}{A}} H sin(\omega t) d\omega t$$ Equation 2.38

$$S_n = 0$$

Computation of the S_n coefficient as per Equation 2.39 and 2.40:

$$C_0 = \frac{1}{T}\int_{-\frac{T}{2}}^{\frac{T}{2}} H dt$$ Equation 2.39

$$C_0 = \frac{1}{2\pi}\int_{-\frac{\pi}{A}}^{\frac{\pi}{A}} H d\omega t$$

$$C_0 = \frac{1}{A}$$

Computation of the C_n coefficient:

$$C_n = \frac{2}{T}\int_{-\frac{T}{2}}^{\frac{T}{2}} H cos(n\omega t) dt,\ n \neq 0$$ Equation 2.40

$$C_n = \frac{1}{\pi}\int_{-\frac{\pi}{A}}^{\frac{\pi}{A}} H cos(n\omega t) d\omega t$$

$$C_n = \frac{2}{n\pi}\sin(n\pi/A)$$

T is the period of the function, A is a constant, and α is an angle, n is an integer that indicates the frequency component in the Fourier series, π is the mathematical constant pi.

Thus, the Fourier series can be written in the form of Equation 2.41:

$$H(\omega t) = \frac{1}{A} + \frac{2}{\pi}\sum_{n=1}^{\infty}[\frac{1}{n}\sin(\frac{n\pi}{A})]\cos(n\omega t)$$ Equation 2.41

Given $\cos(\omega t) = \cos(2\pi - \omega t$, Equation.2.41. can also be represented as Equation 2.42:

$$H(\omega t) = \frac{1}{A} + \frac{2}{\pi}\sum_{n=1}^{\infty}[\frac{1}{n}\sin(\frac{n\pi}{A})]\cos(n\omega t - 2k\pi/A)$$ Equation 2.42

Bringing $1/A$ into Equation 2.42 yields Equation 2.43:

$$H(\omega t) = \frac{1}{\pi}\sum_{n=-\infty}^{\infty}[\frac{1}{n}\sin(\frac{n\pi}{A})]\cos(n\omega t)$$ Equation 2.43

In the previousequation of the Fourier series Equation 2.36, if n is a multiple of A, then the term in sine becomes zero. This implies that the switching function can be represented by a DC component and a time varying signal, which can be a cos or a sine. Equation 2.44 suits the representation of a switching function.

$$S = \frac{1}{2}(1 + M)$$ Equation 2.44

Where S is the switching function and M is the modulation signal. Expanded, the modulation signal can be expressed as Equation 2.45.

$$M = m_a \cos(\omega t - \alpha)$$ Equation 2.45

Where m_a is the modulation, of which the magnitude ranges between 0 and 1.

2.10.8 Voltage source inverter switching

As demonstrated in the prior section, the three-phase Voltage Source Inverter (VSI) may operate in either a half-bridge or full-bridge mode (as shown in Figure 2.61). In the context of a three-phase VSI with two unique switching states per each phase, a total of eight discrete combinations or switching permutations occur (as illustrated in Table 2.2). It is critical to emphasize that due to operational limits, the simultaneous activation of two switches within a particular phase is strictly forbidden.

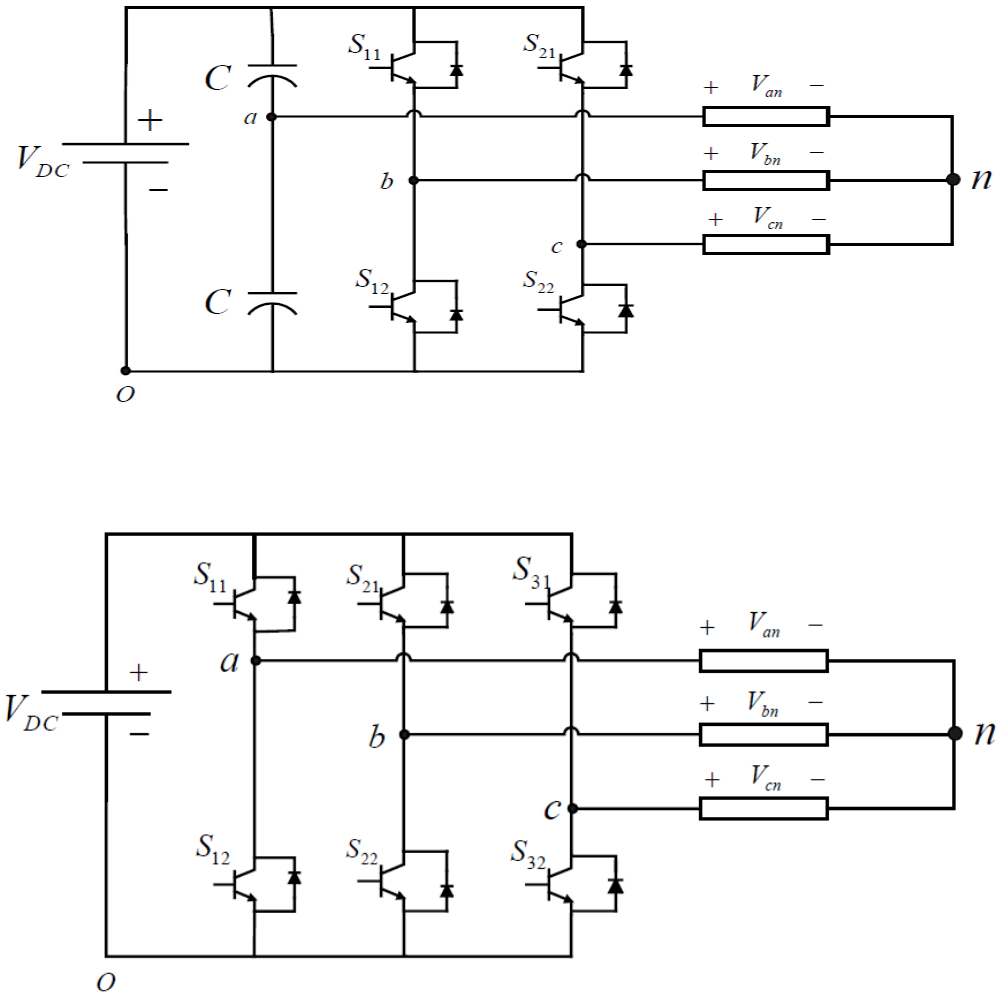

Figure 2. 40: Illustration of three-phase two-state switching VSI

Figure 2.40's intention is to depict the three-phase two-state switching VSI's structural structure and operating principles in a clear, thorough manner so that its operational complexities within the field of power electronics may be better understood.

Table 2.2: Switching states for three-phase VSI

S_{11}	S_{21}	S_{31}	V_{an}	V_{bn}	V_{cn}
0	0	0	0	0	0
0	0	1	0	$-V_{DC}$	V_{DC}
0	1	0	$-V_{DC}$	V_{DC}	0
0	1	1	$-V_{DC}$	0	$-V_{DC}$
1	0	0	V_{DC}	0	$-V_{DC}$
1	0	1	V_{DC}	$-V_{DC}$	0
1	1	0	0	V_{DC}	$-V_{DC}$
1	1	1	0	0	0

According to the data in Table 2.2, a three-phase Voltage Source Inverter (VSI) easily transitions between various states, resulting in discrete output values comprising $-V_{DC,}$ 0, and V_{DC}. A modulation technique is deliberately used to get the required output values while maintaining the system's integrity. This method ensures that the required outputs are produced precisely while also protecting against the use of incorrect states.

Consider the last row in Table 2.2, where all switches are simultaneously triggered. This configuration reflects an illegal state due to its intrinsic incompatibility with the system's operating restrictions. This specific incident emphasizes the importance of enacting safeguards to prevent the development of such invalid conditions. The mathematical formulas denoted by Equations 2.46 through 2.48 are critical in understanding the modulation process, illustrating how it acts to systematically reduce the possibility for these undesired states to occur.

In essence, the use of modulation techniques in conjunction with the clarified equations not only assures the attainment of precise and desired output states, but also functions as a safeguard against the unintended activation of states that might jeopardize the usefulness of the system.

$$\frac{1}{2}V_{DC}(S_{11} - S_{12}) = V_{an} + V_{no} \qquad \text{Equation 2.46}$$

$$\frac{1}{2}V_{DC}(S_{21} - S_{22}) = V_{bn} + V_{no} \qquad \text{Equation 2.47}$$

$$\frac{1}{2}V_{DC}(S_{31} - S_{32}) = V_{cn} + V_{no}$$ Equation 2.48

In terms of modulating signals, Equations 2.46–2.48 becomes Equations 2.49–2.51.

$$\frac{1}{2}V_{DC}(M_{11}) = V_{an} + V_{no}$$ Equation 2.49

$$\frac{1}{2}V_{DC}(M_{21}) = V_{bn} + V_{no}$$ Equation 2.50

$$\frac{1}{2}V_{DC}(M_{31}) = V_{cn} + V_{no}$$ Equation 2.51

The total output of the VSI can be calculated as follows (Equation 2.52):

$$\frac{1}{2}V_{DC}(S_{11} + S_{21} + S_{31} + S_{12} - S_{22} - S_{32}) = V_{an} + V_{bn} + V_{cn} + 3V_{no}$$ Equation 2.52

Given the voltage balance rule, $V_{an} + V_{bn} + V_{cn} = 0$, we have Equation 2.53.

$$V_{no} = \frac{V_{DC}}{6}(2S_{11} + 2S_{21} + 2S_{31} - 3)$$ Equation 2.53

Substituting V_{no} in Equations 2.49–2.51,

$$\frac{1}{3}V_{DC}(2S_{11} - S_{21} - S_{31}) = V_{an}$$ Equation 2.54

$$\frac{1}{3}V_{DC}(2S_{21} - S_{11} - S_{31}) = V_{bn}$$ Equation 2.55

$$\frac{1}{3}V_{DC}(2S_{31} - S_{21} - S_{11}) = V_{cn}$$ Equation 2.56

2.10.9 Sinusoidal PWM in three phase VSI

The procedure of producing sinusoidal pulse-width modulation (PWM) requires combining a sinusoidal signal with the required frequency with a high-frequency triangle waveform. Within a comparator, this triangle waveform, known as the carrier signal, is combined with the intended output signal. When the amplitude of the desired signal exceeds the equivalent amplitude of the triangle carrier signal, the comparator emits a logical high level of '11'. When the amplitude of the desired signal goes below that of the carrier signal, the comparator outputs a low-level signal, indicated as '0'.

Figures 2.41-2.44 depict the operating principles discussed in this section. The annexed information in Appendix 2.2 provides the relevant code used for the explicit description of PWM production. It is worth noting that the output of the Voltage Source Inverter (VSI) has a discontinuous character, lacks smoothness, and is therefore prone to harmonic aberrations. To alleviate this worry, modulation signals can be used to reduce harmonic distortions while

simultaneously increasing the fundamental frequency. These modulation methods have a wide range of applications.

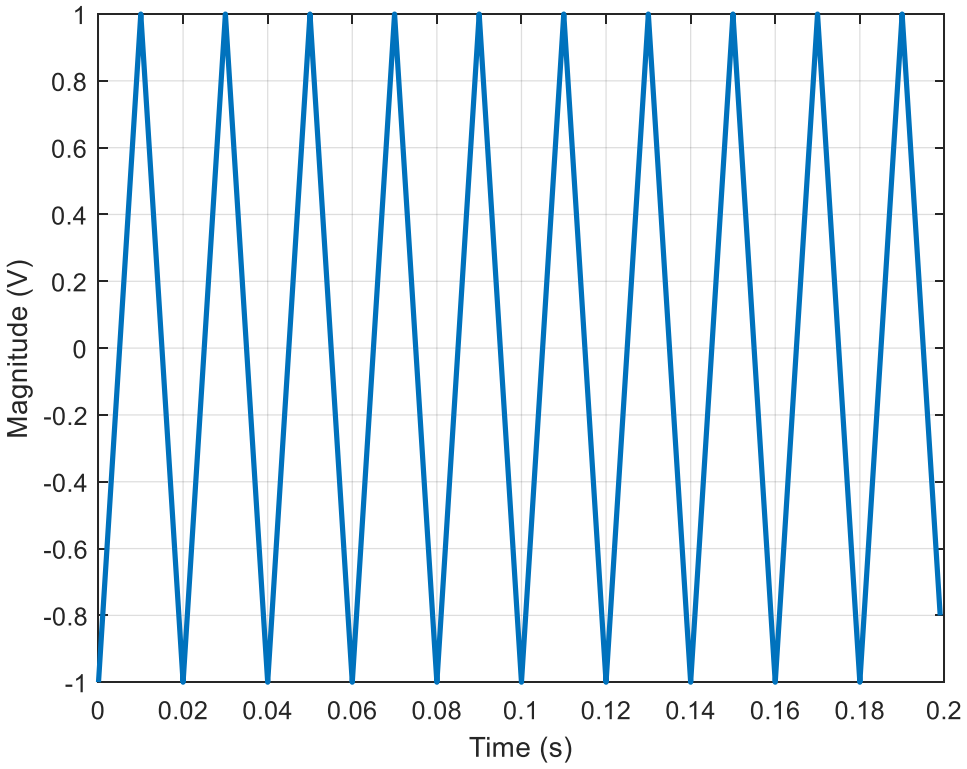

Figure 2.281: Triangular modulating signal

Figure 2.41 depicts a triangle modulating signal in detail, illustrating its properties and significance in the field of signal processing and modulation techniques. This illustration helps us comprehend the fundamental concepts underpinning various modulation methods, which improves our knowledge of their practical applications in a variety of technical sectors.

The horizontal axis in this illustration often represents time, showing how the signal has changed over the course of a certain amount of time. We look at the signal's amplitude or intensity on the vertical axis. A characteristic feature of the triangular modulating signal is its shape, which resembles an ascending and descending sequence of linearly linked segments arranged in a triangle-like pattern. This form results from a linear amplitude rise and drop over predetermined time periods.

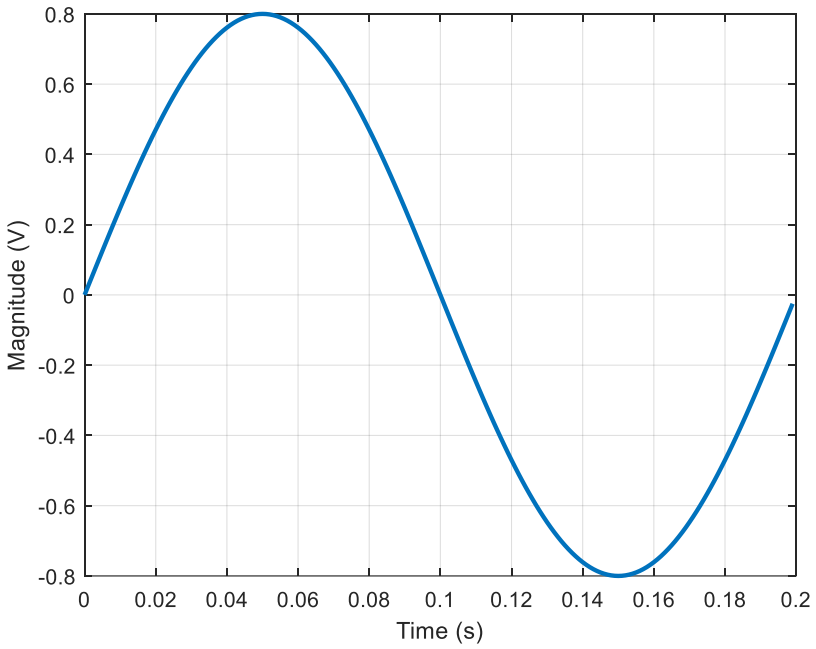

Figure 2.292: Modulated signal

In this figure 2.42 the modulated signal is shown as its changes overtime.

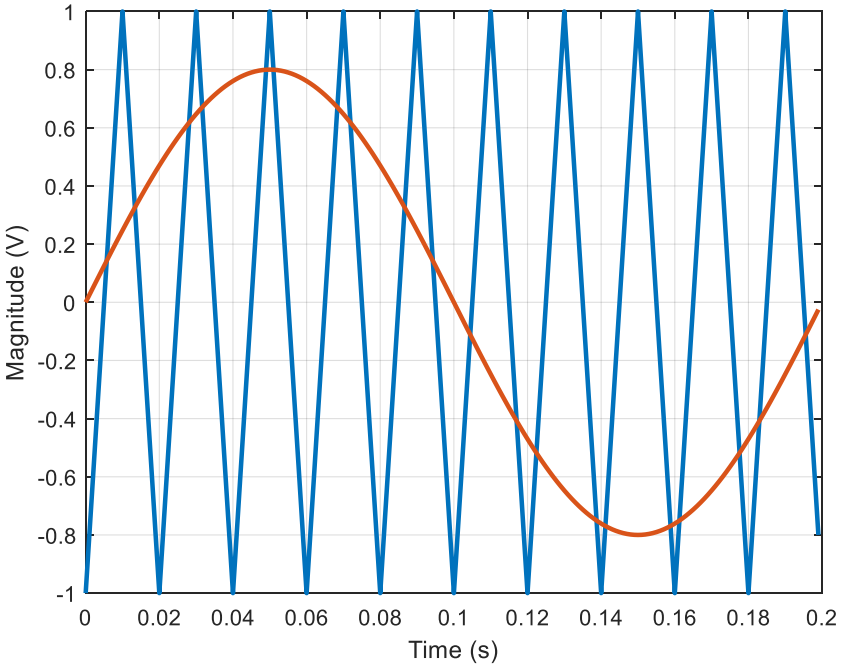

Figure 2.303: Both modulating and modulated signals together

For further explanation the figure 2.43 shows the modulating and modulated signals.

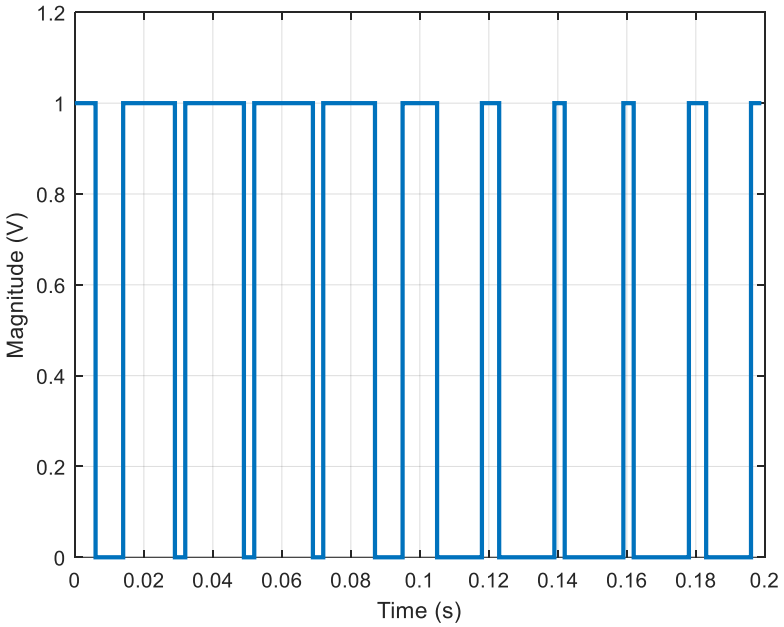

Figure 2.314: a) The input to the comparator. b) The PWM signal from the comparator

In the previous figures 2.44 a and figure 2.44b shows the input and output signals from the comparator.

Furthermore, phase voltage can be represented as per Equation 2.57.

$$\begin{pmatrix} V_{ab} \\ V_{bc} \\ V_{ca} \end{pmatrix} = \begin{pmatrix} V_{an} - V_{bn} \\ V_{bn} - V_{cn} \\ V_{cn} - V_{ca} \end{pmatrix} \qquad \text{Equation 2.57}$$

The equation system above can transform into Equation 2.58.

$$\begin{pmatrix} V_{ab} \\ V_{bc} \\ V_{ca} \end{pmatrix} = \begin{pmatrix} 1 & -1 & 0 \\ 0 & 1 & -1 \\ -1 & 0 & 1 \end{pmatrix} \begin{pmatrix} V_{an} \\ V_{bn} \\ V_{cn} \end{pmatrix} \qquad \text{Equation 2.58}$$

As this equation system cannot be solved due to the singularity of the matrix involved, and considering the fact that the sum of the phase voltages equals zero, the alternative equation system can be (Equation 2.59):

$$\begin{pmatrix} V_{ab} \\ V_{bc} \\ 0 \end{pmatrix} = \begin{pmatrix} 1 & -1 & 0 \\ 0 & 1 & -1 \\ 1 & 1 & 1 \end{pmatrix} \begin{pmatrix} V_{an} \\ V_{bn} \\ V_{cn} \end{pmatrix} \qquad \text{Equation 2.59}$$

Making the phase voltages the subject of the equation yields Equation 2.60.

$$\begin{pmatrix} V_{an} \\ V_{bn} \\ V_{cn} \end{pmatrix} = \frac{1}{3} \begin{pmatrix} 2 & 1 & 1 \\ -1 & 1 & 1 \\ -1 & -2 & 1 \end{pmatrix} \begin{pmatrix} V_{ab} \\ V_{bc} \\ 0 \end{pmatrix} \qquad \text{Equation 2.60}$$

This implies that the expressions of the phase voltages are as per Equations 2.60–2.63.

$V_{an} = \frac{1}{3}(2V_{ab} + V_{bc})$ Equation 2.61

$V_{bc} = \frac{1}{3}(-V_{ab} + V_{bc})$ Equation 2.62

$V_{bc} = -\frac{1}{3}(V_{ab} + 2V_{bc})$ Equation 2.63

In order to represent these quantities graphically, their mathematical representations need to be translated into the space vector.

2.2.1 Generalized discontinuous PWM

To achieve the generalized discontinuous PWM, a space vector method is applied. Keeping in mind that V_{an}, V_{bn}, and V_{cn} are phase voltages, and V_{no} is the load voltage with respect to the neutral, the generalized discontinuous PWM is laid out in Table 2.3, showing the switching states together with the stationary reference voltages.

Table 2.3: Generalized discontinuous PWM

S_{11}	S_{21}	S_{31}	V_{qs}	V_{ds}	V_{os}
0	0	0	0	0	$-V_{DC}/2$
0	0	1	$-V_{DC}/\sqrt{3}$	$V_{DC}/\sqrt{3}$	$-V_{DC}/6$
0	1	0	$-V_{DC}/3$	$-V_{DC}/\sqrt{3}$	$-V_{DC}/6$
0	1	1	$-2V_{DC}/3$	0	$V_{DC}/6$
1	0	0	$2V_{DC}/3$	0	$-V_{DC}/6$
1	0	1	$V_{DC}/3$	$-V_{DC}/\sqrt{3}$	$V_{DC}/6$
1	1	0	$V_{DC}/\sqrt{3}$	$V_{DC}/\sqrt{3}$	$V_{DC}/6$
1	1	1	0	0	$V_{DC}/2$

From this table, output voltages can be represented using a space diagram in the hexagonal form, as shown in Figure 2.44. Vectors U1 through U6 are active switching states, while U0 and U7 are null voltage sequences. The switching turn-on times of the active states and the null states help determine and program the duty cycle of the switching element. During the operation of an inverter, the sum of times of two switching modes for active states is less than the operation period of the switching device. The remaining time is meant for the null states.

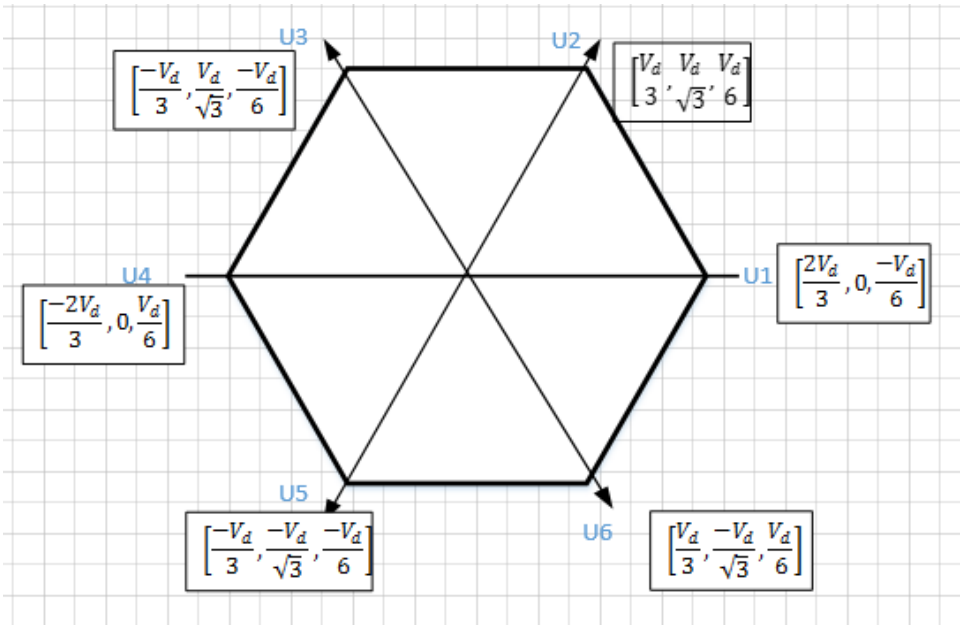

Figure 2.325: Space diagram for eight switching states including zero voltage sequences

The average of the neutral voltage V_{no} over the time period is expressed by Equation 2.64.

$$V_{no} = V_{oa}t_a + V_{ob}t_b + V_{oo}t_o + V_{O7} \qquad \text{Equation 2.64}$$

Where t_a, t_b are the normalized times set in accordance with the converter sampling frequency.

The expression of the neutral voltage per quadrant of the space representation is shown in Table 2.4 below.

Table 2.4 Expression of the neutral voltage over the six sectors

Sector	Neutral voltage
I	$0.5V_{bn} + 0.5V_{DC}(1-2\alpha) + 0.5[V_{cn} - V_{an}]$
II	$0.5V_{an} + 0.5V_{DC}(1-2\alpha) + 0.5[V_{cn} - V_{bn}]$
III	$0.5V_{cn} + 0.5V_{DC}(1-2\alpha) + 0.5[V_{an} - V_{bn}]$
IV	$0.5V_{bn} + 0.5V_{DC}(1-2\alpha) + 0.5[V_{an} - V_{cn}]$
V	$0.5V_{an} + 0.5V_{DC}(1-2\alpha) + 0.5[V_{bn} - V_{cn}]$
VI	$0.5V_{cn} + 0.5V_{DC}(1-2\alpha) + 0.5[V_{bn} - V_{an}]$

The next step is to generate the output of the VSI. A six-step inverter in a half bridge configuration is being used. Three phases are phased with $2\pi/3$ from one to the other. Figure 2.46 shows the switching states from the positive and negative signals.

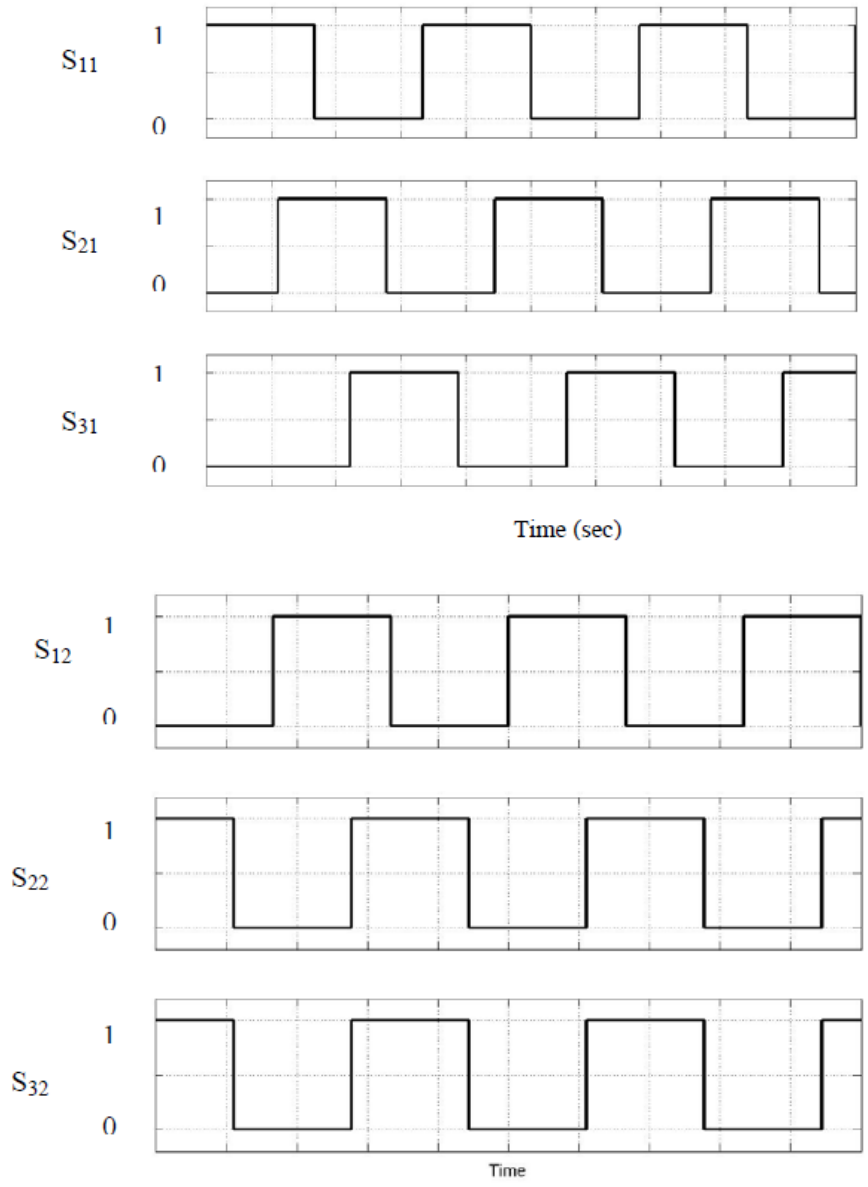

Figure 2.336: Square wave switching signal

Where in this figure the time switching shows in time second, in the switches.

Phase to neutral voltages can be described by Equations 2.65–2.67.

$$V_{ao} = \frac{2V_{DC}}{\pi}\left[\cos(\omega t) - \frac{1}{3}\cos(3\omega t) + \frac{1}{5}\cos(5\omega t)_{.} - \cdots\right$$ Equation 2.65

$$V_{bo} = \frac{2V_{DC}}{\pi}\left[\cos\left(\omega t - \frac{2\pi}{3}\right) - \frac{1}{3}\cos\left(3\left(\omega t - \frac{2\pi}{3}\right)\right) + \frac{1}{5}\cos\left(5\left(\omega t - \frac{2\pi}{3}\right)\right)_{.} - \cdots\right$$ Equation 2.66

$$V_{co} = \frac{2V_{DC}}{\pi}\left[\cos\left(\omega t + \frac{2\pi}{3}\right) - \frac{1}{3}\cos\left(3\left(\omega t + \frac{2\pi}{3}\right)\right) + \frac{1}{5}\cos\left(5\left(\omega t + \frac{2\pi}{3}\right)\right)_{.} - \cdots\right$$ Equation 2.67

The line voltages can then be deduced from the abovementioned equations and equalities:

$V_{ab} = V_{an} - V_{bn}$,

$$V_{ab} = \frac{2\sqrt{3}V_{DC}}{\pi}\left[\cos\left(\omega t - \frac{\pi}{6}\right) - \frac{1}{5}\cos\left(5(\omega t - \frac{\pi}{6})\right) - \frac{1}{7}\cos\left(7(\omega t - \frac{\pi}{6})\right) + \cdots\right] \quad \text{Equation 2.68}$$

Similarly, Equation 2.69 and 2.70 can be deduced.

$$V_{bc} = \frac{2\sqrt{3}V_{DC}}{\pi}\left[\cos\left(\omega t - \frac{\pi}{2}\right) - \frac{1}{5}\cos\left(5(\omega t - \frac{\pi}{2})\right) - \frac{1}{7}\cos\left(7(\omega t - \frac{\pi}{2})\right) + \cdots\right] \quad \text{Equation 2.69}$$

$$V_{ca} = \frac{2\sqrt{3}V_{DC}}{\pi}\left[\cos\left(\omega t + \frac{5\pi}{6}\right) - \frac{1}{5}\cos\left(5(\omega t + \frac{5\pi}{6})\right) - \frac{1}{7}\cos\left(7(\omega t + \frac{5\pi}{6})\right) + \cdots\right] \quad \text{Equation 2.70}$$

The resulting signal is protrayed in Figure 2.47.

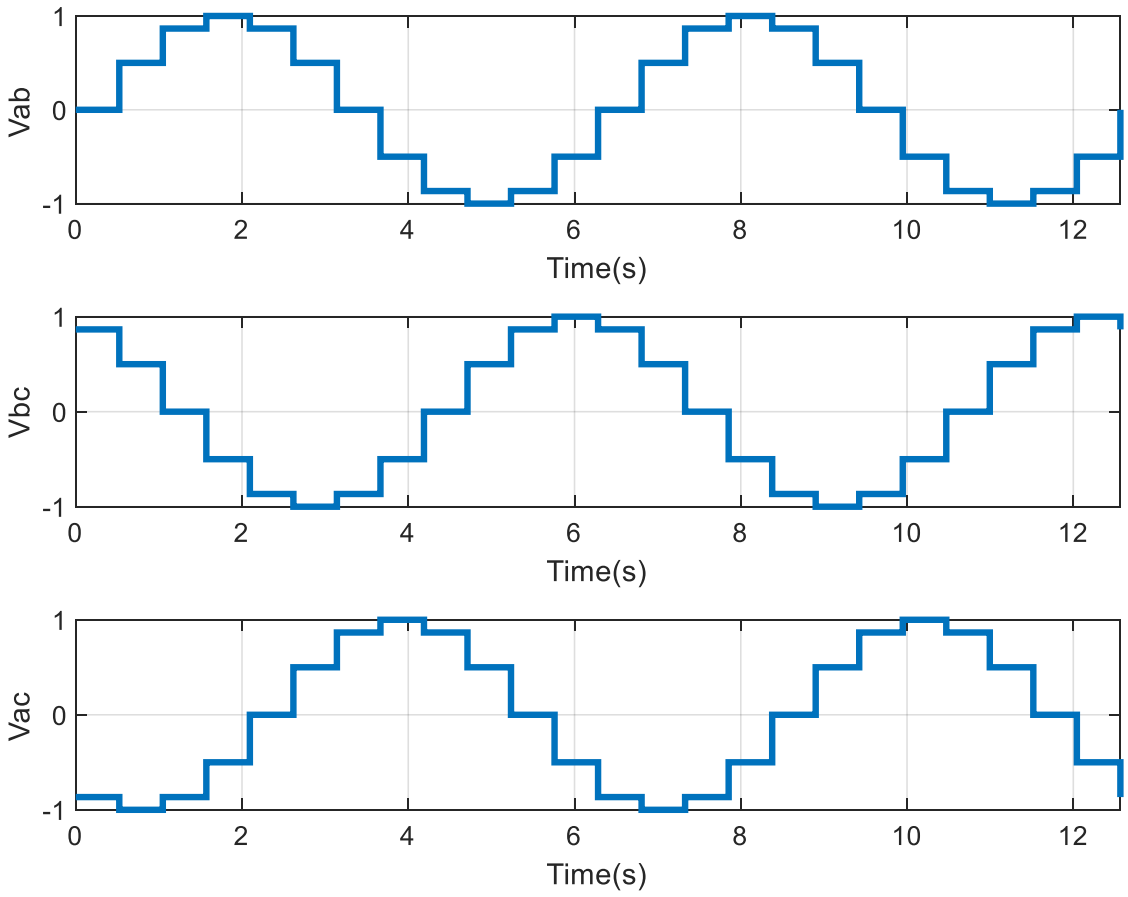

Figure 2.347: Three VSI output

In the previous figure 2.47 the three VSI output Vac and Vbc and Vab are showing in time second.

2.11Harmonic distortions

2.11.1 Introduction

The harmonic distortions (HDs) manifest in the deviation in the sinusoidal waveform voltage in the network or the load. In other words, the voltage at the load level or in the network, for instance, from the VSI, does not match what is expected. The presence of HDs affects the quality of the power being delivered in various aspects. It may cause efficiency losses, circuit breaker tripping, motors and generators malfunction, disturbance or interference with logic circuit functioning, etc.

Nonlinear loads have been identified as the main source of HDs. A nonlinear load can be understood as a load in which the current across is not related to the voltage by a proportionality ratio. Linear loads can be classified as resistive, capacitive, and inductive, and will have a current flowing through that is inversely proportional to the voltage. A nonlinear load changes impedance when a time-varying voltage is applied. Typical examples of nonlinear loads are half-wave and full-wave diode rectifiers. Harmonic distortions necessitate the analysis of the output voltage. Which will be explored in the following section.

2.11.2 Harmonic distortions analysis of the output voltage

As seen in previous sections, the output of the inverter is non-sinusoidal and bears the contents of a square wave. Therefore, the analysis of the output voltage can be done using the Fourier series equation.

$$f(\omega t) = \frac{a_0}{2} + \sum_{n=1}^{\infty}() a_n \cos(n\omega t) + b_n \sin(\omega t) \qquad \text{Equation 2.71}$$

$f(\omega t)$ This represents a periodic function of time (t), with an angular frequency ω, a_0 is the coefficient of the DC (zero-frequency) component in the Fourier series of the function $f(\omega t)$

a_n These coefficients represent the amplitudes of the cosine terms with frequencies $n\omega$ in the Fourier series of the function, b_n refers to coefficients represent the amplitudes of the sine terms with frequencies.

Fourier series coefficients are as per Equations 2.72–2.74.

$$\frac{a_o}{2} = \frac{1}{2\pi}\int_0^{2\pi} f(\omega t) d\omega t \qquad \text{Equation 2.72}$$

$$a_n = \frac{1}{\pi}\int_0^{2\pi} f(\omega t)\cos(n\omega t) d\omega t \qquad \text{Equation 2.73}$$

$$b_n = \frac{1}{\pi}\int_0^{2\pi} f(\omega t)\sin(n\omega t) d\omega t \qquad \text{Equation 2.74}$$

π This symbol represents the mathematical constant pi, which is the ratio of a circle's circumference to its diameter, n this is a positive integer index representing the harmonic number in the Fourier series. It starts from 1 and goes to infinity.

Solving for these coefficients yield Equation 2.75:

$b_n = 0$ and $\frac{a_o}{2} = 0$

$$b_n = \begin{cases} 0, n \epsilon [2,4,6, \dots] \\ \frac{4V_{DC}}{n\pi}, n \epsilon [1,3,5, \dots] \end{cases}$$ Equation 2.75

Therefore, the voltage equation can be written using Equation 2.76.

$$v_{on}(\omega t) = \sum_1^\infty \frac{4V_{DC}}{n\pi} \sin(n\omega t)$$ Equation 2.76

The rms value of the n[th] harmonic is as per Equation 2.77.

$$v_{on}(\omega t) = \frac{4V_{DC}}{n\sqrt{2}\pi}$$ Equation 2.77

From Equation 2.77, the harmonics can be portrayed as in Figure 2.47.

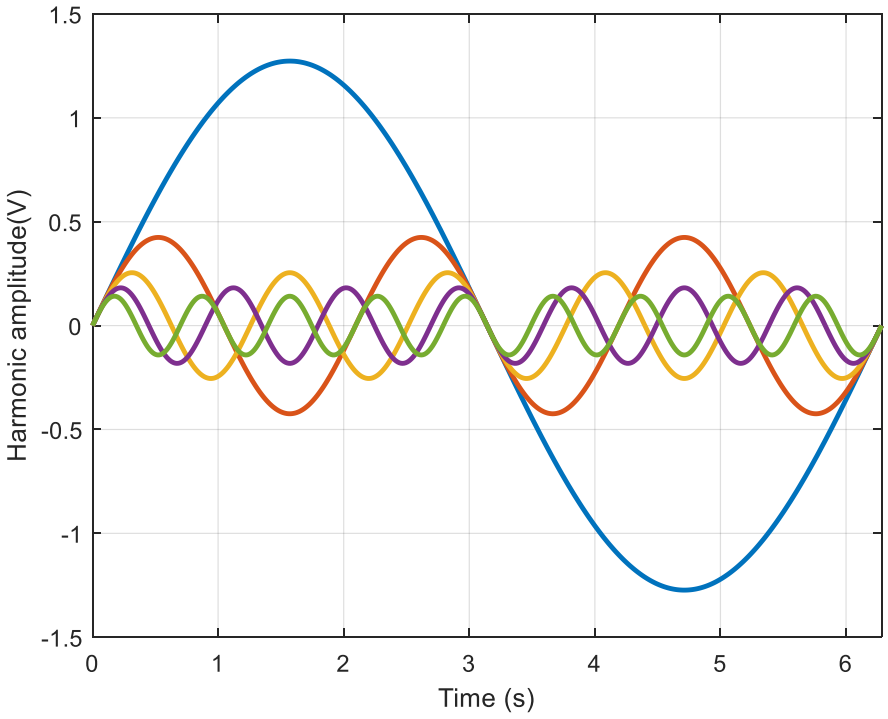

Figure 2.358: Amplitude of harmonic distortions component from the fundamental to n^{th} harmonic

In the previous figure (2.48) the amplitude of the harmonic distortions is presented. The analysis of the output voltage done using the Fourier series equation

2.11.3 Inverter performance parameters

Harmonic distortions are harmful to the load and system as they are the source of heat losses and mechanical vibrations in AC motors. The amount of distortion produced in the output voltage can be assessed based on the following parameters.

2.11.4 Distortion factor

The distortion factor (DF) is a factor that helps assess the amount of distortion residues after the output voltage has been filtered (Equation 2.78).

$$DF = \frac{1}{V_1}\left[\sum_{n=2}^{\infty} \frac{V_n}{n^2}\right]^2 \qquad \text{Equation 2.78}$$

Where V_1 and V_n are the rms value of the fundamental and n^{th} harmonic (Figure 2.49).

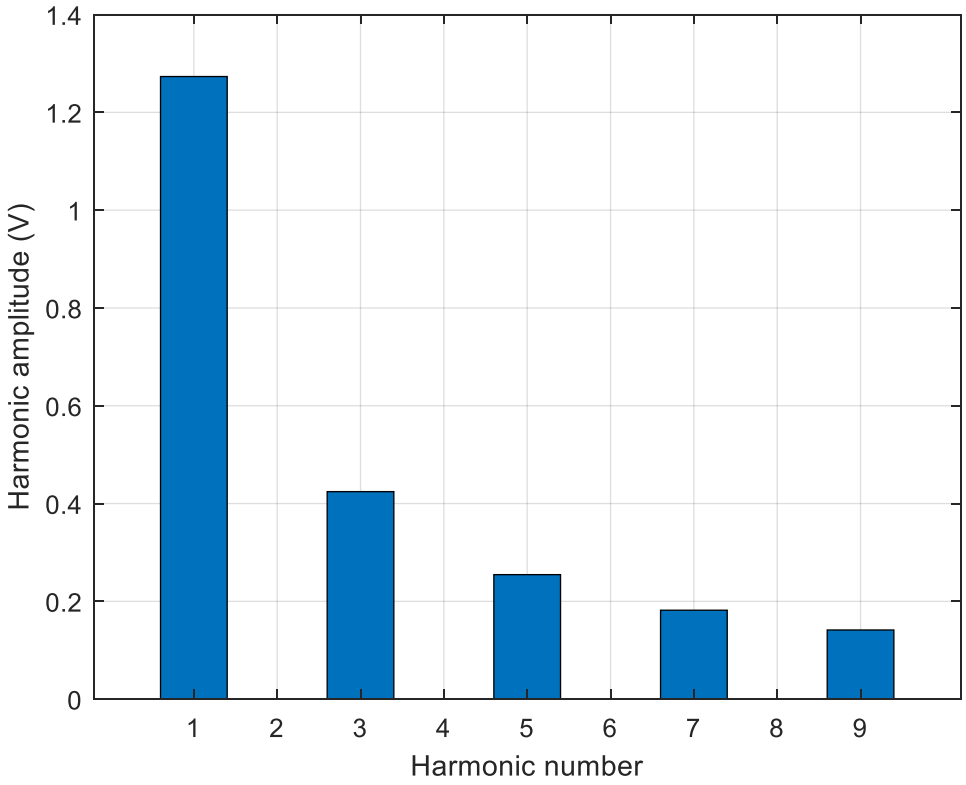

Figure 2.369: Illustration of the HDs magnitude till the n^{th} order

In the previous figure 2.49 the Harmonic amplitude (V) showed in vertical axis, while the Harmonic number showed in horizontal axis.

The contribution of the n^{th} order component in the distortion is, therefore, given by Equation 2.79:

$$DF_n = \frac{V_n}{n^2 V_1} \qquad \text{Equation 2.79}$$

2.11.5 The harmonic factor

The harmonic factor (HF) of the n^{th} component is the ratio of the n^{th} component over the rms value of the fundamental component (Equation 2.80).

$$HF = \frac{V_n}{V_1} \qquad \text{Equation 2.80}$$

This factor helps assess the contribution of each harmonic component and identify which component is dominant.

2.11.6 Total harmonic distortions

The total harmonic distortions (THD) represent the ratio of the total harmonics to the rms value of the fundamental component. This quantity also helps evaluate how close the waveform is to becoming the perfect waveform (Equation 2.81).

$$THD = \sqrt{\frac{\sum_{n=1}^{\infty} V_n^2}{V_1}} \qquad \text{Equation 2.81}$$

2.11.7 Lowest order harmonic factor

The lowest order harmonic factor (LOHF) indicates the harmonic of which the frequency is close to that of the fundamental frequency and has an amplitude within 3% close to that of the fundamental frequency.

2.12 Chapter conclusion

The study which aims to design an islanded minigrid that integrates various renewable energy sources, including solar, wind, generator, and energy storage systems. This combination of sources is motivated by the fact that the system in development will work off-grid and the renewable energy sources, namely solar and wind, are naturally intermittent due to their dependency on weather and season. This justifies the injection of generators in case solar and wind do not meet the load demand. Energy storage systems were also considered to ensure the energy excess is stored. The different options explored showed that the discharge time of energy storage systems can last up to eight hours through which they can be recharged during periods when the electricity tariff is low.

However, to ensure that energy systems are optimally utilized, especially those with an intermittent character, control systems need to be implemented. This will help save energy where possible or inject energy in the minigrid from sources via storage systems. In this thesis, the use of excess energy was considered only for storage and reuse in the minigrid. The control system will thus be multivariable since some of the energy sources involve multiple variables. As in the case of wind energy generation, there are mechanical quantities that are involved in the generation of electrical quantities. Therefore, all these quantities

would require a comprehensive control system capable of dealing with the transition from mechanical quantities to electrical quantities.

Furthermore, the control system of the minigrid is meant to monitor all kinds of energy sources involved (solar, wind, storage system, generator). Each of these energy sources comprise an input to the control system, and the whole would comprise a multivariable control system. As such, the aims and objectives to be met by this study are primarily to implement control systems schemes, mainly the proportional integral (PI) controller, to ensure that the voltage source inverter (VSI) with an LC filter output will match the energy demand regardless of the load profile variability. Therefore, going forward, the study will limit itself to that scope.

CHAPTER THREE

MINIGRID CONTROL STRATEGIES

3.1 Introduction

The current study is about designing a control system for an islanded renewable energy-based system to supply an off-grid, remote rural area with electricity. The intention is to maximize the use of possible RESs where solar energy, wind energy, and generator storage systems have been called into play. Before discussing the requirement and design of such an energy system, the aim and objectives of the study should kept in mind.

The first objective is to design a system that will effectively and efficiently control the use of energy from the abovementioned variety of sources when connected to a variable load. Objective number two is to evaluate the multivariable PI voltage and current control for a three-phase voltage source inverter under different conditions with a focus on the THDs in the output stage in the converter. Objective number three consists of testing, investigating, and analyzing the performance and efficiency of the arbitrary consumer load profiles using the Hardware-in-the-loop real-time simulation platform. This chapter tackles these objectives on a one-by-one basis.

3.2 Control system for an islanded minigrid

It is important to elaborate on why there is a need for control regarding the RESs involved in the minigrid of interest. Firstly, some of the resources are intermittent by nature, namely solar and wind-driven energy systems that are weather or season dependent. To circumvent this intermittence that would signal times of blackouts in a rural area, generator and energy storage technologies become necessary. The implication of this energy pool is that generator technologies will serve as a backup energy system, while energy storage technologies would help keep the energy from exceeding the load demand at a point in time and be ready to release it when needed.

The overall performance of the minigrid will be a product of the behaviour and the contribution of the individual source. Some require more pre-processing steps than others, whereas others possess all the characteristics and are almost ready to be fed into a stable impedance load. Therefore, the characteristics, processing, and processing requirements must be explored so as to identify the design of the control constraints and boundaries.

3.3 Minigrid operation modes and controlling architecture

The grid and control systems were not built to manage distributed energy resources (DER) on a small scale. Therefore, a new form of grid and control structures are required to accommodate this new reality of the electric grid.

Recent years have seen the creation and development of a new kind of grid, the Minigrid, which can meet some of the industry's new demands. Regarding control architecture, a novel control that can be employed in Minigrids and adapt to DER requirements is required. The grid sees a Minigrid 's DER and loads as a single entity, allowing the Minigrid to perform regulatory functions. The Minigrid structure is predicated on a collection of micro loads and micro-sources functioning as a single system, providing electricity and heat. The bulk of the micro-sources must be based on power selection to offer essential flexibility for regulated operation as a single aggregated system. This control diversity enables the Minigrid to present itself to the bulk power system as a single controlled unit, have plug-and-play simplicity for any micro source, and match the the locals' demands demands. These requirements include enhanced local dependability and safety. In addition, the minigrid features control for each power source, power flow, and voltage management.

The objectives of control designs might vary; this section focuses on minigrid control architectures.

There are two types of operation for minigrids. The controls of a minigrid are necessary to accommodate fluctuating loads and generating capacities.

The majority of DERs rely on climatological circumstances; for instance, a solar farm cannot select how much electricity to inject, while a wind farm's power output is directly related to wind speed. The control must guarantee that the voltage and frequency are constantly near their nominal levels and that all loads get the necessary amount of power. Depending on the mode of operation, the controller's goals vary. In both instances, the control must guarantee that the minigrid loads are consistently supplied with the necessary power required.

3.4 Grid-connected mode

In grid-connected mode, the voltage and frequency are controlled by the primary grid, which is in charge of the system. Therefore, the minigrid is considered as one source of power only (Balaguer et al., 2011). A steady supply of active power (P) and reactive power (Q) is supplied by local sources. Power-sharing strategies play a prominent role in this mod; in case the power generated is more than needed; it will be sold back to the utility grid after the ESSs are fully charged (Katiraei et al., 2004).Grid-connected mode views the minigrid as a single unit. Since the network is substantially more extensive than the minigrid, the network

determines the voltage and frequency. With grid-connected mode, the minigrid transfers active and reactive electricity. The complete entity is known as an aggregator and manages the associated DERs. Minigrids also regulate the frequency of the primary grid. The network transmits a regulation signal, and minigrids provide frequency control by modifying the power reference. The minigrids constantly strives to make its ACE equal to zero so that the necessary amount of power is exchanged with the network and the frequency is near the reference value.

This is how the vast majority of minigrids operate. This method requires the inverters to be in grid-feeding mode (injecting the active and reactive power desired). There is also a chance that minigrids will be networked. Moreover, the control goals differ between grid-connected mode and island mode. Until an issue arises, the minigrid typically operates in grid-connected mode. The "Switch" will be activated in such an instance, and the minigrid will enter islanded mode.

To conclude, voltage and frequency are set by the network in this mode of operation since the microgrid is linked to the main grid, and the grid is regarded as limitless compared to the microgrid. The control then has two fewer variables to govern. In this situation, the grid connects with the control device and transmits the microgrid reference power demands. The control must reorganize the power production in all DERs to ensure that the power exchange with the grid is as intended. In this mode, the purpose of the controls should be to achieve ACE=0.

3.5 Islanded mode

In islanded mode, the minigrid disturbs the demanded load between the different units in this mode. Therefore, the microgrid/minigrid operating in autonomous mode occurs when the upstream network has a failure or is going under planned maintenance,, at which point, the system will operate smoothly and supply the demanded load (Karimi et al., 2017).The power balance of the system in islanded mode and the faults that may occur during the load sharing among the micro-sources and the energy storage systems (ESSs) was addressed in the literature (Moradi et al., 2016).Furthermore, in this situation, each one of the DG inverter systems will switch to the voltage and current mode to stabilize the system by granting a steady voltage to the load (S. Yang et al., 2011).

This mode is commonly encountered when an error occurs. For instance, in the event of a grid outage, minigrids are available to provide power to certain vital structures that must always have access to electricity. One peculiarity of minigrids functioning in islanded mode is that nuclear power facilities use minigrids to maintain a steady electricity supply to their cooling systems. In fact, the Chernobyl tragedy was a failed islanding test to see how quickly

the minigrid could restore electricity while the grid went down. Additionally, as indicated before, there are instances in which the minigrid operates continuously in islanded mode, such as aboard military vessels or in locations where the network is inaccessible.

As indicated before, there are instances in which the microgrid operates continuously in islanded mode, such as aboard military vessels or in locations where the network is inaccessible. In such cases, the microgrid must now support all loads. The inverters, if present, should be operating in grid-forming mode since frequency and voltage are no longer set by the network. Inverters and distributed energy resources should establish and maintain the voltage and frequency at the reference values. In order to maintain the electrical infrastructure, the control goals have shifted from managing the power exchange with the grid in grid-connected mode to regulating voltage and frequency, ensuring that they are near to their nominal values.

In conclusion, in this mode, the microgrid is disconnected from the primary power grid, thus the voltage and frequency are no longer set. Therefore, the controller needs to adjust voltage and frequency, which should always be near nominal levels to prevent equipment damage. In islanded mode, the control should be comparable to the primary grid to achieve near-zero frequency and voltage deviations. This aim is identical to providing constant active and reactive power to all loads, as active power is directly proportional to frequency and reactive power to voltage. In total, the control goals are as follows:

- Constantly adjusting the generation to meet the demand.
- Performing an economic dispatch and ensuring that the system generates at the lowest possible cost.
- Ensuring a high-quality energy supply i.e., frequency that is constant and around nominal, and voltage that is constant and near nominal.

Distributed energy generation technologies, known as DG units, are modest, customer-proximate energy sources. The following DG units are modest, customer-proximate energy sources: small wind turbines, solar arrays, fuel cells, an energy recovery system for brakes, internal combustion engines with generators, micro-turbines, batteries, super-capacitors, flywheels, and superconductors. Storage containers may accommodate short-term and long-term applications. Moreover, through power electronic interfaces, the components are linked to networks that operate at medium or low voltages. The power electronics interface could contribute to the system's overall power balancing. Hence, the loads component of a minigrid responsible for the consumption of electrical power is referred to as the load(s). As mentioned above, all these compounds of a microgrid need to be controlled. Therefore,

control and communication is a vital part of a minigrid as these components run and control distributed generation units, distributed storage units, and controlled loads. To communicate between all of the components in a coordinated minigrid management system, advanced power electronic conversion and control skills are required. The different types of control methods implemented in the minigrid system will therefore be explored.

Integrating renewable energy sources through power converters in microgrids necessitates control to ensure voltage stability and maintain power balance. Micro-source-based DGs are often managed and linked to the grid through power converters. By coordinating and regulating these power electronics interfaces, the minigrid has great flexibility to meet system needs for efficiency, security, reliability, and power quality. In addition, with adequate regulation and communication, a minigrid comprised of DGs may offer several auxiliary services to the primary power system (Y. W. Li & Kao, 2009).

As mentioned earlier, there are two modes of operation for minigrids: grid-connected mode and islanded mode. The stable and economically effective functioning of a minigrid is contingent upon its correct management (Olivares, Mehrizi-Sani, et al., 2014). The following are the primary functions of the minigrid control structure:

- Voltage and frequency control for both modes of operation.
- Appropriate load distribution and DG coordination.
- Resynchronization of the minigrid with the main grid.
- Controlling the flow of electricity between the minigrid and the main grid.
- Optimizing the operational cost of the minigrid.
- Correct handling of transients and restoration of appropriate conditions while transitioning between connected and islanded modes.

3.6 Microgrid control classification

Microgrid control systems may be generically classified into four categories: decentralized, centralized, distributed, and hierarchical architecture (Kzaviri et al., 2017)is shown in Figure 3.1.

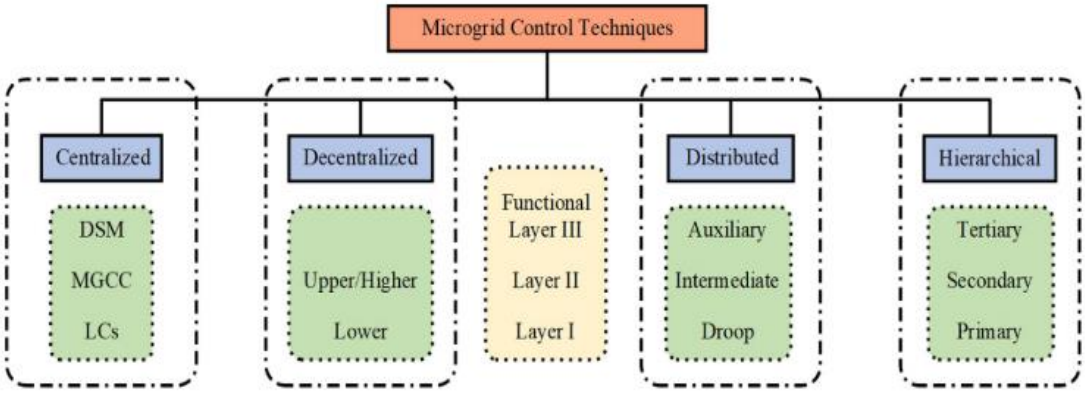

Figure 3. 1: Structure and classification of* m*icrogrid control methods (Sen & Kumar, 2018).

As the pervious figure presents the different types of the microgrid system in the following sections the different types of the microgrid system are discussed.

3.6.1 Centralized architecture

The centralized control design necessitates that each generating resource and the central processor communicate directly. Since all decisions are made by the central processor, all generating resources must remain in continual communication with it. If there is a communication issue between a node and the central controller, that node will not be able to offer effective system stabilization regulation. The fact that all nodes broadcast and receive information from a single control node makes this control efficient and straightforward. Additionally, this control is costlier than distributed, and the design of centralized control is susceptible to a single point of failure (Figure 3.2).

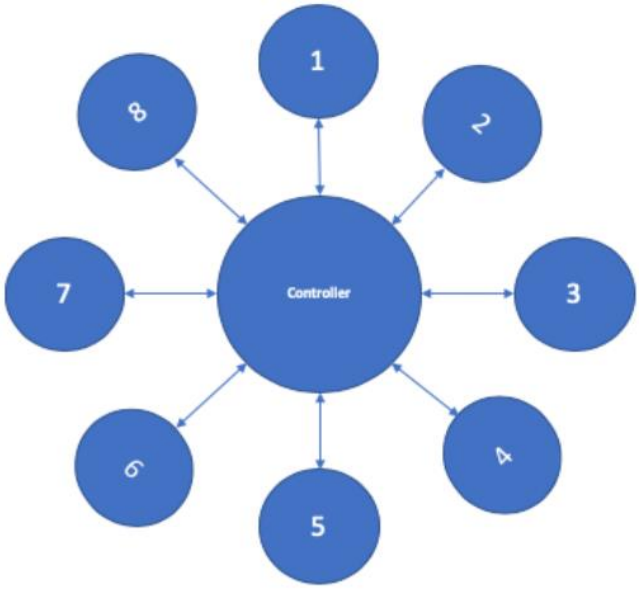

Figure 3. 2: Centralized control architecture

The centralized method proposes that the central processing unit (CPU) gather all measurements and select the next step for coordinated operation inside the microgrid. The objective is to arrange and coordinate the operation of controlled loads and generators to get the greatest possible financial benefit from participation in the energy market (Bahrami et al., 2017)**.**

3.6.2 Decentralized architecture

When using a decentralized strategy, it is recommended to create a distributed control system by placing controllers at various nodes around the network. The decentralized control technique uses local measurements and operates based on pre-defined algorithms incorporated in each node. This approach makes decisions about what actions should be taken at the component level.

3.6.3 Distributed architecture

In distributed control, several control nodes are interconnected. In distributed control, several control nodes are interconnected, resulting in several computational nodes. This control is better suited for managing DER. In addition, this regulation is consistent with the project's purpose, which is to reduce the cost of microgrid development. It needs fewer infrastructure modifications than a centralized system. Therefore, Therefore, this type of architecture is required to manage a microgrid (the expense of adding or removing a DER is significantly reduced due to this control's adaptability) (Figure 3.3).

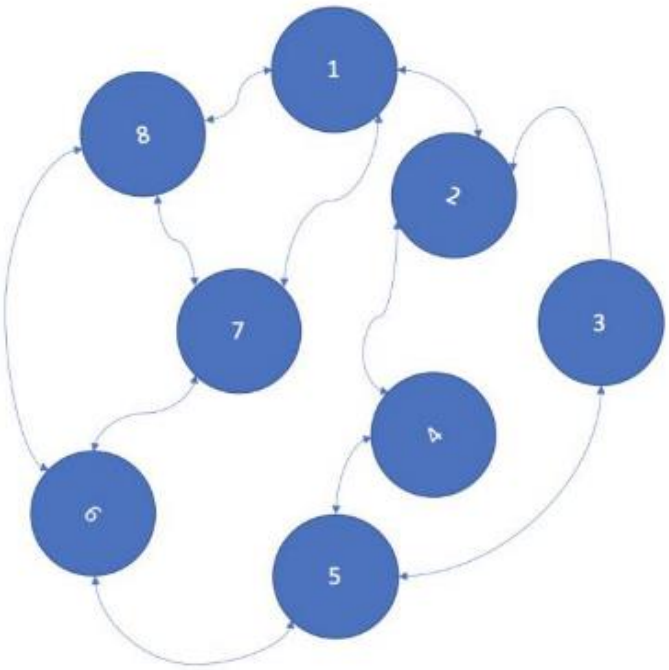

Figure 3. 3: Distributed d architecture scheme

The distributed control architecture provides many advantages over centralized control. Firstly, it is more dependable since the system can continue functioning normally even if one of its nodes fails. Hence, a longer response time can be expected for this additional dependability since all nodes must calculate the method and establish consensus (Olivares, Canizares, et al., 2014)**.**

Finally, the distributed control architecture is a variation of the decentralized approach, in which each Local Controller communicates with its neighbours to get some of the benefits of the centralized design intended for the whole MG. This implies that each device is managed based on local measurements, taking into consideration the behaviour of its neighbours (Sen & Kumar, 2018).

3.6.4 Hierarchical control

The hierarchical control structure is based on the disparity between the time scales of different control needs. Microgrids operate with many control loops (Lam, 2018) , as shown in Figure 3.4. The different control strategies in hierarchical control levels are shown in respect of each power sources.

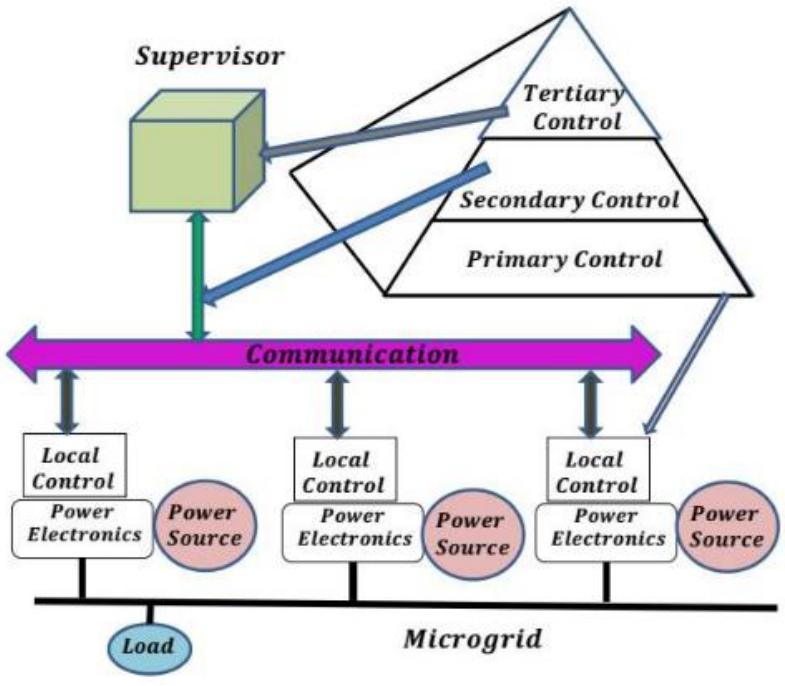

Figure 3.4: Hierarchical control levels

Power systems require control strategies to ensure their proper operation. The control strategies must take into account all time scales of the system. Hence, this is usually done

by a hierarchical control structure of MGs that may present three control levels to have the structure of AC grids: primary control, secondary control, and tertiary control.

The primary controller is responsible for local voltage regulation and ensuring adequate power distribution between several DG units and microgrid stability. The secondary and tertiary controllers assist the functioning of the microgrid by often including the ideas of optimality, communication, and prediction, thus meeting numerous goals. The primary control is an independent local control method that enables the autonomous operation of each DG unit. Primary controllers are accountable for the system's dependability and stability. Due to the quick dynamics of the microgrid, which lacks a significant amount of spinning inertia, the principal controller needs to be fast on millisecond time scales. This local primary control comprises the hardware's essential control. It must ensure the stability of the DGs' internal voltage and current (often via separate control loops) by monitoring and managing the local signals. Furthermore, primary controls are often categorized as follows: droop control, voltage and frequency control, active and reactive power-sharing, and energy management system (EMS) (Sen & Kumar, 2018).

Secondary control allows for power-sharing using a communication-based mechanism for the parallel setup of DGs. It also adjusts for voltage and frequency errors brought on by fluctuations in demand and local control operation (Vandoorn et al., 2013)**.**

The tertiary control level and tertiary reserve allocation are intended to optimize the dispatch of distributed energy resources and provide load balancing in a local power distribution network. Economic, technological, and environmental optimization may be a part of dispatch optimization (Unamuno & Barrena, 2015)**.**

Tertiary control is responsible for directing the functioning of many microgrids and their exchanges with the main grid (buying or selling power, providing ancillary services such as voltage support and frequency regulation). This level of control generally runs with a time step of several minutes to hours .In addition, it provides signals to the secondary level at microgrids and other subsystems that comprise the whole grid. In contrast, secondary control coordinates internal primary controls inside microgrids and subsystems in minutes. Finally, essential controls are meant to work autonomously and respond instantly in predetermined ways to local occurrences (Morstyn et al., 2018)**.**

3.6.5 General summary of the local control found in microgrids

Traditionally, a variety of control strategies, such as PI/PID linear control, sliding mode, and linear quadratic control, have been used to control microgrids.

PI/PID linear control: Due to its simple design, PI/PID controllers are widely used in the industrial sector for power systems. It is durable and dependable and delivers near-optimal control system performance with suitable gain adjustment. However, the PI/PID tuning approaches are restricted in their capacity to tune the PID gains for nonlinear and complicated systems properly. Within this context, the PID performance is highly dependent on the optimal PID parameter values. In addition, being a linear technique, its performance may vary significantly if the system is used throughout a broad operational range (Roslan et al., 2019).

Linear quadratic regulator: The objective of linear quadratic regulation (LQR) is to reduce or maximize a utility cost function and determine the appropriate control strategy. The problematic aspect of the linear quadratic regulator is selecting the weighted matrices Q and R to get the desired response (Mahmud et al., 2014)**.** Moreover, since microgrids are nonlinear systems, nonlinear techniques such as feedback linearization, and PI/PID are necessary. In designing the controller for these systems, nonlinear control and backstepping are used. Hence, these techniques have been investigated extensively for the stability of the microgrids (Mahmud et al., 2014)**.**

Sliding mode control: Sliding mode control has been the topic of a significant amount of research for robust nonlinear control to guarantee stability subject to parameter limitations (Mahmoud et al., 2017).

Model predictive control: Enhanced predictive control methods are used to anticipate reference signal values. An intriguing aspect of these methods is their potential to decrease tracking inaccuracy (Mahmoud et al., 2017).

Artificial-intelligence-based control: Various heuristic techniques, including particle swarm optimization, fuzzy logic, neural network, and genetic algorithm, have been used in the literature to enhance the control and optimization of MGs and DG units. Thus, both grid-connected and islanded modes of microgrid operation make efficient use of intelligence and evaluative methodologies (Mahmoud et al., 2017).

Adaptive control: Adaptive control techniques are mainly used to address parametric uncertainties and disturbances. Under moderate circumstances, adaptive control techniques may successfully provide sustained stability, robustness convergence, and system dynamics tracking (Mahmoud et al., 2017). However, it should be mentioned that the system's operating point is very variable. Consequently, the plant's controller performance may not be ideal. Adaptive solutions are employed extensively to seek out near-optimal operating conditions to overcome such obstacles (Parisio & Glielmo, 2011).Table 3.1 shows the summary of local control in microgrids.

Table 3. 1: Summary of control schemes found in microgrids

Controller		Reference
PI/PID linear control	Simple architecture makes PI/PID controllers popular in industrial power systems. With proper gain modification, PID/PI provides near-optimal control system performance. PI/PID tuning techniques can't appropriately tune PID gains for nonlinear and complex systems. PID performance depends on ideal parameter values in this situation. Being linear, its performance may fluctuate if the system is utilized across a wide operating range.	range (Roslan et al., 2019)
Linear quadratic regulation (LQR)	The linear quadratic regulator is a method used to minimize or maximize a utility cost function and determine the appropriate control strategy. However, a problematic aspect of this method is selecting the appropriate weighted matrices Q and R to achieve the desired response.	(Mahmoud et al., 2017).
Sliding mode control	A significant amount of research for robust nonlinear control to guarantee stability subject to parameter limitations.	(Mahmoud et al., 2017).
Model predictive control	Used to anticipate reference signal values. An intriguing aspect of these methods is their potential to decrease tracking inaccuracy.	(Mahmoud et al., 2017).
Artificial-intelligence-based control	Various heuristic techniques, including particle swarm optimization, fuzzy logic, neural network, and genetic algorithm, have been used in the literature to enhance the control and optimization of MGs and DG units. Thus, both grid-connected and islanded modes of microgrid operation make efficient use of intelligence and evaluative methodologies.	(Mahmoud et al., 2017).
Adaptive control	Mainly used to address parametric uncertainties and disturbances. Under moderate circumstances, adaptive control techniques may successfully provide sustained stability, robustness convergence, and system dynamics tracking.	(Lam, 2018)

3.6.6 Characteristics, pre-processing, and control requirements

In terms of solar energy-based plants, in terms of solar energy-based plants, as the power__ comes from solar cells or modules, the voltage is DC and most of the time does not meet the voltage level required by the inverter. As seen in the literature review, a maximum power point tracking system will be required to maximize energy usage. A DC-DC converter may also be used to step up or down the input voltage. The resulting voltage can then be subjected to the inversion process to generate a sinewave voltage of the grid frequency. The output voltage from the inverter contains harmonics that affect the system efficiency and may damage or harm other loads, such as motors. Therefore, the harmonics need to be filtered out prior to feeding the load.

Wind energy requires some processing but not as much as the solar counterparts. Torque results from the wind rotating the blades of the WT. Wind may have variable speeds and the blades/turbine may rotate at different frequencies; the gearbox within the WT adjusts the speed to produce the desired frequency. Variable speed WTs can adjust the speed not only from the gearbox level but also from the control of the blade pitching. The output from the WT generator is a three-phase sinewave with a frequency that meets the requirements of the network. Another area of WTs that may require control is the start-up and the stop, which need to be smooth.

Energy storage systems are diverse, and so are the stages in getting their power used. Batteries will need inversion and filtering stages prior to their energy being fed into the load. In terms of control, batteries require monitoring the state of charge (SOC) and depth of discharge (DOD). These two parameters determine the blanket of operation of the battery. Outside that blanket, the battery is operated in the risk area. Thermal storage, flywheel, and hydropower produce the power readily available for use. Depending on the level of excess power, storage technology will be used. Therefore, there will be, short-term storage systems and long-term storage systems to ensure that the power is well managed.

A generator supplies power that is ready for use. Originally meant to be used in emergency cases as a backup energy supply, generators have levelled up and are part of the mainstream energy supply. The control required for a generator mostly pertains to start-ups and stops that need to be smooth without current overshoots, as well as controlling the noise they may make while in operation.

A comparison of the processing requirements between the energy sources is simplified in Table 3.2.

Table 3. 2: Comparison of pre-processing requirements for renewable energy resources

	Mechanical to electrical conversion	DC-DC conversion	DC-AC conversion	Filtering	Frequency adjustment	Ready to use
Solar		✓	✓	✓	✓	
Wind	✓				✓	
Generator	✓					✓
hydropower	✓				✓	
Batteries			✓	✓	✓	
Flywheel					✓	
Thermal	✓			✓	✓	
Fuel cell			✓		✓	

3.7 Typhoon HIL and Microgrid control

This section is evaluating Typhoon HIL and its capabilities for simulations and testing microgrid and other electronic systems.

Typhoon Hardware-in-the-Loop (HIL) is a method that simulates systems in real time while they are being tested in a closed-loop setting. It is frequently used to validate and test control algorithms and hardware components across a variety of sectors, including power systems. Typhoon HIL systems offer a controlled and reproducible method for simulating and testing complex systems, such as microgrids. Before implementing microgrids in practical applications, researchers and engineers can use this technology to evaluate the effectiveness of control strategies, fault situations, and other operational elements(Tiwari et al., 2021).

3.7.1 Schematic Editor

The Schematic Editor is used to create complex models that accurately represent real-time operations. Its use is in the creation of models that faithfully represent real-time occurrences and follow the normative graphical representations used in electrical systems. This software program includes a variety of functionalities, such as model configuration options, accelerated design shortcuts, compilation starting, initialization script modification, and traditional file management features.

Correct selection of a High-Fidelity Hardware-in-the-Loop (HIL) device is essential for the accurate modeling of a particular system. Configuring simulation phases and discretization techniques within the solver is required for this choice. Notably, the Library Explorer can be

found in the bottom-left corner of the Schematic Editor interface, making it easier to choose all necessary parts quickly and easily for model integration.

At the center of the interface, where it is identifiable by its black coloring, the electrical circuit portion of the model is conceptualized and displayed. On the other hand, the signal processing facet, shown in blue, is located next to it. The signal processing elements work as controllers within the Typhoon HIL control center, developed independently from the hardware controller yet faithfully replicating its behavior within the model framework.

Additionally, these signal processing modules provide a platform for examining a controller design's functionality, enabling the necessary pre-validation before starting simulation projects. Their crucial importance in the general modeling paradigm is furthered by their central function in virtual mode simulations.

3.7.2 HIL SCADA

A crucial component of the Typhoon HIL software architecture, the HIL SCADA (Hardware-in-the-Loop Supervisory Control and Data Acquisition) plays a key role in coordinating the simulation and evaluation of various widgets. These widgets have the ability to display a variety of data readings, activate relays, administer control gains, change reference signals, and perform a variety of ancillary tasks. The conceptualization and creation of the model within the Schematic Editor are the first steps in the operationalization of the HIL SCADA. The model is then integrated into the HIL SCADA environment. Following this combination, the compiled model is deployed onto the physical HIL device in cases of tethered interconnection with the host computer; in the absence of a physical connection, the model seamlessly interfaces with a virtualized HIL environment, where the computational capabilities of the host CPU emulate the presence of the HIL hardware entity. It is crucial to remember, however, that the virtualized simulations inside this environment deviate from real-time operation, necessitating a noticeable lengthening of the time step.

The materialization of an HIL device is required for the proper execution of HIL simulations as well as supplementary functionalities, according to the operational matrix of the HIL domain. The Typhoon HIL software ecosystem's integrated hardware platform serves as the fundamental enabler for HIL simulations and related activities. The host computer's inherent specifications and processing power have a significant impact on the conceptual model's complexity, providing a direct link between computational power and model complexity.

Widgets serve as essential evaluative agents once the model has been deployed, based on the fundamental principle of facilitating postulation inspection and simulation evaluation. Although the monitoring interfaces seen throughout these widgets conform to a user-centric

design ethos, it is crucial to emphasize that their applicability goes beyond simple data collection from simulations.

The Typhoon Test IDE serves as a key facilitator for the integration of automated test paradigms with automated data recovery functions, which broadens the scope of the utility. It is important to note that, given that this tool was not used in the simulation projects described in this article, its explanation is still outside the scope of the discussion at hand.

The HIL SCADA interface has the option of configuring the basic model parameters before the simulation starts. These cover a wide range of crucial characteristics, such as the battery's level of charge, voltage ranges, relay status indications, and switching devices' working status. Additionally, the overall SCADA environment extends its control over digital and analog signal design, providing a thorough sphere of control over these features inside the larger operational domain.

3.7.3 Hardware component

In order to provide real-time operations, the simulation's execution requires the insertion of an additional computational device. This gadget acts as a middle interface, capable of swiftly conveying signals between the software and hardware components while guaranteeing an astounding level of accuracy in signal fidelity. In order to function as the hardware component of this arrangement, Typhoon HIL has integrated the Hardware-in-the-Loop (HIL) device. Field-Programmable Gate Arrays (FPGAs) are a component of this assembly that allow for the quick execution of the underlying model, which determines how quickly the device operates. The HIL device is outfitted with built-in DIN-compliant DIN connectors with a variety of pins that allow for bidirectional signal transmission in both analog and digital forms.

The Typhoon FPGA solver, the System CPU, and the User CPU are the three basic computing components that make up the HIL device. As a specialized multicore processor, the Typhoon FPGA solver is in charge of carrying out precise and exacting simulations of diverse electrical domain models. It takes on a crucial function in the HIL device by carefully tackling the challenging task of solving the differential equations entailed in the electrical circuit. This task is carried out at each nodal intersection of the model, so defining the temporal progression of the simulation by skillful establishment of the simulation time step.

The System CPU assumes a versatile role, dedicated to the emulation of low-dynamic functionalities intrinsic to distinct components within the electrical domain. Moreover, it is entrusted with the proficient facilitation of signal exchanges amidst communication protocol stacks. In parallel, the User CPU parallels the capabilities of the System CPU, serving as a

comprehensive processor responsible for the instantiation of sub-models comprising signal processing constituents. Notably, it extends its functionality to the emulation of non-electrical domain components, encompassing domains such as thermal or mechanical models.

In the context of temporal progression, the HIL device's simulation time step is intricately interlinked with the presence of User CPUs. Notably, this time step necessitates a considerable elevation over the simulation step interval.

3.7.4 Hardware in the loop simulation

The main goal of integrating this model into the Typhoon HIL framework through high-power simulation is to validate results obtained in the MATLAB/Simulink environment. This validation project includes a wide range of elements, most notably the supply system's control loop. This system carefully manages the power supply in tandem with variations in demand by coordinating the interaction of various energy sources. Additionally, it incorporates the complex energy management system algorithms and harmonizes them with the demands of the system requirements.

In a paper by (Nigam et al., 2020) a basic microgrid with dual sources is envisioned and investigated under various load scenarios. Typhoon HIL real-time simulation software is used to implement the full system in a virtual environment that includes a variety of scenarios. The effectiveness of supplying loads from a single source vs connecting two sources to the loads is being evaluated. The findings of the experiment indicated above shed light on the complex nature of source-load interactions.

Where in (Pavan Kumar & Bhimasingu, 2017) evaluation includes how well the two sources perform when they are coupled to various loads. Contactors are used to examine source behavior on the loads. The two sources provide the two loads while the Source contactor is in use. When the sources are cut off, a steady load with characteristics of frequency droop is powered by them. The load contactor must be connected to a second resistive load that runs in parallel with the first in order to be activated. The integration of a core coupling component is done to maintain circuit integrity due to the modeling of constant power blocks as current sources. SCADA widgets are used to monitor simulated signal data and include a variety of measurement and monitoring tools.

Where in a study by (Bagudai et al., 2019) a hybrid DC/AC microgrid's control system is modelled and validated in this work. Simulation approaches are used to do this. The enormous difficulty in evaluating control functionality at the system level is shown by early simulation research. As a result, hardware-in-the-loop simulations are used to shorten simulation times and increase effectiveness.

Where the authors (Som et al., 2022) conducted study on in an isolated microgrid , a battery energy storage system (BESS) assumes a crucial role in the regulation of system frequency and voltage. A robust control mechanism based on -synthesis methodology has been established to achieve the regulation of the direct current (dc) link voltage of the BESS, enabling frequency regulation and improving voltage quality within the isolated microgrid. Variations in the alternating current (ac) microgrid's operating circumstances have a significant impact on how the BESS converter operates. In developing this control technique, parametric uncertainties resulting from the dynamic nature of ac microgrid operating circumstances are considered, along with the presence of unpredictable variations. Importantly.

In order to evaluate the effectiveness of both centralized and distributed secondary frequency control procedures inside AC microgrids operating in islanded conditions, the work of (Lamo et al., 2021) defines a methodological framework using controller hardware-in-the-loop (C-HIL) techniques. The exegesis explains the secondary frequency control conundrum and the theoretical foundations guiding the application of both centralized and distributed instantiations of these control paradigms. A description of the C-HIL experimentation platform used in these evaluation efforts follows. Finally, a thorough examination of the testing results is proposed, enabling a comparison of performance metrics—primarily system response time—as well as the robustness of these schemes, assessed in terms of their ability to continue operating in the event that a control device fails. However, for microgrid secondary frequency control, a comparison of centralized and distributed techniques is provided. Response time and resilience are two crucial performance measures that the study uses to identify the inherent advantages of the schemes under investigation. When compared to its distributed version, the analysis shows that the centralized frequency control technique performs best in terms of response time. However, the distributed system outperforms the centralized one in terms of robustness.

Moreover, researchers (Lahmer et al., 2023) suggested a distributed hierarchical control approach based on adaptive droop control and a secondary control with a proportional consensus to ensure DC-microgrid control objectives. In ESUs with various beginning SOCs and capacities, the primary control ensures SOC balancing and current sharing, while the secondary control returns the bus voltage to its nominal value in the event of both transmission delay and self-processing delay.

A theoretical foundation for managing a rural microgrid is developed in a research study carried out by (Lautert et al., 2022) the structure includes many different loads, batteries, energy storage technologies, and the wind, photovoltaic, and diesel generators. A notable

level of grid flexibility and security was provided by the synchronized control technique, which not only resulted in significant cost reduction but also in a heightened guarantee of energy availability. The addition of power plants that use sporadic energy sources and an increase in dispersed generation have made the Brazilian electrical system more complex. Microgrids (MGs) include a wide range of crucial elements that are crucial for the smooth operation of the overall system. A more secure and flexible operational paradigm for the grid is being developed thanks in large part to the integration of MGs. The microgrid model proposed in this academic study provides support for these claims. The reliability and uninterrupted nature of the energy supply are enhanced by combining renewable power sources with energy storage infrastructure. Moreover, its value has been effectively proved by the expert oversight of Distributed Energy Resources (DERs) inside the microgrid environment, highlighting its crucial function within the larger system architecture. Microgrids' current trajectory and suitability within the current electrical landscape are invariably validated by a variety of empirical research and strategic expenditures aimed at their fulfilment.

3.8 Chapter conclusion

In this chapter, energy management and control systems have been reviewed with focus on islanded minigrids, operation modes, and control systems classification. As well as Typhoon HIL software explained and recent studies in microgrid control. Despite each stage demonstrating that an energy source requires control, this study will stick to the main objectives with focus on the novelty of minigrid. Therefore, Chapter Four will discuss the development of the control system encompassing all the energy resources feeding into a variable load. Secondly, the PI and PID control schemes will be used to ensure that the current, voltage, and frequency are in the range of an arbitrary load demand.

CHAPTER FOUR

DESIGN AND IMPLEMENTATION OF AN ALGORITHM FOR ENERGY TRANSACTION MANAGEMENT

4.1 Introduction

The control system of the islanded minigrid will be dealt with based on the first objective, which entails ensuring that the resources are controlled to meet the demand of an arbitrary or variable load and storing the energy that exceeds the instantaneous demand of the load. The study consists of a simulation of scenarios where over a day, renewable resources fluctuate with the risk of leading to power failure if not well managed. The weather-dependent nature of solar and wind power, the risk of storage systems depleting, and the demand itself increasing and decreasing are sufficient factors to suggest the need for a system that will monitor and manage the operation of a minigrid. Centralized control system for a multivariable islanded minigrid

The design of the control system is guided by the energy resources that will be involved and the concept of a minigrid. A minigrid is viewed as a power network that can generate between 10 kW and 10 MW, where solar and wind resources are the power sources with energy storing facility and a standby generator to attend to power failure emergencies (Kimera et al., 2012). A minigrid can also be conceived based on the population it can serve. A population of up to two hundred households in a rural area falls under the category of minigrid (Hazelton et al., 2014). The control system being developed will be multivariable, given the various resources and energy transactions expected to take place within the islanded minigrid.

For this study, the power consumption per household is set to 1 kW, which amounts to 200 kW maximum power required in total. The energy produced, consumed, or stored will be expressed in Watt-hours as per Equation 4.1:

$$Energy = P * t \qquad \text{Equation 4.1}$$

Where P represents the power and t represents the time.

4.2 Power rating requirements

The power rating of the energy resources has been set to the baseline load consumption, meaning 200 kW. The rationale behind this is due to the intermittent nature of solar and wind, which are the main energy sources. The aim is to avoid disappointment on when the wind and sun have parameters that do not meet requirements. Thus, all the energy

resources will be rated at 200 kW, and the same applies to the energy storage facility and the generator. However, the control system will be able to cater for the increase in the power rating.

4.3 Control system functionalities

The functionalities of the control system need to be identified first, and then a control algorithm will follow.

- The control system will be able to monitor the status of the energy resources and ensure the load requirements are met.
- The control system will be able to read the data and take necessary action to manage the resources.
- The control system will be able to provide an update about the energy produced, consumed, and stored per resource at any time of the day. Graphs and numerical figures shall be used.
- The control system is meant to connect or disconnect an energy source to ensure that the load demand is met at any time.
- The control system will be able to connect or disconnect an energy resource depending on the need.

4.4 Centralized and multivariable control system algorithm

The algorithm developed to control the islanded minigrid would be able to monitor the energy status of the stakeholders (solar, wind, storage system, and generator) and give the energy levels of each of them at any time of the day.

Step one: Energy data loading

- The user should enter the amount of energy resources.
- The user should enter the capacity of the combined plant.

Step two: Check the supply and the energy demand

- At a point in time, if the energy generated/supplied exceeds the load demand:
    - Only a portion equal to the load demand is supplied.
    - The energy excess is stored.
    - The data must be updated.
- Else, if the supply is less than the load demand, connect other energy sources till the supply is at least equal to the load demand.
    - Calculate the difference and store it.
    - Update data.

To implement this algorithm, one needs to have a load profile. The profile of an arbitrary load has considered peak and off-peak time use of energy. The algorithm was implemented referring to a code written in MATLAB R2018 (Appendix 3.1).

4.4.1 Arbitrary load profile for residences in the rural area

The structure of the load profile for residences in the rural area is such that there is a peak in the morning, around noon, and evening time. In the morning, the peak energy use is due to the energy required to heat space and water, as well as for lighting and preparing breakfast. Around noon, the peak is due to energy spent on cooking, heating, and lighting. At night, energy consumption hits its lowest level only to rise again in the morning. However, the profile is expected to be to be a bit more prominent in the evening than in the morning in terms of cooking time and space heating. Such a load profile can be modelled as pictured below (Figure 4.1).

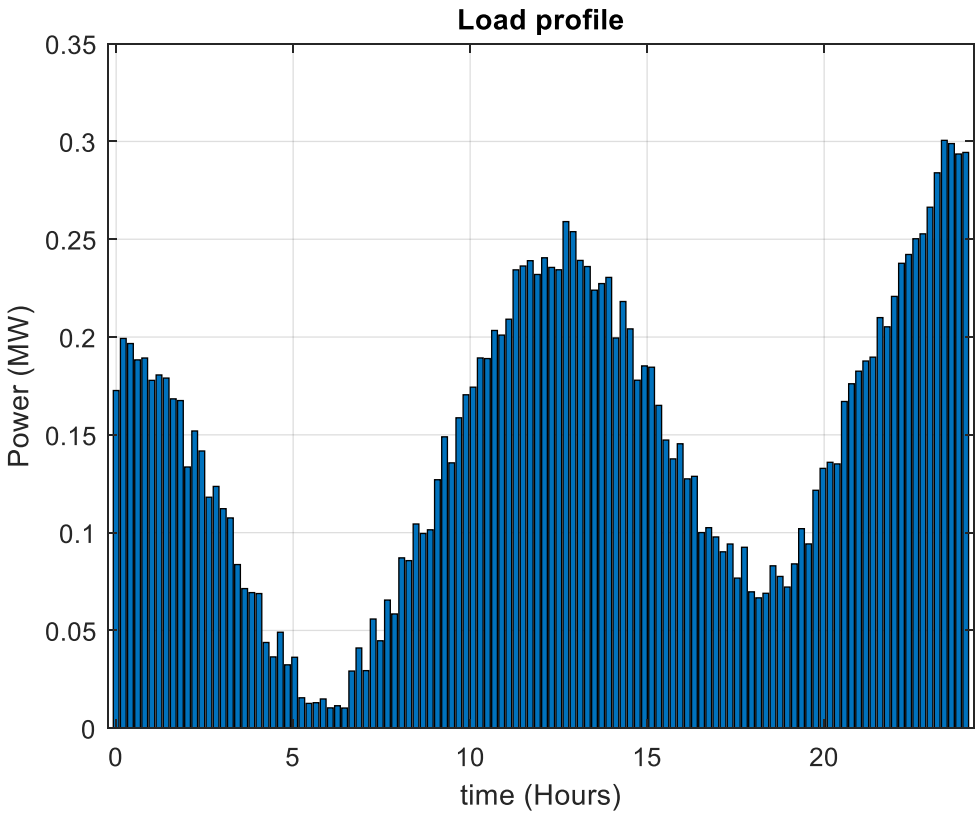

Figure 4.1: Arbitrary load profile

The pervious figure shows the arbitrary load profile during the hours of the day in heretical axis (time), and the power (MW) is presented in the vertical axis.

4.4.2 Profiles for energy resources

The solar energy profile depends on the irradiance levels, whichis at its lowest value before sunrise and after sunset. Following the rotational movement of the sun, the irradiance rises at sunrise and hit its maxima at noon, before gradually decreasing after noon till the sunset (Figure 4.2). Such a profile is known to have a Gaussian shape and can be mathematically approximated as per Equation 4.1.

$$SolarEn = S_{emax}(\frac{1}{\sigma\sqrt{\pi}})e^{-\frac{1}{2}(x-\mu)^2} \quad \text{Equation 4.1}$$

Where $SolarEn$ is the solar energy, S_{epeak} is the peak value of solar energy, σ is the standard deviation.

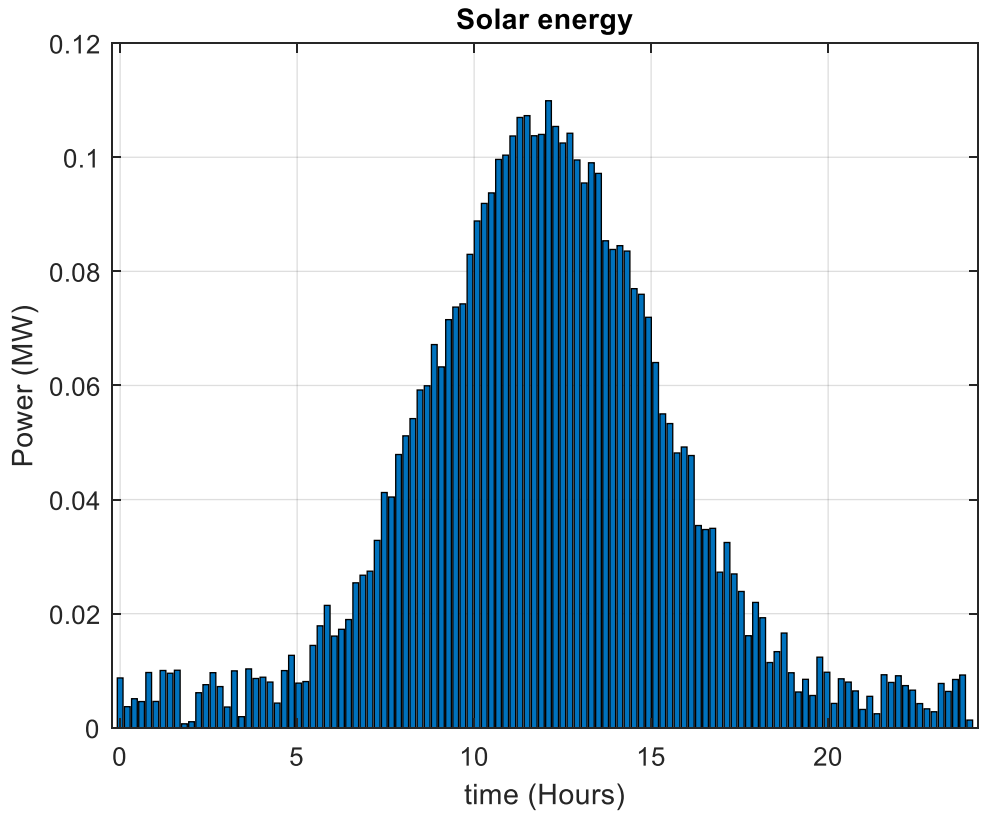

Figure 4.2: Solar source energy profile

The pervious figure 4.2 shows the solar energy profile where the irradiation is high during midday and in its lowest at evening when the sun is down.

The wind plant profile depends on the speed and torque. These are the control elements. However, the literature indicates that wind with a speed of 4m/s can turn on a WT. In this

prime time, it will be assumed that this minimum requirement is met in terms of wind speed (Figure 4.3).

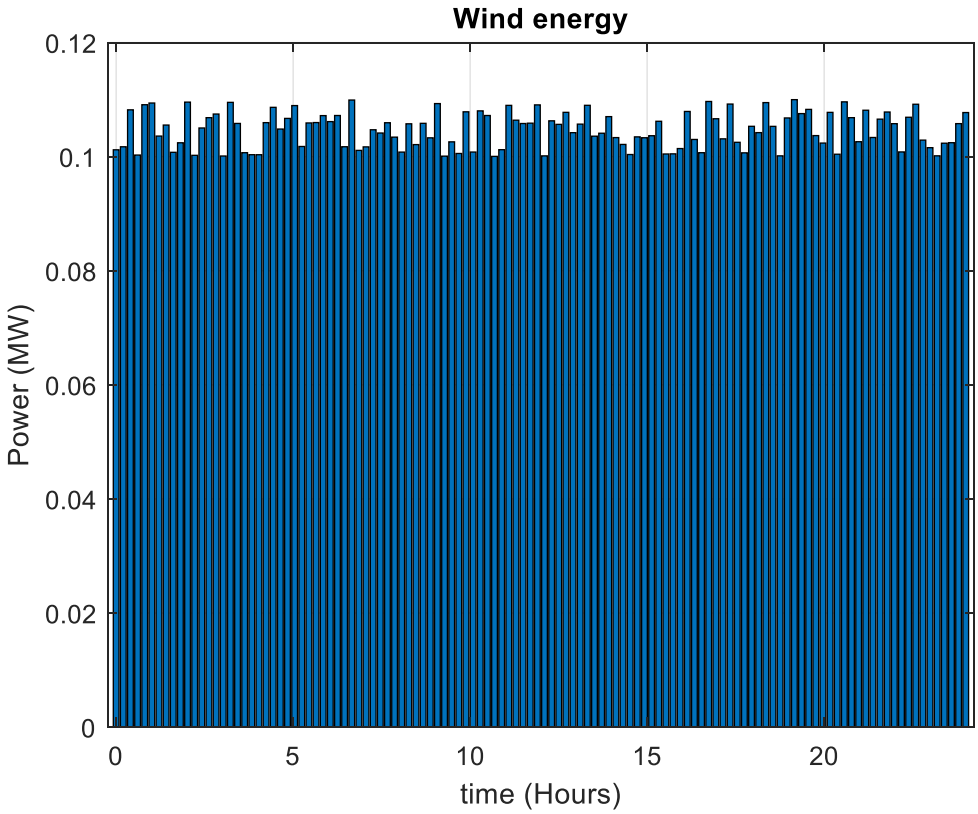

Figure 4.3: Wind energy profile

Thereafter, in the previous figure 4.3 the wind energy profile is presented; hence, the vertical axis presents the power in (MW), and the horizontal axis shows the time in hours.

The generator has a constant level wattage in its permanent regime of operation; this can be illustrated as per Figure 4.4.

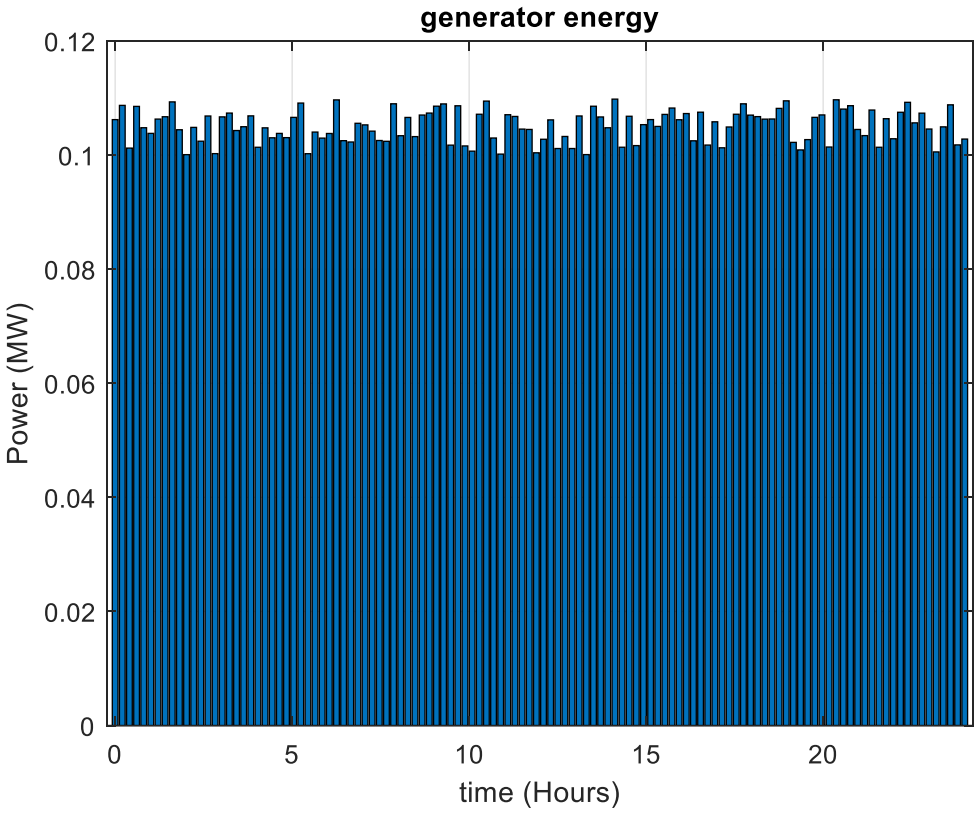

Figure 4.4: Generator energy profile

In the previous figure (4.4) the generator energy profile is shown, as the power (MW) is in vertical axis and the time (hour) in the horizontal axis.

The total energy will be the sum of the contributions of the individual contributions from the solar and wind sources and the storage system. The generator will be left out of this because it will be counted on in situations where all other energy sources cannot meet the load demand or in case of a network fault pre-load (Figure 4.5).

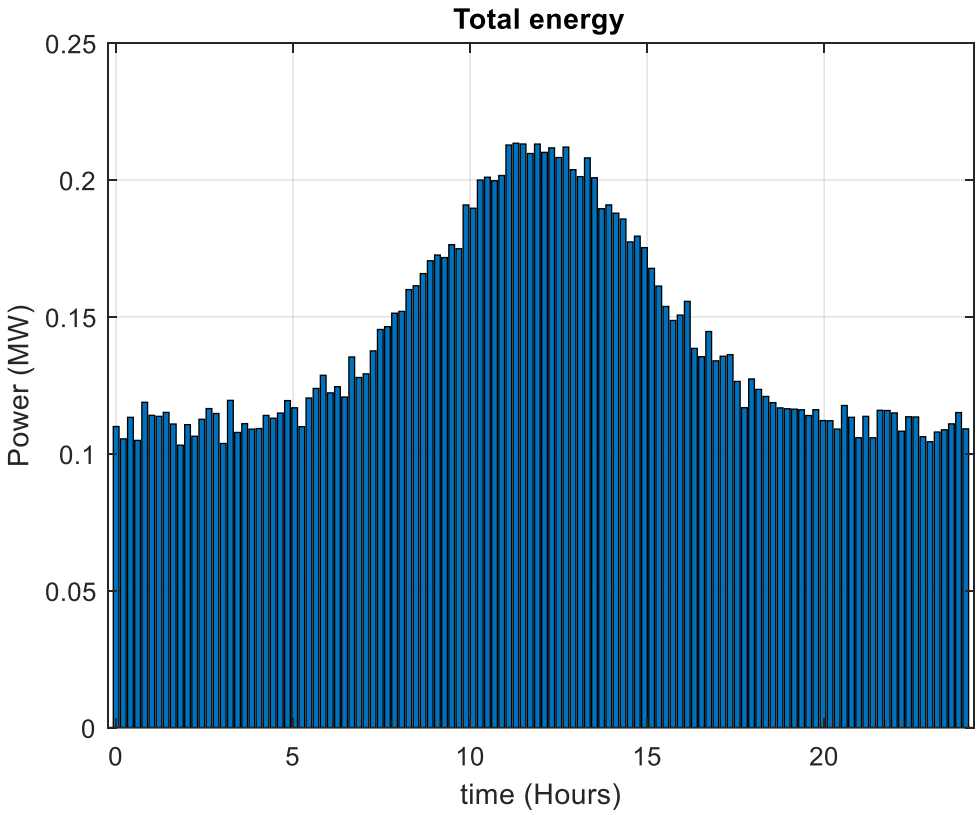

Figure 4.5: Total energy profile

Where the total energy profile is presented, the power in (MW) showed in the vertical axis, and the time in hours in horizontal axis.

Figure 4.6 shows the stored energy, which can be calculated as the total energy minus the load energy or the energy consumed by the load. One point to take note of is that when the load energy exceeds the total energy, the storage devices will supply the load, hence the negative output on the profile of stored energy.

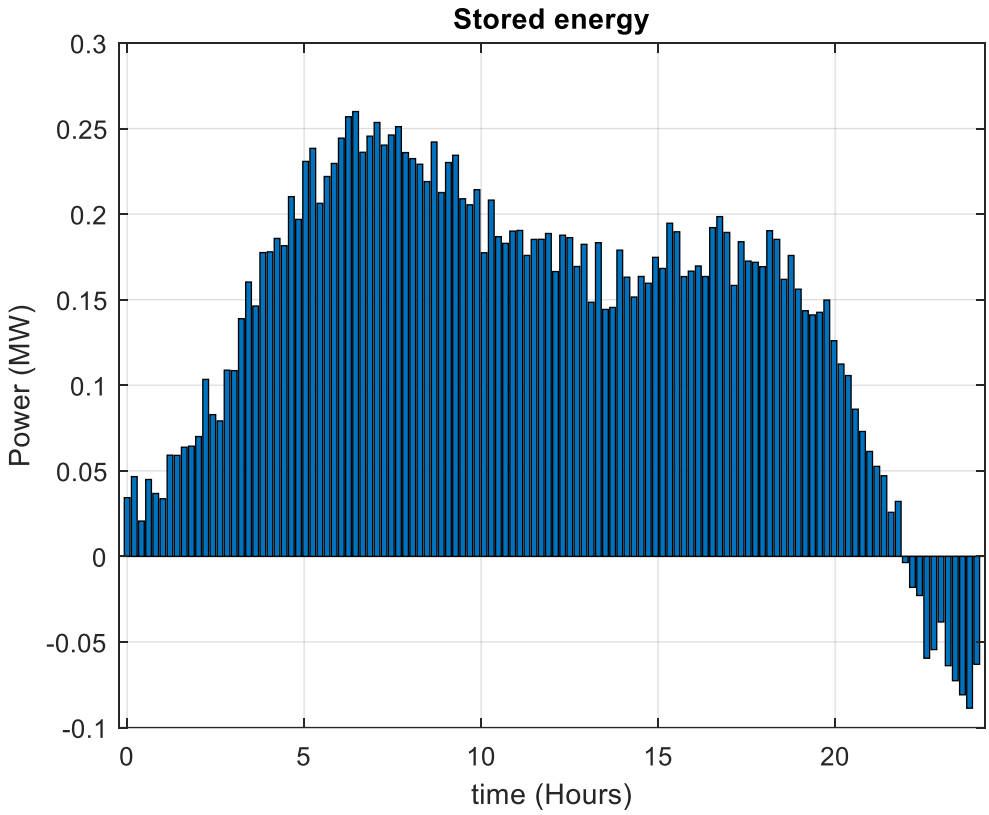

Figure 4.6: Stored energy profile

In the previous figure 4.6 the total energy stored showed, where in the vertical axis the power in (WM) is illustrated and time in hours in horizontal axis in configured.

Figure 4.7 shows the outlook of the energy system at a glance. This will help have an overall view of the profiles of the energy sources versus the load energy as well as of the generator profile.

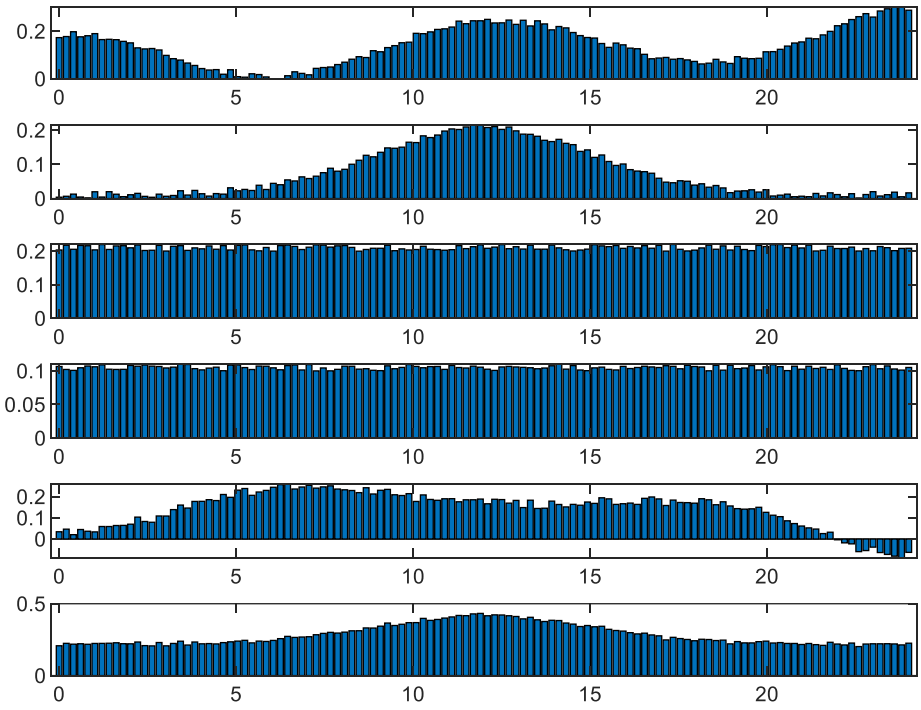

Figure 4.7: Overall energy outlook

In the previous figure 4.7 overall energy of the system is presented, where a thorough summary of the viewpoint of the energy system. This graphic depiction makes it easier to get a comprehensive grasp of the energy source profiles in relation to the load energy and generator profile.

4.4.3 Monitoring the status of the plant at any time of the day

The algorithm implemented in MATLAB is able to give the status at any time of the day by showing the profiles of the desired time. A prompt is used to ask the user to enter the time he or she desires to monitor (Figure 4.8).

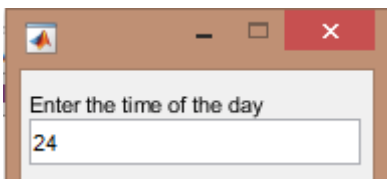

Figure 4. 8: Screen request to enter the time with 24 entered in

Refer to Figure 4.8 for further information on how a user prompt is used to get the user's input on the exact monitoring time they want to look at. The time specified is 24:00 in the example situation.

4.4.4 Instantaneous update check

The time of the day can range from 0:00 to 24:00. In case one wants to monitor the performance of the minigrid at a time with minutes, minutes will need to be converted into a fractional number which will strictly range between 0 and 1 i.e., interval [0, 1]. For instance, 30 minutes would be represented by 0.5, 15 minutes by 0.25, 45 minutes by 0.75, and so forth. Figure 4.9 shows the message box for the user who entered the time of 12:30.

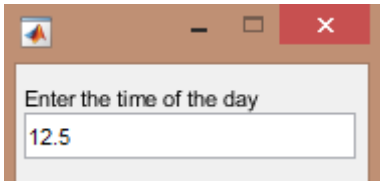

Figure 4.9: Entry request for update at 12:30

A graphic representation is given in Figure 4.9, which is offered for reference. This graphic illustrates a user interface component known as a "message box," which allows users to enter temporal data. The user has specified the time as 12:30 in this case. The architecture and design of the interface are depicted in the figure, which also shows how the fractional conversion is applied to the specified time in accordance with the previously established principles. As a real implementation of the idea, the message box enables users to communicate with the system and set time intervals in this particular format. During the conversion procedure, certain minute values are represented by their fractional equivalents. For instance, 30 minutes would equal 0.5, which means half an hour, and 15 minutes would equal 0.25, which means a quarter of an hour. To represent three-quarters of an hour, 45 minutes would be transformed to 0.75. The same pattern holds true for additional minute values.

4.4.5 Adjusting the levels of the energy sources

So far, the algorithm allows the user to monitor the minigrid based on the time. However, there is a need to also control the levels or amplitude of the energy sources, mainly solar and wind. This can be motivated by negative values observed in the profile of the stored energy. This can simply imply that the load demand has exceeded the supply, and a possible way to address this is to adjust the levels of the energy sources. Therefore, the control algorithm of the minigrid has to be designed minding the possibility to adjust those levels. The message box will thus be prompted to the user to make necessary adjustments, as shown in Figure 4.10.

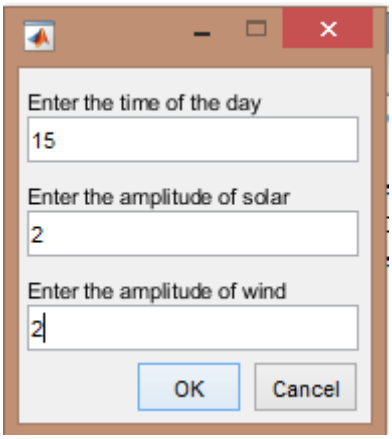

Figure 4.10: Input screen asking to check the energy update at 15:00

The suggested message box interface is depicted in Figure 4.10 within the framework of the minigrid control system. The graphic illustrates how a message box appears on the user interface in response to the algorithm's reaction to negative energy levels. The message box's purpose is to draw the user's attention and convey the energy shortage that has been seen. It acts as a reminder for the user to take the appropriate action, specifically by altering the solar and wind energy sources' output levels.

4.4.6 Displaying the minigrid energy update at any time of the day

One of the functionalities required of a minigrid is to provide an update about the energy resources at any time of the day. Visual presentations in graphical and numerical forms were used and is shown in Figures 4.10–4.18. On this graph (4.11), it can be seen that the energy levels of solar and wind were reduced to a maximum of 0.1 MW.

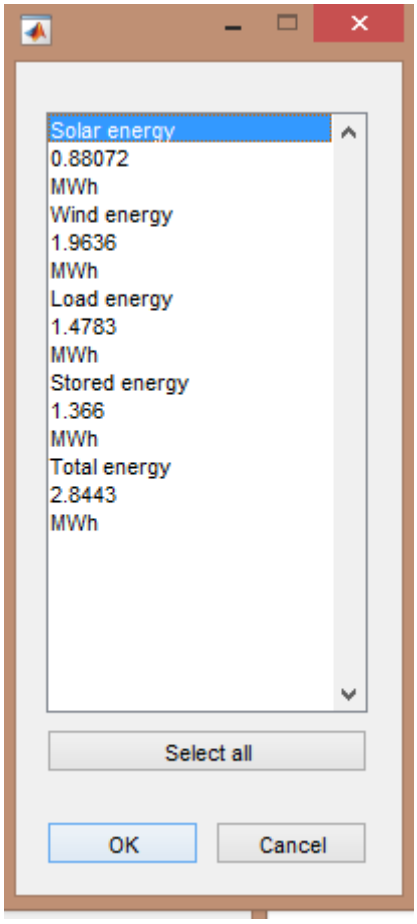

Figure 4. 11: The output screen for the energy outlook at 15:00

The output screen depicted in Figure 4.11 shows the energy perspective at the precise moment of 15:00. The graphical depiction shows the minigrid system's current energy situation. Notably, this illustration conveys the current situation of different energy sources, assisting in the evaluation of their contributions and availability within the system.

The profiles of the energy sources are shown one by one before the overall outlook of the minigrid energy (Figures 4.12–4.17).

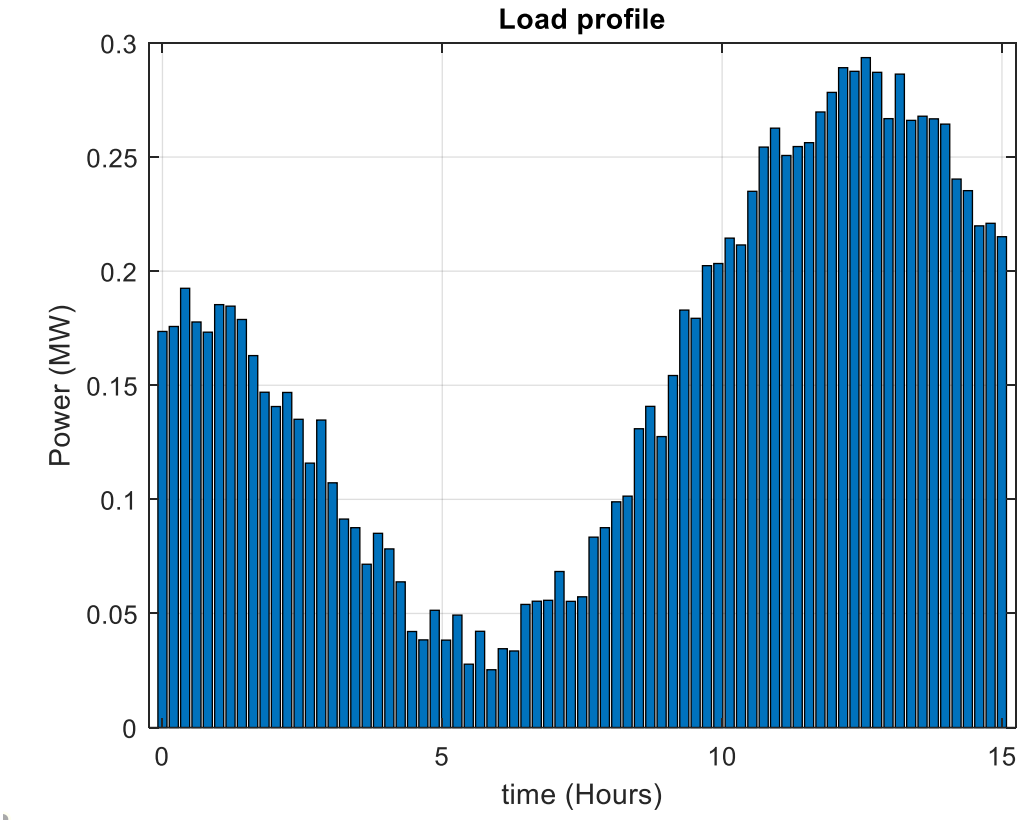

Figure 4.12: The load profile at 15:00

The load profile corresponding to the predetermined period of 15:00 is shown in Figure 4.12. The minigrid system's electrical demand is represented visually by the load profile for this particular temporal period. This data is important because it sheds light on consumption trends and helps formulate plans for the effective distribution and management of energy resources.

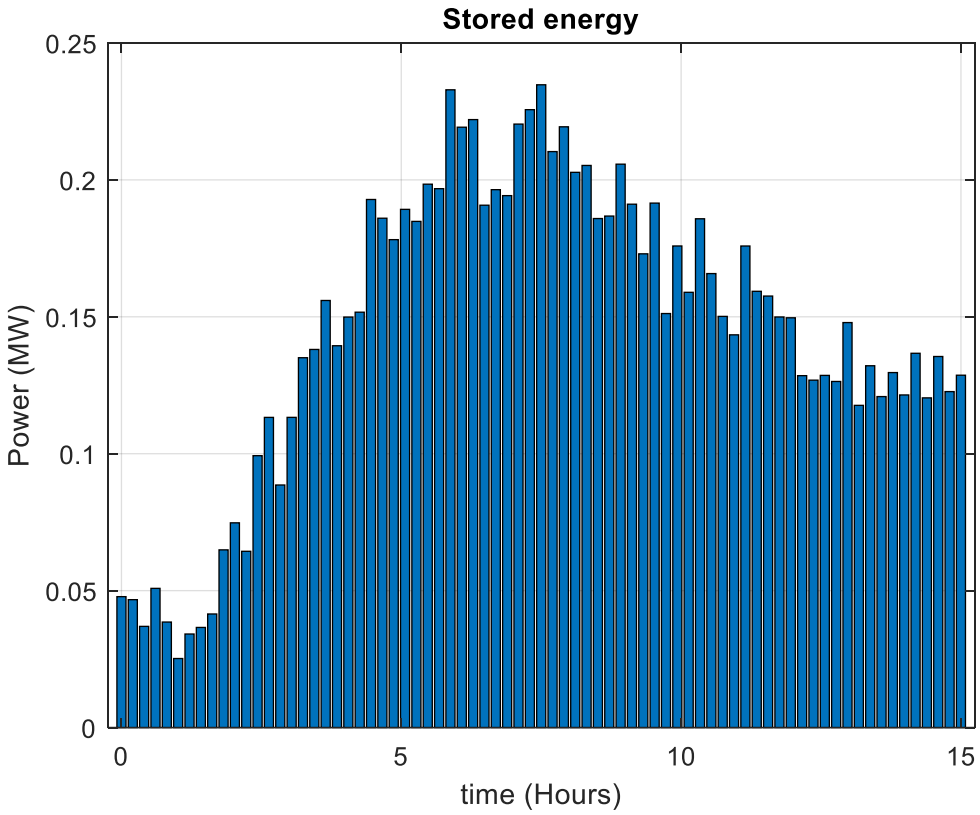

Figure 4.13: Solar energy source at 15:00

Figure 4.13 accurately depicts the dynamic behavior of the solar energy source at 15:00. This illustration emphasizes the natural intermittency of renewable sources by depicting the changes in solar energy output. This research is essential for determining the solar energy's potential contribution to the energy mix of the system and its ability to match demand.

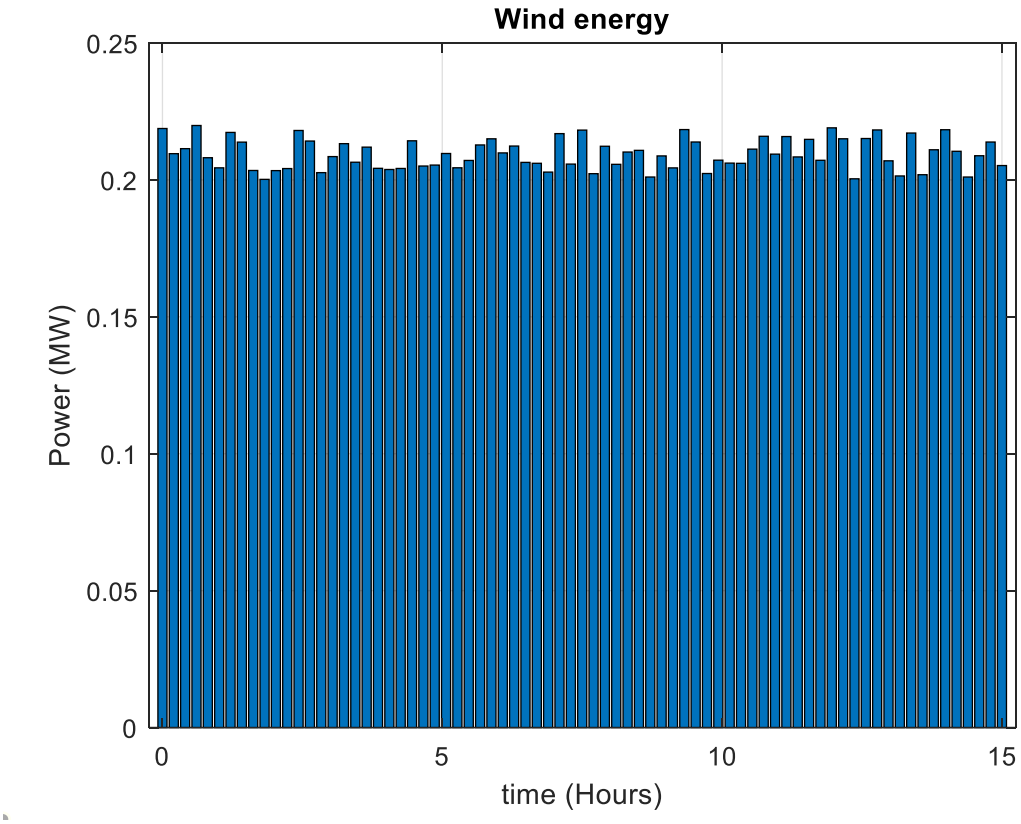

Figure 4. 14: Wind energy source at 15:00

Figure 4.14 displays the wind energy source's performance at the specified time of 15:00. This illustration illustrates the energy that was provided by the wind source during this particular time period. Insights on wind energy's instability are provided by the figure, which makes it easier to come up with plans to deal with its swings and best integrate it into the system.

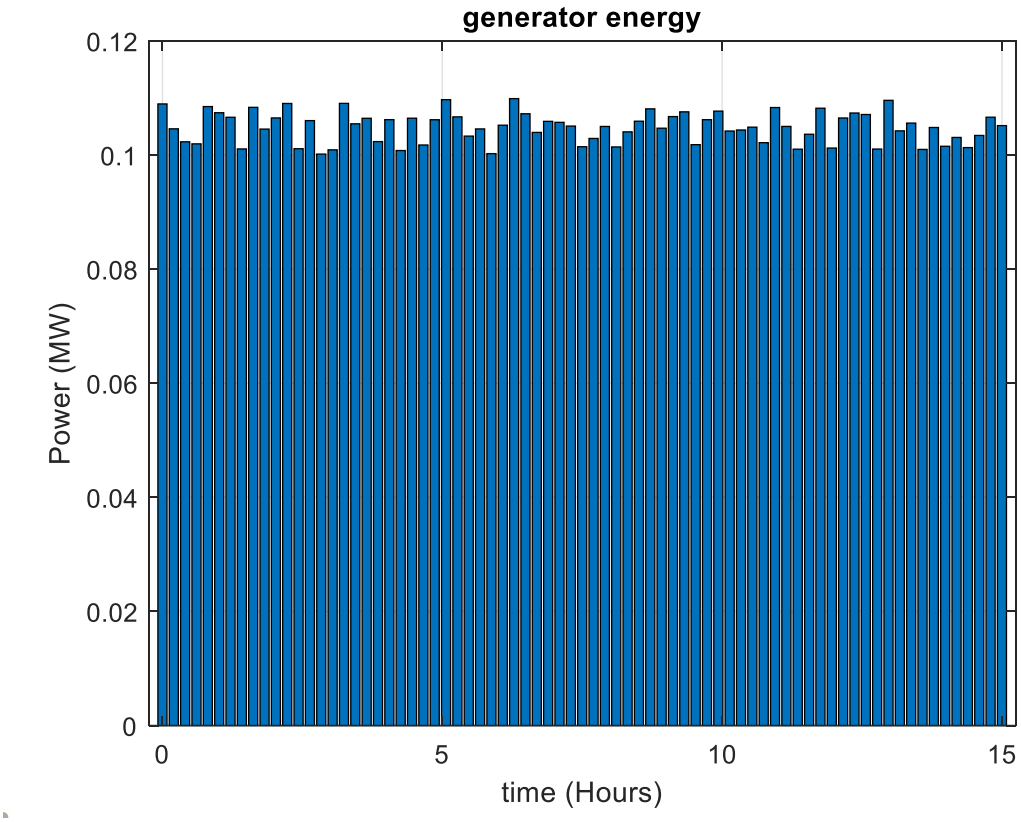

Figure 4.15: Generator energy profile at 15:00

The energy profile of the generator at precisely 15:00 is shown in Figure 4.15. This illustration shows how traditional generation techniques can supply the need for energy. The generator's steady output helps to stabilize the grid by making up for the fluctuation that comes with renewable energy sources.

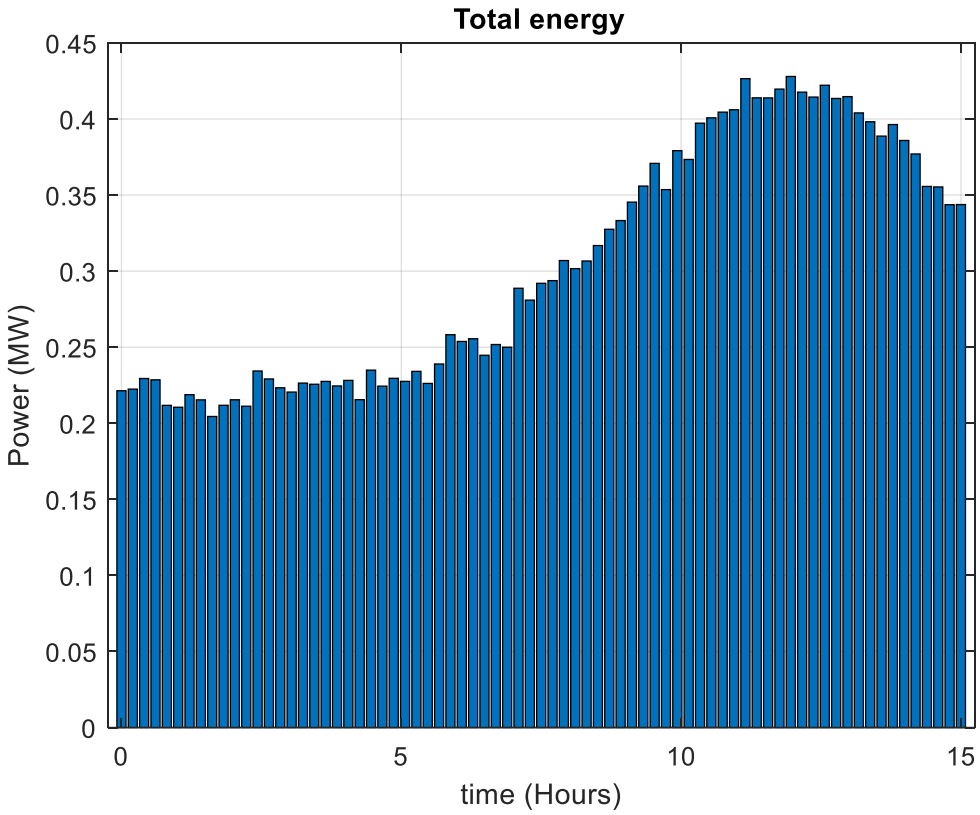

Figure 4.16: Total energy at 15:00

The total amount of energy used by the minigrid system at the specified time of 15:00 is shown in Figure 4.16. This illustration captures the overall energy intake from all sources, representing the total amount of energy available for consumption. This data serves as the basis for assessing the system's ability to meet demand and address possible shortages.

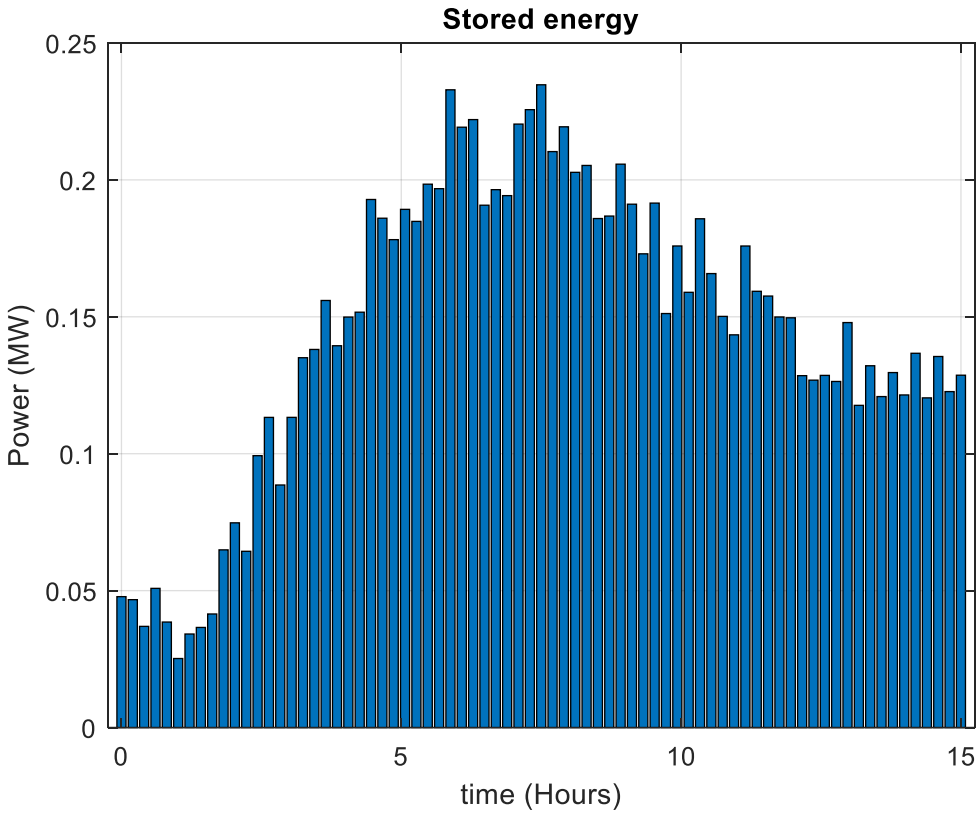

Figure 4.17: Stored energy at 15:00

The system's stored energy quantum is shown in Figure 4.17 at the specified time of 15:00. Understanding how energy storage devices like batteries are used to control energy surplus or shortage depends on understanding this depiction. It emphasizes the function of energy storage in guaranteeing grid stability and enabling a constant flow of electricity.

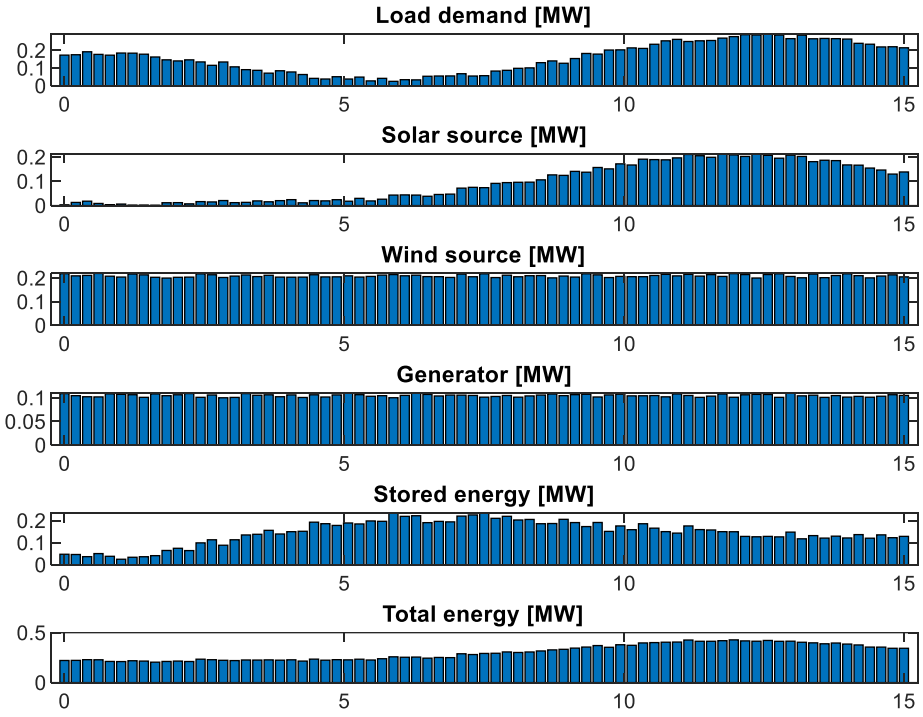

Figure 4.18: Overall outlook of the energy update and transaction at 15:00

The energy update and transaction status inside the minigrid system at 15:00 are presented in detail in Figure 4.18. This illustration combines knowledge from earlier illustrations and captures the energy produced, used, and stored. The illustration highlights the complex interplay of energy sources, consumption patterns, and storage systems, which results in a comprehensive representation of the energy dynamics of the minigrid.

The outlook of the energy transaction until 15:00 reflects that the load was supplied using solar energy and wind sources exclusively. Furthermore, storage devices were charging continually.

4.4.7 Usage of the storage facility when needed

According to data provided there is still a remark about the stored energy, which is still negative towards the evening hours. This would simply mean that the energy from the solar and wind sources could not add up to meet the demands of the load. This implies that the load was supplied using the storage system. In this regard, it is important to monitor the state of charge (SOC) and the depth of discharge (DOD) of the storage system. In the following figure 4.19 the scenario of the storage system supplying the load is presented.

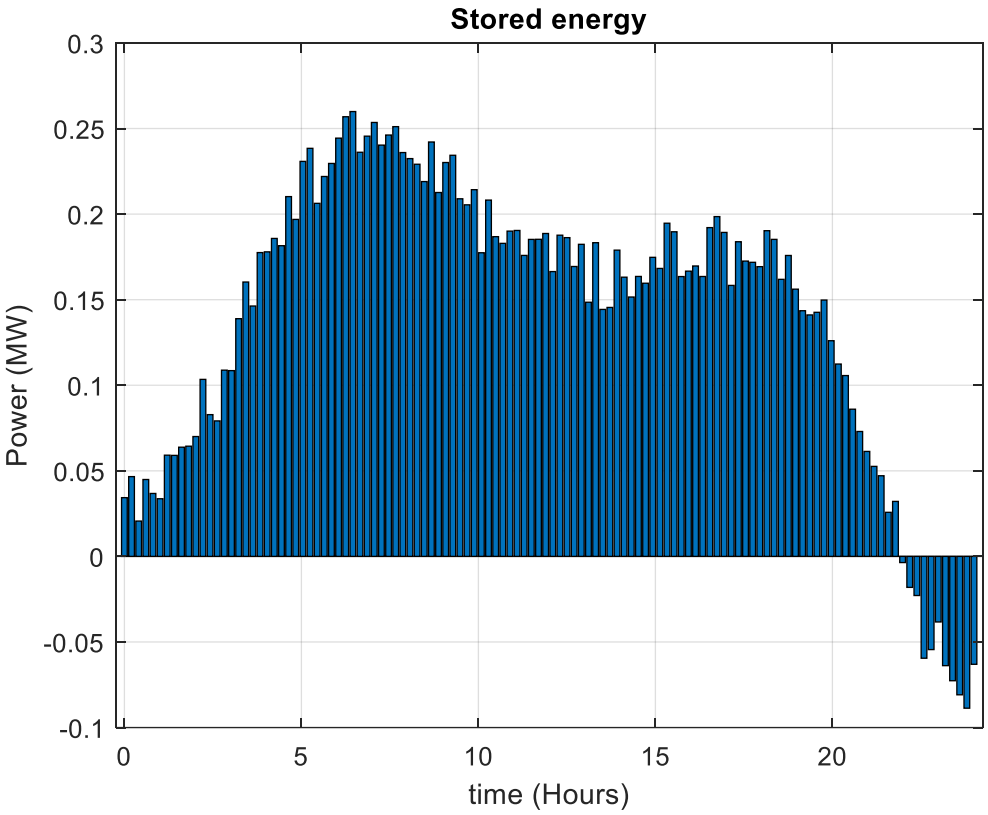

Figure 4.19: Scenario of the storage system supplying the load

The scenario where the stored energy displays a persistently downward trend throughout the night time hours is portrayed graphically in Figure 4.19. This shows that the total amount of energy produced by wind and solar sources is insufficient to meet the demands of the concurrent loads. As a result, the energy stored within the storage system is used to make up for the lack of power supply.

4.5 Chapter conclusion

The centralized control system of a multivariable minigrid was successfully developed and implemented in its defined functionalities. To test the functionality of the algorithm, the profiles were modelled and stored and could be accessed on demand. This simulates a system that senses the load demand and supplies the required power. The driving algorithm has shown the ability to read or track the levels of energy at any time of the day and provide an update through interactive box messages and displays. The algorithm has also demonstrated the ability to utilize available resources efficiently as the storage system could intervene when both solar and wind could not meet the load energy demand.

CHAPTER FIVE

CONTROL OF THE OUTPUT VOLTAGE WITH VARIABLE LOAD CONNECTED TO AN LC FILTER

5.1 Introduction

This section goes beyond the interconnection of the multivariable system, where the focus was on energy transactions between resources and the load. What it seeks to address are issues pertaining to the power delivered to the variable/dynamic load. Parameters such as current, voltage, and frequency are then examined, as they are the determinants of power quality. The literature has shown that a dynamic load is a source of harmonic distortions that have adverse effects on the power quality and connected devices. This study commenced by first modelling a dynamic load. The method followed to address the aforementioned issues consisted of defining subject of interest and focusing on it, thus keeping in mind the second objective of this study, which deals with harmonic distortions occurring as a result of nonlinear loads.

In this chapter, the LC filter, which is the element at the back end of the network, and its mathematical model are established in both time and s-domain. Then the study proceeds to model the output when the LC filter was connected to the purely resistive load and then to the variable RL load. From there, mathematical models or transfer functions specifically for the load current and voltage are developed. Both the open-loop and closed-loop transfer functions are then evaluated in terms of response for AC and step input coming from the VSI output. As the responses presented distortions, control schemes were developed with a focus on linear control systems. Proportional (P) and proportional-integral (PI) were applied to the transfer functions, and their responses were studied to see which control scheme provides better load voltage responses to the AC input. Overall, the study started with and focused on the dynamic load.

5.2 Dynamic load

Besides motors and generators, a load is ideally considered purely resistive. However, the nature of conductors in the presence of an Alternating Current (AC)results in an impedance which can be decomposed in a resistance and an inductance connected in series (Equation 5.1).

$$Load = R + jL \qquad \text{Equation 5.1}$$

Where R is the resistance and L is the inductance.

The voltage expression with respect to the current is formulated as per Equation 5.2.

$$V_{in}(t) = Ri(t) + L\frac{di(t)}{dt}$$ Equation 5.2

V_{in} represents the input voltage at time t. It's a function that changes over time and is the voltage applied to the circuit. R is the resistance, L this symbol represents the inductance of the circuit, $\frac{di(t)}{dt}$ is the rate of change of current with respect to time. It represents how fast the current is changing at a particular moment.

Laplace transform for Equation 5.2 is given by Equation 5.3:

$$V_{in}(S) = I(S)(R + SL)$$ Equation 5.3

The relationship between the current and the voltage is derived through a transfer function of the input current voltage over the output voltage (Equation 5.4).

$$\frac{I(S)}{V_{out}(S)} = \frac{1}{R+SL}$$ Equation 5.4

S In the Laplace domain, S is a complex variable that is used to transform time-domain equations into frequency-domain equations. $V_{out}(S)$ is the output voltage in the Laplace domain. It represents the voltage across the output of the circuit in the frequency domain.

$I(S)$ represents the current in the Laplace domain. It's the transformed version of the current function $i(t)$ in the frequency domain, $\frac{1}{R+SL}$ is the transfer function's expression. It integrates the circuit's resistance and inductance and connects the Laplace-transformed input current to the Laplace-transformed output voltage.

Subjecting an AC in the form of a sinewave would yield an output current, as illustrated in Figure 5.1.

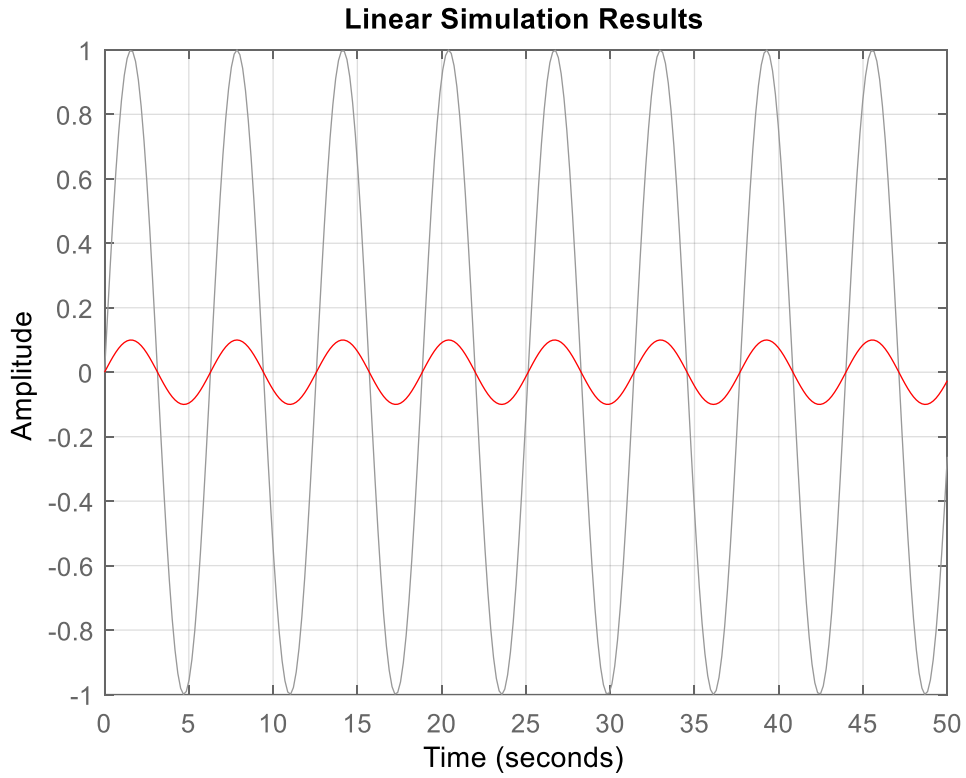

Figure 5.1: Output current for an RL load with L = 10 mH and R = 10 Ω

For this particular case, the current waveform appears to be in phase with the input current in red and voltage in Gray Y-axis. However, changing the values of the inductance is expected to increase the value of the output impedance and the phase angle with respect to the resistive power. Different values of the inductance of values 10 mH and 100 mH are shown in (Figure 5.2 and 5.3).

phaseAngle

5x1 double

	1
1	0.0573
2	0.5729
3	5.7106
4	45.0000
5	84.2894

Figure 5.2: Phase angle for values of R = 10 Ω and L = 10, 100, 1000, 10000, 100000 mH radians

Figure 5.2 shows a visual illustration of how the phase angle might change when different inductance values are used while still keeping a constant resistance of 10. A wide variety of inductance values, notably 10 mH, 100 mH, 1000 mH, 10000 mH, and 100000 mH, are

examined in the inquiry. The values of the illustrated phase angle provide information on how inductance and phase angle interact under the given circumstances.

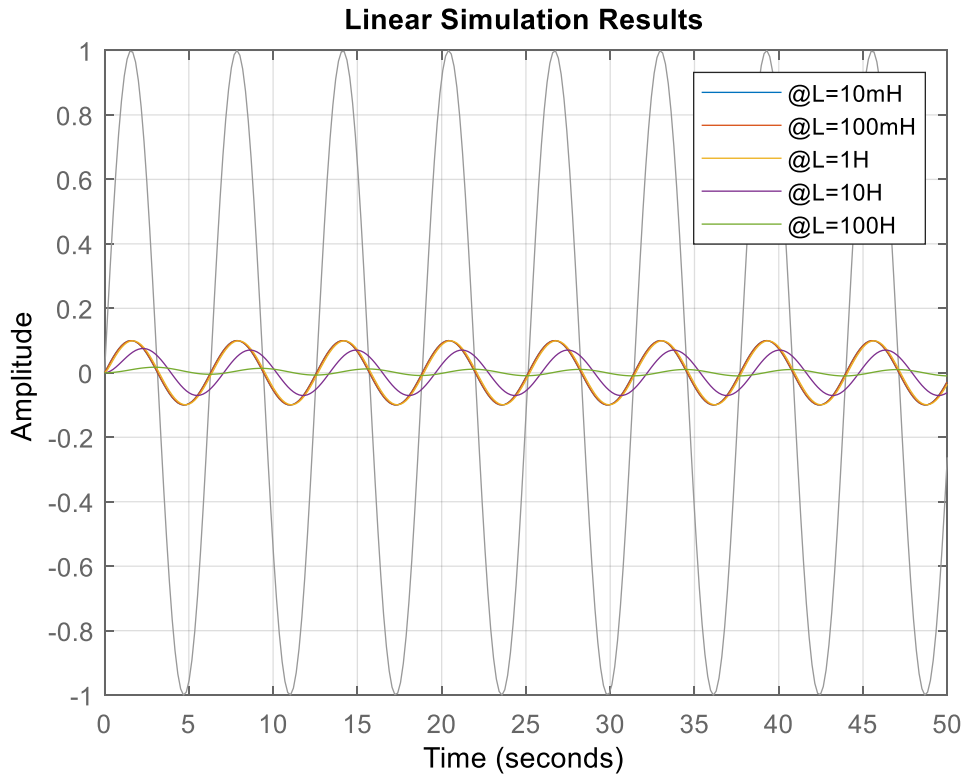

Figure 5.3: Phase angle for values of R = 10 Ω and L = 10, 100, 1000, 10000, 100000 mH

From the graph in Figure 5.3, as the value of the inductance increases, the phase shift increases while the amplitude decreases. There is, therefore, an imperative to control the reactance of the inductor.

5.3 LC filter

Prior to connecting the load to the inverter, there is a need to ensure that the harmonic distortions will not affect the load and its performance. As total harmonic distortions are of a higher frequency than the fundamental frequency, a low pass filter (LPF) suits this purpose. A simple representation of an LC filter consists of an inductor and a capacitor, with the inductor placed at the input and the capacitor place at the output, which is the input of the load (Figure 5.4).

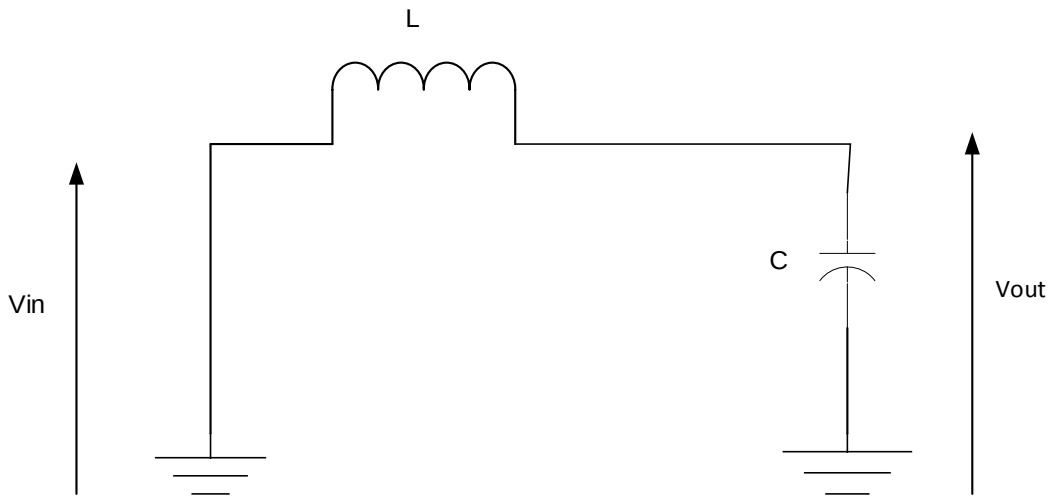

Figure 5.4: Simple representation of an LC

A fundamental circuit design for reducing unwanted fluctuations or noise in electrical signals is the LC filter. It is made up of an inductor and a capacitor, two crucial passive parts. The purpose of the inductor is to prevent abrupt changes in current, only allowing slow fluctuations to flow through. The capacitor, on the other hand, allows high-frequency components to pass while inhibiting low-frequency ones. In this illustration, the inductor is placed strategically near the filter's input, which is where the electrical signal enters the device for the first time. In contrast, the capacitor is carefully positioned at the output, also known as the final stage, immediately before the signal is sent to the load, or intended receiver.

5.4 LC mathematical representation

The time-domain mathematical representation of an LC according to the Kirchhoff's laws can be expressed as follows (Equation 5.5):

$$V_{in}(t) = Li(t) + V_{out} \qquad \text{Equation 5.5}$$

As the filter layout is a series network, the current flowing through the components is the same. Expressing the current as a function of the inductor yields Equation 5.6.

$$i_c(t) = \frac{1}{C}\int V_{out}(t)dt \qquad \text{Equation 5.6}$$

Substituting Equation 5.6 in Equation 5.5 yields:

$$V_{in}(t) = \frac{L}{C}\int V_{out}\,(t)dt + V_{out}(t) \qquad \text{Equation 5.7}$$

The frequency-domain or s-domain representation of the LC is described as per Equation 5.8.

$$V_{in}(S) = \frac{L}{CS} V_{out}(S) + V_{out}(S) \quad \text{Equation 5.8}$$

Factorizing Equation 5.8 becomes Equation 5.9:

$$V_{in}(S) = (1 + \frac{L}{CS}) V_{out}(S) \quad \text{Equation 5.9}$$

The transfer function of the LC LPF can be represented as follows (Equation 5.10):

$$\frac{V_{out}(S)}{V_{in}(S)} = \frac{1}{1+\frac{L}{CS}} \quad \text{Equation 5.10}$$

Working out the denominator gives Equation 5.11.

$$\frac{V_{out}(S)}{V_{in}(S)} = \frac{1}{\frac{CS+L}{CS}} \quad \text{Equation 5.11}$$

$$\frac{V_{out}(S)}{V_{in}(S)} = \frac{S}{S+L/C}$$

The expression of the output versus the input is given by Equation 5.12.

$$V_{out} = V_{in}(t)(1 - e^{-\frac{L}{C}t}) \quad \text{Equation 5.12}$$

The exponent constant $\frac{L}{C}$ is known as a time constant and is denoted τ.

The first assessment of the output is that the LC subjects the input to an exponentially decaying function. This can be demonstrated by taking some values of the inductor and capacitor.

The step response to the transfer function in Equation 5.12 is represented in Figure 5.5.

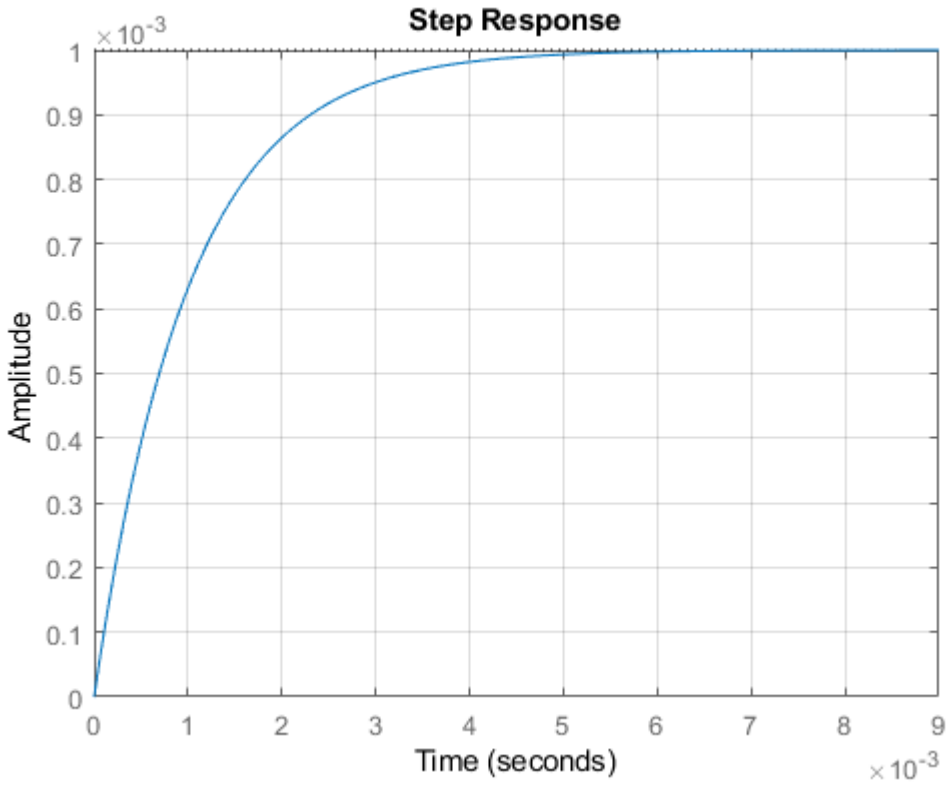

Figure 5.5: The output of an LC LPF with a step input voltage of 240 Volts, an inductor of 10 mH and a capacitor of 10 μF

A visual illustration of an LC LPF's reaction to a step input voltage is shown in Figure 5.5, emphasizing the complex interplay between the circuit's inductive and capacitive components. A Low-Pass LC Filter (LPF) is shown responding to a 240-volt step input voltage in Figure 5.5. The components of the LC LPF setup are a capacitor with a capacitance of 10 µF and an inductor with a 10 mH inductance value.

Increasing the value of the time constant with multiple ratios of 10 gives curves as in Figure (5.3)

From Figure 5.5, one notes that the best is the response as the time constant increases. The filter response when the input is a DC 240 V is represented in (Figure 5.6).

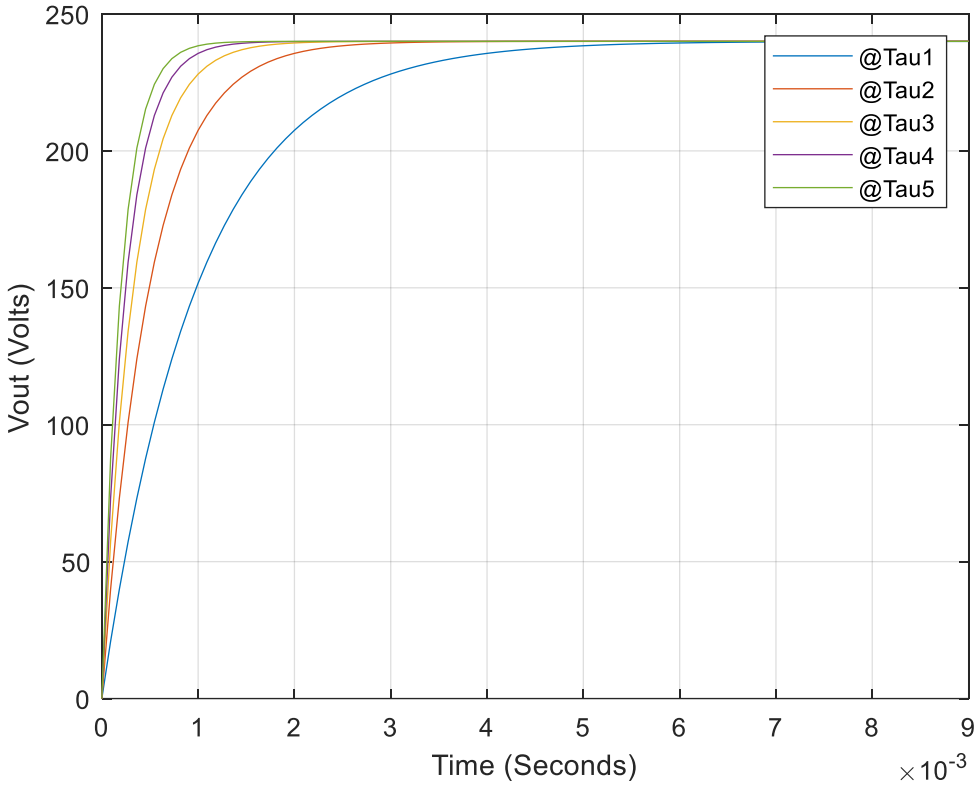

Figure 5.6 The step's filter response at time constants ranging from 1 through 5 milli for an input voltage of 240 Volts

The response of the filter to a step function is depicted graphically in Figure 5.6. A range of temporal constants, notably those between 1 and 5 milliseconds, are examined while analyzing this response. A value of 240 Volts is chosen as the input voltage for this investigation. The filter's response to changes in the input signal throughout this range of time constants is graphically depicted in the graph, which also provides details on the filter's properties and behavior in this parameter space.

5.5 Output LC filter coupled to the resistive load

In the case of a purely resistive load, an LC filter is connected to a load resistance as illustrated in Figure 5.7.

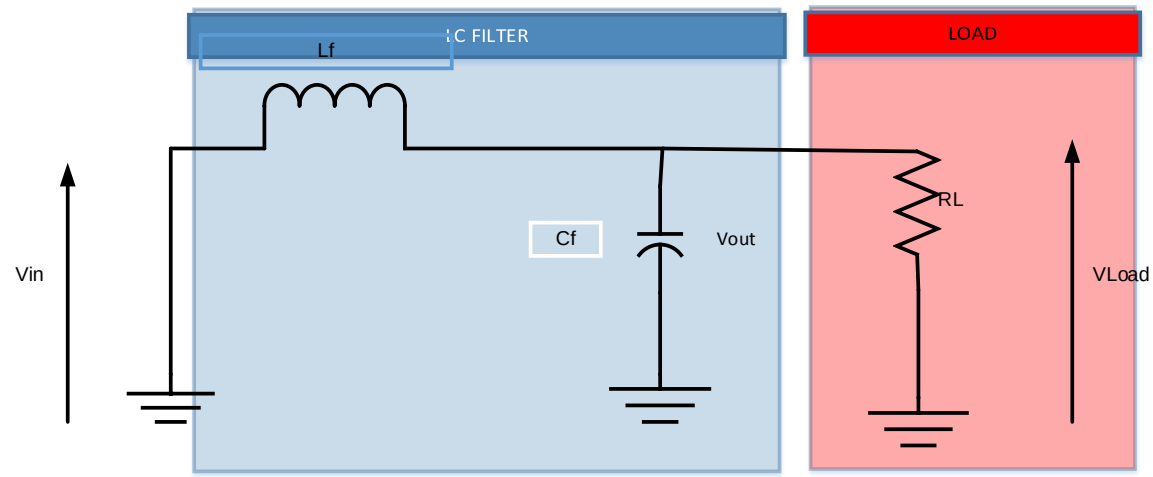

Figure 5.7 Schematic diagram for an LC filter with a resistive load

An LC filter with a resistive load is shown in Figure 5.7. This system blocks undesirable frequencies while letting desired ones through. Power dissipation is managed by the resistive load. It combines efficient filtering with load control in systems like power supply and communication networks.

The total impedance of the whole network needs to be determined in order to determine the resonance frequency (Equations 5.13).

$$Z = j\omega L_f + \frac{(\frac{R_L}{j\omega C_f})}{R_L + \frac{1}{j\omega C_f}} \qquad \text{Equation 5.13}$$

Putting the fraction part of the Z on the common denominator and simplifying leads to (Equation 5.14)

$$Z = j\omega L_f + \frac{(R_L)}{j\omega C_f R_L + 1} \qquad \text{Equation 5.14}$$

Simplifying the fractional part yields Equation 5.15.

$$Z = \frac{j\omega L_f(j\omega C_f R_L + 1) + R_L}{j\omega C_f R_L + 1} \qquad \text{Equation 5.15}$$

Putting the whole expression on the same denominator yields Equation 5.16.

$$Z = \frac{-\omega^2 L_f C_f R_L + j\omega L_f + R_L}{j\omega C_f R_L + 1} \qquad \text{Equation 5.16}$$

Multiplying the denominator with the conjugate yields Equation 5.17.

$$Z = \frac{(j\omega C_f R_L + 1)(-\omega^2 C_f L_f R_L + j\omega L_f + R_L)}{1 + \omega^2 C_f^2 R_L^2} \qquad \text{Equation 5.17}$$

Working out Equation 5.17 yields Equation 5.18.

$$Z = \frac{-j\omega^3 L_f C_f^2 R_L^2 - \omega^2 C_f R_L L_f + j\omega C_f \quad R_L^2 - \omega^2 L_f C_f R_L + j\omega L_f + R_L}{1+\omega^2 C_f^2 R_L^2} \qquad \text{Equation 5.18}$$

Multiplying the numerator and denominator by the conjugate gives Equation 5.19.

$$Z = \frac{-2\omega^2 C_f R_L L_f + R_L - j(\omega^3 L_f C_f^2 R_L^2 - \omega(C_f R_L^2 + L_f))}{1+\omega^2 C_f^2 R_L^2} \qquad \text{Equation 5.19}$$

The imaginary part of the impedance is per Equation 5.20.

$$Z = j\left(\omega^3 L_f C_f^2 R_L^2 - \omega\left(C_f R_L^2 + L_f\right)\right) \qquad \text{Equation 5.20}$$

The resonance condition is that the imaginary part of the impedance must be null (Equation 5.21).

$$\omega^2 L_f C_f^2 R_L^2 - \left(C_f R_L^2 + L_f\right) = 0 \qquad \text{Equation 5.21}$$

The angular velocity is expressed by Equation 5.22.

$$\omega = \sqrt{\frac{C_f R_L^2 + L_f}{L_f C_f^2 R_L^2}} \qquad \text{Equation 5.22}$$

The expression of the resonance frequency is per Equation 5.23.

$$f_r = \frac{1}{2\pi}\sqrt{\frac{C_f R_L^2 + L_f}{L_f C_f^2 R_L^2}} \qquad \text{Equation 5.23}$$

5.6 Open-loop transfer function for an LC filter coupled to a resistive load

Referring to the circuit diagram of an LC filter coupled to the resistive load, the input voltage to the resistive load can be expressed as per Equation 5.24.

$$v_{in}(t) = \frac{L_f di(t)}{dt} + v_o(t) \qquad \text{Equation 5.24}$$

Applying the current divider rule, the expression of the current is given by Equation 5.25.

$$i_{L_f}(t) = i_{C_f}(t) + i_{R_L}(t) \qquad \text{Equation 5.25}$$

Equation 5.27 can be further developed into Equation 5.26.

$$i_{L_f}(t) = C_f \frac{dv_o(t)}{dt} + \frac{v_o(t)}{R_L} \qquad \text{Equation 5.26}$$

By plugging the expression of the inductor current in Equation 5.26, we obtain Equation 5.27.

$$v_{in}(t) = L_f \frac{d}{dt}\left(C_f \frac{dv_o(t)}{dt} + \frac{v_o(t)}{R_L}\right) + v_o(t)$$ Equation 5.27

Working out Equation 5.27 yields Equation 5.28.

$$v_{in}(t) = \left(L_f C_f \frac{d^2 v_o(t)}{dt^2} + \frac{L_f}{R_L}\frac{dv_o(t)}{dt}\right) + v_o(t)$$ Equation 5.28

The corresponding Laplace transform is per Equation 5.29.

$$V_{in}(S) = (L_f C_f S^2 + \frac{L_f}{R_L} S + 1) V_o(S)$$ Equation 5.29

The transfer function of the output or the load voltage and the input voltage is described by Equation 5.30.

$$\frac{V_o(S)}{V_{in}(S)} = \frac{1}{L_f C_f (S^2 + \frac{1}{C_f R_L} S + \frac{1}{L_f C_f})}$$ Equation 5.30

Considering that the LC filter is tuned at resonance, the values of the inductor and capacitor have been set accordingly. For instance, by taking the filter's components as $L_f = 3.3\ H$ and $C_f = 2.2\ \mu F$ and also putting the R variable load with various values, the time response to the step input voltage and an AC input voltage can be obtained (Figure 5.8. and 5.9).

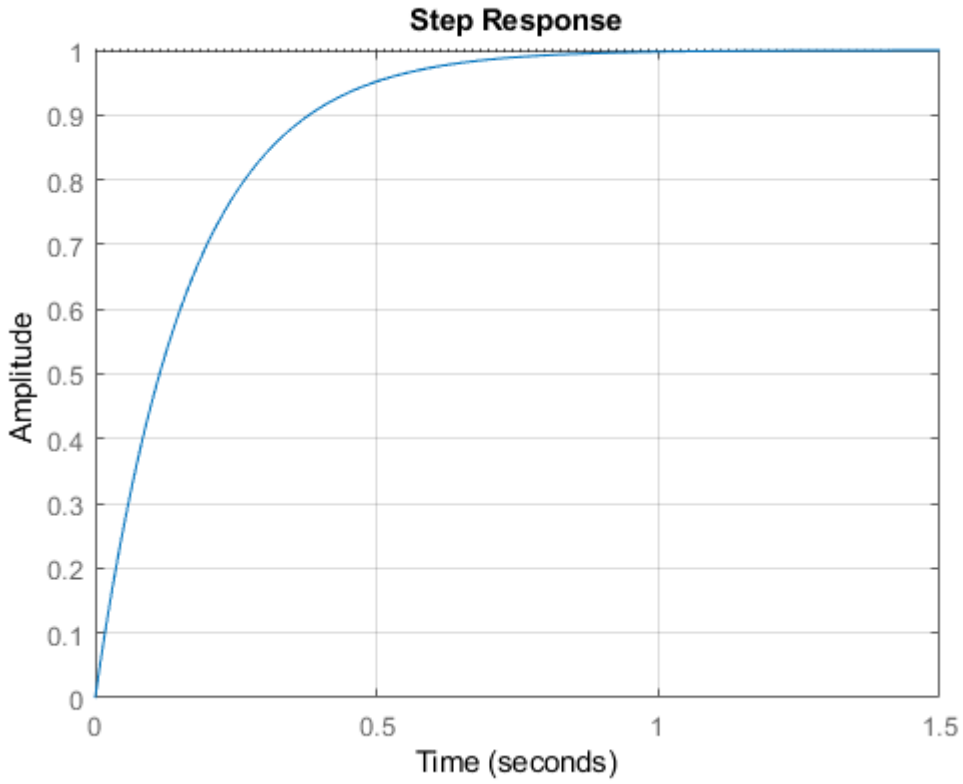

Figure 5.8: Step response of the control system with the load resistor $R_L = 20\Omega$

Figure 5.8 shows how the control system responds to a step input, illustrating how the system responds to a rapid change. This behavior is examined in respect to the load resistor R L, whose value is specified as being 20Ω. The step response graph highlights any transient or steady-state features impacted by the selected load resistor value while representing the system's response over time. Understanding the dynamic performance of the control system under the existing circumstances is made easier with the help of this empirical description.

Figures 5.9 and 5.10 shows AC responses in the resistive load with values of 20 Ω and 500 Ω.

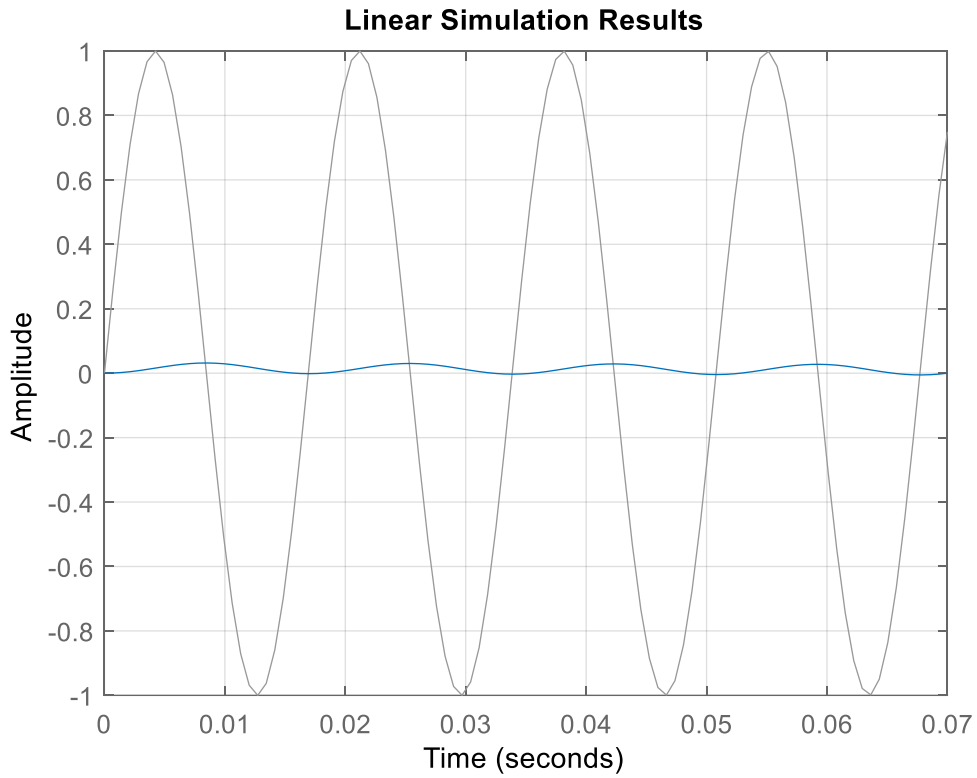

Figure 5.9: Step response of the control system with the load resistor $R_L = 20\,\Omega$

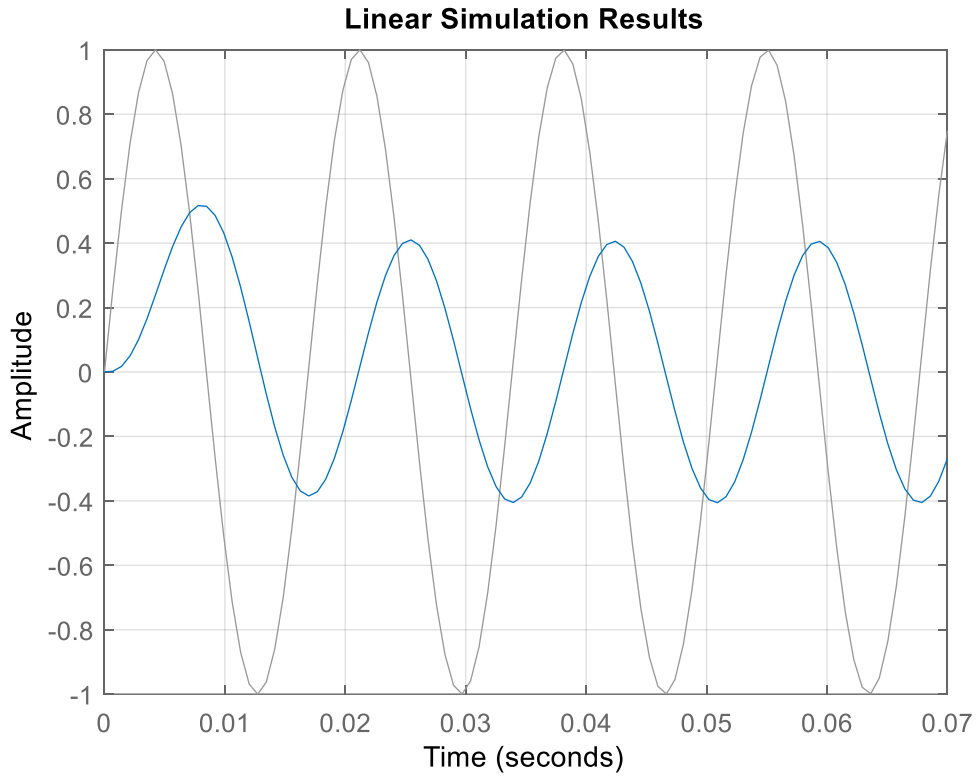

Figure 5.10:Step response of the control system with the load resistor $R_L = 500\,\Omega$

The observation is that when a resistive load is connected with a low resistance, the output voltage is low, which is fitting because the voltage is directly proportional to the resistance. When a load with a higher resistance is connected, the output is proportionally higher and the response shows levels of instability in a transition that lasts less than $10\,ms$ while it is permanently stable.

5.7 The LC filter connected to the variable (LR) load

The LC filter, consisting of an inductor and a capacitor meant to eliminate the harmonic distortions, is coupled to a variable load comprising an inductor and a load resistance, as shown in Figure 5.11.

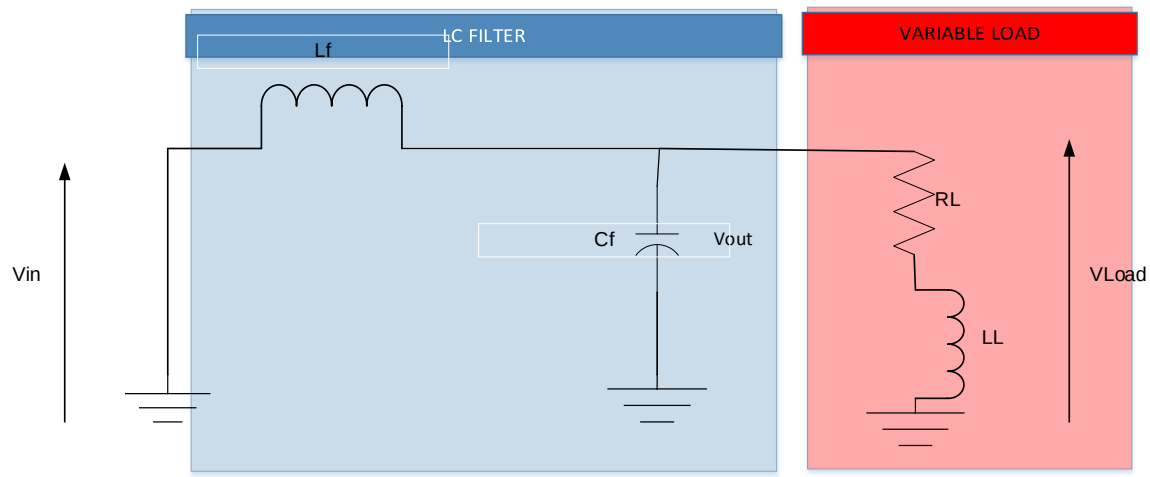

Figure 5.11: LC filter coupled to a variable load (LR load)

By combining the LC filter with this specific variable load arrangement, engineers and researchers may efficiently explore and evaluate the filter's performance under dynamic circumstances. An extra element of inductance is introduced by the inductor in the variable load, which may interact with the inductor and capacitor in the LC filter. The features of the filter's impedance, how it reacts to resonance, and how well it attenuates harmonics all together can be affected by this interaction.

5.8 Total impedance and resonance frequency

From Figure 5.11 above, there is an output LC filter that is coupled to an RL load in a parallel configuration. In terms of impedance, there is a parallel configuration between an LC branch and an RL branch.

$$Z = j\omega L_L + \frac{\frac{1}{j\omega C_f} + R_L + j\omega L_L}{(\frac{1}{j\omega C_f})(R_L + j\omega L_L)} \qquad \text{Equation 5.31}$$

Putting the numerator and denominator to the common denominator gives Equation 5.32.

$$Z = j\omega L_L + \frac{\frac{1 + j\omega C_f R_L - \omega^2 C_f L_L}{j\omega C_f}}{(\frac{R_L + j\omega L_L}{j\omega C_f})} \qquad \text{Equation 5.32}$$

Working out Equation 5.32 gives Equation 5.33.

$$Z = j\omega L_f + \frac{1 + j\omega C_f R_L - \omega^2 C_f L_L}{R_L + j\omega L_L} \qquad \text{Equation 5.33}$$

Putting the first term on the right-hand side on the same denominator gives Equation 5.34.

$$Z = \frac{j\omega R_L L_f - \omega^2 L_L^2 + 1 + j\omega C_f R_L - \omega^2 C_f L_L}{R_L + j\omega L_L} \qquad \text{Equation 5.34}$$

Multiplying both the numerator and the denominator by the conjugate yields (Equation 5.35):

$$Z = \frac{(R_L + j\omega L_f)(j\omega R_L L_L - \omega^2 L_L^2 + 1 + j\omega C_f R_L - \omega^2 C_f L_L)}{R_L^2 + \omega^2 L_L^2} \quad \text{Equation 5.35}$$

Multiplying the conjugate through the numerator yields Equation 5.36 and 5.37.

$$Z = \frac{(-\omega^2 R_L^2 L_f L_L - j\omega^3 R_L L_f L_L^2 + j\omega L_f R_L - \omega^2 R_L^2 L_f C_f \ \ - j\omega^3 R_L C_f L_f L_L)}{R_L^2 + \omega^2 L_L^2} \quad \text{Equation 5.36}$$

$$Z = \frac{-\omega^2 (R_L^2 L_f L_L + R_L^2 L_f C_f) - j(\omega^3 (R_L L_f L_L^2 + R_L C_f L_f L_L) - \omega L_f R_L)}{R_L^2 + \omega^2 L_L^2} \quad \text{Equation 5.37}$$

The resonance condition is that the imaginary part should be equal to zero (Equation 5.38).

$$Z_{im} = -j\left(\omega^3 (R_L L_f L_L^2 + R_L C_f L_f L_L) - \omega L_f R_L\right) \quad \text{Equation 5.39}$$

The imaginary part equal to zero implies Equation 5.40.

$$\left(\omega^3 (R_L L_f L_L^2 + R_L C_f L_f L_L) - \omega L_f R_L\right) = 0 \quad \text{Equation 5.40}$$

Factorizing Equation 5.45 leads to Equation 5.41.

$$\omega^2 \left(L_L^2 + C_f L_L\right) - 1 = 0 \quad \text{Equation 5.41}$$

Solving Equation 5.41 for ω gives Equation 5.42.

$$\omega = \sqrt{\frac{1}{L_L^2 + C_f L_L}} \quad \text{Equation 5.42}$$

Expressing Equation 5.42 in terms of frequency yields Equation 5.43.

$$f_r = \frac{1}{2\pi} \sqrt{\frac{1}{L_L^2 + C_f L_L}} \quad \text{Equation 5.43}$$

5.9 Open-loop transfer function for the output current in the LR load

The mathematical model of the current is governed by equations of the current and voltage following Kirchhoff's current and voltage laws (Equations 5.44 and 5.45).

$$i_{in}(t) = i_C(t) + \ i_o(t) \quad \text{Equation 5.44}$$

$$v_{in}(t) = L_f \frac{di_{in}(t)}{dt} + L_L \frac{di_o(t)}{dt} + \ R_L i_o(t) \quad \text{Equation 5.45}$$

Where the capacitor current $i_c = C \frac{dv_o(t)}{dt}$ and $v_o(t) = \ i_o(t) R_L + \ L_L \frac{di_o(t)}{dt}$

Replacing the expressions of the capacitor current and output current in Equation 5.45 expressing the input voltage yields Equation 5.46.

$$i_{in}\,(t) = C\frac{d}{dt}\left(i_o(t)R_L + L_L\frac{di_o(t)}{dt}\right) + i_o(t) \qquad \text{Equation 5.46}$$

Also considering the fact that $v_{in}(t) = v_L(t) + v_o\,(t)$

The input voltage can be written from Equation 5.46 to Equation 5.47 as follows:

$$v_{in}(t) = Lf\frac{d}{dt}\left(Cf\frac{d}{dt}\left(i_o(t)R_L + L_L\frac{di_o(t)}{dt}\right) + i_o(t)\right) + i_o(t)R_L + L_L\frac{di_o(t)}{dt} \qquad \text{Equation 5.47}$$

Factoring out Equation 5.47 yields, Equation 5.48.

$$v_{in}\,(t) = \left(L_fC_f\frac{d^2}{dt^2}i_o(t)R_L + C_fL_fL_L\frac{d^3i_o(t)}{dt^3} + L_f\frac{di_o(t)}{dt}\right) + i_o(t)R_L + L_L\frac{di_o(t)}{dt} \qquad \text{Equation 5.48}$$

Rearranging and putting Equation 5.53 in the time domain gives Equation 5.49:

$$V_{in}(S) = (C_fL_fL_LS^3 + LfCfR_LS^2 + (L_f + L_L)S + R_L)I_o(S) \qquad \text{Equation 5.49}$$

The transfer function between the input voltage and the output current is as (Equation 5.50):

$$\frac{I_O(S)}{V_{in}(S)} = \frac{1}{C_fL_fL_LS^3+L_fC_fR_LS^2+(L_L+L_f)S+R_L} \qquad \text{Equation 5.50}$$

The AC response for the open-loop transfer function is illustrated in Figure 5.12.

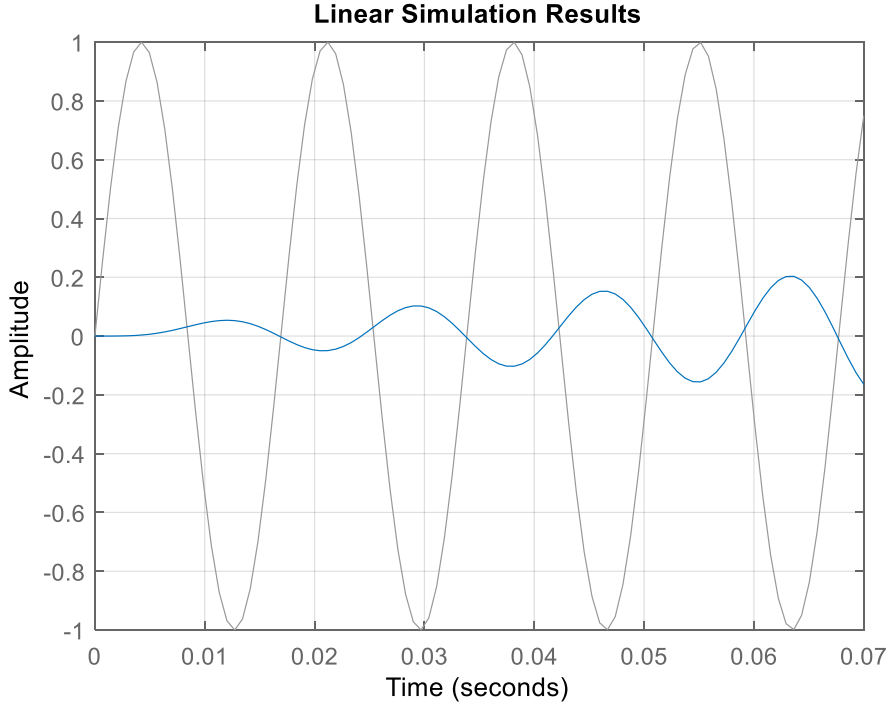

Figure 5.12: AC response for an open-loop transfer function for the RL = 20 and L_L=3.3 H

The AC response in Figure 5.12 shows that the output current will be unstable and grow exponentially. Moreover, it shows how an electrical system responds to alternating current (AC) signals. The system has certain components, and for this graph, we're looking at a situation where one inductance (RL) is 20 henries and another inductance (LL) is 3.3 henries. The graph helps us understand how the system behaves with these values when exposed to AC signals.

5.9.1 Observation on the open-loop transfer function

Increasing the value of the load resistor results in an unstable output, while increasing the value of the load inductor decreases the exponentially growing output voltage and tends to stabilize it. However, this approach cannot be relied on, there is a need to have a reliable approach to stabilize the load voltage.

5.9.2 Closed-loop controller for the RL load output voltage

There are a number of control schemes and those that have been proposed for this study are the proportional integral and proportional integral and derivative schemes. But before going deep into the control schemes, it is important to look into how to determine the stability of a controller. One of the most reliable ways to do so is the Routh-Hurwitz method.

5.9.3 Routh-Hurwitz criterion

The Routh-Hurwitz criterion is helpful to determine the number of closed-loop roots of the controller that are in the right half side of the s-plane in the linear time-variant controller. The criterion is especially helpful in systems of order higher than 2, where there might be challenges factoring the characteristic equation. To understand the Routh-Hurwitz algorithm, it is worth examining at the generic closed-loop system represented by Equation 5.56.

$$H(S) = \frac{b_o\, s^m + b_1 s^m + \cdots + b_{m-1}s + b_m}{a_o\, s^n + a_1 s^n + \cdots + a_{n-1}s + a_n} \qquad \text{Equation 5.51}$$

Where $m \leq n$, a_i and b_i are the coefficients of the denominator and the numerator, respectively.

The characteristic equation is $D(S) = a_o\, s^n + a_1 s^n + \cdots + a_{n-1}s + a_n$ Equation 5.52

One of the ways to implement the Routh-Hurwitz criterion is by using a table of this form (Table 5.1):

Table 5.1: Routh-Hurwitz for controller stability study

s^n	a_o	a_2	a_4	a_6	…
s^{n-1}	a_1	a_3	a_5	a_7	…
s^{n-2}	b_1	b_2	b_3	b_4	
s^{n-3}	c_1	c_2	c_3	c_4	
s^{n-4}	d_1	d_2	d_3	d_4	
. . .					
s^2	e_1	e_2			
s^1	f_1				
s^0	g_1				

Where:

$$b_1 = \frac{a_1 a_2 - a_0 a_3}{a_1}$$

$$b_2 = \frac{a_1 a_4 - a_0 a_5}{a_1}$$

$$b_3 = \frac{a_1 a_6 - a_0 a_7}{a_1}$$

And so forth. In the same way, d_i and all other coefficients can be calculated.

This Routh-Hurwitz criterion can then be used to determine the proportional, integral, and derivative gains to ensure that the voltage in the load component is stable.

To determine the proportional gain that will make the controller produce a stable voltage in the load component, the Routh-Hurwitz shall be used with the coefficients formed by the values of the components in the closed-loop controller.

Recalling that the values for the filter and the load components are:

$L_f = 3.3\ H, C_f = 2.2\ \mu F, R = 50\ \Omega, L_L = 3.3$ where R and L_L can be variable given the information that the load is variable.

The open-loop transfer function of the current over the input voltage will become (Equation 5.53):

$$\frac{I_O(S)}{V_{in}(S)}(OL) = \frac{1}{2.4*10^{-5}\ s^3+36.3*10^{-5}s^2+6.6s+50}$$ Equation 5.53

The closed-loop transfer function with a unit feedback is as per Equation 5.54:

$$\frac{I_O(S)}{V_{in}(S)} = \frac{1}{1+\frac{1}{2.4*10^{-5}\,s^3+36.3*10^{-5}s^2+6.6s+50}} \qquad \text{Equation 5.54}$$

Putting the function on the same denominator yields Equation 5.55.

$$\frac{I_O(S)}{V_{in}(S)} = \frac{1}{2.4*10^{-5}\,s^3+36.3*10^{-5}s^2+6.6s+50+1} \qquad \text{Equation 5.55}$$

The characteristic equation is: $2.4 * 10^{-5}\, s^3 + 36.3 * 10^{-5}s^2 + 6.6s + 50$

The updated Routh-Hurwitz table would thus look like:

s^3	50	$36.3 * 10^{-5}$	0	
s^2	6.6	$2.4 * 10^{-5}$	0	
s^1	$b_1 = \left(\frac{6.6 * 36.3 * 10^{-5} - 50 * 2.4 * 10^{-5}}{6.6}\right)$ $18 * 10^{-5}$	0		
s^o	$2.4 * 10^{-5}$			

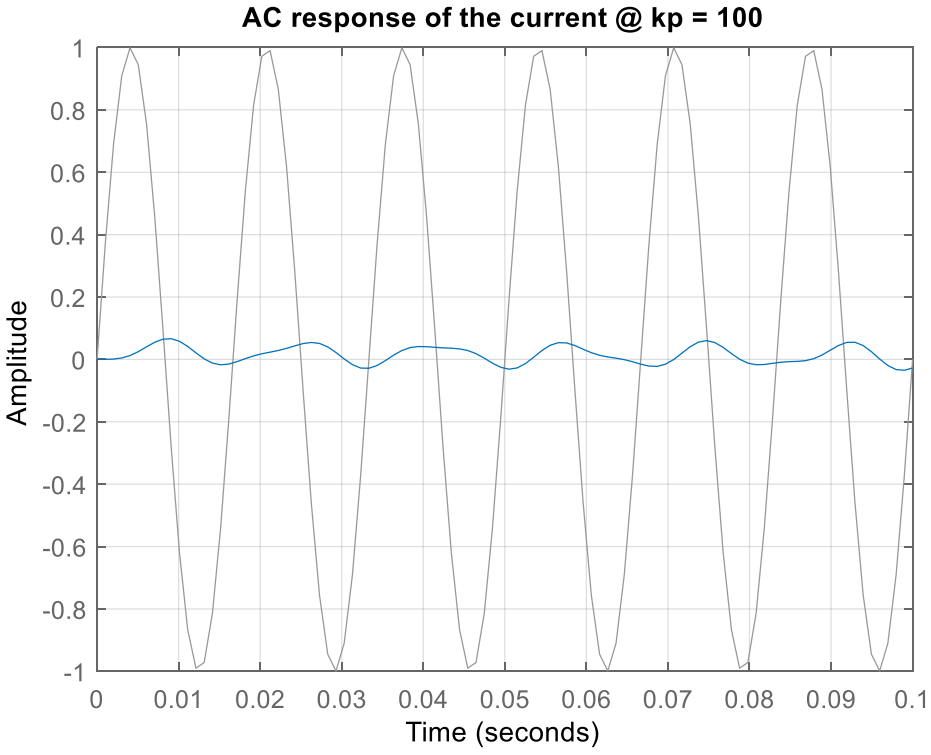

Figure 5.13: AC response of the closed-loop system with the load resistor kp =100

The previous figure (5.13) shows the closed-loop system's frequency response characteristics. The load resistor, shown by $K_p = 100$, is necessary for the system to function. Therefore, the displayed response explains how the system behaves in relation to alternating current (AC) impulses over a range of frequencies.

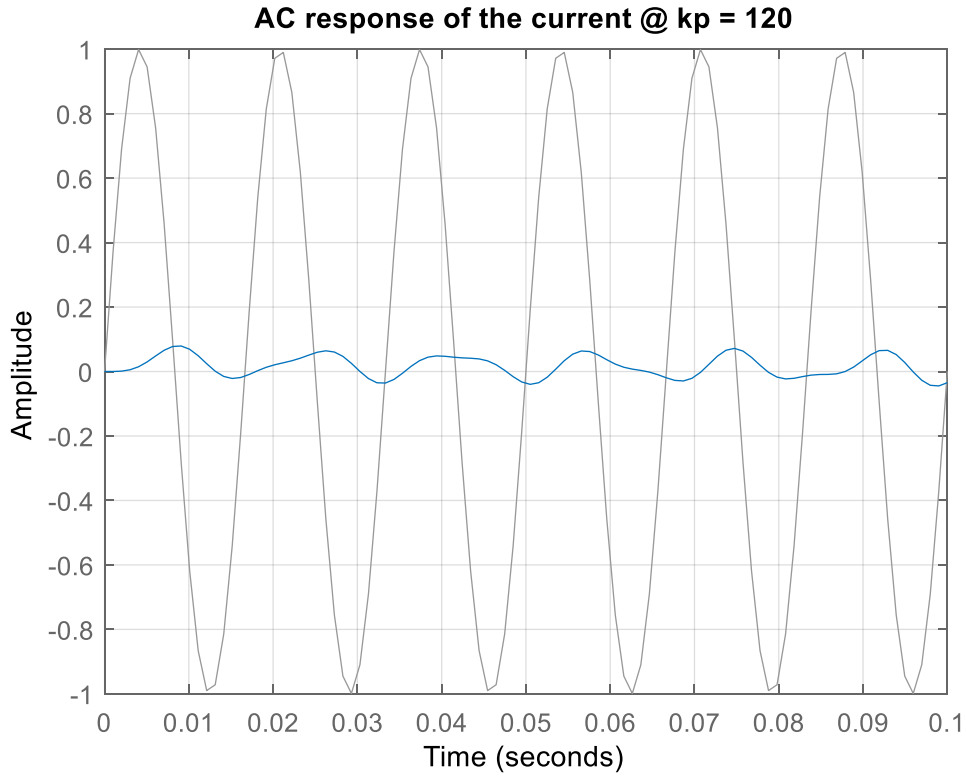

Figure 5.14: AC response of the closed-loop system with the load resistor kp =120

In the previous Figure 5.14 the closed-loop system's response to alternating current (AC) considering a load resistor with the prescribed parameter value of $K_p = 120$,. With the required load resistor setting included, this graph explains how the system behaves under AC circumstances. The AC response analysis sheds light on the interactions between the closed-loop setup, denoted by the provided kp value, and the various frequencies present in the AC domain. A visual assistance for understanding how the system performs in response to alternating current disturbances is provided by the resulting graphical depiction.

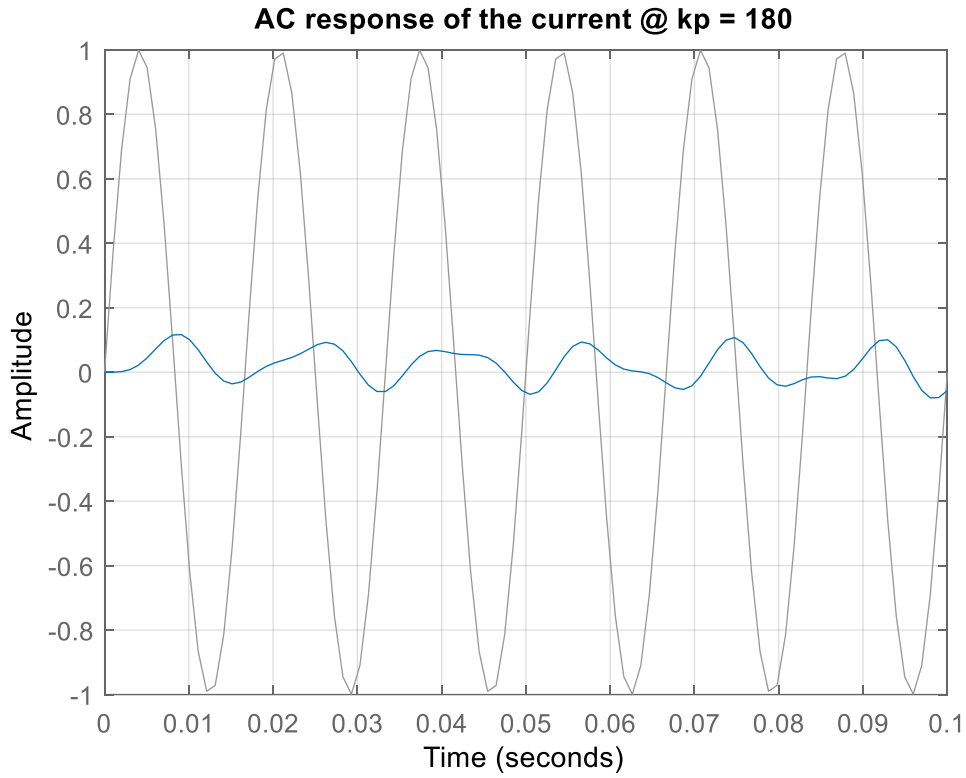

Figure 5.15: AC response of the closed-loop system with the load resistor kp =180

Figure 5.15 shows the closed-loop system's alternating current (AC) response when the load resistor is configured to have a value of $K_p = 180$. An example of a closed-loop system is one in which the output is sent back and compared to the desired input to govern system behavior. The load resistor in this situation assumes a value of 180 for its parameter K_p. The system's response to different frequencies or alternating current signals when the load resistor is set to the configuration shown in the figure's AC response.

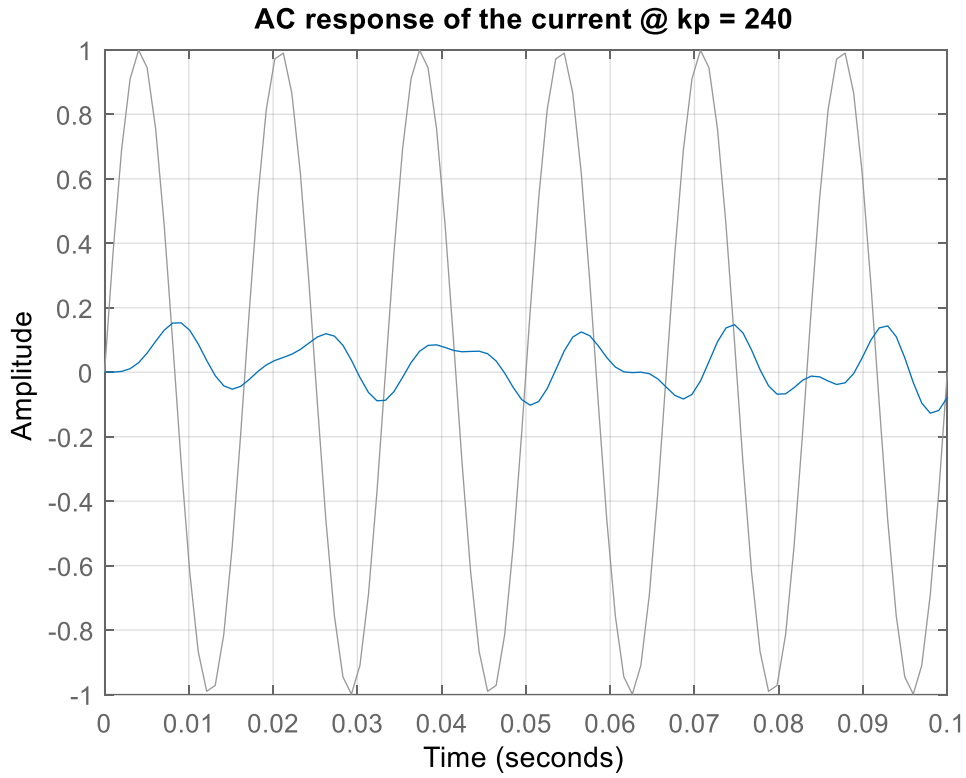

Figure 5.16: AC response of the closed-loop system with the load resistor kp 240

The alternating current (AC) response of the closed-loop system with a load resistor and a gain coefficient (kp) set to 240 is shown in Figure 5.16. This graphical illustration shows the impact of the load resistor's size on the system's performance characteristics and sheds light on how the system behaves when subjected to AC input.

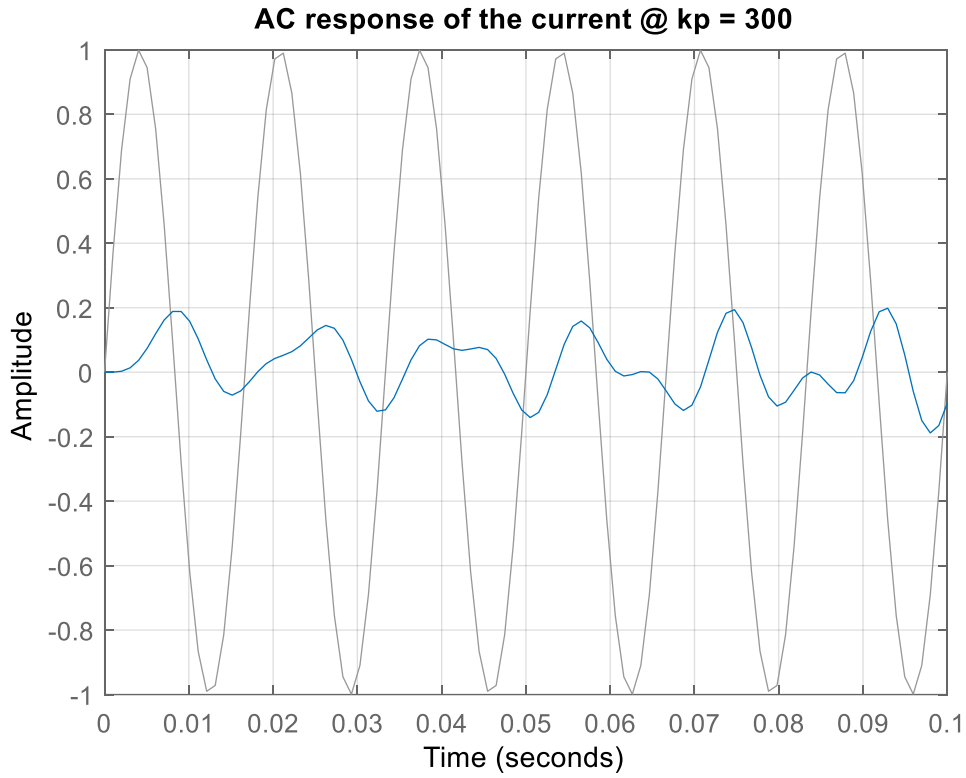

Figure 5.17*:* AC response of the closed-loop system with the load resistor kp =300

Figure 5.17 illustrates how the closed-loop system reacts to AC signals when integrated with a load resistor with the properties $K_p = 300$. This information helps to clarify how the system operates proportional gain and load setup scenarios.

The proportional gain of the system is shown by the value $K_p = 300$. A control system's response to the difference between desired and actual outputs is determined by a parameter called proportional gain. If not adjusted properly, a larger proportional gain can cause instability but often produces a more prominent response.

5.9.4 Observation

The load current comes out distorted for an AC input. The input voltage has a frequency of 50 Hz, and this has been maintained in the distorted output. The output current appears to have a 90^0 phase shift. Further control schemes are required to eliminate the harmonic distortions.

5.10 Output voltage across variable load

The voltage across the variable RL load can be formulated based on Equation 5.56.

$$V_{in}(S) = V_{Lf}(S) + V_o(S) \qquad \text{Equation 5.56}$$

With the KCL, the currents can be given by following Equation 5.57.

$$I_{Lf}(S) = I_{Cf}(S) + I_o(S) \quad \text{Equation 5.57}$$

Expressing currents by their Laplace's equations yields Equation 5.58.

$$I_{Lf} = C_f S V_o(S) + \frac{V_o(S)}{SL_L + R_L} \quad \text{Equation 5.58}$$

Putting the terms of Equation 5.58 on the same denominator yields Equation 5.59:

$$I_{Lf}(S) = \frac{(C_f S^2 L_L + SC_f R_L + 1)V_o(S)}{SL_L + R_L} \quad \text{Equation 5.59}$$

On the other hand, $V_{Lf} = SL_f I_{Lf}$.

The input voltage can be expressed as per Equation 5.60.

$$V_{in}(S) = SL_f \frac{(C_f S^2 L_L + SC_f R_L + 1)V_o(S)}{SL_L + R_L} + V_o(S) \quad \text{Equation 5.60}$$

Putting Equation 5.60 on same denominator and cancelling out the denominator gives Equation 5.61 below.

$$(SL_L + R_L)V_{in}(S) = SL_f(C_f L_L S^2 + SC_f R_L + 1))V_o(S) + (SL_L + R_L)V_o(S) \quad \text{Equation 5.61}$$

Factoring the terms in the right-hand side leads to Equation 5.62.

$$(SL_L + R_L)V_{in}(S) = (L_f C_f L_L S^3 + L_f C_f R_L S^2 + (L_f \quad + L_L)S + R_L)V_o(S) \quad \text{Equation 5.62}$$

The open-loop transfer function for the RL load is expressed in Equation 5.63.

$$\frac{V_o(S)}{V_{in}(S)} = \frac{SL_L + R_L}{L_f C_f L_L S^3 + L_f C_f R_L S^2 + (L_f \quad + L_L)S + R_L} \quad \text{Equation 5.63}$$

From the open loop transfer function, the AC response can be seen in Figure 5.18.

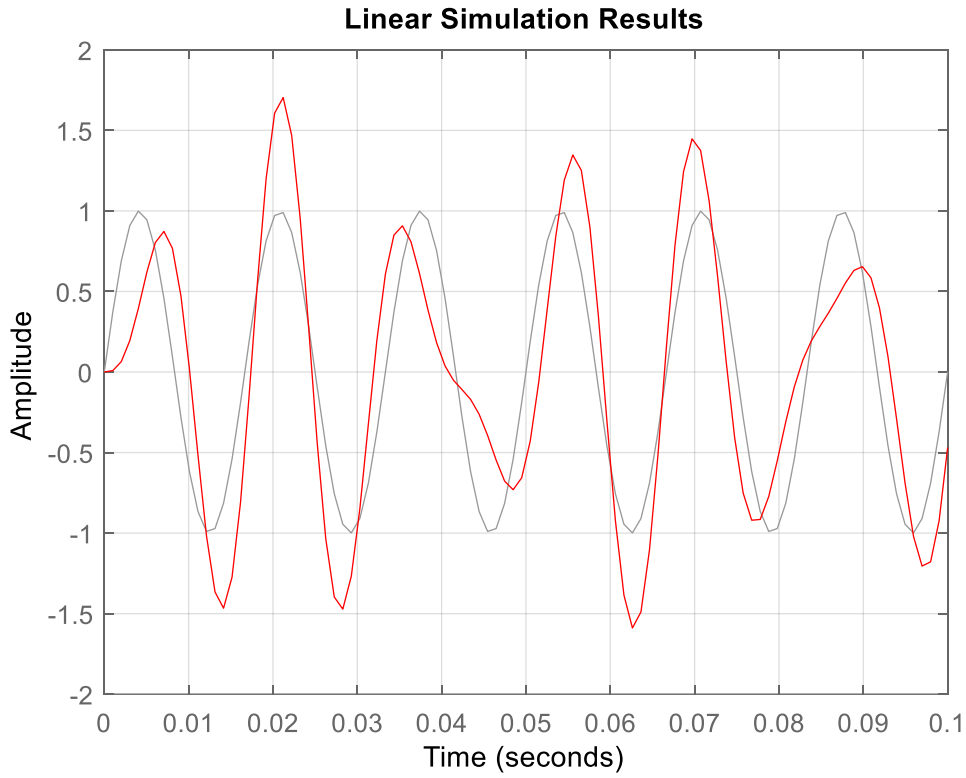

Figure 5.18: The response to the AC input voltage of the OPEN-loop transfer function

In response to an input voltage of alternating current (AC), Figure 5.18 shows how the open-loop transfer function behaves. The open-loop transfer function's ability to modify its output in response to changes in the AC input voltage is exemplified by the response that is shown. Using an open-loop arrangement as an example, this figure shows the dynamic connection between the input voltage and the consequent output response.

Since we are dealing with a variable load, increasing the value of the inductor is one of the ways of varying the load. Figure 5.19 shows the responses to the AC input provided with different values of the load inductor.

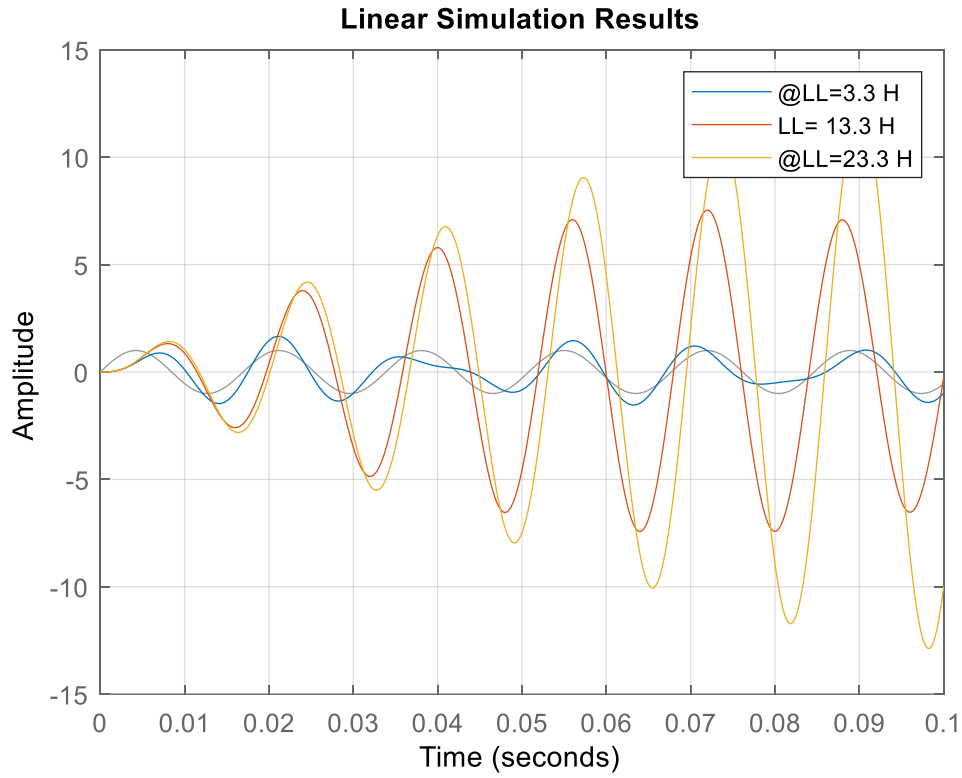

Figure 5.19: Response to the AC input with various values of load inductance

The response to the input of alternating current (AC) is shown in Figure 5.19 for various amounts of load inductance. In particular, the yellow waveform represents LL at 23.3 H, the red sinusoidal waveform represents LL at 13.3 H, and the blue sinusoidal waveform depicts the reaction when the load inductance (LL) is set at 3.3 H. The system's responses to various LL values are shown in the figure, which also highlights the unique properties of the AC input under various load-inductance scenarios.

5.10.1 Closed-loop transfer function and its response to the AC input

The closed-loop transfer function with unity feedback is expressed by Equation 5.64:

$$\frac{V_o(S)}{V_{in}(S)}cl = \frac{\frac{SL_L+R_L}{L_fC_fL_LS^3+L_fC_fR_LS^2+(L_f+L_L)S+R_L}}{1+\frac{SL_L+R_L}{L_fC_fL_LS^3+L_fC_fR_LS^2+(L_f+L_L)S+R_L}} \qquad \text{Equation 5.64}$$

Working out Equation 5.64 and cancelling out denominators yields Equation 5.65.

$$\frac{V_o(S)}{V_{in}(S)}cl = \frac{SL_L+R_L}{L_fC_fL_LS^3+L_fC_fR_LS^2+(L_f+2L_L)S+2R_L} \qquad \text{Equation 5.65}$$

The transfer function's response to the AC input for this closed loop is shown in Figure 5.20.

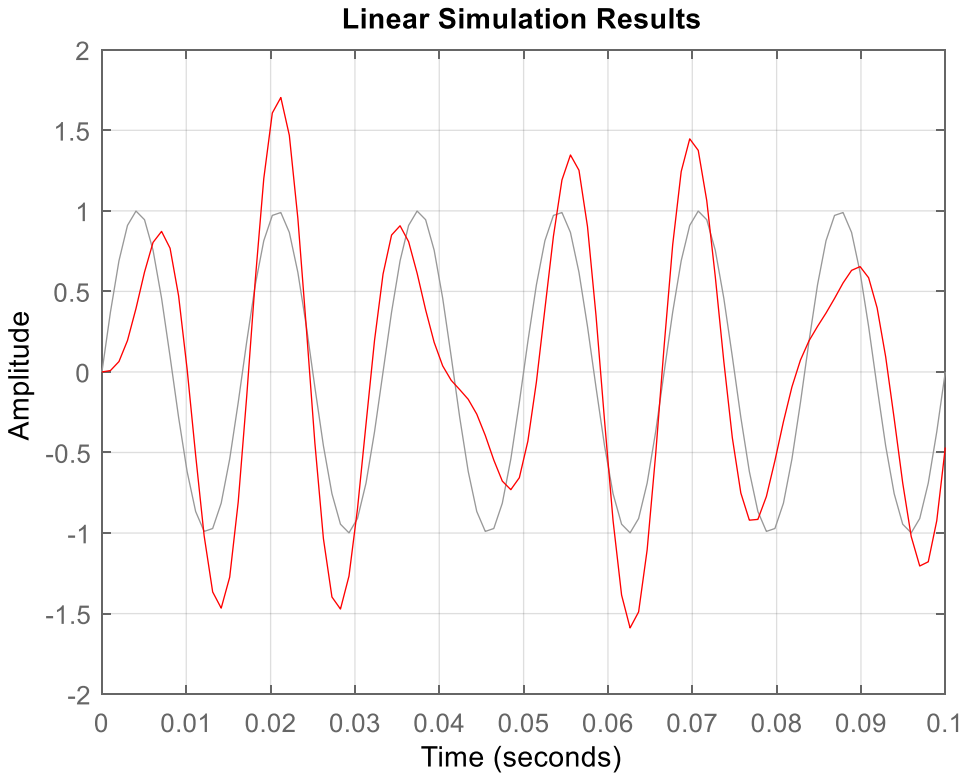

Figure 5.20: Response of the closed-loop transfer function for the output voltage

The closed-loop transfer function's reaction to the output voltage is shown in Figure 5.20. With regard to feedback, this illustration shows how the system's output voltage fluctuates in reaction to various inputs. For evaluating system performance, stability, and transient behavior, this understanding is essential. Designing and improving control systems for a range of applications is made easier by analyzing this connection.

Since the study is about the variable load, changing the values of the load inductor ranging from 3.3 H, 13.3 H, and 13.3 H results in the profiles in Figure 21.

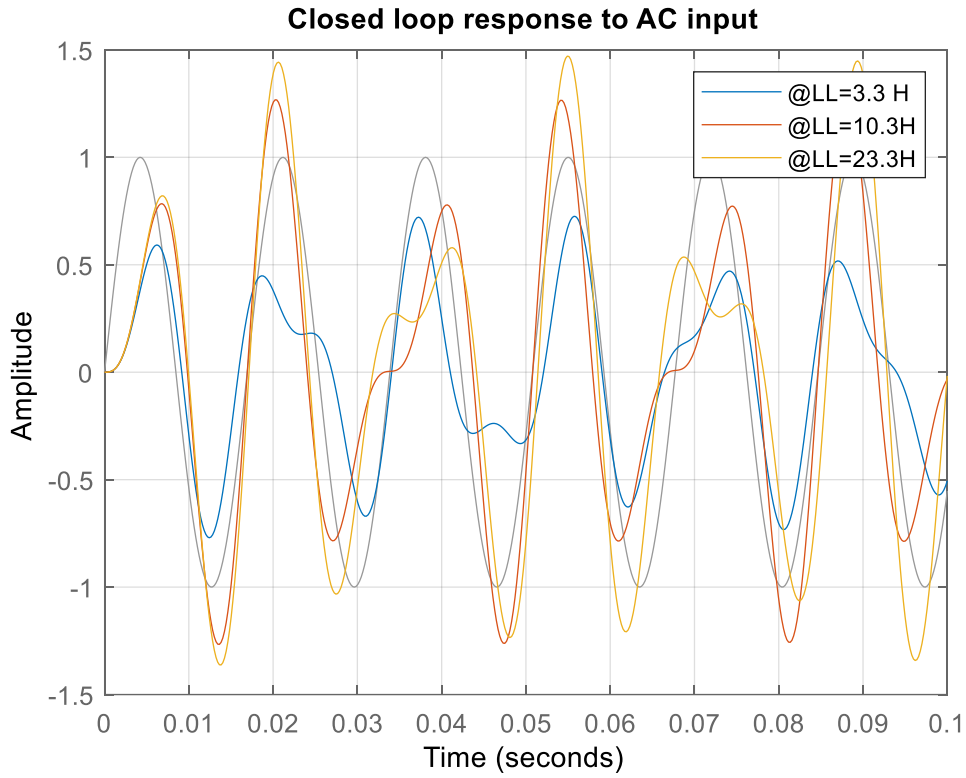

Figure 5.21: Responses from the unit feed transfer function of the output voltage varying the load inductance

The figure shows how alterations to the load inductance parameter affect the unit feed transfer function and therefore affect how the output voltage behaves. The link between the input and output parameters in the provided system is clarified using the unit feed transfer function, a mathematical tool used in control systems analysis. In this case, changes in the load inductance serve as the input, while changes in output voltage serve as the output.

In order to study the performance of the transfer function, the step responses were studied. The values of the components of the filter and the variable load remained the same ($L_f = 3.3\ H, L_c = 6.6\ \mu F$, $R_L = 50\Omega$, $L_L = 3.3\ H$). The response is shown in Figures 5.22–5.26.

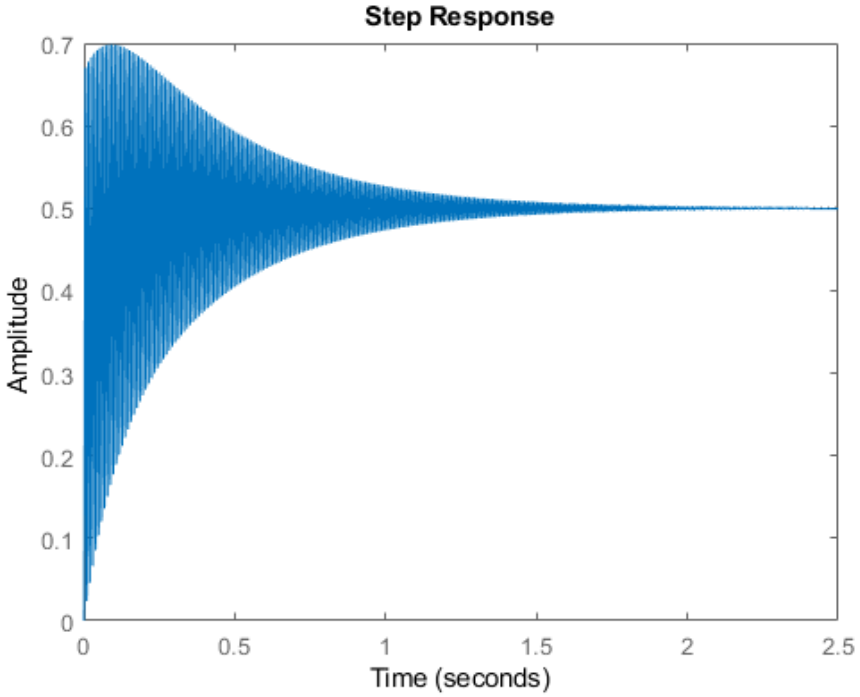

Figure 5.22: Step response to a unit feedback closed-loop function when the load inductor is 3.3 H

An arrangement for closed-loop control includes a feedback mechanism that modifies the system's behavior based on the data from the output. The term "unit feedback" indicates the process of comparing the desired input signal to the output signal, which often represents the system's reaction. The load inductor, which contributes to the system's impedance and energy storage capacities and has an inductance value of 3.3 H, is a crucial component. The dynamic interaction between the closed-loop control system, the unit feedback configuration, and the effect of a 3.3 H load inductor on its step response is shown visually in Figure 5.22. This image makes it easier to comprehend the system's behavior over time as well as how well it controls input changes within the defined parameter setup.

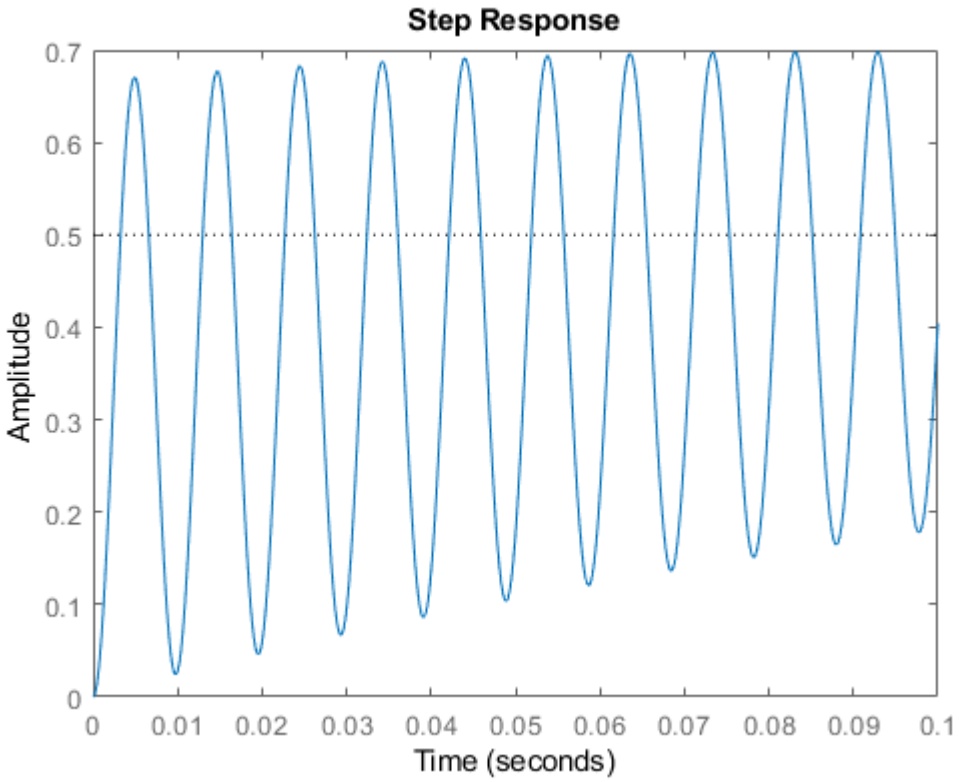

Figure 5.23: Step response of the output voltage zoomed when the load inductor is 3.3 H

In relation to a load inductor value of 3.3 H, Figure 5.23 shows the step response characteristics of the output voltage with an emphasis on an improved magnification level. The graphic illustrates the transient behavior of the system's output voltage in response to a step input, with a focus on the temporal development at 3.3 H for the load inductor. This focus on the selected inductance value enables a careful examination of the system's dynamic performance in the first few seconds after the input change. This analytical examination's goal is to give the reader a fuller understanding of the system's responsiveness and inherent behavior under the given circumstances.

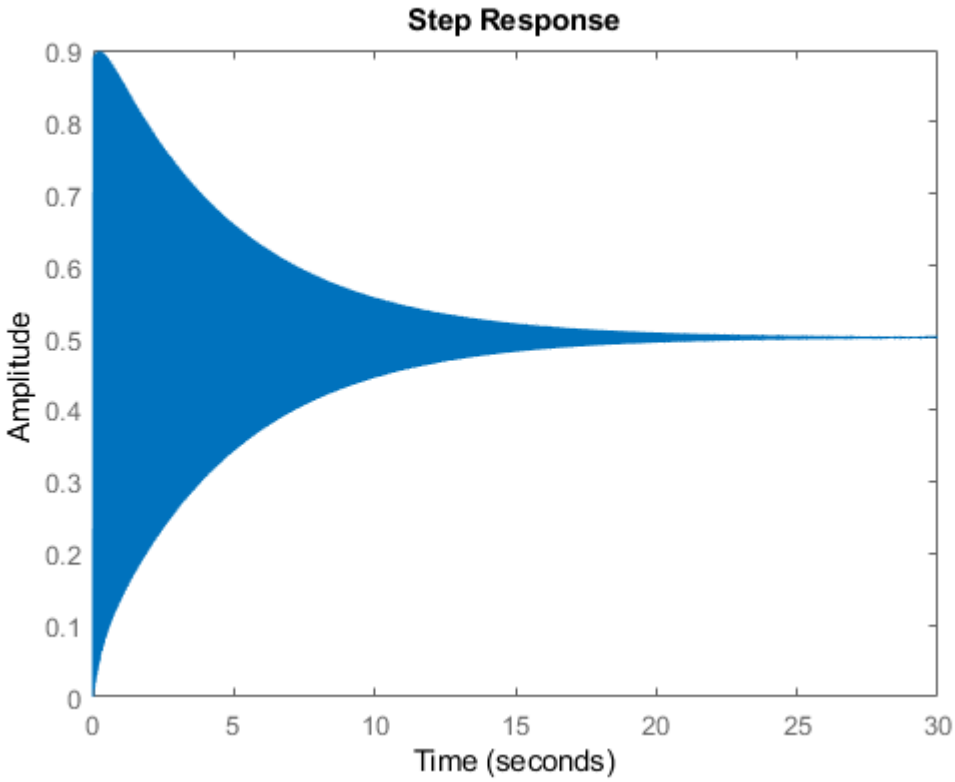

Figure 5.24: Step response to a unit feedback closed-loop function when the load inductor is 13.3 H

Figure 5.24 shows the step response of a closed-loop unit feedback function when a load inductor with a 13.3 henry inductance value is present. The shown graph shows the system's transitory behavior in response to an immediate change in input, concentrating on how the system output changes over time. The closed-loop setup creates a dynamic interaction between the load inductor and the properties of the system by feeding the output back to the input with a gain of unity. The step response depicts how the system's output changes over time as it attempts to find a new equilibrium in reaction to the rapid input change. With an inductance of 13.3 H, the load inductor's impact on this response is clearly audible.

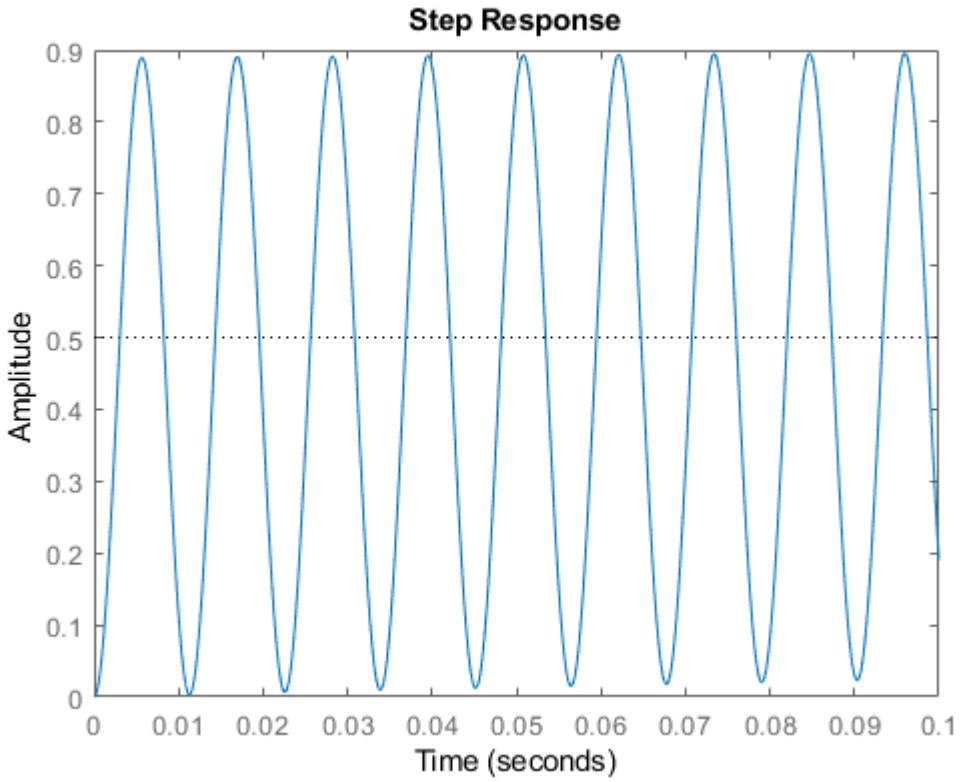

Figure 5.25: Step response of the output voltage zoomed when the load inductor is 13.3 H

Figure 5.25 shows the step response of the output voltage for situations when the load inductor is precisely 13.3 Henries, painstakingly enlarged to show details. With a strong emphasis on the time development of the output voltage under this particular inductive load situation, the graphical depiction captures the dynamic behavior of the system after a step input. This zoomed-in representation enables a deft examination of the complex transient response characteristics, providing a thorough knowledge of the interaction between the inductor's magnitude and the subsequent changes to the voltage profile.

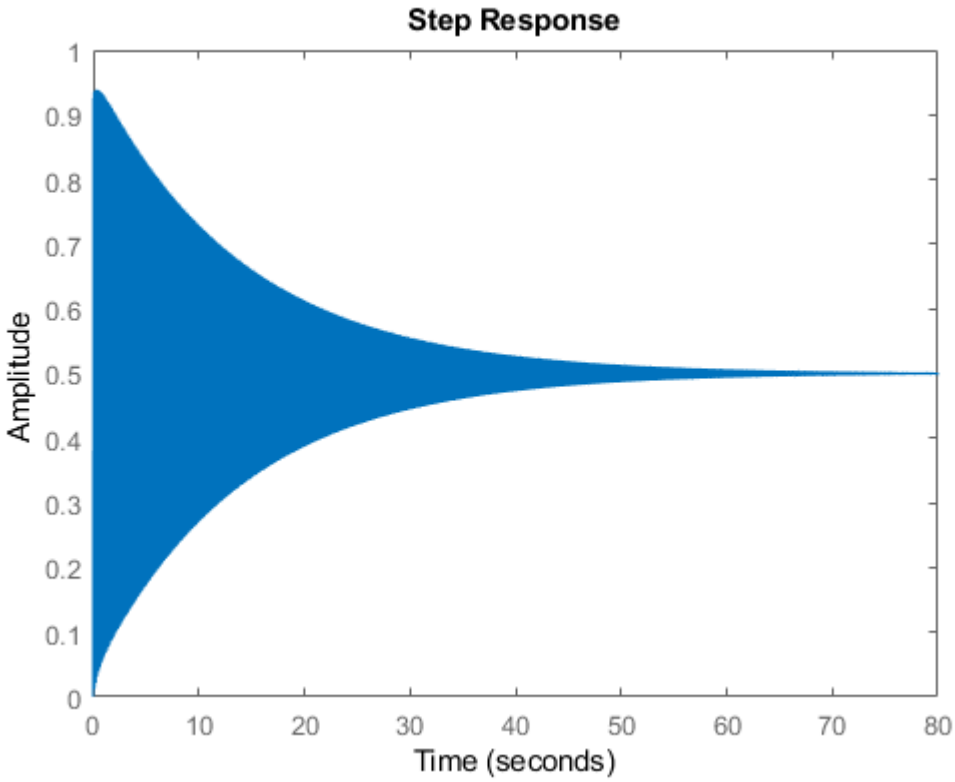

Figure 5.26: Step response of the output voltage zoomed when the load inductor is 23.3 H

Figure 5.26 methodically magnifies the step response of the output voltage and focuses on the situation when the load inductor is given a value of 23.3 henries. This graphical illustration explains the behavior of the voltage output in response to a step input, paying special attention to the strong amplification provided by the stated load inductance value. The figure contributes to a deeper understanding of the complex dynamics of the system by serving as an informative visual witness to the influence of the stated load inductor size on the transient response characteristics of the output voltage.

From the step responses obtained from Figures.5.22–5.26 above, the unit feedback of the transfer function for the output voltage tends to stabilize at 0.5. Furthermore, the response presents damped oscillations and takes more than 2.5 seconds to stabilize.

5.11 Proportional Integral and Derivative (PID) control

5.11.1 The proportional gain

The role of the proportional gain, commonly denoted K_p, is to push the output signal to the desired level. However, by so doing, the error level increases proportionally. The system reacts fast but overshoots more. The proportional controller reduces the error but does not eliminate it. Hence, other options are to be explored.

5.11.2 The derivative gain

The effect of the derivative gain, K_d, is to anticipate the error by for instance reducing the overshoot slope. It actually dampens the magnitude of the error if it has a large slope. The derivative gain reshapes the profile of the error by reducing its magnitude, but does not eliminate the steady-state error.

5.11.3 The integral gain

The effect of the integral term, K_i, is reducing the steady-state error. By integrating, the profile builds upwards and compensates for the steady-state error. The drawback of the integral term is that it can make the system slow and oscillatory, especially when it changes signs.

Table 5.2 summarizes the effects of the P, I and D gains on the steady-state error.

Table 5.2: Effects of P, I, and D gains on controllers

CL RESPONSE	RISE TIME	OVERSHOOT	SETTLING TIME	S-S ERROR
Kp	Decrease	Increase	Small Change	Decrease
Ki	Decrease	Increase	Increase	Decrease
Kd	Small Change	Decrease	Decrease	No Change

Implementing the overviewed gains on the system is explored in the following sections.

5.11.4 Proportional controller design

The setup of a system with a proportional controller can be illustrated in Figure 5.27 below.

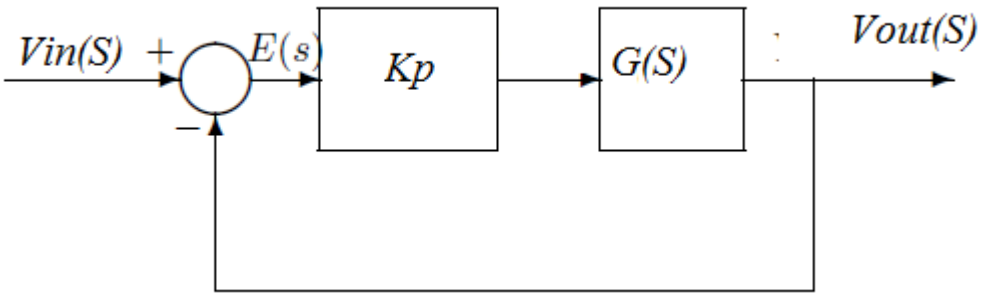

Figure 5.27: Block diagram for a plant controlled by a proportional gain

The unit feedback for this transfer function is given by Equation 5.66:

$$\frac{V_{out}(S)}{V_{in}(S)} = \frac{K_p G(S)}{1+K_P G(S)} \qquad \text{Equation 5.66}$$

Applying Equation ...to the actual transfer function, we get Equation 5.67:

$$\frac{V_o(S)}{V_{in}(S)}cl = \frac{K_p\frac{L_LS+R_L}{L_fC_fL_LS^3+L_fC_fR_LS^2+(L_f+L_L)S+R_L}}{1+K_p\frac{SL_L+R_L}{L_fC_fL_LS^3+L_fC_fR_LS^2+(L_f+L_L)S+R_L}} \quad \text{Equation 5.67}$$

Putting the numerator and denominator to the common denominator and cancelling it out gives Equation 5.68.

$$\frac{V_o(S)}{V_{in}(S)}cl = \frac{K_p(L_LS+R_L)}{L_fC_fL_LS^3+L_fC_fR_LS^2+(L_f+K_pL_L)S+K_pR_L} \quad \text{Equation 5.68}$$

Now that the proportional gain has been applied, the final value shall be (Equation 5.69):

$$F_V = \lim_{S\to+\infty} S\frac{K_pL_LS+K_pR_L}{S(L_fC_fL_LS^3+L_fC_fR_LS^2+(L_f+K_pL_L)S+K_pR_L)} \quad \text{Equation 5.69}$$

$F_V = 1$, the final value for a step input is equal to 1. This means that from the 0.5 settling point we were getting, the level output voltage can match that of the input. This can be demonstrated through the simulation in Figure 5.28. The figure will also reflect the quality of output one can expect. The step response gives a clear indication that the output levels area matches the input levels (Figure 5.28).

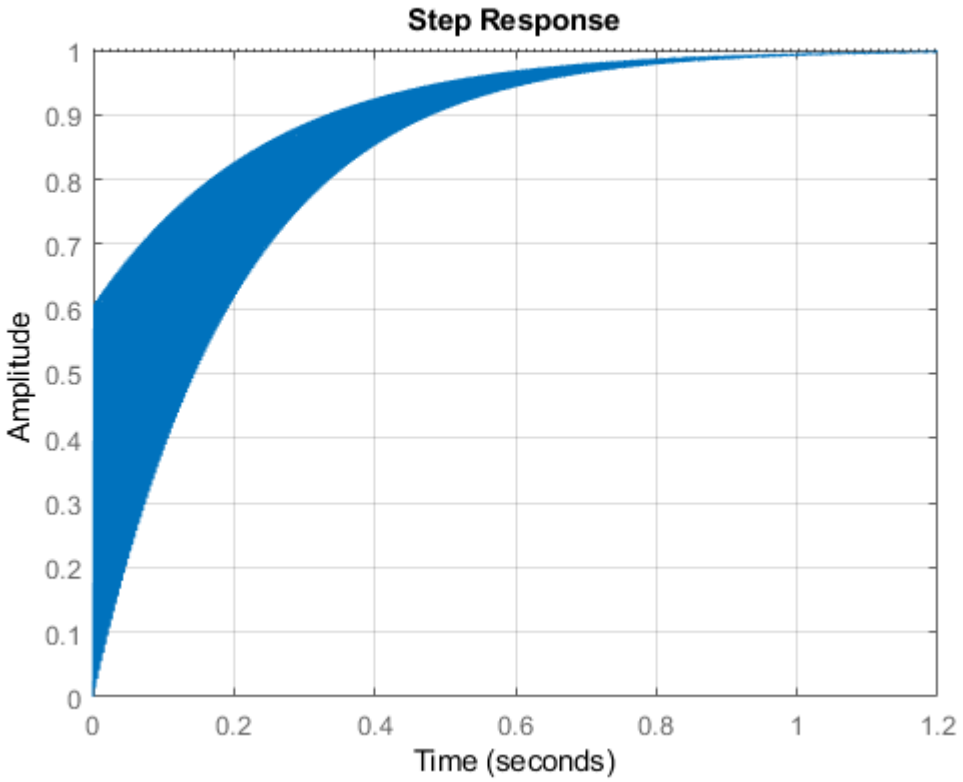

Figure 5.28: Step response for an output voltage controlled using a proportional gain

The concepts of proportional control and its effect on system behavior are illustrated clearly in Figure 5.28. By giving a concrete example of the control system's transient reaction to a perturbation, this visual depiction helps understand how the control loop functions in real-world circumstances. These educational tools are essential for creating a complex grasp of control theory, particularly with regard to the proportional control strategy's function in regulating system variables.

The responses to the AC input are for different values of the proportional gains provided in Figure 5.29 below. The code can be found in Appendix 5.1.

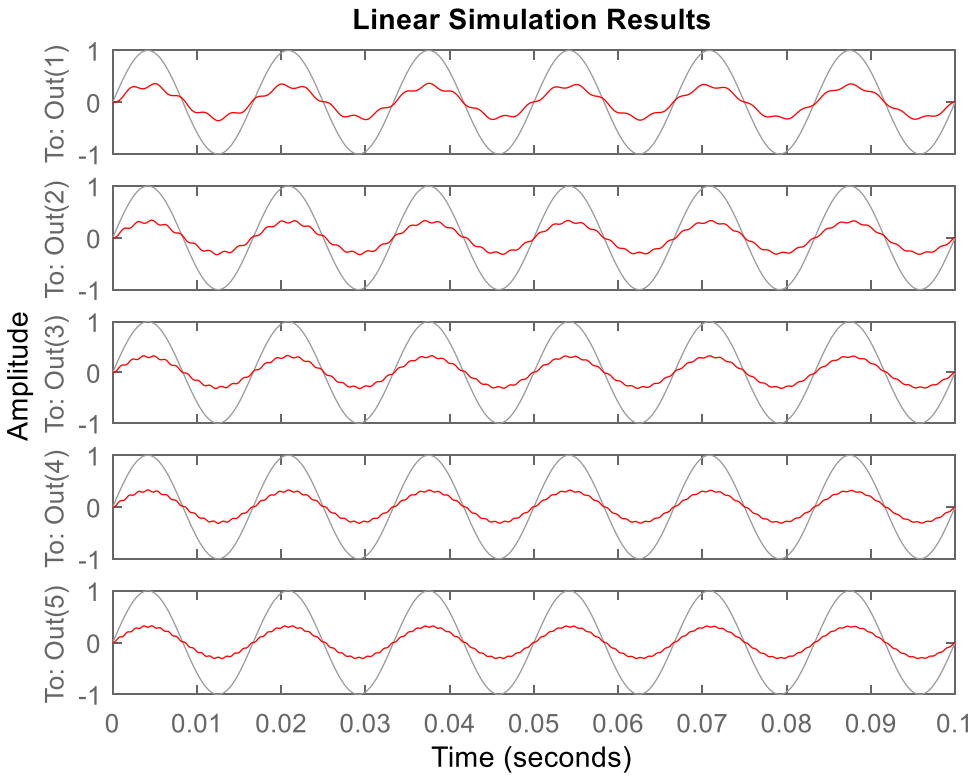

Figure 5.29: Response to AC input for a closed-loop transfer function with Kp varying between 20 and 100

A closed-loop transfer function's dynamic behavior under the influence of alternating current (AC) input is depicted visually in Figure 5.29. This figure considers the parametric alteration of the proportional gain (Kp) over the range of values from 20 to 100. The figure has been painstakingly separated into five distinct sections, each of which has been painstakingly named to represent the desired outcome at various stages of the system's reaction. To indicate specific points in the system's trajectory, the designations "To: out (5)," "To: out (4)," "To: out (3)," "To: out (2)," and "To: out (1)" are used. These markers essentially represent the fifth, fourth, third, second, and initial stages of the reaction, respectively, of the output at the completion of the simulation.

Zooming into the step input responses, one can see how oscillatory they are and thus in need of further control (Figures 5.30–5.34).

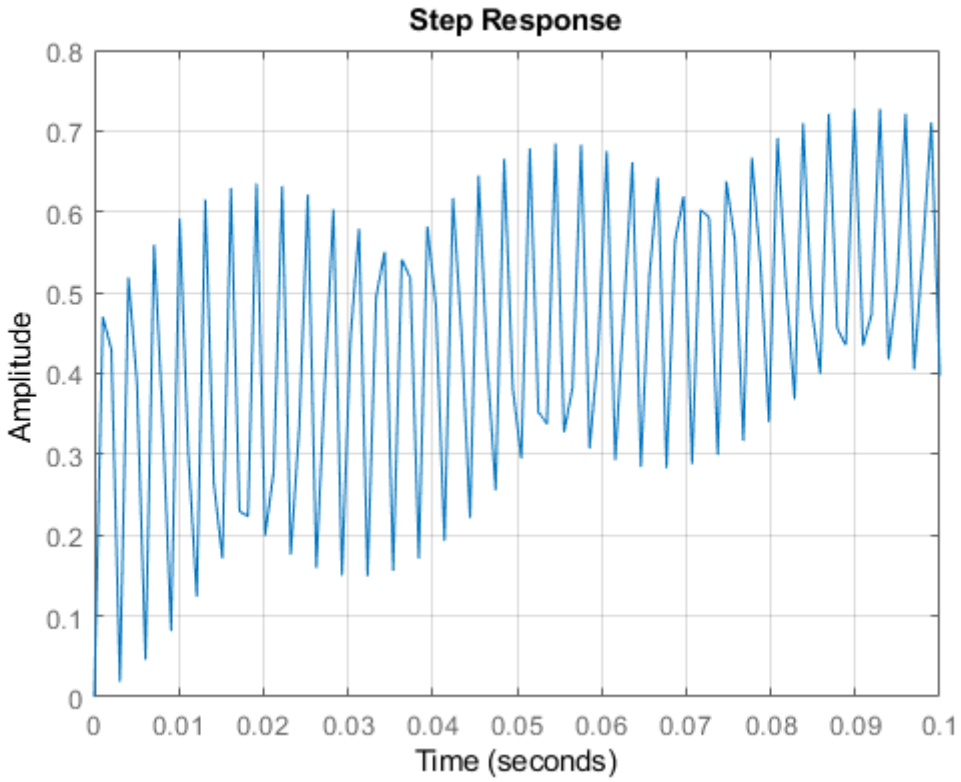

Figure 5.30: Zoomed step response when the proportional gain is 10

Figure 5.30 shows the enlarged step response that was produced with a proportional gain of 10. This graphical depiction offers a more thorough understanding of the system's response to a step input. The fundamental control system parameter known as proportionate gain has a big impact on how the system behaves. In respect to the error signal, a larger proportionate gain amplifies the control action, which might impact the system's responsiveness, stability, and overall performance. The dynamic properties and transient behavior of the controlled system can be better understood by concentrating on the step response in this particular situation.

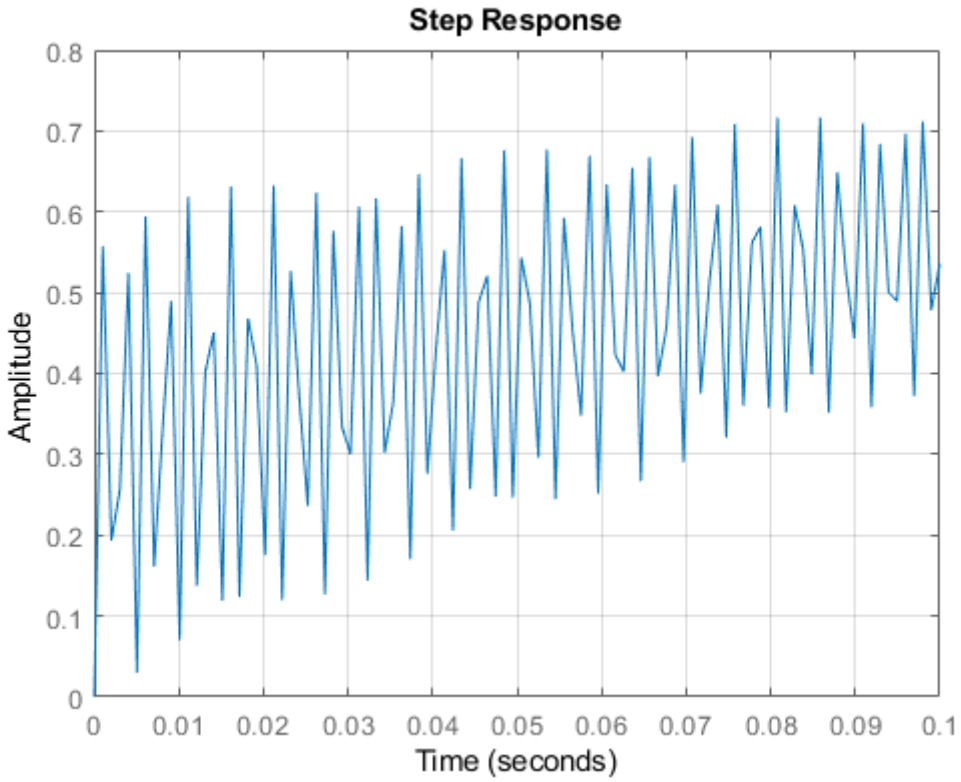

Figure 5.31::**Zoomed step response when the proportional gain is 30**

Figure 5.31 illustrates an enlarged version of the step response attained by a control system, emphasizing the unique behavior seen when the proportional gain parameter is set to a value of 30. This illustration clarifies the system's dynamic reaction to an input step change and provides a better understanding of how the system output changes over time when the specified proportional gain setting is used. A more thorough evaluation and comprehension of the control system's performance is made possible by the enlarged representation, which highlights the fine nuances and peculiarities of the behavior of the control system at this specific gain value.

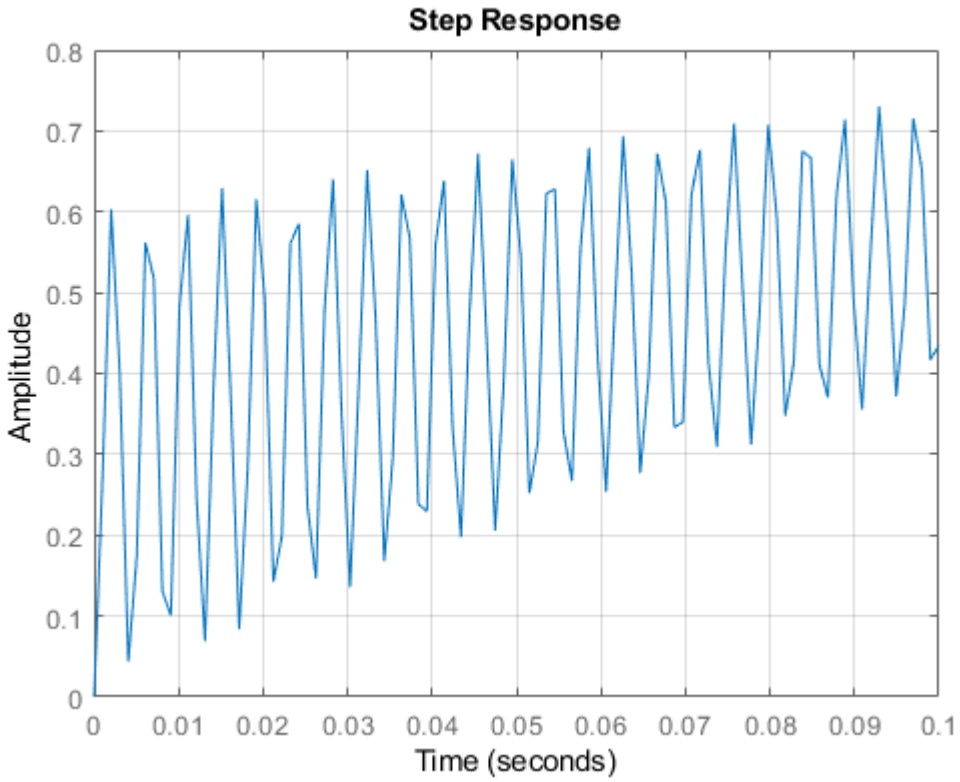

Figure 5.32 :Zoomed step response when the proportional gain is 50

The enlarged step response is shown in Figure 5.32 when the proportional gain is adjusted to a value of 50. This graphical depiction provides a focused analysis of the response characteristics under such a particular parameter configuration by showing the system's dynamic behavior after a step input. The essential element of proportional-integral-derivative (PID) control systems, the proportional gain, has a significant impact on the stability and responsiveness of the system. A proportionate gain value of 50 is noticeably high and may cause the system to exhibit strong oscillations or even instability. Our knowledge of control system dynamics is enriched by the careful study of this reaction, which reveals the complex interplay between control parameters and system performance.

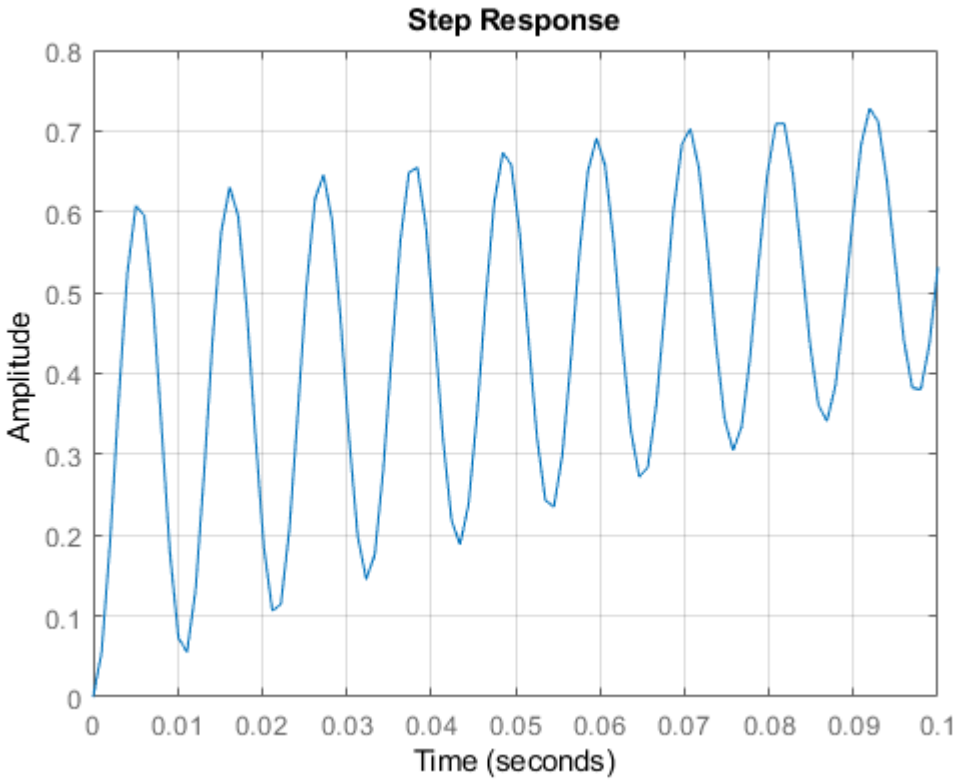

Figure 5.32:Zoomed step response when the proportional gain is 70

The zoomed-in step response corresponding to a proportionate gain value of 70 is shown in Figure 5.32. This illustration enables a thorough understanding of the effect of a particular proportional gain value on the system's transient response by providing a detailed assessment of the output behavior of the system following a step input. The figure makes it easier to grasp how the system's dynamics play out throughout the early phases of its reaction to changes in input by concentrating on this specific gain level. Such insight into the behavior of proportional control mechanisms under various parameter configurations is crucial in the field of control systems and helps to influence the design and optimization of feedback control systems.

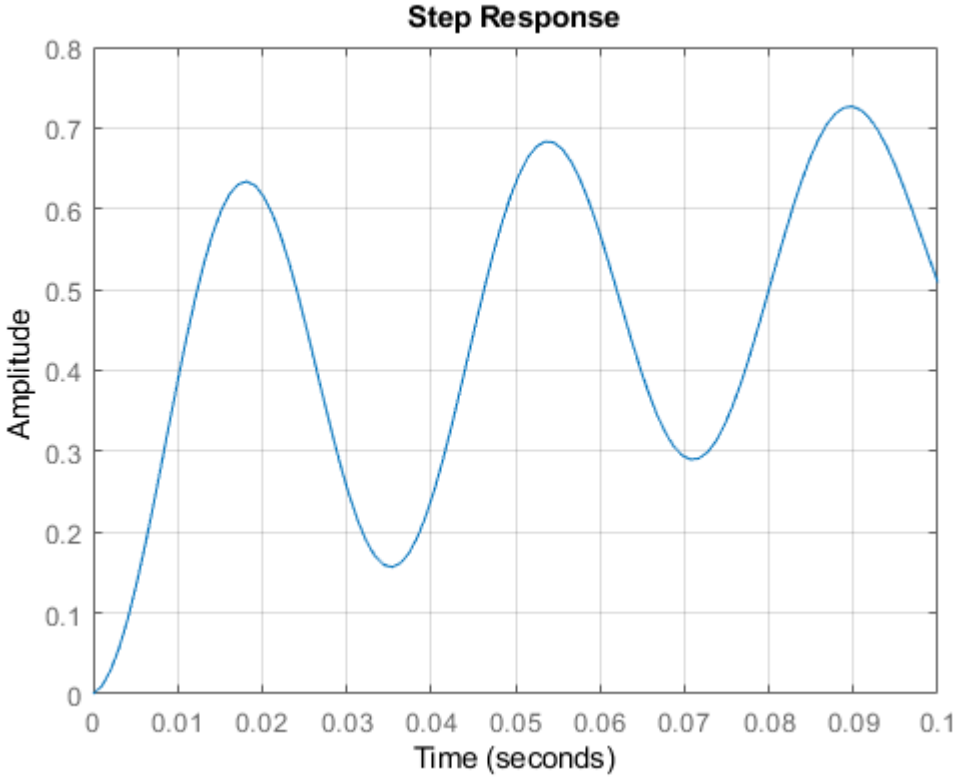

Figure 5.33: Zoomed step response when the proportional gain is 90

The amplified step response produced by a significant proportional gain value of 90 is shown in Figure 5.33. This graphical depiction offers a more thorough understanding of the system's dynamic behavior after a step input. The system's response characteristics are significantly influenced by the system's strong proportional gain, which acts as a control parameter. The increased proportional gain emphasizes the system's responsiveness, as seen in the figure, leading to a quicker rising time, a shorter settling time, and a higher peak overshoot. This illustration serves to emphatically highlight the complex interaction between the proportional gain setting and the system under consideration's transient performance.

The step responses give a good indicator of how much distorted shall occur. Observing the responses to the step input depicted in Figures 5.30–5.34, the responses obtained with a low proportional gain portray high frequency distortions, while the frequencies and amplitudes of distortions in the output voltage decrease as the proportional gain increase. This can also be seen in the responses shown in Figure 5.29. Studying the signal stability can be confirmed using the Routh-Hurwitz method.

5.11.5 Determining the Kp value for a better response

The value of Kp can be determined using the Routh-Hurwitz method as per the following table:

Table 5.3: Stability study for a proportional controller

s^3	$K_p R_L$	$L_f C_f R_L$	0	
s^2	$(L_f + K_p L_L)$	$L_f C_f L_L$	0	
s^1	$\left(\frac{(L_f + K_p L_L) L_f C_f R_L - K_p R_L L_f C_f L_L}{(L_f + K_p L_L)}\right)$ $\frac{L_f^2 C_f R_L}{L_f + K_p L_L}$	0		
s^o	$L_f + L_L$			

From the Routh-Hurwitz table above (Table 5.3), the coefficients are all positive, given the fact that the values of the components can only be positive. This leads to the conclusion that all the roots are on the left-hand side of the s-plane, thus the plant is stable. As for the value of the proportional gain, it can be any positive value. Therefore, the output will be stable and signal distortions could be gradually eliminated by increasing the proportional gain. Next, the performance of the proportional integral controller (PI) is explored..

5.12 Proportional Integral controller

The proportional integral mathematical expression is expressed by Equation 5.70 and the block diagram below (Figure 5.35):

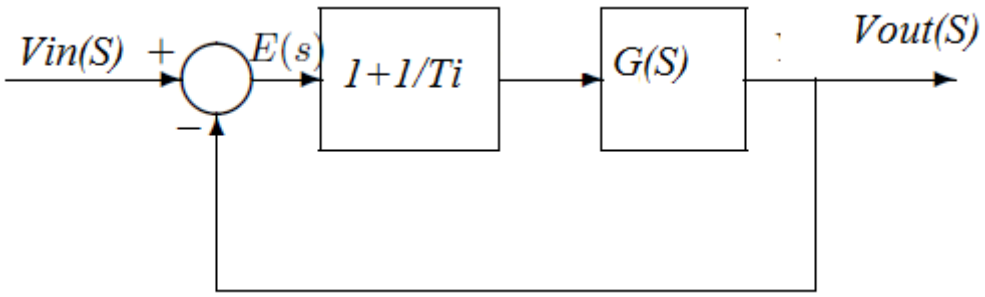

Figure 5.34: Block diagram of PI controller

To be able to use a PI controller, one needs to know the value of the parameter T_i, which is the integral time. As this parameter is associated with another parameter called dead-time, obtained from the step input response, the latter is examined first (Figure 5.36).

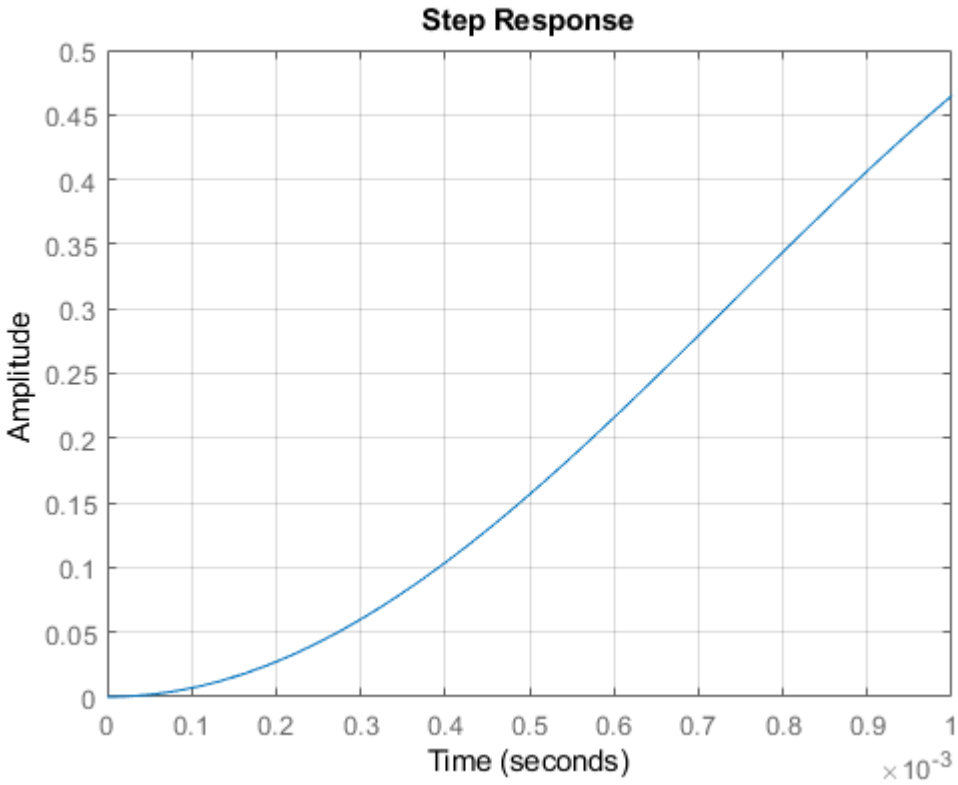

Figure 5.35: Step input response showing the dead-time

Figure 5.35 shows the response of the system to a sudden change in input, which is represented as a step input. The graph clearly displays dead-time, which is the period that passes before a system's reaction is evident. The delay between an input change and the system's initial reaction is referred to as dead-time. The cause of this delay may be due to inertia or signal transmission.

The time elapsed between an input change and the beginning of an output change is known as the dead-time interval. Dead-time has an impact on system control since it slows down how quickly the system reacts to changes. This delay must be considered by engineers for precise modeling and efficient control. As a result, Figure 5.35 provides a clear visual understanding of the function of dead-time in dynamic systems.

The unit feedback for this transfer function can be expressed as per Equation 5.71:

$$\frac{V_{in}(S)}{V_{out}(S)}cl = K_P(1 + \frac{1}{ST_i})G(S) \qquad \text{Equation 5.71}$$

Where T_i is the integral time measured, referring to the dead time, meaning the time the step response takes before it rises. For instance, referring to Figure 5.37, the dead-time for the transfer function of the output voltage is $L = 10^{-4} seconds$.

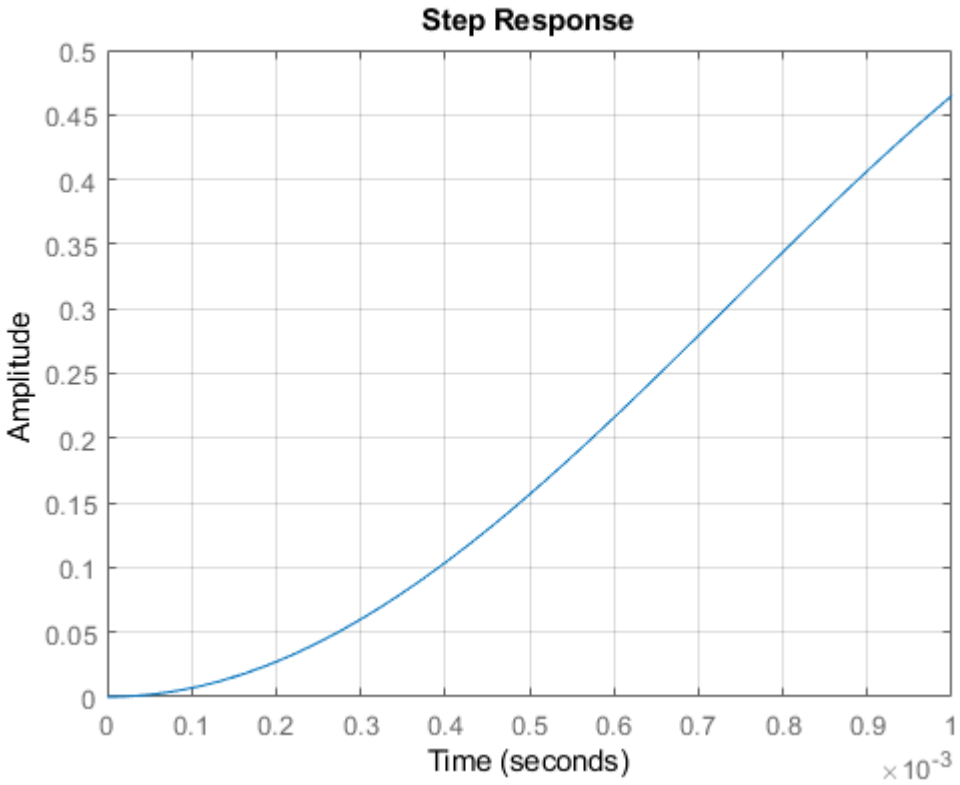

Figure 5.36 Illustration of the dead-time

A graphical explanation of the dead time phenomena in the context of dynamic systems is provided by Figure 5.36. Dead time is the amount of time that passes after an input but before there is any observable reaction. This graphical representation captures the essence of dead time by showing the temporal period in which the system's output is inert before any change is perceptible. Understanding the idea of dead time, which is important in the study and modeling of systems with innate delays, is made easier by such a visual depiction. This image can help one better understand the dynamics and control of dynamic systems by providing insights into how dead time emerges and affects system behavior.

Where is the mathematical representation of the PI controller with respect to a variable load being fed by an LC filter.

The transfer function will be represented as per Equation 5.72.

$$\frac{V_{out}(S)}{V_{in}(S)}cl = \frac{K_p\left(1+\frac{1}{ST_i}\right)\left(\frac{L_LS+R_L}{L_fC_fL_LS^3+L_fC_fR_LS^2+(L_f+L_L)S+R_L}\right)}{1+\frac{K_p\left(1+\frac{1}{ST_i}\right)L_LS+R_L}{L_fC_fL_LS^3+L_fC_fR_LS^2+(L_f+L_L)S+R_L}} \qquad \text{Equation 5.72}$$

Factoring out the numerator yields Equation 5.77:

$$\frac{V_{out}(S)}{V_{in}(S)}cl = \frac{\left(\frac{K_p\left(1+\frac{1}{ST_i}\right)(L_LS+R_L)}{L_fC_fL_LS^3+L_fC_fR_LS^2+\left(L_f+L_L\right)S+R_L}\right)}{1+\frac{K_p\left(1+\frac{1}{ST_i}\right)L_LS+R_L}{L_fC_fL_LS^3+L_fC_fR_LS^2+\left(L_f+L_L\right)S+R_L}}$$ Equation 5.73

Putting the Equation to the common denominator gives Equation 5.74 below.

$$\frac{V_{out}(S)}{V_{in}(S)}cl\_PI = \frac{\left(\frac{K_p\left(1+\frac{1}{ST_i}\right)(L_LS+R_L)}{L_fC_fL_LS^3+L_fC_fR_LS^2+\left(L_f+L_L\right)S+R_L}\right)}{1+\frac{K_p\left(1+\frac{1}{ST_i}\right)(L_LS+R_L)}{L_fC_fL_LS^3+L_fC_fR_LS^2+\left(L_f+L_L\right)S+R_L}}$$ Equation 5.74

Cancelling out the redundant denominator yields Equation 5.75.

$$\frac{V_{out}(S)}{V_{in}(S)}cl\_PI = \frac{K_p\left(1+\frac{1}{ST_i}\right)(L_LS+R_L)}{L_fC_fL_LS^3+L_fC_fR_LS^2+\left(L_f+L_L\right)S+R_L+K_p\left(1+\frac{1}{ST_i}\right)(L_LS+R_L)}$$ Equation 5.75

Factoring out the numerator gives Equation 5.80.

$$\frac{V_{out}(S)}{V_{in}(S)}cl\_PI = \frac{K_pL_LS^2+K_p\left(R_L+\frac{L_L}{T_i}\right)S+\frac{R_L}{T_i}}{L_fC_fL_LS^4+L_fC_fR_LS^3+\left(L_f+L_L+K_pL_L\right)S^2+K_p\left(R_L+\frac{L_L}{T_i}\right)S+R_L\left(1+\frac{1}{T_i}\right)}$$ Equation 5.76

5.12.1 Proportional Integral responses to an AC input

Figures 5.38 to 5.45 show the responses of the PI controller for gain ranging between 30 and 300. The responses were obtained using a MATLAB code in Appendix 5.2.

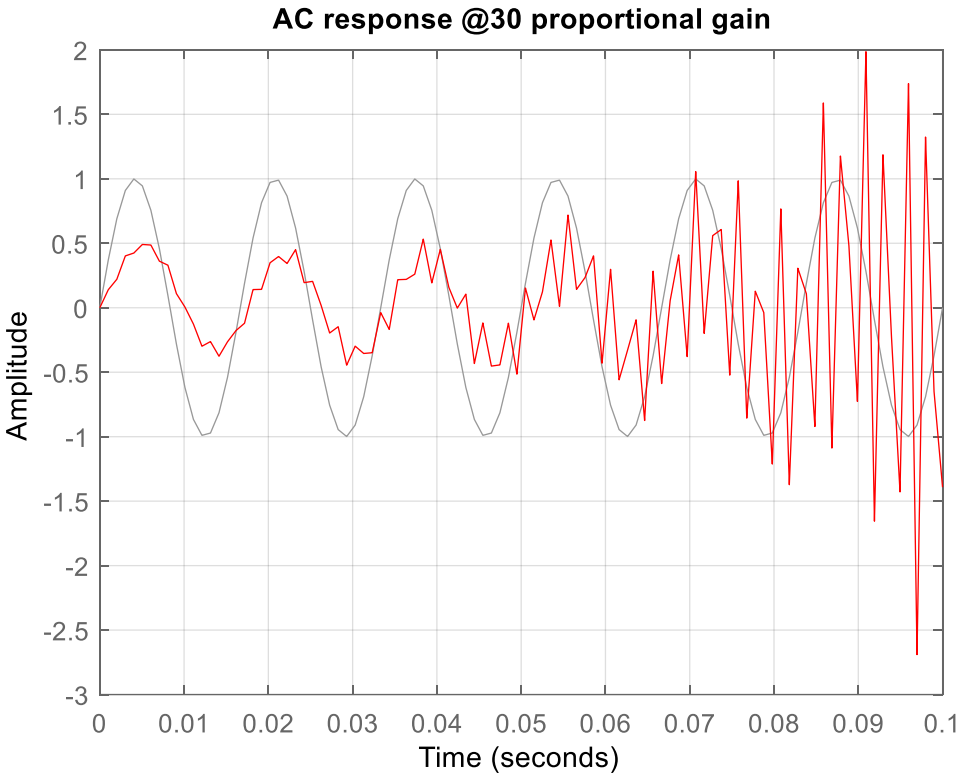

Figure 5.37: Response for the PI controller for the output voltage with a gain of 30

Figure 5.37 shows a graphic illustration of what happens when a proportional-integral (PI) controller is used to manage a system's output voltage. The "gain," or parameter controlling the impact of the controller's action, has been set to a value of 30 in this situation. To further understand the influence and efficiency of the PI controller at this particular gain level in attaining the required output voltage control, refer to the figure.

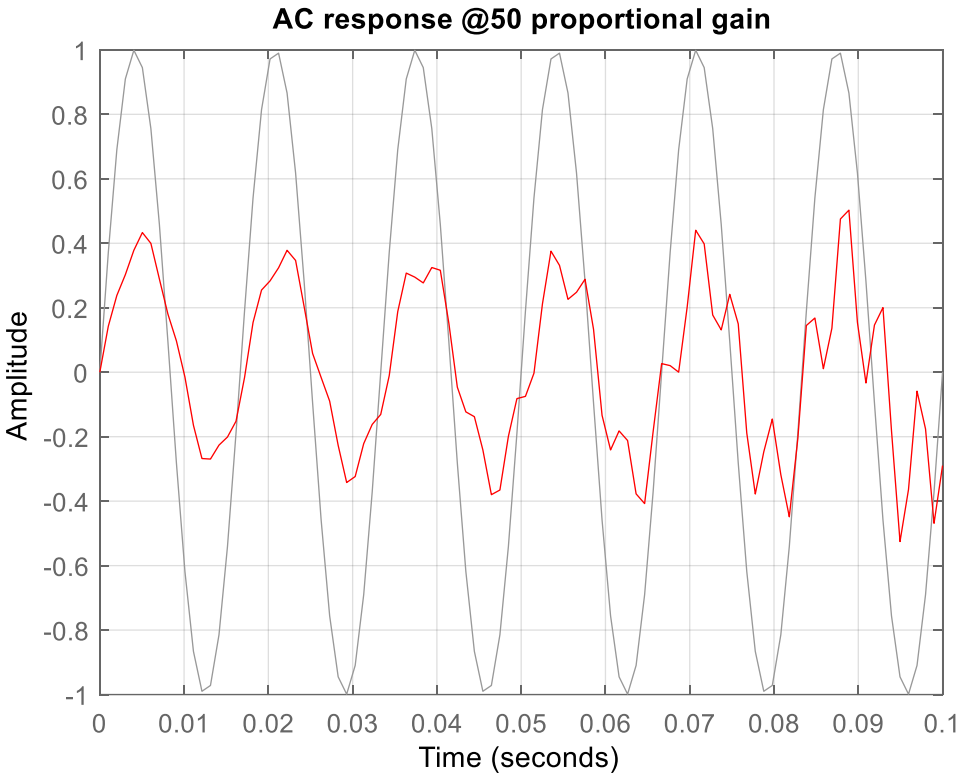

Figure 5.38: Response for the PI controller for the output voltage with a gain of 50

A graphical illustration of the behavior of a control system using a proportional-integral (PI) controller is shown in Figure 5.38. The output voltage of the system is the main subject of this image. It is noteworthy that the controller is set up with a gain coefficient of 50. The output voltage changes over time under the effect of the PI controller with the specified gain value, as shown in the graph, which graphically represents the dynamic response of the control system.

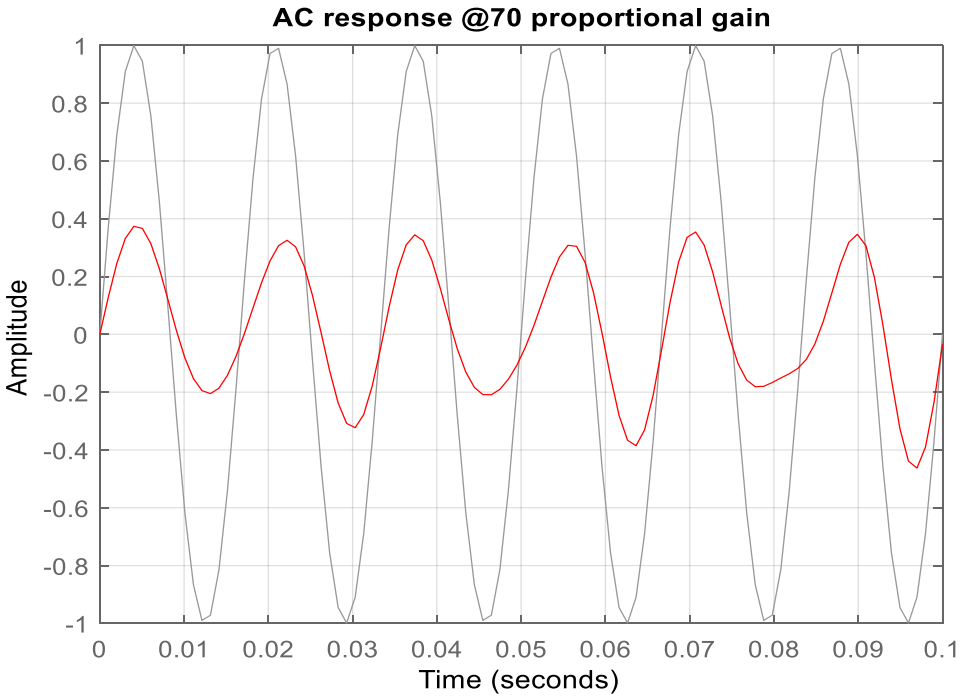

Figure 5.39: Response for the PI controller for the output voltage with a gain of 70

In particular, Figure 5.39 shows how the Proportional-Integral (PI) controller responded to an output voltage with a gain value of 70. This graph shows how the system responds to the PI control method with this specific gain level in terms of voltage regulation. Where the PI controller, set up with a gain of 70, regulates and maintains the output voltage in response to changing circumstances, therefore describing its regulatory effect on the controlled variable.

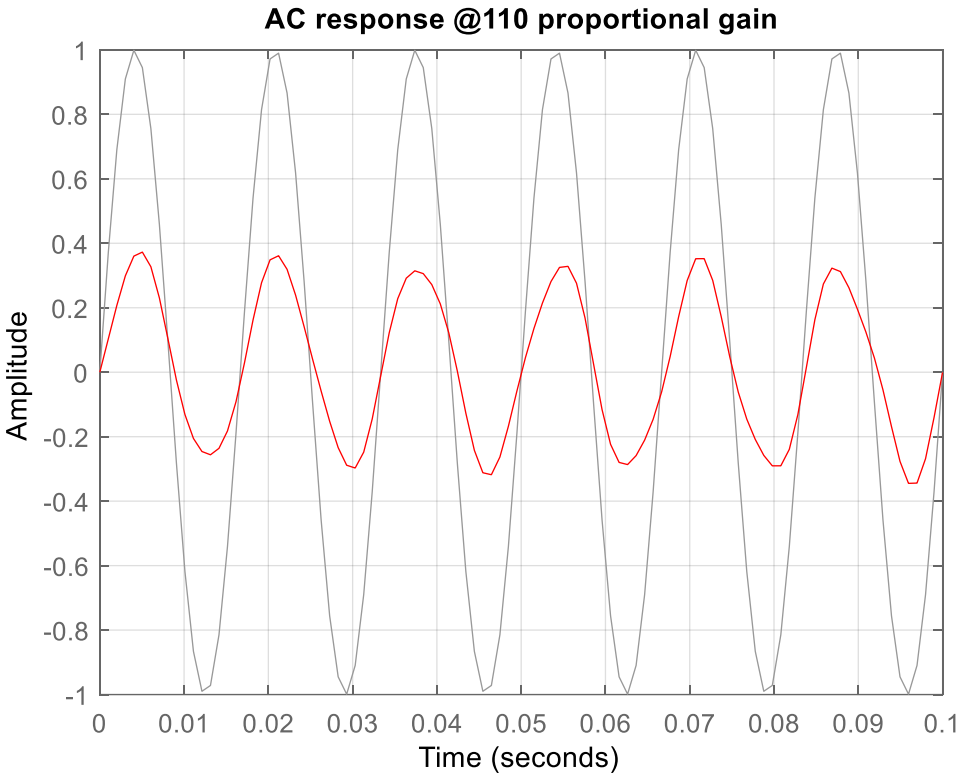

Figure 5.40: Response for the PI controller for the output voltage with a gain of 110

The results of using a proportional-integral controller with a gain of 110 to control the output voltage are shown graphically in Figure 5.40. The graph acts as a visual aid to understand how the controller affects the transient behavior of the system, illuminating how well it is able to maintain the target output under the existing circumstances.

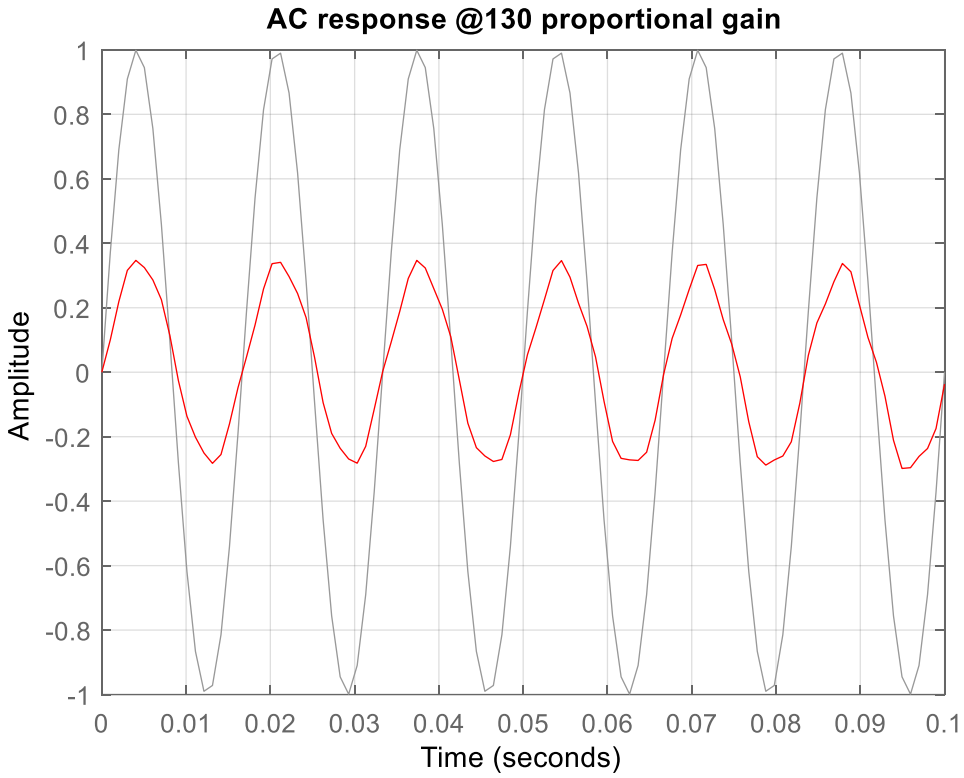

Figure 5.391*:* Response for the PI controller for the output voltage with a gain of 130

The response produced by the proportional-integral (PI) controller applied to the output voltage with a gain value of 130 is shown in Figure 5.41. This illustration captures how the system behaves in response to the supplied controller parameters, providing insight into the effectiveness of voltage regulation attained in this setup. The controller's ability to prevent deviations from the target output voltage is influenced by how well it amplifies the erroneous signal, as shown by the utilized gain of 130.

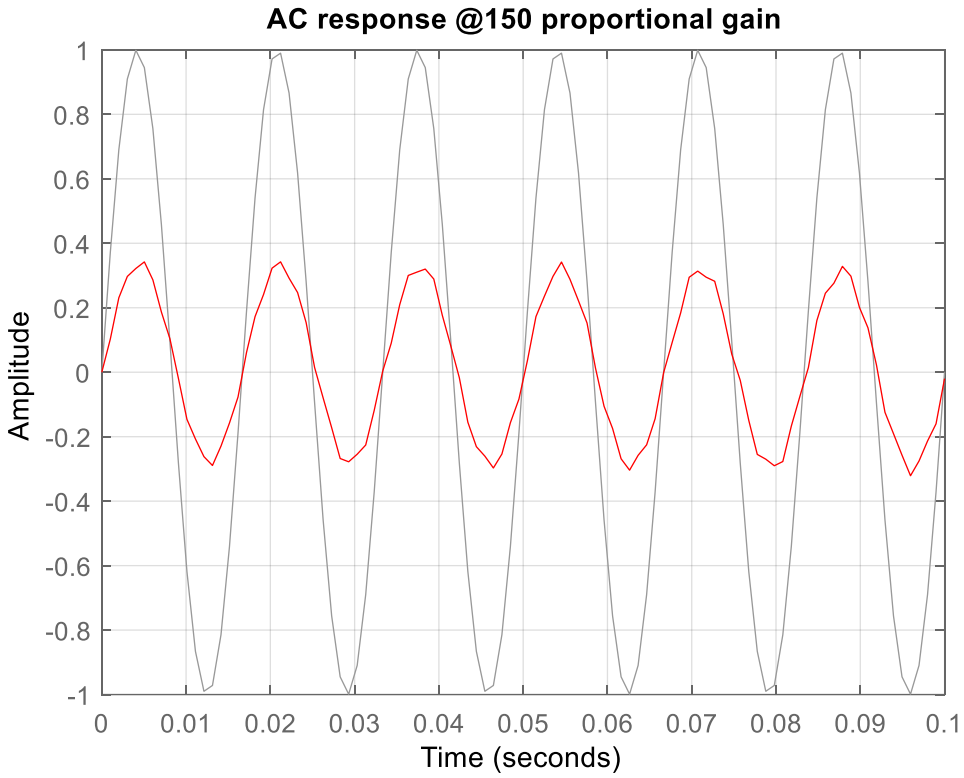

Figure 5.402: Response for the PI controller for the output voltage with a gain of 150

Figure 5.42, which is donated, serves to graphically illustrate the results of using a proportional-integral (PI) controller on the output voltage in a specific situation. The gain parameter is set to a value of 150 in the control setup. This exact gain setting affects the controller's responsiveness and overall effect on the system by determining the amplification factor by which the input signal is multiplied. The graphic probably depicts a plot or graph that highlights the consequences of the selected PI controller setup by showing how the output voltage changes over time or in response to an input stimulus.

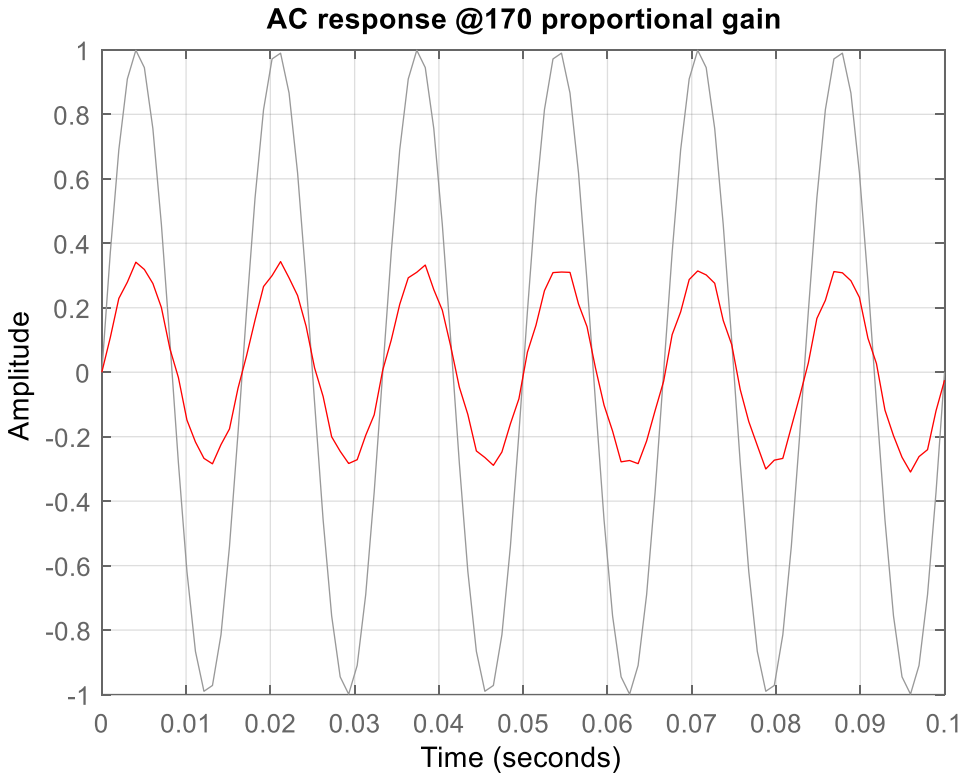

Figure 5.413*:* Response for the PI controller for the output voltage with a gain of 170

The response produced by the proportional-integral (PI) controller applied to the output voltage with a controller gain set at 170 is shown in Figure 5.43. The graph shows how the controlled system responds dynamically to changes or disturbances, with a focus on output voltage regulation. The controller's proportional contribution to altering the system's response is shown by the gain value of 170, which ensures a suitable trade-off between stability and corrective speed. The effectiveness of the PI controller in maintaining the intended output voltage level under the given control parameter is illustrated by this graph.

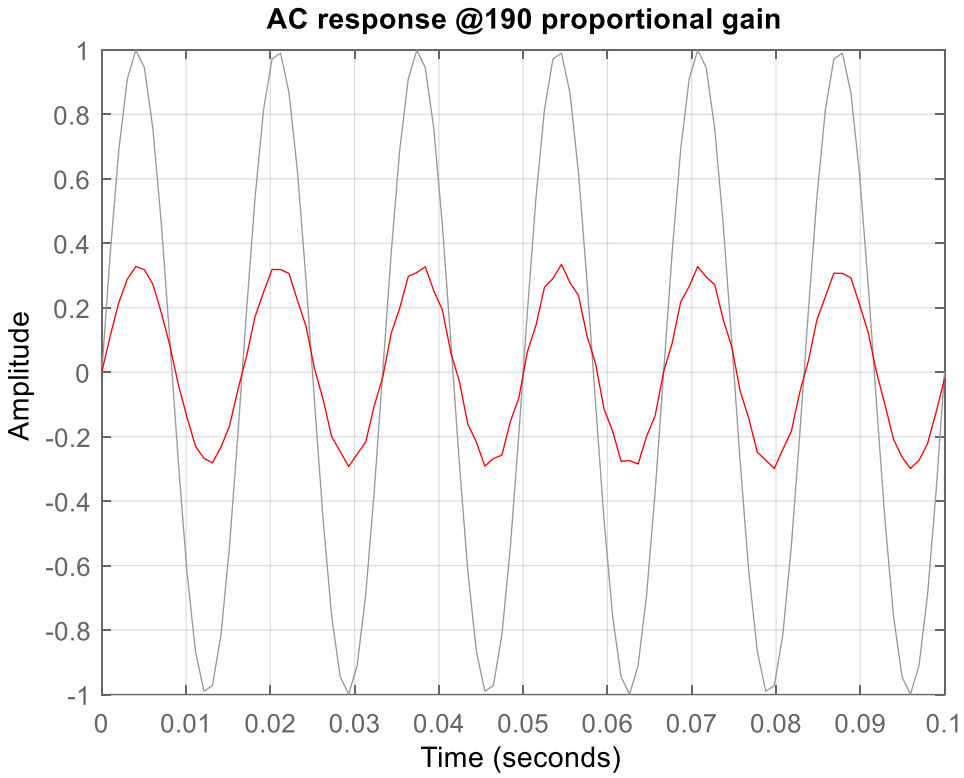

Figure 5.424: ***Response for the PI controller for the output voltage with a gain of 190***

A graphical illustration of the results of using a proportional-integral (PI) controller in the context of controlling the output voltage is shown in Figure 5.44. In the specific setup being examined, the PI controller is using a gain factor of 190. The visual representation of the control system's dynamic behavior and efficacy in response to these parameters is provided by the figure.

5.13 Chapter conclusion

The output current and voltage in the load connected to an LC filter was successfully studied. The mathematical formulation of the LC filter connected to the load for both the purely resistive load and variable LR load was completed through differential and Laplace formulations. The profiles or the responses for the output currents and output voltages to an AC input voltage in both types of loads were portrayed for both the open-loop and closed-loop transfer functions for the output current and voltage. The study showed that for the open-loop transfer function, as in just the mathematical model of the filter and load, the output current will be unstable as its amplitude will be growing exponentially in time. For the closed-loop response, both the output current and voltage will be stable. This was confirmed using the Ruth-Hurwitz method, which showed that the characteristic equation did not have

roots on the right-hand side of the s-plane. However, the output AC signal obtained presented distortions.

To solve this issue of distortions, control schemes were utilized, namely proportional and integral controllers. Starting with the proportional controller, the study showed that the output response was improving as the proportional controller gain (Kp) was increased. The shape of the output voltage was an AC signal of the sinewave type with the same frequency as the input signal. It is necessary to bear in mind that the control testing signal or the input signal was a sinewave of a frequency of 50 Hz. The LC filter was also designed to have a resonant frequency of 50 Hz. The proportional gain ranging from 30 to 100 showed a huge improvement in the voltage signal.

Next, a proportional integral (PI) controller was considered as was recommended in the proposal. The PI controller showed the ability to remove the distortions over a wide range of gain. Recalling that the integral gain is directly related to the proportional gain, the proportional gain ranging from 30 to 300. and the study showed that increasing the proportional gain led to a better output response. The PI controller was able to remove the distortions over this range of proportional gains, indicating that the integral gain was effectively compensating for any steady-state error introduced by the proportional controller. Moreover, the profiles of the output voltage showed that at the proportional gain of 30, the output voltage will be hugely distorted and tend to be unstable for just over 10 milliseconds. However, the profile will improve fast and become stable as soon as the proportional controller becomes 100. However, the more the proportional gain increased, the shape of the output signal lost the curves.

The conclusion was that the same proportional gain that was used to determine the integral time (T_i) should be maintained when simulating the output voltage. In other words, when the gain is lower than the integral time, there are going to be distortions, and the same will happen when it is higher. For this section, the control systems were successfully designed to mitigate the harmonic distortions and maintain the output voltage in a variable load stable.

Now that the energy management framework for distributed energy generators (DEGs) and the control of the output voltage in a variable load have been successfully realized and put in place, the study will then explore the implementation of DEGs. The case study focus is on supplying the rural area with electricity in a non-intermittent manner.

CHAPTER SIX

IMPLEMENTATION AND CONTROL OF DISTRIBUTED ENERGY SYSTEMS USING TYPHOON HIL: RURAL AREA CASE STUDY

6.1 Introduction

Distribution network developers have become increasingly interested in using renewable energy sources as an alternative to those that rely on the combustion of fossil fuels to produce power. Moreover, as fuel prices have rapidly increased in recent years, renewable energy sources have become more attractive. The advantages of the different renewable energy sources are that they are easy to use with lower environmental damage. Hence, it is a suitable option to fulfill the power demand throughout the day, especially during peak hours, and to implement this model in remote regions with limited access to grid electricity. It is more practical to integrate renewable energy sources such as wind and solar power into one system. Furthermore, some renewable sources depend on the availability of the sun and wind, which may negatively affect the demand due to shortages. Since this study aims to design a renewable energy system operating on renewable energy sources with an energy storage system for supplying rural areas with electricity, the proposed model consisted of PV and wind turbines with a battery, including a diesel generator. Hence, the system was designed using the schematic editor in the TYPHOON HIL software and uploaded to virtual HIL for simulation..

6.2 Related work

The traditional power system is distinguished by unidirectional power flows with enormous synchronous generators acting as the principal source of electricity generation. The shift toward more renewable energy has paved the way for new aspects, such as grid-based energy storage systems (Zhang et al., 2021) .Energy storage, voltage regulation, and state of charge management of energy storage systems are common obstacles for power electronic-based distributed generator system components. The complications grow as the number of decentralized sources, such as solar PV and wind integration, grows. As a result, many techniques, such as decentralized, centralized, distributed, hierarchical, and consensus-based solutions, have been developed to address control issues (Alam, 2022).

The evolution of the hybrid storage system throughout the last two decades, including its most current and historical research developments, is analyzed and categorized by (Khalid, 2019). Moreover, combining a lead-acid battery energy storage system (ESS) with supercapacitors is found to be promising option for dealing with increasing battery deterioration in isolated microgrids with variable electrical profiles. (Luo et al., 2021) offers a

novel control method, a new model of battery deterioration, and an economic viability analysis. Furthermore, microgrid management and control using PV panels, batteries, supercapacitors, and DC loads in the presence of variable solar radiation are proposed by (Louzazni et al., 2020).

In (Yan et al., 2021) presents a new coordinated control approach called over speed-while-storing control for PMSG-based WTG. The suggested control strategy alone adjusts the rotor speed to lower the machine-side converter's input power (MSC) amid modest voltage sags. When a significant voltage sag arises, the coordinated control system adjusts the rotor speed to the optimum to lower the MSC's input power to the most significant degree possible. In contrast, the excess power is captured by the supercapacitor energy storage (SCES) to minimize the peak capacity. Microgrids may operate on either an alternating current (AC) or direct current (DC) supply. Energy sources that generate DC electricity, including PV panels and a fuel cell, will require DC-AC conversion to link to AC microgrids' lines. Power from AC-generating sources like wind, hydro, and geothermal may need AC-DC-AC inverters for a more perfectly synchronized link to the network.

In the 1960s and 1970s, model predictive control or Receding Horizon Control (RHC) was developed in industrial control applications, particularly in the chemical sector. Then, this approach to control penetrated the academic and scientific realms, where it was appreciated by scholars. As a result, numerous publications have thoroughly defined and contrasted the forms of predictive controllers (Tricarico et al., 2022). Model protective control (MPC) is an intuitive technique for constraint-based systems. Therefore, predictive controllers are more popular than other controllers. The predictive controller generally sends the correct control signal to the converter by minimizing the cost function that ensures the correct system behaviour. At each sampling time, MPC calculates a succession of control signals that reduce the cost function, with the first signal being transmitted to the converter (Young et al., 2014).

The MPC has a significant impact on microgrid performance and system dependability. Therefore, compared with their control methodologies, a study of MPC-based control structures was conducted by (Razmi & Lu, 2022).

Furthermore, (Ardriani et al., 2021) present a DC microgrid system capable of powering remote areas, providing a novel DC microgrid system design for rural and isolated places without grid connectivity. The design’s modularity makes it portable and flexible. In addition, DC-interfaced points may be combined without synchronization, unlike AC-interfaced points, While in another study (Alturki & Awwad, 2021), a hybrid wind turbine /photovoltaic /biomass /pump hydro storage energy system was built and optimized in terms of technical, economic,

and environmental characteristics to meet the load demand at the least cost of energy (COE). The suggested system is compared against a hybrid PV/WT/biomass/battery-storage system based on prices, pollution, and efficiency. The suggested approach relies on hourly wind, radiation, and temperature data. Moreover, in a paper by (Lee et al., 2022) to solve the stochastic unit commitment (SUC) issue, optimum scheduling of microgrids with battery energy storage systems was suggested, taking into account the inconsistencies of WTs, PVs, and the load. To decrease the total operation cost (TOC) of the MG, the focus was on optimizing operation scheduling and reducing battery energy storage system (BESS) life deterioration. A study by (Kuźniak et al., 2022) was designed to ascertain the required power and BESS capacity for maximum shaving performance.

Supposing the grid operator implements this study's peak power management techniques, it may be able to provide grid flexibility services, including frequency regulation, voltage regulation, and demand response (demand-side response). These features will enable business owners to apply the peak shaving strategy by creating new income streams through BESS apps.

Stand-alone microgrids that include renewable energy sources have emerged as an effective energy option for energizing distant regions such as islands. Based on the requirements and regulations of a specific location, a microgrid's design incorporates many relevant aspects, including technical advancement, economic feasibility, and environmental implications. In a publication by Lee et al. (2021), the case study findings support the significance of addressing location factors and the effects of power system circumstances on effective microgrid construction. Therefore, microgrids, a cutting-edge idea for future energy systems, necessitate electrical and control structures and equipment for maximum functioning. Controlling distributed power sources to supply local demand is a fundamental and critical challenge for microgrids. Hence, to ensure the microgrid's economic performance, proper procedures must be utilized to regulate electronic power converters, which connect most distributed generation sources to the grid (Razmi & Lu, 2022).

As mentioned above, a microgrid is a decentralized cluster of electricity resources and loads that regularly run in combination and synchronization with the conventional broad-radius synchronous grid (microgrid). Nevertheless, it is also competent in separating from the interconnected grid and functioning independently in "island mode" as well as "off-grid" when technical or economic conditions dictate. Moreover, conventional energy systems are changing to include renewable energy sources as renewable technologies such as solar photovoltaics, wind power, and hydropower become more widespread (Abdulmohsen & Omran, 2022) **.** Distributed control techniques rely on the interactions between the units,

allocating the control task to various units considering the operation in assorted time frames. The idea is that the control hierarchy technique builds on primary, secondary, and tertiary controls where the demand for distributed approaches increases due to better security and reliability.

A distributed control system (DCS), or decentralized control system, is a computerized control system for a process in the plant, usually with many control loops, in which autonomous controllers are distributed throughout the system. Furthermore, it is a process-oriented system that uses closed-loop control. This control is the initial control level and has the fastest response time (Gulzar et al., 2022).The control duty ensures tracking voltage and frequency set points due to speed ramifications, power-sharing, and output control. Furthermore, subsequent changes to the system controller modes are based on this control level. Primary control depends on signals that are locally measured.

The design of an AC microgrid for use in rural areas is a outline the significant contributions made in this thesis.. Moreover, it presents an important control strategy for the microgrid, which the system tested and proved its ability to provide a significant amount of power for consumers.

6.3 Materials and Methods

In this section, the methodology used in this study is presented. Typhoon HIL software is used for simulation and testing. The proposed energy storage system utilizes an algorithm to monitor and control the load sharing distributed control system, which was implemented using the API Typhoon HIL software. This algorithm was chosen for its robustness and efficiency, and the distributed control system was designed to ensure that the load is shared between the sources. This approach was implemented to enhance the system's performance and reliability. Typhoon HIL was used for HRES' HIL implementation. Use of Typhoon HIL was made for the system's mechanical parts. A personal computer (PC) was used as the host platform to evaluate the functioning of the several devices and supervise the testing board's monitoring. With the aid of its products and resources, Typhoon HIL primarily focuses on the inspection and verification of power electronics. The use of the Typhoon HIL system was put into practice in this inquiry. A USB connection on the host PC is used to connect the Typhoon HIL system. The primary tools used in the Typhoon HIL system are the HIL Schematic Editor and the HIL SCADA. The Typhoon HIL Control Center provides access to these resources. Python may be used to build automated tests that make use of script editors and integrated development environments (IDEs) like Typhoon Test's to check the accuracy of the models. The model compilation and loading into the HIL SCADA testing environment are made easier by the Typhoon HIL Schematic Editor. In HIL SCADA,

the 'Model Settings' interface enables the real-time adjusting of model characteristics that are programmable and editable, such as controller gains, for external and internal hardware inputs.

The proposed system implemented in the HIL SCADA is shown below (Figure 6.1).

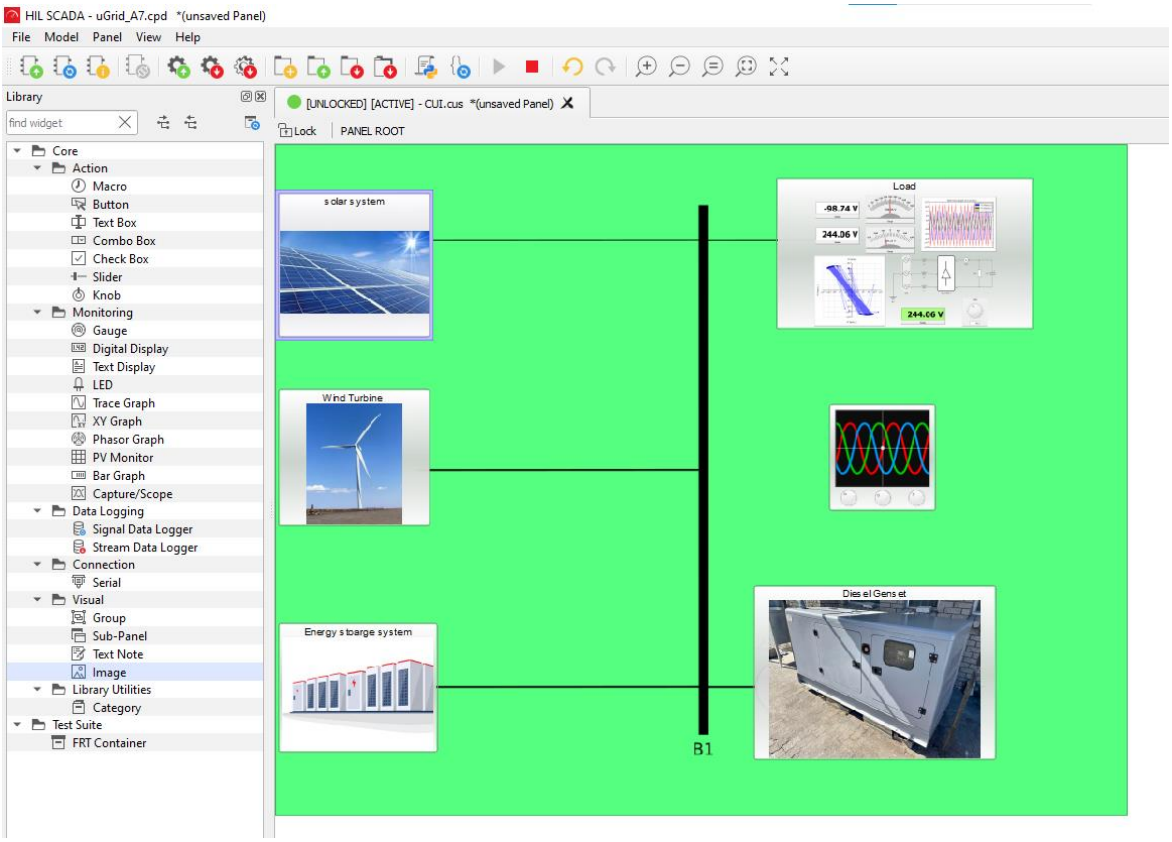

Figure 6.1: Overview of the proposed system in SCADA

Hence, the methodology involves several steps. First, the model is designed in the Schematic Editor of Typhoon HIL software. Then, the system is tested, and if it does not pass the test, it is sent back for further refinement. Once the model is finalized, it is uploaded into the HIL SCADA system, where it is run. The results are then exported to the HIL signal analyzer, where they are interpreted. The proposed energy storage system uses a load-sharing distributed control system algorithm that is implemented in Typhoon HIL software. This algorithm was selected for its robustness and efficiency, and it allows for the load to be shared between different sources. The following figure (6.2) shows the flowchart for this methodology:

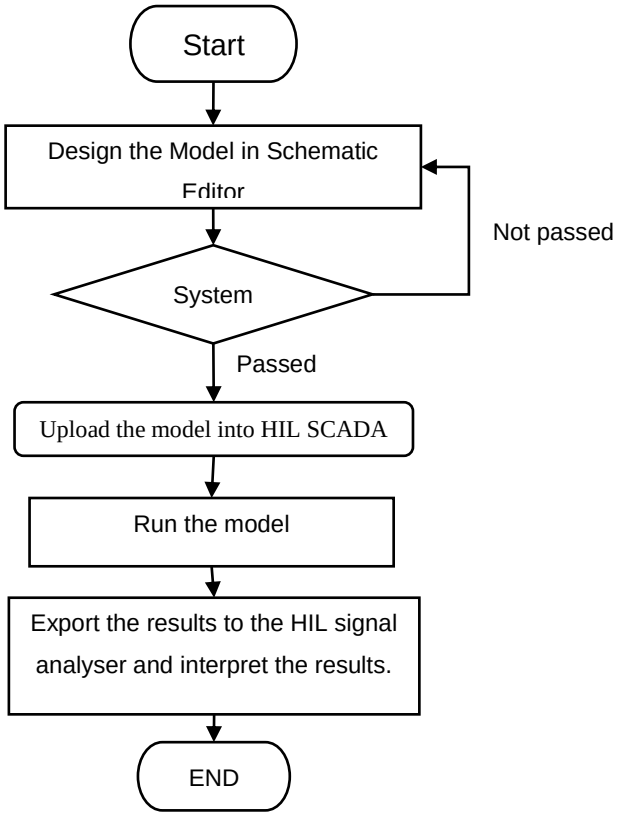

Figure 6.2: System design flow chart

6.4 Energy management system

The primary objective of the microgrid is to offer sustainable, cost-effective electricity through a dependable infrastructure. The advanced energy management system (AEMS) facilitates the microgrid's energy flow. In recent years, several studies have been conducted to examine areas such as energy sustainability, demand response methods, control systems, and energy management systems using various optimization approaches to improve the microgrid system (Gulzar et al., 2022).The energy management system (EMS) of the multi-energy microgrid (MG) can cut operational expenses and improve energy usage efficiency(Iqbal et al., 2020). Nonetheless, distribution generation consists of renewable energy sources such as biomass, photovoltaic, wind turbines (WTs), and fuel cells (FCs), as well as non-renewable energy sources such as generating units, naturally aspirated engines(Gulzar et al., 2022).

6.5 Islanded minigrid modelling and description

In this section, the model disruption and material used are discussed, and, this system is designed in Typhoon HIL software.

Since the islanded minigrid has to ensure self-sustenance, possible resources that can operate off the grid have been considered, namely solar, wind, generators, and energy storage systems. These energy resources have been allocated nominal powers, always minding the necessity of meeting the energy demand. The parameters used as inputs in Typhoon HIL can be seen in the tables below (6.1-6.4), presenting PV plant, wind plant, battery, and diesel generator parameters.

Table 6.1: PV plant parameters

Name	Value	Unit
Number of cells in series	72	
Nominal voltage	480	V
Nominal power	$250*10^3$	VA
Nominal frequency	50.0	Hz
Inverter switching frequency	1000.0	Hz
Nominal DC Voltage	1000	V
PV Plant area	1348	m^2
Efficiency	25	%
Execution rate	200	μs

Table 6.2: Wind plant parameters

Name	Value	Unit
Nominal voltage	480.0	V
Nominal power	$500*10^3$	VA
Nominal frequency	50.0	Hz
Inverter switching frequency	10000.0	Hz
Nominal DC Voltage	1000.0	V
Effective disk area	448	m^2
Wind turbine efficiency	75.0	%
Air density	1.225	Kg/m^3
Execution rate	Ts	S

Table 6.3: Battery parameters

Name	Value	Unit
Battery type	Lithium-Ion	-
Nominal voltage	1000.0	V
Capacity	10^6/1000.0	Ah
Initial SOC	80.0	%
Full charge voltage	116.0	%
Nominal discharge current	20	%
Internal resistance	0.025	
Capacity at nominal voltage	93.5	%
Capacity at exponential zone	85.0	%
Voltage at exponential zone	103	%

Table 6.4: Diesel generator parameters

Name	Value	Unit
Nominal Power	$2.2*10^6$	VA
Phase Nominal Voltage	480.0	V
Nominal electrical frequency	50.0	Hz
Shunt snubber load percentage of nominal power	5	%
Execution rate	200	μs

6.6 Operation mode and simulation

For the solar and wind plants, the maximum power is made available for the load through the maximum power tracking algorithms, which set the output at a maximum threshold. As such, there is no need for further control strategies or communication protocols to monitor the power. However, in case of abnormal situations, such as the unexpected low demand or the unavailability of the energy system that may result from operations such as maintenance in the network, the PV and WT systems are set to operate in low-efficiency mode by isolating suitable PV arrays and WTs to ensure the required power is available for the load.

Diesel generators are to be operated in droop control mode to maintain firm control over the voltage and the network frequency. Alternatively, they can be operated in active

power/reactive power control mode, thus providing the power parameters by the centralized controller or with the energy storage system including constant voltage/ frequency control with the inclusion of accessible droop parameters and active/reactive power control. Figure 6.3 shows the result screen as well as the experimental setup.

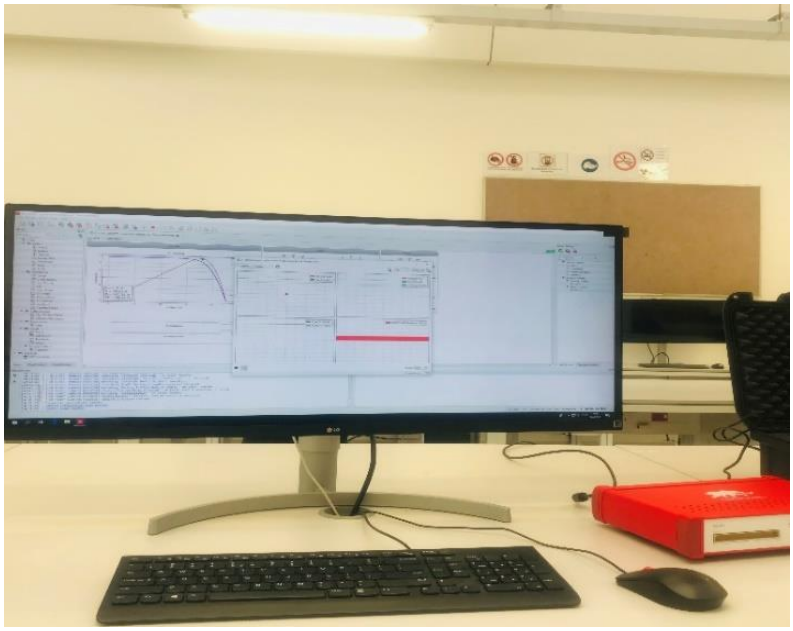

Figure 6. 3: Experimental and results of simulation

When operated in diesel mode, diesel generators are under droop control where the voltage and frequency decreases while the energy storage system is in active-reactive control. In this mode, when energy output exceeds the load demand, diesel generators run at their minimal loading state, which is generally 25% of rated power while the energy excess is channelled to the storage system.

When the diesel mode is off, the storage system is controlled by the constant-voltage-constant-frequency (CVCF) system as the reference source, creating the microgrid voltage and frequency and reacting to instantaneous power fluctuations. The most crucial aspect of this coordinated control method is that each diesel generator may be switched off if the energy stored in the energy storage system and renewable energy sources sufficiently meets the load demand, especially during the day as sunlight might be available throughout. This can help optimize the exploitation of renewable energy sources while minimizing fuel use.

The power system design consisting of the PV dynamic model, a WT, an energy storage system, and a diesel generator was created in Typhoon HIL for this study. The design is composed of photovoltaic panels, a DC link capacitor, a three-phase pulse-width modulation (PWM) inverter, and an LC filter. The model incorporates the MPPT algorithm as PV systems function as current sources, and PV inverters are operated in the grid-feeding or active/ reactive (P/Q)option.

The wind power system's dynamic model contains a WT, a permanent magnet synchronous generator (PMSG), a full-scale back-to-back converter made up of a machine-side converter (MSC) DC link capacitor, and a grid-side inverter (GSI) operated in grid-feeding mode. A battery bank, a PWM converter, a DC link capacitor, and an LC filter are the elements that make up an energy storage system. Both the voltage and current are controlled using a closed-loop control structure.

The generator's architecture consists of the following major components: a synchronous machine to convert mechanical energy into electricity, a diesel engine to produce the mechanical energy, a governor, and an excitation system that directs DC to the winding of the asynchronous machine. The governor processes the angular speed of the diesel engine to ensure that the electrical frequency is maintained at a predetermined value irrespective of the fluctuations observed in the load demand. An automated voltage regulator (AVR) typically regulates the generator output voltage to a predetermined set point value in an excitation system.

The simulation accuracy of the dynamic response of diesel generators primarily depends on the model implementation and parameter selection of synchronous machines and their controllers. Several standard models are generally incorporated in the built-in library of simulation tools for power systems. Models of synchronous machines get their dynamic properties from the generator datasheets. Operation scenarios are presented in Table 6.5 below.

Table 6.5: Scenarios

Scenario	Condition
1	With load and high wind speed
2	With Load and Low solar radiation
3	With Load and High solar radiation
4	With Load and Low wind speed

Figure 6.4 shows the results when the load connected while high wind speed,

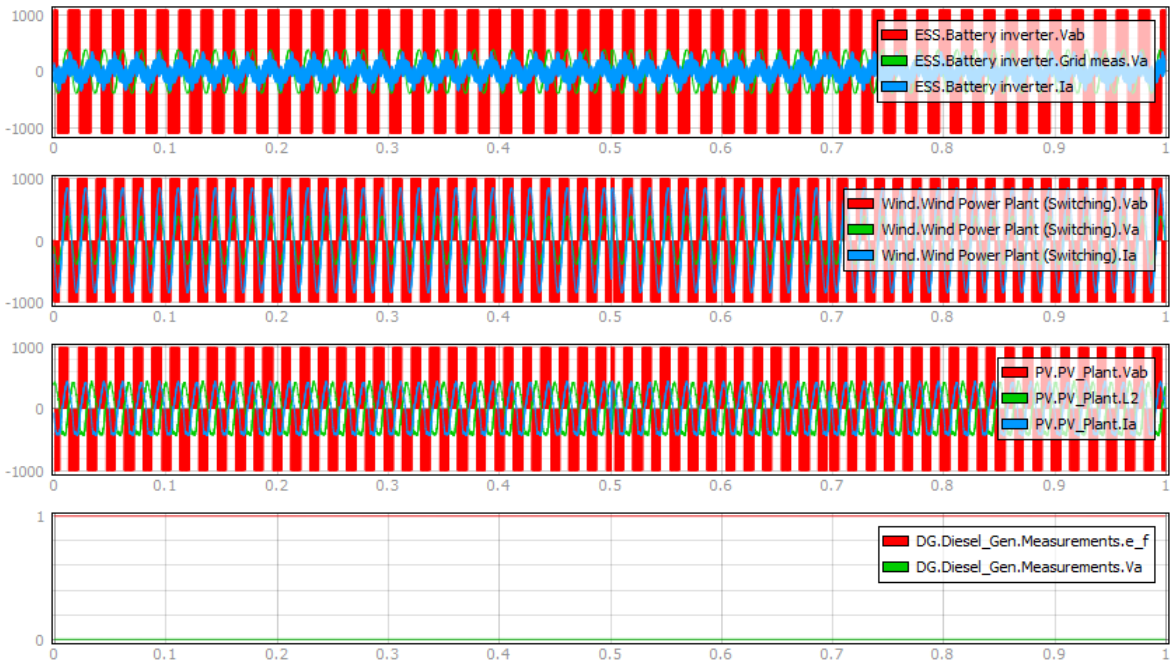

Figure 6.3: With load and high wind speed

Scenario 1 focuses on a particular situation involving the production and consumption of electricity in which the incident solar energy on the panels is set at 1000 watts per square meter (W/m2). sun irradiance is a measure of how much sun energy actually reaches the solar panels. 24 meters per second (m/s) is a strong wind speed in this situation. The efficiency of wind turbines is directly impacted by wind speed, making it a crucial factor in the production of wind energy. The outdoor temperature is 25 degrees Celsius (°C). Temperature has an impact on the efficiency of wind and solar power systems. Solar panel efficiency may slightly decrease as temperatures rise. When subjected to the required sun irradiance and temperature conditions, solar panels transform solar energy into electricity.

Figure 6.5 shows the results when the load was connected while the solar radiation was low.

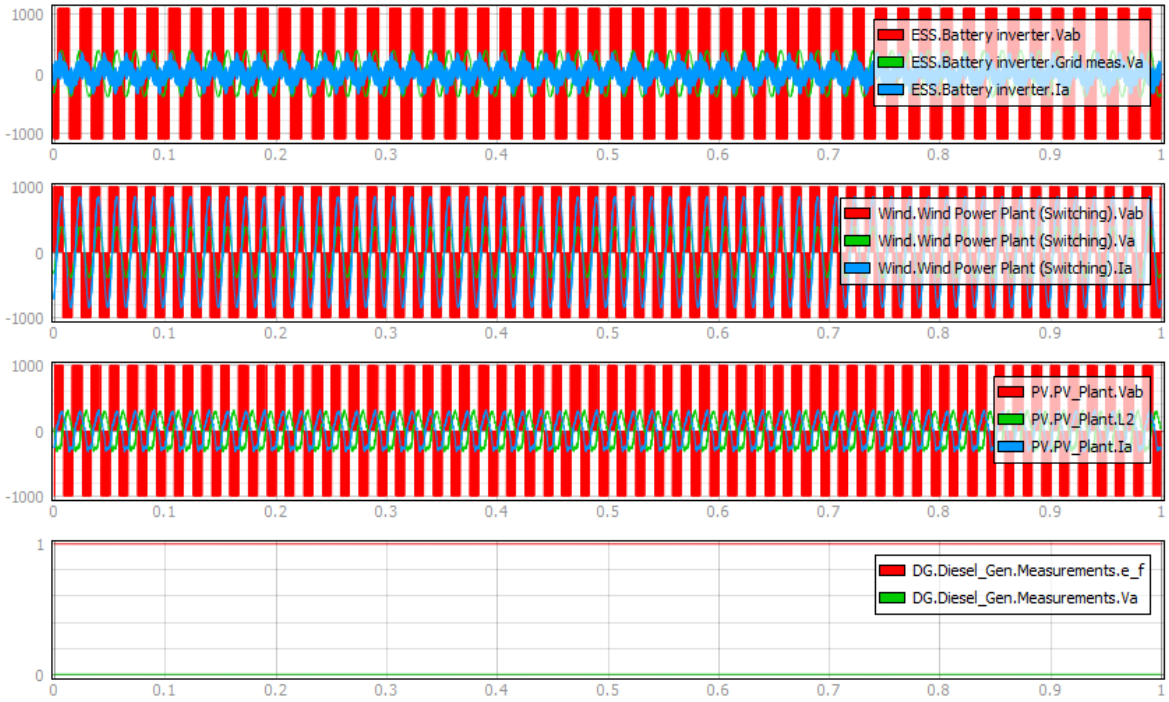

Figure 6.4: With load and low solar radiation

Figure (6.5) depicts two fundamental renewable energy sources in this scenario: sun and wind. However, due to inclement weather or other factors, the sun's irradiance has reduced to 500W/m2, while the wind speed has decreased to 20 m/s. As a result, the energy generated by these renewable sources must be increased to meet the system's electrical needs. The main purpose in this situation is to ensure that load demand, which reflects the electricity necessary to power different devices and appliances, is still met despite the decline in solar and wind energy output. To do this, an energy storage system and a diesel generator are utilized.

Figure 6.6 shows the results for the energy system when the load was connected, and the wind speed was low.

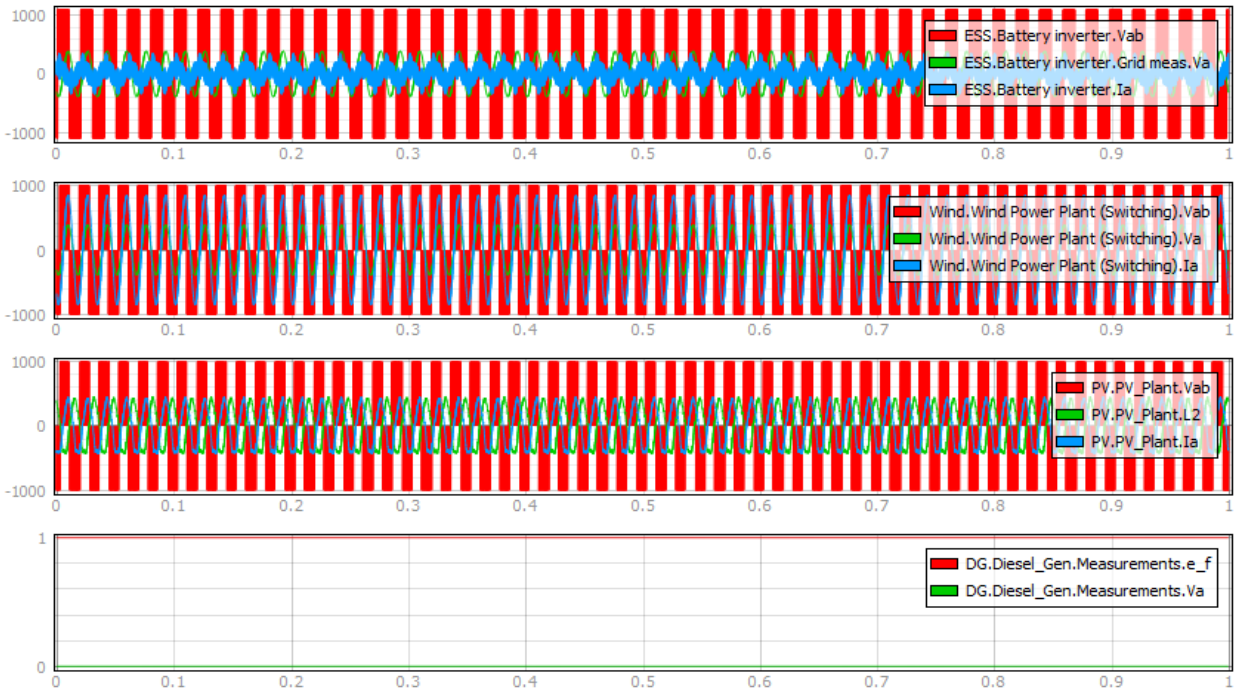

Figure 6.5: With load and high solar radiation

The third scenario includes a load and strong sun radiation; in this case, the wind speed is increased to 25 m/s, and the solar radiation is set at 1500 w/m2. With the sun's irradiance adjusted to 1500W/m2, solar panels would operate at maximum capacity and generate a sizable amount of power. As a consequence, solar power would contribute more to the overall energy mix, reducing reliance on other traditional sources of electricity like fossil fuels.

Figure 6.7 shows the scenario where the minigrid is connected to the load while the wind speed is low.

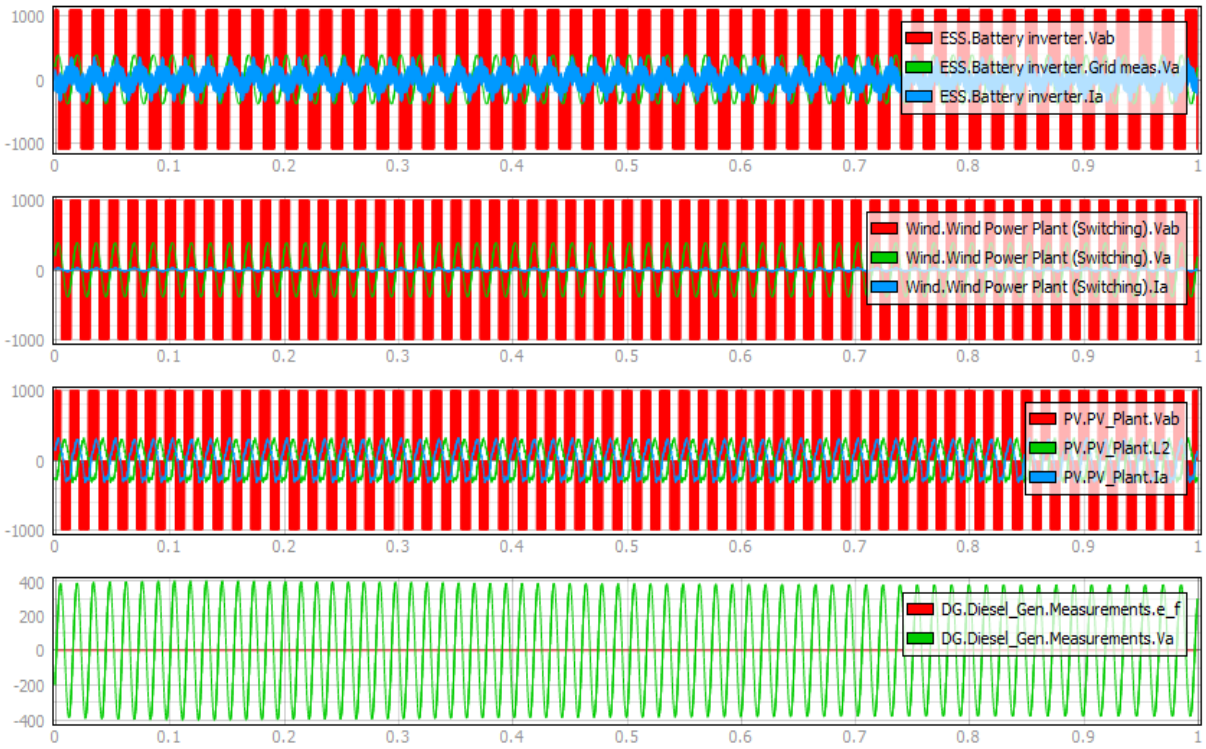

Figure 6.6: With load and low wind speed

In this case, the diesel generator is turned on to deliver electricity to the load when the load is low and the wind speed is reduced to 5m/s and the sun irradiation is 500w/m2. The output power of the wind turbine will be significantly lower at five m/s wind speeds than it will be at higher wind speeds. This drop in wind energy production could not be enough to meet the entire demand. Solar Energy:

The solar panels may still produce power, although at a lower rate than during times of higher sun irradiance levels, as evidenced by a solar irradiance of 500W/m2. Solar electricity generation will increase the total amount of power produced.

6.7 Chapter conclusion

The proposed strategy was applied toa model of a community microgrid. The simulation results showed that the proposed strategy is able to initiate power exchanges when one or more power sources experience a power shortage while maintaining the rated frequency and voltage for each participating microgrid and economically optimizing the exchanged power. Therefore, it allows for a community microgrid's economic, efficient, and flexible coordination.

CHAPTER SEVEN

7.1 CONCLUSION

This study focused on the "design and implementation of power converter minigrids for embedded generation" in order to address electricity access issues commonly encountered in off-grid, remote, and rural areas. In these regions, renewable energy resources were found to be the most suitable option due to their availability and cost-effectiveness. Solar energy, wind energy, generators, and energy storage systems were considered as potential resources for energy supply, which could be integrated into micro or minigrid configurations.

The primary objective of this study was to provide continuous and uninterrupted power to rural populations, despite the intermittent nature of solar and wind-based energy sources, which are influenced by weather conditions, time of day, seasons, and geographical location. Achieving a consistent energy supply required an interactive controller that could manage the various energy sources. This involved the need to connect one power source while disconnecting another, ensuring sufficient energy availability to meet the load requirements.

An islanded minigrid refers to a minigrid operating in conditions where the energy supply and demand are self-regulated. Given the intermittent nature of the resources involved, a reliable and efficient control strategy was essential to deliver an uninterrupted power supply in the aforementioned areas. This study aimed to develop such a control strategy. The objectives were twofold: firstly, to manage the energy available from different sources at any given time in relation to the variable load demand throughout the day, and secondly, to ensure that the power (voltage and current) delivered to the load, which may also vary, remained free from harmonic distortions.

The methodology employed in this study consisted of several steps. First, a literature review was conducted on distributed energy resources and energy management and control systems specifically related to islanded minigrids. The literature review covered concepts, behaviours, modelling, and simulations of distributed energy resources. For the solar energy source, the photovoltaic effect and the influence of weather conditions, time of day, and season were elucidated and modelled. Additionally, the voltage source inverter was investigated, modelled, and simulated. MATLAB was used as the integrated development environment for simulating and creating profiles for these energy sources.

Overall, this study aimed to design and implement power converter minigrids for embedded generation, addressing electricity access issues in off-grid, remote, and rural areas. The focus was on achieving continuous power supply through an efficient control strategy, managing variable load demand and ensuring the delivery of high-quality power to the load.

The methodology involved reviewing literature, modelling and simulating distributed energy resources, and utilizing MATLAB as the simulation tool.

In relation to wind energy, wind turbines (WTs) have been extensively studied in terms of different wind technologies, including horizontal and vertical WTs. various classifications of WTs have been examined, considering factors such as speed, speed control, and generator type. The discussion encompassed fixed-speed WTs and those capable of accommodating variable wind speeds, highlighting their respective advantages and potential drawbacks. The review also encompassed wind speed control, wherein both passive and active control techniques were detailed. Continuing the discussion on WTs, an exploration of generator technology focused on asynchronous induction generators and synchronous permanent magnet generators.

Once the classification and technology underlying WTs were understood, the study delved into the process of converting wind energy into electrical energy. This entailed breaking down the entire turbine system, including both aerodynamic and electrical components. The aerodynamic block addressed the mechanical energy derived from the wind and its transmission to the turbine through the blades, which is then processed via gears. On the other hand, the electrical block focused on converting the mechanical energy, obtained from the gears, into alternating current (AC) through a generator.

To ensure the accurate operation of the aforementioned blocks, precise knowledge of the input wind speed and AC output is necessary. Accordingly, the mathematical formulation of the mechanical input energy was presented, considering variables such as wind speed, WT coefficient of performance, and incoming wind mass. Additionally, the modelling of torque at the primary and secondary gears was discussed, taking into account blade topology, relevant angles, tip-to-seed ratio (TSR), and the number of teeth.

Following the discussion on WTs, generators were examined in terms of fundamental concepts, types, and functionalities. Given the similarity between the electrical processes of generators and WTs, this aspect was thoroughly elucidated in the generator section. Faraday's law was reviewed, emphasizing its significance in understanding the generation of electricity. Various generator types were also explored, with classifications based on rotating components (armature or magnetic field), number of phases, and rotor poles, all of which were appropriately modelled as required.

Subsequently, energy storage systems were introduced, encompassing various technologies such as pumped-hydro storage, thermal energy storage, and a range of batteries. Among these, batteries emerged as the most widely employed solution in the field of energy storage, with different variations explored, including lithium-ion, lead-acid, and flow batteries.

Additionally, alternative energy storage methods were discussed, namely hydrogen and flywheels.

The literature and modelling of energy systems then delved into the examination of a voltage source inverter (VSI). It is important to emphasize that the VSI holds significant relevance in energy systems, particularly those involving solar and direct current sources, as it enables the conversion of DC to AC. The study commenced by presenting distinct categories of VSIs, subsequently providing an in-depth explanation of their underlying concepts and operational principles. The discussion encompassed both single-phase and three-phase VSIs, along with their respective switching states and sequences.

Mathematically, the VSI was described in terms of switching matrices, Fourier representations, and mathematical expressions representing all the switching states. Due to limitations inherent to the switching devices, which are constrained by a limited frequency operation, the output waveforms from the VSI exhibited nonlinearity. As a result, further processing was required to rectify the irregularities present in the AC signal intended for the load.

The subsequent focus of the literature review was the investigation of total harmonic distortions. This aspect was deemed relevant due to the response of the VSI output when the load contains nonlinear elements or inductive components. The theoretical foundations and mathematical formulations of harmonic distortions were presented, accompanied by graphical representations, within this study. Following this, a review chapter was dedicated to exploring control strategies for distributed energy systems, specifically tailored to the types of energy sources examined in this study.

Chapter Three provides an overview of control strategies for micro and minigrids, aiming to gather existing knowledge in this field and identify potential contributions of this study. The focus of the review was on energy management, exploring centralized, decentralized, and distributed control architectures. Additionally, traditional control systems such as proportional, integral, and derivative controllers were discussed. The insights gained from this section played a crucial role in designing the energy management system for distributed renewable energy sources connected to a variable load, as presented in Chapter Four. Moreover, this knowledge facilitated the effective control of power output quality in the presence of dynamic loads.

Chapter Four presents the design and simulation of a centralized energy management system using the MATLAB integrated development environment. An algorithm was developed to demonstrate the system's capability to effectively operate the minigrid, regardless of the solar and wind plant levels at any given time. Additionally, the algorithm

considered the storage system, which relied on the level of discharge at specified times. Its objective was to prioritize the optimal utilization of available energy and ensure that the variable load's demand was met.

The algorithm was designed under the assumption that it would manage a minigrid catering to 200 households, with each household consuming approximately 12 kWh, equivalent to a power of 1 kW. Furthermore, it was assumed that each plant within the minigrid had the capacity to fulfil the load demands at any time of the day, implying that all plants were rated at 200 kW each. This assumption aimed to guarantee that at least one energy source could independently sustain the minigrid's operation, facilitating thorough testing of various power delivery scenarios to the variable load. The peak power demand of the variable load was set at 200 kW.

To assess the algorithm's functionality, the initial scenario involved determining whether the PV plant alone could meet the load demand at a specific time of day. If this condition was satisfied, only the PV plant would be activated or connected to the load, while the remaining plants remained inactive. Any surplus energy beyond the load demand would be stored in a battery system to maintain energy balance. Conversely, if the PV plant could not meet the load demand, the algorithm would instruct the activation of an additional energy source until the load demand was fulfilled. Any excess energy would then be stored in the battery system. In the event that all the plants fell short of power to supply the load, the algorithm would command the utilization of the battery bank to fulfil the load demand.

When defining the characteristics of different power plants, their typical behaviour throughout the day was taken into account. In the case of a photovoltaic (PV) plant, a Gaussian-shaped power profile was considered. This means that in the morning, the power output is at its lowest level, close to zero at sunrise. It reaches its peak value of approximately 200 kW at noon and gradually decreases towards the evening or sunset. For a wind plant, it was assumed that the power profile fluctuates around 200 kW during the day. In the case of a generator, a steady power output of 200 kW was considered, which was also assumed for the initial power of the battery storage.

All the power profiles for the plants were pre-defined using the MATLAB IDE. These profiles could be accessed at any time during the day to check the power levels, compare them with the load demand, and simulate the necessary actions, such as connecting or disconnecting a plant, or storing excess energy in the battery system. The algorithm was designed to be user-friendly, allowing users to enter the desired time and display the power profiles of all the plants at that specific time, along with the corresponding power figures in kilowatts.

In conclusion, the algorithm proved to be effective in simulating the centralized control of the minigrid, ensuring its self-regulation and self-sustainability in terms of providing a continuous and reliable power supply to the load. The algorithm provided the capability to command the activation or deactivation of one or more plants, as well as the ability to store excess energy for future use. Additionally, the algorithm was designed with a user-friendly interface, displaying pop-up messages to request user input and present the output accordingly.

In Chapter Five, the study focused on assessing the quality of power received by the load, which, in this particular case, was nonlinear due to the inclusion of an inductive element in addition to the resistance. Based on the findings from the literature review, it was determined that the presence of such a load would result in harmonic distortions in the output power, leading to motor vibrations, speed instability, and potential damage to appliances connected to the network. Furthermore, due to the utilization of a VSI for DC-AC conversion of power from the PV plant, the resulting voltage was not a perfect AC signal and introduced harmonic distortions.

To address these issues, an LC filter was proposed to be connected between the LC filter and the load, ensuring that the desired voltage was available at the output. However, considering the presence of a variable load, additional control measures were necessary to regulate the output power. The study examined the output network of a single phase, with the findings assumed to be applicable to the remaining two phases of the three-phase system. The investigation commenced by examining the network's performance without implementing any control scheme.

The backend network comprised an LC filter and an LR load, which represented a variable load. The network's performance was evaluated by first studying and designing the LC filter. The filter was initially modelled, and its responses to the AC input signal were analyzed. The resonance frequency of the signal was set at 50 Hz, as it is a commonly used network frequency. Although the study of the LC filter was conducted generally, its performance was evaluated with respect to the resonance frequency of 50 Hz. The chosen values for achieving this resonance frequency were a 3.3 H inductor and a 2.2 µF capacitor.

The network's performance was systematically examined by formulating the mathematical expressions for the network in both the time and s-domain. The stability and quality of the output current or voltage were investigated under uncontrolled conditions and then under controlled conditions. Subsequently, a control system was proposed to attain the desired output signal. The study utilized both open-loop and closed-loop transfer functions as starting points to determine the necessity of control. It is worth noting that the transfer functions were found to be of third order.

Initially, the study focused on a purely resistive load, revealing that there was no need for controlling the output power as the voltage and current were already well-regulated. This conclusion was supported by the responses to step inputs, which demonstrated a stable and undamped output, as well as the response to AC input, which exhibited steady behaviour with a brief transition. Consequently, the study proceeded to investigate the variable load scenario.

The investigation of the LR load demonstrated that the response of the open-loop system to a step input resulted in unstable and exponentially growing current and voltage. As a result, the closed-loop system with unit feedback for both current and voltage transfer functions was examined. The responses indicated stable but distorted signals. The AC output displayed significant levels of distortion, requiring further processing, while the response to a step input exhibited an under damped signal.

The stability study was verified using the Routh-Hurwitz method, which demonstrated that all the roots resided on the left-hand side of the s-plane. In order to address the concerns related to signal distortions, the proportional-integral (PI) controller was considered. Initially, employing the P control, it was observed that the signal exhibited improvements in terms of distortions and amplitude level as the proportional gain was increased. Proportional gains of 100 and higher successfully eliminated distortions while maintaining the desired signal level, specifically with reference to the step input.

Subsequently, transitioning to the PI controller, the integral time constant, Ti, was initially determined by applying the Ziegler-Nicholson PI tuning method to ascertain the dead-time of the step response at a proportional gain of 100. At very low proportional gain values, the responses to the AC input displayed significant distortion, but improved considerably as the proportional gain reached 100. However, beyond this threshold, the AC output gradually reverted back to experiencing distortions. Consequently, it was concluded that the proportional gain used for calculating the dead-time should align with the proportional gain utilized by the PI controller. Stated differently, if the dead-time was computed at a proportional gain of 100, the PI controller would perform optimally at the same proportional gain.

Chapter Six focused on the design and implementation of a distributed energy system for supplying energy to rural areas. The system utilized integrated software called Typhoon HIL, where HIL stands for hardware in the loop. To fulfil the energy demands, a combination of PV and wind plants, along with a generator and energy storage batteries, was utilized. The specifications of these components were carefully determined. Various operational scenarios were considered to assess the performance of the designed system.

The setup comprised a 250 kVA PV plant, a 500 kVA wind plant, a 1 MAh storage battery system, and a 2.2 MVA generator. The selected scenarios encompassed situations such as no load connected to the minigrid, low solar radiation with the load connected, high solar radiation with the load connected, and the load being on with low wind speed. Despite the supply fluctuations, the minigrid consistently functioned and provided a stable power supply to the load throughout all scenarios.

The research successfully addressed the challenges associated with managing energy in an islanded minigrid. It introduced a novel algorithm and employed a PI controller in MATLAB IDE to regulate harmonic distortions in a nonlinear load. The simulation of an islanded minigrid was conducted using the real-time simulator, Typhoon HIL.

By carefully designing and implementing the distributed energy system, considering various operational scenarios, and employing advanced control algorithms, this study achieved its objectives in effectively managing energy supply in a rural setting. The utilization of Typhoon HIL as a real-time simulator further enhanced the accuracy and reliability of the research outcomes.

7.2 Recommendations and future work

The study successfully demonstrated the control of a multivariable minigrid through a novel algorithm. Future work could focus on expanding the experimental setup to include more renewable energy sources and evaluating the system's performance under various weather conditions.

To improve the accuracy of the simulation, future research could explore the use of more advanced control algorithms, such as model predictive control, and integrate them into the existing control system. Additionally, incorporating energy storage devices with different chemistries and capacities could enhance the system's flexibility and robustness.

To enhance the system's reliability and reduce the reliance on backup generators, it is recommended to incorporate advanced energy storage technologies such as advanced batteries or hydrogen fuel cells.

Future work could involve further optimization of the energy system design and performance by incorporating more advanced control algorithms, exploring the use of other renewable energy sources, and conducting field testing to validate the simulation results. Additionally, a cost-benefit analysis could be carried out to evaluate the economic viability of the proposed energy system for rural area energy supply.

Further research could also investigate the the potential of integrating other types of renewable energy sources, such as hydro or geothermal, to enhance the system's reliability and stability.

Collaboration with local communities, stakeholders, and policymakers is critical for the successful implementation and adoption of renewable energy systems in rural areas.

Lastly, extending the study to encompass real-world deployments of minigrids in rural areas would be beneficial in determining the system's feasibility and effectiveness in practical scenarios. This could include assessing the economic and social impact of implementing minigrids in remote regions and investigating potential policy interventions to promote their widespread adoption.

REFERENCES

Abdulmohsen, A. M., & Omran, W. A. (2022). Active/reactive power management in islanded microgrids via multi-agent systems. *International Journal of Electrical Power and Energy Systems*, *135*(June 2021), 107551. https://doi.org/10.1016/j.ijepes.2021.107551

Abualigah, L., Zitar, R. A., Almotairi, K. H., Hussein, A. M., Elaziz, M. A., Nikoo, M. R., & Gandomi, A. H. (2022). Wind, Solar, and Photovoltaic Renewable Energy Systems with and without Energy Storage Optimization: A Survey of Advanced Machine Learning and Deep Learning Techniques. *Energies*, *15*(2). https://doi.org/10.3390/en15020578

Al-Salloomee, A. G. S., Khosroabadi, S., & Albukariat, A. A. A. (2022). Study of power management of standalone DC microgrids with battery supercapacitor hybrid energy storage system. *International Journal of Electrical and Computer Engineering*, *12*(1), 114–121. https://doi.org/10.11591/ijece.v12i1.pp114-121

Alam, M. S. (2022). Power Management for Distributed Generators Integrated System. *Energies*, *15*(16), 5813. https://doi.org/10.3390/en15165813

Alturki, F. A., & Awwad, E. M. (2021). Sizing and cost minimization of standalone hybrid wt/pv/biomass/pump-hydro storage-based energy systems. *Energies*, *14*(2). https://doi.org/10.3390/en14020489

Alzahrani, A. M., Zohdy, M., & Yan, B. (2021). An Overview of Optimization Approaches for Operation of Hybrid Distributed Energy Systems with Photovoltaic and Diesel Turbine Generator. *Electric Power Systems Research*, *191*(September 2020), 106877. https://doi.org/10.1016/j.epsr.2020.106877

Arbetter, H., Erickson, R., & Maksimović, D. (1995). DC-DC converter design for battery-operated systems. *PESC Record - IEEE Annual Power Electronics Specialists Conference*, *1*, 103–109. https://doi.org/10.1109/PESC.1995.474799

Ardriani, T., Dahono, P. A., Rizqiawan, A., Garnia, E., Sastya, P. D., Arofat, A. H., & Ridwan, M. (2021). A DC Microgrid System for Powering Remote Areas. *Energies*, *14*(2), 493. https://doi.org/10.3390/en14020493

Badrzadeh, B., & Kingdom, U. (2004). Modelling wind turbine -generators for fault. *39th International Universities Power Engineering Conference, 2004. UPEC 2004.*, 634–638. https://ieeexplore.ieee.org/abstract/document/1492097

Bagheri-Sanjareh, M., Nazari, M. H., & Hosseinian, S. H. (2021). Energy management of

islanded microgrid by coordinated application of thermal and electrical energy storage systems. *International Journal of Energy Research*, *45*(4), 5369–5385. https://doi.org/10.1002/er.6160

Bagudai, S. K., Ray, O., & Samantaray, S. R. (2019). Evaluation of Control Strategies within Hybrid DC/AC Microgrids using Typhoon HIL. *2019 8th International Conference on Power Systems: Transition towards Sustainable, Smart and Flexible Grids, ICPS 2019*, 1–6. https://doi.org/10.1109/ICPS48983.2019.9067331

Bahrami, S., Mohammadi, A., Design, F., Implementation, L., Wolthusen, S. D., Wang, R., Wang, P., Xiao, G., Farhangi, H., Energy, I. E. T., Series, E., Fathima, A. H., Prabaharan, N., Palanisamy, K., Kalam, A., Mekhilef, S., Justo, J. J., Bevrani, H., Francois, B., … Mahmoud, M. S. (2017). Cooperative Synchronization in Distributed Microgrid Control: Advances in Industrial Control. In *Intelligent Microgrid Management and EV Control Under Uncertainties in Smart Grid* (Vol. 1, Issue April).

Balaguer, I. J., Lei, Q., Yang, S., Supatti, U., & Peng, F. Z. (2011). Control for grid-connected and intentional islanding operations of distributed power generation. *IEEE Transactions on Industrial Electronics*, *58*(1), 147–157. https://doi.org/10.1109/TIE.2010.2049709

Bidram, A., Davoudi, A., & Balog, R. S. (2012). Control and circuit techniques to mitigate partial shading effects in photovoltaic arrays. *IEEE Journal of Photovoltaics*, *2*(4), 532–546. https://doi.org/10.1109/JPHOTOV.2012.2202879

Bordons, C., Garcia-Torres, F., & Ridao, M. A. (2020). Model Predictive Control of Microgrids. In *Advances in Industrial Control Series*. http://link.springer.com/10.1007/978-3-030-24570-2

Buraimoh, E., Aluko, A. O., Oni, O. E., & Davidson, I. E. (2022). Decentralized Virtual Impedance- Conventional Droop Control for Power Sharing for Inverter-Based Distributed Energy Resources of a Microgrid. *Energies*, *15*(12), 4439. https://doi.org/10.3390/en15124439

Che, L., Shahidehpour, M., Alabdulwahab, A., & Al-Turki, Y. (2015). Hierarchical coordination of a community microgrid with AC and DC microgrids. *IEEE Transactions on Smart Grid*, *6*(6), 3042–3051. https://doi.org/10.1109/TSG.2015.2398853

Choudhary, P., & Srivastava, R. K. (2019). Sustainability perspectives- a review for solar photovoltaic trends and growth opportunities. *Journal of Cleaner Production*, *227*, 589–612. https://doi.org/10.1016/j.jclepro.2019.04.107

Emmanuel, B., Nsafon, K., Butu, H. M., Owolabi, A. B., Roh, J. W., Suh, D., & Huh, J.

(2020). Integrating multi-criteria analysis with PDCA cycle for sustainable energy planning in Africa : Application to hybrid mini-grid system in Cameroon. *Sustainable Energy Technologies and Assessments*, *37*(November 2019), 100628. https://doi.org/10.1016/j.seta.2020.100628

Fershalov, A. Y., Fershalov, Y. Y., & Fershalov, M. Y. (2021). Principles of designing gas microturbine stages. *Energy*, *218*, 119488. https://doi.org/10.1016/j.energy.2020.119488

Frederiks, E. R., Stenner, K., & Hobman, E. V. (2015). The socio-demographic and psychological predictors of residential energy consumption: A comprehensive review. *Energies*, *8*(1), 573–609. https://doi.org/10.3390/en8010573

Gerlach, A. K., Gaudchau, E., Cader, C., & Breyer, C. (2013). Comprehesive country ranking for renewable energy based mini-grids providing rural off-grid electrification. *28th European Photovoltaic Solar Energy Conference*, *September*, 24–28. https://reiner-lemoine-institut.de/wp-content/publications/1_Comprehensive_country_ranking/Gerlach2013.pdf

Gulzar, M. M., Iqbal, M., Shahzad, S., Muqeet, H. A., Shahzad, M., & Hussain, M. M. (2022). Load Frequency Control (LFC) Strategies in Renewable Energy-Based Hybrid Power Systems: A Review. *Energies*, *15*(10), 1–23. https://doi.org/10.3390/en15103488

Hazelton, J., Bruce, A., & MacGill, I. (2014). A review of the potential benefits and risks of photovoltaic hybrid mini-grid systems. *Renewable Energy*, *67*, 222–229. https://doi.org/10.1016/j.renene.2013.11.026

Hernández-Escobedo, Q., Saldaña-Flores, R., Rodríguez-García, E. R., & Manzano-Agugliaro, F. (2014). Wind energy resource in Northern Mexico. *Renewable and Sustainable Energy Reviews*, *32*, 890–914. https://doi.org/10.1016/j.rser.2014.01.043

Hossain, M. A., Pota, H. R., Issa, W., & Hossain, M. J. (2017). Overview of AC microgrid controls with inverter-interfaced generations. *Energies*, *10*(9), 1–27. https://doi.org/10.3390/en10091300

Ibrahim, S. A., Nasr, A., & Enany, M. A. (2021). Maximum Power Point Tracking Using ANFIS for a Reconfigurable PV-Based Battery Charger under Non-Uniform Operating Conditions. *IEEE Access*, *9*, 114457–114467. https://doi.org/10.1109/ACCESS.2021.3103039

Igwemezie, V., Mehmanparast, A., & Kolios, A. (2019). Current trend in offshore wind energy sector and material requirements for fatigue resistance improvement in large wind

turbine support structures – A review. *Renewable and Sustainable Energy Reviews*, *101*(November 2018), 181–196. https://doi.org/10.1016/j.rser.2018.11.002

Iqbal, A., Ying, D., De, T., Hayat, M. A., Saleem, A., & Jamal, R. (2020). Design and simulation for co-ordinated analysis of wind/solar with storage microgrid. *Energy Reports*, *6*, 1504–1511. https://doi.org/10.1016/j.egyr.2020.10.063

Jasiński, J., Kozakiewicz, M., & Sołtysik, M. (2021). Determinants of energy cooperatives' development in rural areas—evidence from Poland. *Energies*, *14*(2). https://doi.org/10.3390/en14020319

Johari, M. K., Jalil, M. A. A., & Shariff, M. F. M. (2018). Comparison of horizontal axis wind turbine (HAWT) and vertical axis wind turbine (VAWT). *International Journal of Engineering and Technology(UAE)*, *7*(4), 74–80. https://doi.org/10.14419/ijet.v7i4.13.21333

Karimi, Y., Oraee, H., & Guerrero, J. M. (2017). Decentralized Method for Load Sharing and Power Management in a Hybrid Single/Three-Phase-Islanded Microgrid Consisting of Hybrid Source PV/Battery Units. *IEEE Transactions on Power Electronics*, *32*(8), 6135–6144. https://doi.org/10.1109/TPEL.2016.2620258

Katiraei, F., Iravani, M. R., & Lehn, P. (2004). Micro-grid autonomous operation during and subsequent to islanding process. *2004 IEEE Power Engineering Society General Meeting*, *2*(1), 2175. https://doi.org/10.1109/pes.2004.1373266

Khalid, M. (2019). A review on the selected applications of battery-supercapacitor hybrid energy storage systems for microgrids. *Energies*, *12*(23). https://doi.org/10.3390/en12234559

Kimera, R., Okou, R., Sebitosi, A. B., & Awodele, K. O. (2012). A concept of dynamic pricing for rural hybrid electric power mini-grid systems for sub-Saharan Africa. *IEEE Power and Energy Society General Meeting*, 1–6. https://doi.org/10.1109/PESGM.2012.6344618

Kuźniak, R., Pawelec, A., Bartosik, A., & Pawełczyk, M. (2022). Determination of the Electricity Storage Power and Capacity for Cooperation with the Microgrid Implementing the Peak Shaving Strategy in Selected Industrial Enterprises. *Energies*, *15*(13), 4793. https://doi.org/10.3390/en15134793

Kzaviri, S. M., Pahlevani, M., Jain, P., & Bakhshai, A. (2017). A review of AC microgrid control methods. *2017 IEEE 8th International Symposium on Power Electronics for Distributed Generation Systems, PEDG 2017*.

https://doi.org/10.1109/PEDG.2017.7972498

Lahmer, A., Chang, J., Jeong, H., & Chae, S. (2023). Distributed Hierarchical Control of Energy Storage Systems in a DC Microgrid under Consensus Based Adaptive Droop Control Method. *2023 11th International Conference on Power Electronics and ECCE Asia (ICPE 2023 - ECCE Asia)*, 568–573. https://doi.org/10.23919/ICPE2023-ECCEAsia54778.2023.10213736

Lam, Q. L. (2018). *Advanced control of microgrids for frequency and voltage stability : robust control co-design and real-time validation*. https://tel.archives-ouvertes.fr/tel-01836292

Lamo, P., de Castro, A., Sanchez, A., Ruiz, G. A., Azcondo, F. J., & Pigazo, A. (2021). Hardware-in-the-loop and digital control techniques applied to single-phase pfc converters. *Electronics (Switzerland)*, *10*(13). https://doi.org/10.3390/electronics10131563

Lasseter, B. (2001). Role of Distributed Generation in Reinforcing the Critical Electric Power Infrastructure. *IEEE*, *3*(1), 10–27. https://ieeexplore.ieee.org/stamp/stamp.jsp?arnumber=917020

Lautert, R. R., De Freitas, A. G., Dorneles, A. P. M., Vinck, A., Da Silva, E. I., Pereira, I. B., Sperandio, M., Carloto, F. G., Canha, L. N., & Da Silva Brignol, W. (2022). Management of Distributed Energy Resources in a Rural Microgrid. *2022 14th Seminar on Power Electronics and Control, SEPOC 2022*, 1–6. https://doi.org/10.1109/SEPOC54972.2022.9976345

Lee, Y. R., Kim, H. J., & Kim, M. K. (2022). Correction to: Lee et al. Optimal Operation Scheduling Considering Cycle Aging of Battery Energy Storage Systems on Stochastic Unit Commitments in Microgrids. (Energies (2021), 14, 470). *Energies*, *15*(6). https://doi.org/10.3390/en15062107

Li, C., Wang, Z. yu, He, Z. jiang, Li, Y. jiao, Mao, J., Dai, K. hua, Yan, C., & Zheng, J. chao. (2021). An advance review of solid-state battery: Challenges, progress and prospects. *Sustainable Materials and Technologies*, *29*(April), e00297. https://doi.org/10.1016/j.susmat.2021.e00297

Li, Y. W., & Kao, C. N. (2009). An accurate power control strategy for power-electronics-interfaced distributed generation units operating in a low-voltage multibus microgrid. *IEEE Transactions on Power Electronics*, *24*(12), 2977–2988. https://doi.org/10.1109/TPEL.2009.2022828

Longe, O. M., Myeni, L., & Ouahada, K. (2019). Renewable energy solution for electricity

access in Rural South Africa. *5th IEEE International Smart Cities Conference, ISC2 2019*, 772–776. https://doi.org/10.1109/ISC246665.2019.9071693

Louzazni, M., Cotfas, D. T., & Cotfas, P. A. (2020). Management and Performance Control Analysis of Hybrid Photovoltaic Energy Storage System under Variable Solar Irradiation. *Energies*, *13*(12), 3043. https://doi.org/10.3390/en13123043

Luo, X., Barreras, J. V., Chambon, C. L., Wu, B., & Batzelis, E. (2021). Hybridizing lead–acid batteries with supercapacitors: A methodology. *Energies*, *14*(2), 1–27. https://doi.org/10.3390/en14020507

Mahmoud, M. S., Alyazidi, N. M., & Abouheaf, M. I. (2017). Adaptive intelligent techniques for microgrid control systems: A survey. *International Journal of Electrical Power and Energy Systems*, *90*, 292–305. https://doi.org/10.1016/j.ijepes.2017.02.008

Mahmud, M. A., Hossain, M. J., Pota, H. R., & Roy, N. K. (2014). Nonlinear distributed controller design for maintaining power balance in Islanded microgrids. *IEEE Power and Energy Society General Meeting*, *2014–Octob*(October). https://doi.org/10.1109/PESGM.2014.6939024

Mbinkar, E. N., Asoh, D. A., Tchuidjan, R., & Baldeh, A. (2021). *Design of a Photovoltaic Mini-Grid System for Rural Electrification in Sub-Saharan Africa*. 91–110. https://doi.org/10.4236/epe.2021.133007

Micangeli, A., Del Citto, R., Kiva, I. N., Santori, S. G., Gambino, V., Kiplagat, J., Viganò, D., Fioriti, D., & Poli, D. (2017). Energy production analysis and optimization of mini-grid in remote areas: The case study of Habaswein, Kenya. *Energies*, *10*(12), 1–23. https://doi.org/10.3390/en10122041

Mohseni, S., Brent, A. C., & Burmester, D. (2020). A comparison of metaheuristics for the optimal capacity planning of an isolated, battery-less, hydrogen-based micro-grid. *Applied Energy*, *259*(July 2019), 114224. https://doi.org/10.1016/j.apenergy.2019.114224

Moradi, M. H., Eskandari, M., & Hosseinian, S. M. (2016). Cooperative control strategy of energy storage systems and micro sources for stabilizing microgrids in different operation modes. *International Journal of Electrical Power and Energy Systems*, *78*, 390–400. https://doi.org/10.1016/j.ijepes.2015.12.002

Morstyn, T., Hredzak, B., & Agelidis, V. G. (2018). Control Strategies for Microgrids with Distributed Energy Storage Systems: An Overview. *IEEE Transactions on Smart Grid*, *9*(4), 3652–3666. https://doi.org/10.1109/TSG.2016.2637958

Nieto-Nieto, L. M., Ferrer-Rodríguez, J. P., Muñoz-Cerón, E., & Pérez-Higueras, P. (2020). Experimental set-up for testing MJ photovoltaic cells under ultra-high irradiance levels with temperature and spectrum control. *Measurement: Journal of the International Measurement Confederation*, *165*, 108092. https://doi.org/10.1016/j.measurement.2020.108092

Nigam, S., Ajala, O., & Dominguez-Garcia, A. D. (2020). A Controller Hardware-in-the-Loop Testbed: Verification and Validation of Microgrid Control Architectures. *IEEE Electrification Magazine*, *8*(3), 92–100. https://doi.org/10.1109/MELE.2020.3005740

Olivares, D. E., Canizares, C. A., & Kazerani, M. (2014). A centralized energy management system for isolated microgrids. *IEEE Transactions on Smart Grid*, *5*(4), 1864–1875. https://doi.org/10.1109/TSG.2013.2294187

Olivares, D. E., Mehrizi-Sani, A., Etemadi, A. H., Cañizares, C. A., Iravani, R., Kazerani, M., Hajimiragha, A. H., Gomis-Bellmunt, O., Saeedifard, M., Palma-Behnke, R., Jiménez-Estévez, G. A., & Hatziargyriou, N. D. (2014). Trends in microgrid control. *IEEE Transactions on Smart Grid*, *5*(4), 1905–1919. https://doi.org/10.1109/TSG.2013.2295514

Orlando, N. A., Liserre, M., Mastromauro, R. A., & Dell'Aquila, A. (2013). A survey of control issues in pmsg-based small wind-turbine systems. *IEEE Transactions on Industrial Informatics*, *9*(3), 1211–1221. https://doi.org/10.1109/TII.2013.2272888

Pagnini, L. C., Burlando, M., & Repetto, M. P. (2015). Experimental power curve of small-size wind turbines in turbulent urban environment. *Applied Energy*, *154*, 112–121. https://doi.org/10.1016/j.apenergy.2015.04.117

Palizban, O., & Kauhaniemi, K. (2016). Energy storage systems in modern grids—Matrix of technologies and applications. *Journal of Energy Storage*, *6*, 248–259. https://doi.org/10.1016/j.est.2016.02.001

Parisio, A., & Glielmo, L. (2011). Energy efficient microgrid management using Model Predictive Control. *Proceedings of the IEEE Conference on Decision and Control*, 5449–5454. https://doi.org/10.1109/CDC.2011.6161246

Pavan Kumar, Y. V., & Bhimasingu, R. (2017). Electrical machines based DC/AC energy conversion schemes for the improvement of power quality and resiliency in renewable energy microgrids. *International Journal of Electrical Power and Energy Systems*, *90*, 10–26. https://doi.org/10.1016/j.ijepes.2017.01.015

Peters, J., Sievert, M., & Toman, M. A. (2019). Rural electrification through mini-grids:

Challenges ahead. *Energy Policy*, *132*(December 2018), 27–31. https://doi.org/10.1016/j.enpol.2019.05.016

Ranjbaran, P., Yousefi, H., Gharehpetian, G. B., & Astaraei, F. R. (2019). A review on floating photovoltaic (FPV)power generation units. *Renewable and Sustainable Energy Reviews*, *110*(April), 332–347. https://doi.org/10.1016/j.rser.2019.05.015

Razmi, D., & Lu, T. (2022). A Literature Review of the Control Challenges of Distributed Energy Resources Based on Microgrids (MGs): Past, Present and Future. *Energies*, *15*(13), 4676. https://doi.org/10.3390/en15134676

Rivera-Barrera, J. P., Muñoz-Galeano, N., & Sarmiento-Maldonado, H. O. (2017). Soc estimation for lithium-ion batteries: Review and future challenges. In *Electronics (Switzerland)* (Vol. 6, Issue 4). https://doi.org/10.3390/electronics6040102

Rodriguez, J., Heydari, R., Rafiee, Z., Young, H., Flores-Bahamonde, F., & Shahparasti, M. (2020). Model-Free Predictive Current Control of a Voltage Source Inverter. *IEEE Access*, *8*. https://doi.org/10.1109/ACCESS.2020.3039050

Roslan, M. F., Hannan, M. A., Ker, P. J., & Uddin, M. N. (2019). Microgrid control methods toward achieving sustainable energy management. *Applied Energy*, *240*(February), 583–607. https://doi.org/10.1016/j.apenergy.2019.02.070

Ruiz, M., Mujica, L. E., Alférez, S., Acho, L., Tutivén, C., Vidal, Y., Rodellar, J., & Pozo, F. (2018). Wind turbine fault detection and classification by means of image texture analysis. *Mechanical Systems and Signal Processing*, *107*, 149–167. https://doi.org/10.1016/j.ymssp.2017.12.035

Salehi, N., & , Herminio Martínez-García, G. V.-Q. (2022). Networked Microgrid Energy Management Based on. *Energies*, 15. https://doi.org/10.3390/en15134915

Sánchez, R. T., & Rios, A. M. (2016). Modeling and control of a wind turbine. *Bond Graphs for Modelling, Control and Fault Diagnosis of Engineering Systems, Second Edition*, *2013*, 547–585. https://doi.org/10.1007/978-3-319-47434-2_15

Sanguesa, J. A., Torres-Sanz, V., Garrido, P., Martinez, F. J., & Marquez-Barja, J. M. (2021). A review on electric vehicles: Technologies and challenges. *Smart Cities*, *4*(1), 372–404. https://doi.org/10.3390/smartcities4010022

Sen, S., & Kumar, V. (2018). Microgrid control: A comprehensive survey. *Annual Reviews in Control*, *45*(March), 118–151. https://doi.org/10.1016/j.arcontrol.2018.04.012

Shravanth Vasisht, M., Srinivasan, J., & Ramasesha, S. K. (2016). Performance of solar

photovoltaic installations: Effect of seasonal variations. *Solar Energy*, *131*, 39–46. https://doi.org/10.1016/j.solener.2016.02.013

Singh, M., & Santoso, S. (2012). Dynamic models for wind turbines and wind power plants. In *Wind Power: Systems Engineering Applications and Design Models* (Issue October).

Slootweg, J. G., De Haan, S. W. H., Polinder, H., & Kling, W. L. (2003). General model for representing variable speed wind turbines in power system dynamics simulations. *IEEE Transactions on Power Systems*, *18*(1), 144–151. https://doi.org/10.1109/TPWRS.2002.807113

Som, S., De, S., Chakrabarti, S., Sahoo, S. R., & Ghosh, A. (2022). A robust controller for battery energy storage system of an islanded ac microgrid. *IEEE Transactions on Industrial Informatics*, *18*(1), 207–218. https://doi.org/10.1109/TII.2021.3057516

Tanesab, J., Parlevliet, D., Whale, J., & Urmee, T. (2018). Energy and economic losses caused by dust on residential photovoltaic (PV) systems deployed in different climate areas. *Renewable Energy*, *120*, 401–412. https://doi.org/10.1016/j.renene.2017.12.076

Tiwari, D., Salunke, M., & Raju, A. B. (2021). Modelling and Real Time Simulation of Microgrid using Typhoon HIL. *2021 6th International Conference for Convergence in Technology, I2CT 2021*, 1–5. https://doi.org/10.1109/I2CT51068.2021.9418178

Tooryan, F., HassanzadehFard, H., Collins, E. R., Jin, S., & Ramezani, B. (2020). Smart integration of renewable energy resources, electrical, and thermal energy storage in microgrid applications. *Energy*, *212*, 118716. https://doi.org/10.1016/j.energy.2020.118716

Tricarico, T., Costa, J. A., Herrera, D., Galván-Díez, E., Carrasco, J. M., & Aredes, M. (2022). Total Frequency Spread: A New Metric to Assess the Switching Frequency Spread of FCS-MPC. *Energies*, *15*(14), 5273. https://doi.org/10.3390/en15145273

Unamuno, E., & Barrena, J. A. (2015). Hybrid ac/dc microgrids - Part I: Review and classification of topologies. *Renewable and Sustainable Energy Reviews*, *52*, 1251–1259. https://doi.org/10.1016/j.rser.2015.07.194

Vandoorn, T. L., Vasquez, J. C., De Kooning, J., Guerrero, J. M., & Vandevelde, L. (2013). Microgrids: Hierarchical Control and an Overview of the Control and Reserve Management Strategies. *IEEE Industrial Electronics Magazine*, *7*(4), 42–55. https://doi.org/10.1109/MIE.2013.2279306

Vins, M., & Sirovy, M. (2019). Sodium-sulfur batteries for energy storage applications.

Proceedings of the 2019 20th International Scientific Conference on Electric Power Engineering, EPE 2019, 1–5. https://doi.org/10.1109/EPE.2019.8778134

Wang, J., Lu, K., Ma, L., Wang, J., Dooner, M., Miao, S., Li, J., & Wang, D. (2017). Overview of Compressed Air Energy Storage and Technology Development. *Energies*, *10*(7), 991. https://doi.org/10.3390/en10070991

Wu, F., Zhang, X. P., & Ju, P. (2008). Modeling and control of the wind turbine with the direct drive permanent magnet generator integrated to power grid. *3rd International Conference on Deregulation and Restructuring and Power Technologies, DRPT 2008*, *April*, 57–60. https://doi.org/10.1109/DRPT.2008.4523379

Yan, X., Yang, L., & Li, T. (2021). The LVRT Control Scheme for PMSG-Based Wind Turbine Generator Based on the Coordinated Control of Rotor Overspeed and Supercapacitor Energy Storage. *Energies*, *14*(2), 518. https://doi.org/10.3390/en14020518

Yang, S., Lei, Q., Peng, F. Z., & Qian, Z. (2011). A robust control scheme for grid-connected voltage-source inverters. *IEEE Transactions on Industrial Electronics*, *58*(1), 202–212. https://doi.org/10.1109/TIE.2010.2045998

Yang, Y., Bremner, S., Menictas, C., & Kay, M. (2018). Battery energy storage system size determination in renewable energy systems: A review. *Renewable and Sustainable Energy Reviews*, *91*(June 2017), 109–125. https://doi.org/10.1016/j.rser.2018.03.047

Young, H. A., Perez, M. A., Rodriguez, J., & Abu-Rub, H. (2014). Assessing finite-control-set model predictive control: A comparison with a linear current controller in two-level voltage source inverters. *IEEE Industrial Electronics Magazine*, *8*(1), 44–52. https://doi.org/10.1109/MIE.2013.2294870

Yu, R., Pong, B. M. H., Ling, B. W. K., & Lam, J. (2012). Two-stage optimization method for efficient power converter design including light load operation. *IEEE Transactions on Power Electronics*, *27*(3), 1327–1337. https://doi.org/10.1109/TPEL.2011.2114676

Zhang, R., Savkin, A. V., & Hredzak, B. (2021). Centralized nonlinear switching control strategy for distributed energy storage systems communicating via a network with large time delays. *Journal of Energy Storage*, *41*(February), 102834. https://doi.org/10.1016/j.est.2021.102834

Zhou, Z., Li, X., Lu, Y., Liu, Y., Shen, G., & Wu, X. (2020). Stability Blind-Area-Free Control

Design for Microgrid-Interfaced Voltage Source Inverters under Dual-Mode Operation. *IEEE Transactions on Power Electronics*, *35*(11), 12555–12569. https://doi.org/10.1109/TPEL.2020.2988565

APPENDIX

APPENDIX 2. 1:ILLUSTRATION OF SEASON'S ON SOLAR ENERGY RECEIVED

```
%Illustration of season's impact on solar performance
clear
close all
clc
night1 = zeros(1,60);
night2 = zeros(1,60);
longitude = linspace(0,180,120)
latitude = linspace(23, 157, 3);
fullDay = [night1, longitude, night2];
Gm = 1000;

figure;

plot(sind(fullDay))
figure;
[O,A] = meshgrid(longitude,latitude);
Glat = Gm *(sind(A)) .* sind(O);
mesh(Glat)
xlabel('latitude (degrees)')
ylabel('longitude (degrees)')
zlabel('Irradiance [W/m^2]')

xh = get(gca,'XLabel'); % Handle of the x label
set(xh, 'Units', 'Normalized')
pos = get(xh, 'Position');
set(xh, 'Position',pos.*[1,1,1],'Rotation',18)

yh = get(gca,'YLabel'); % Handle of the y label
set(yh, 'Units', 'Normalized')
pos = get(yh, 'Position');
set(yh, 'Position',pos.*[1,1,1],'Rotation',-25)

zh = get(gca,'ZLabel'); % Handle of the z label
set(zh, 'Units', 'Normalized')
pos = get(zh, 'Position');
set(zh, 'Position',pos.*[1,1,0],'Rotation',90)

 figure;
 map(Glat)
```

APPENDICES

APPENDIX 2. 2: ILLUSTRATION OF PWM SIGNAL IN VSIs

```
%VSI:PWM modulation
clear
close all
clc
T = 10*(1/60);
Fs = 1200;
dt = 1/Fs;
t = 0:dt:T-dt;
x = sawtooth(2*pi*60*t, .5);
y = .8 * sin(2*pi*6*t);
figure
plot(t,x,'linewidth',2)
xlabel('Time (s)')
ylabel('Magnitude (V)')
grid on
figure
plot(t,y,'linewidth',2)
xlabel('Time (s)')
ylabel('Magnitude (V)')
grid on
figure
plot(t,x, t,y, 'linewidth',2)
xlabel('Time (s)')
ylabel('Magnitude (V)')
grid on
figure
y(y>x) = 1;
y(y<x) = 0;
stairs(t,y, 'linewidth',2)
xlabel('Time (s)')
ylabel('Magnitude (V)')
grid on
axis([0 .2 0 1.2])
```

APPENDIX 4.1: MATLAB CODE IMPLEMENTING THE ALGORITHM FOR ENERGY MANAGEMENT FOR AN ISLANDED MINIGRID

```
%Energy management:algorithm for a scenario
clear
close all
clc
%LOAD PROFILE
a = inputdlg({'Enter the time of the day', 'Enter the amplitude of solar',
'Enter the amplitude of wind'});
timeS = str2num(a{1});
alpha = str2num(a{2});
beta = str2num(a{3});

% timeS = input('Enter the time: ');
% alpha = input('alpha: ');
% beta = input('beta');
t = timeS/24*(linspace(0, 5 * pi/2, 120*timeS/24));
load1 = cos(.5 * pi * t);
increase = rand(1,120*timeS/24);
increaseAsc = 1.2 * sort(increase, 'ascend');
loadEn = (.7 + load1 + increaseAsc + .3 * rand(1,120*timeS/24)) *.1;
ts = timeS/24 * linspace(0, 24, 120 * timeS/24);
solarEn =   (.1 * (gaussmf(ts,[3 12]) +.1 * rand(1, 120 * timeS/24))) *
alpha;
solarEn(solarEn < 0) = 0;
windEn = (ones(1,timeS*120/24) + .1 * rand(1, timeS*120/24)) * .1 * beta;
genEn = .1 * (ones(1,timeS*120/24) + .1 * rand(1, timeS*120/24));
totalEn = solarEn + windEn;
storedEn = totalEn - loadEn;
%Energy computation
solarEnergy = num2str(sum(solarEn * timeS/120));
windEnergy = num2str(sum(windEn *timeS /120));
loadEnergy = num2str(sum(loadEn * timeS /120));
EnergyStored = num2str(sum(storedEn * timeS/120));
totalEnergy = num2str(sum(totalEn *timeS/120));

%Energy display
Energy1 = [ {'Solar energy' solarEnergy 'MWh'; 'Wind energy' windEnergy
'MWh';'Load energy' loadEnergy 'MWh';'Stored energy' EnergyStored 'MWh';
'Total energy' totalEnergy 'MWh'}]';
Energy2 = {solarEnergy, windEnergy,loadEnergy, EnergyStored, totalEnergy}'
%Energy = [Energy1 Energy2];
listdlg('liststring', Energy1)
 e = msgbox([Energy1])

%  str2 = x;
%  s = strcat(str1,str2,'MW');


time = linspace(0,timeS,120*timeS/24);

subplot(6,1,1)
        bar(time, loadEn)
        title('Load demand [MW]')

     subplot(6,1,2)
        bar(time, solarEn)
        title('Solar source [MW]')
```

```
    subplot(6,1,3)
        bar(time, windEn)
        title('Wind source [MW]')

 subplot(6,1,4)
        bar(time, genEn)
        title('Generator [MW]')

  subplot(6,1,5)
    bar(time, storedEn)
    title('Stored energy [MW]')
 subplot(6,1,6)
    bar(time, totalEn)
    title('Total energy [MW]')
 figure
    bar(time , loadEn);
    title('Load profile')
    xlabel('time (Hours)')
    ylabel('Power (MW)')
    grid on

figure
    bar(time, solarEn);
    title('Solar energy')
    xlabel('time (Hours)')
    ylabel('Power (MW)')
    grid on

figure
    bar(time, windEn);
    title('Wind energy')
    xlabel('time (Hours)')
    ylabel('Power (MW)')
    grid on
figure
    bar(time, genEn);
    title('generator energy')
    xlabel('time (Hours)')
    ylabel('Power (MW)')
    grid on
figure
    bar(time, totalEn);
    title('Total energy')
    xlabel('time (Hours)')
    ylabel('Power (MW)')
    grid on
figure
    bar(time, storedEn);
    title('Stored energy')
    xlabel('time (Hours)')
    ylabel('Power (MW)')
    grid on


:
```

APPENDIX 5.1: PROPORTIONAL CONTROL FOR VOLTAGE IN LR LOAD

```
%Proportional control for voltage in variable load
clear
close all
clc
kp = [10:20:200];
t = linspace(0,.1,500);
LF = 3.3;
CF = 2.2 *10^-6;
RL = 50;
LL = 3.3
f = 60;

t= linspace(0,.1);
u = sin(2*pi*f*t);
n = length(kp);
figure
for i = 1:length(kp)
num1(i,:) = kp(i)*[0 0 LL RL];
den1(i,:) = [LL*LF*CF LF*CF*RL LF*kp(i)*LL, kp(i)*RL];
l(i,:) = tf(num1(i,:), den1(i,:));
figure

lsimplot(l(i,:),u,t,'r');
end
figure
for i = 1:length(kp)
num1(i,:) = kp(i)*[0 0 LL RL];
den1(i,:) = [LL*LF*CF LF*CF*RL LF*kp(i)*LL, kp(i)*RL];
l(i,:) = tf(num1(i,:), den1(i,:));
step(l(i,:));
grid on
figure
end
```

APPENDIX 5.2: PROPORTIONAL INTEGRAL CONTROLLER FOR OUTPUT VOLTAGE IN LR LOAD

```
%Proportional integral controller for output voltage in LR load
clear
close all
clc
kp = [10:20:200];
t = linspace(0,.1,500);
LF = 3.3;
CF = 2.2 *10^-6;
RL = 50;
LL = 3.3
f = 60;
t= linspace(0,.1);
u = sin(2*pi*f*t);
n = length(kp);
T= .2*(10*10^-4);
n1 = zeros(n,5)
d1= zeros(n,5);

figure
for i = 1:length(kp)
n1(i,:) = [0 0 kp(i)*LL RL+LL/T RL/T];
d1(i,:) = [LL*LF*CF LF*CF*RL LF+LL*kp(i)*LL kp(i)*RL+LL/T RL*(1+1/T)];
l(i,:) = tf(n1(i,:), d1(i,:));
figure

lsimplot(l(i,:),u,t,'r');
grid  on
title(sprintf(' AC response @%d proportional gain', kp(i)))
end
figure
for i = 1:length(kp)
n1(i,:) = [0 0 kp(i)*LL RL+LL/T RL/T];
d1(i,:) = [LL*LF*CF LF*CF*RL LF+LL+kp(i)*LL  kp(i)*RL+LL/T RL*(1+1/T)];
l(i,:) = tf(n1(i,:), d1(i,:));
step(l(i,:));
grid on
figure
end
```

APPENDIX 6.1: TYPHOON HIL DESIGN

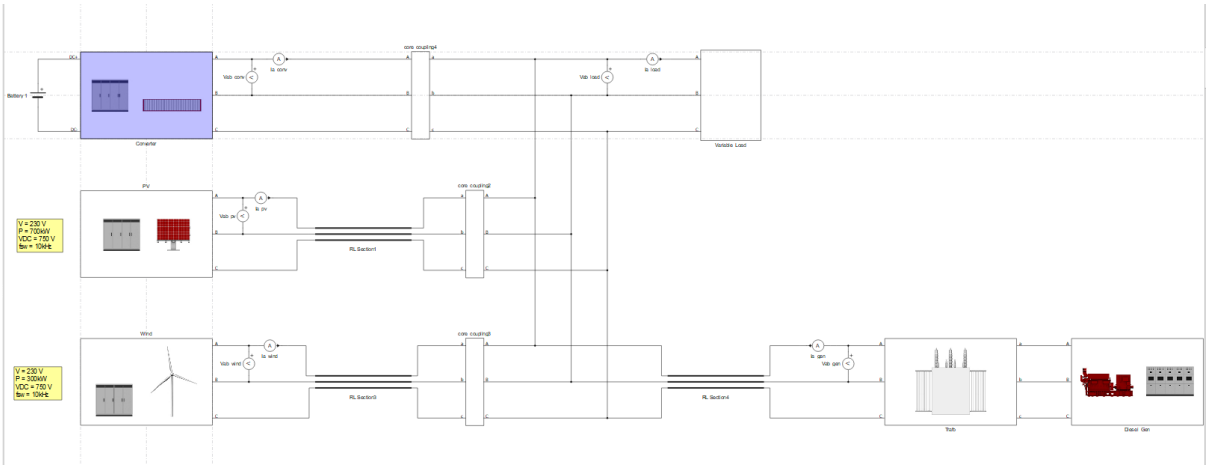

Overall system in the schematic editor

Battery

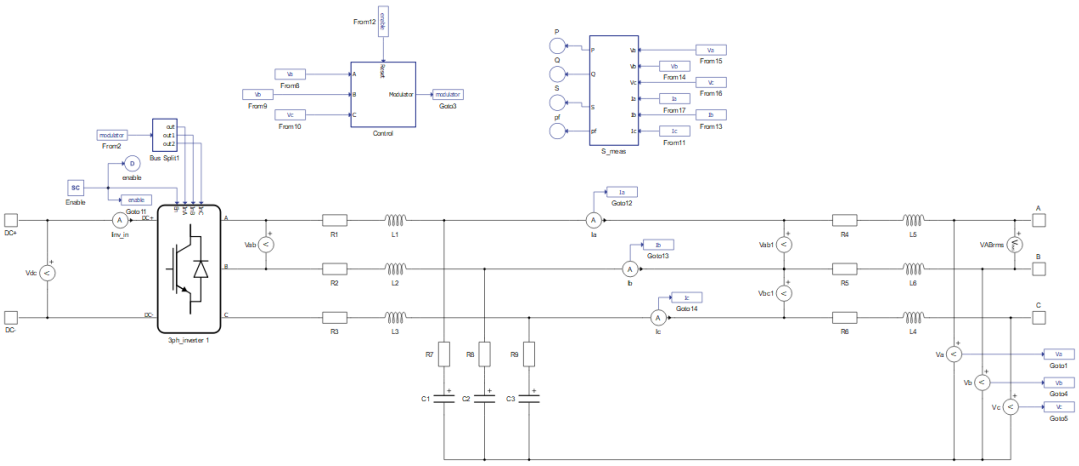

Converter diagram schematic editor

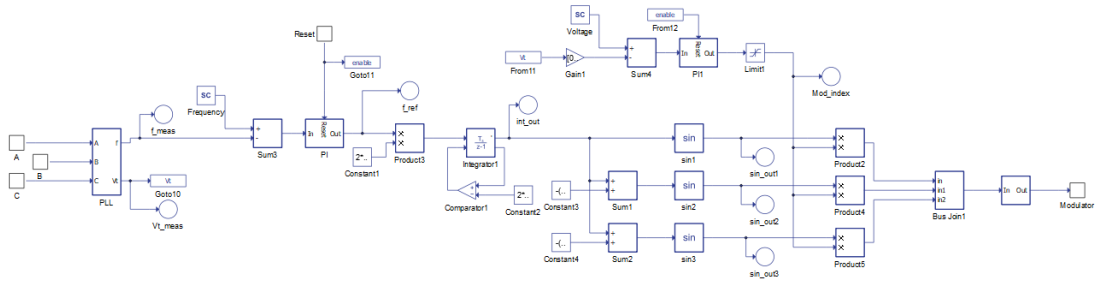

Energy storage system control

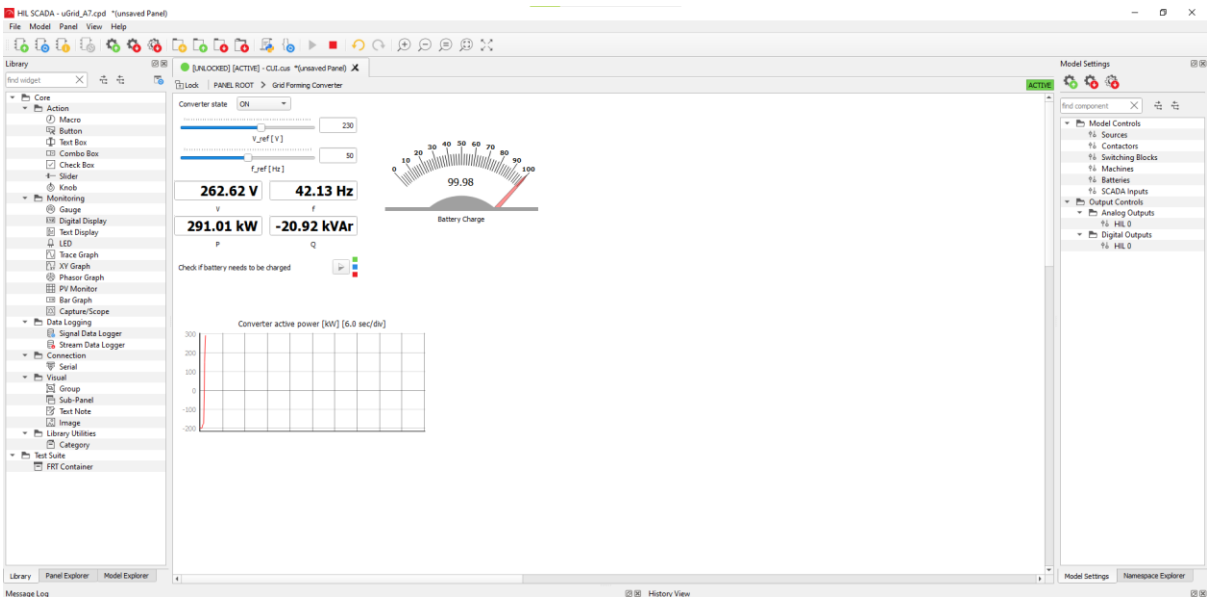

In SCADA ESs

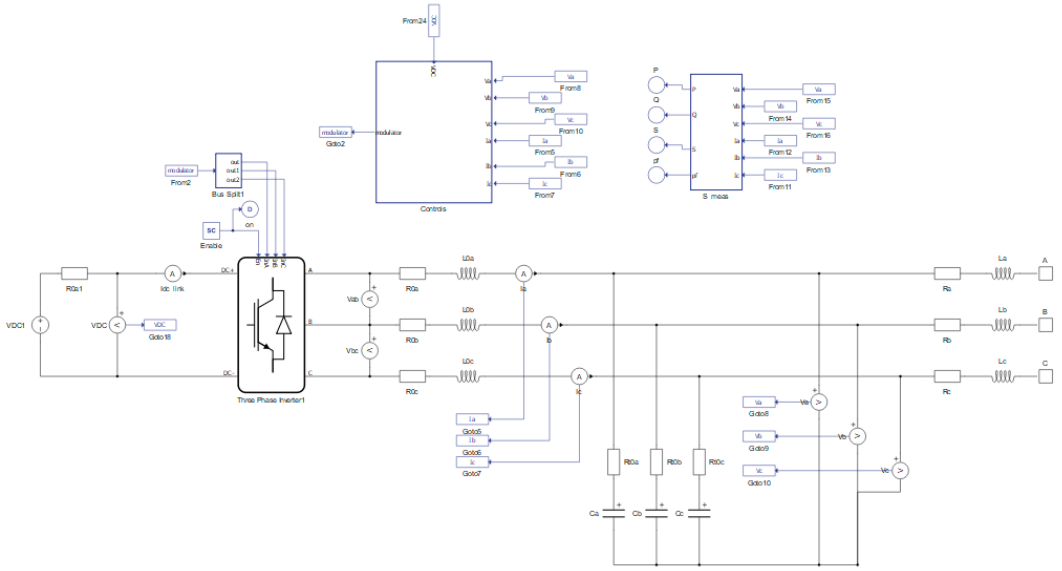

PV

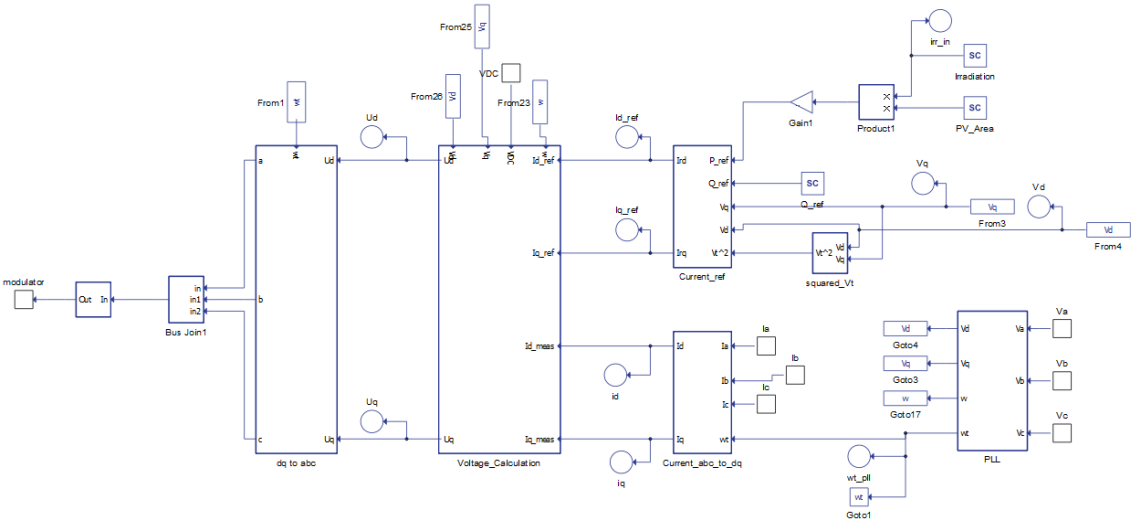

PV control system

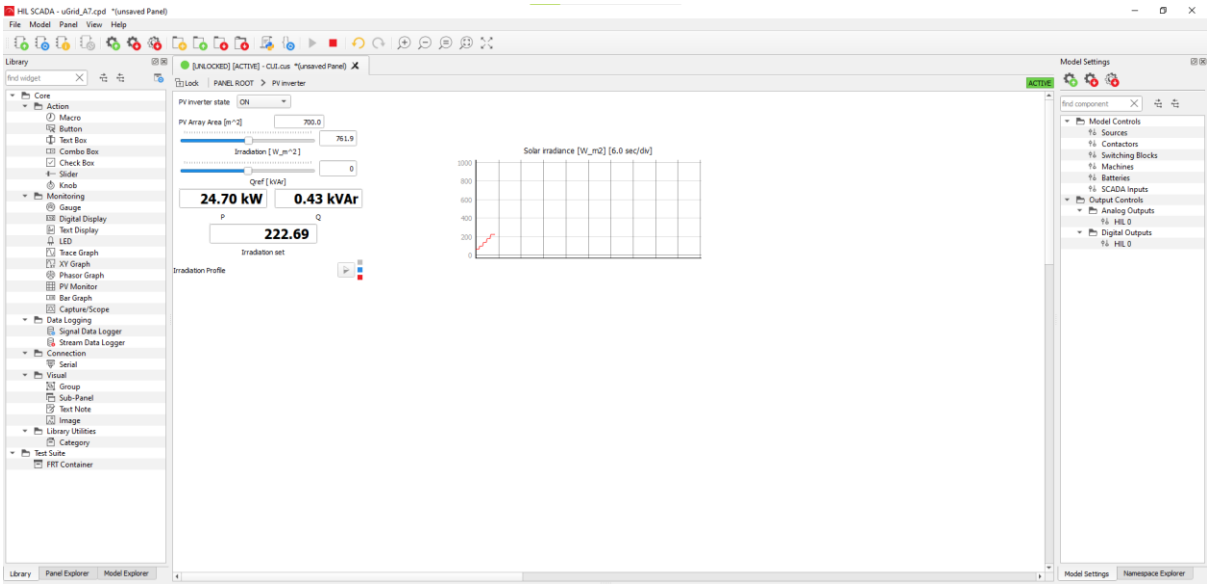

In SCADA PV

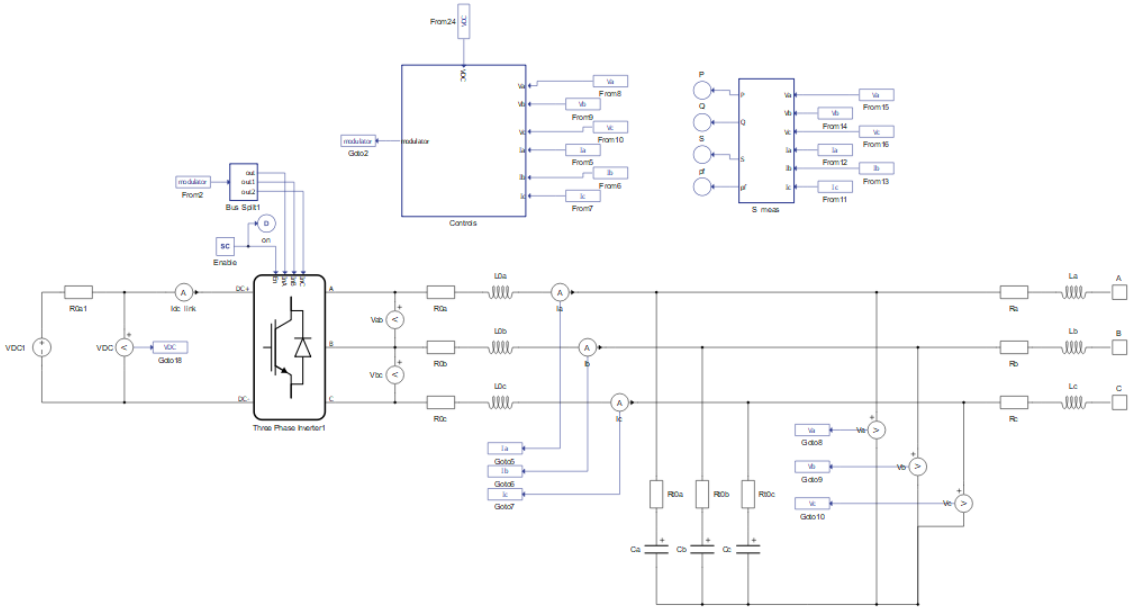

Wind

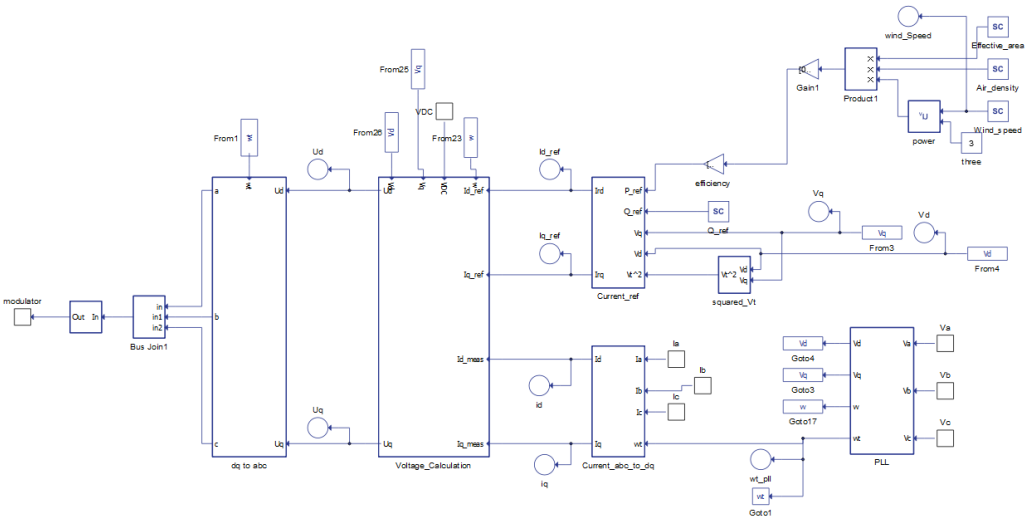

Wind control

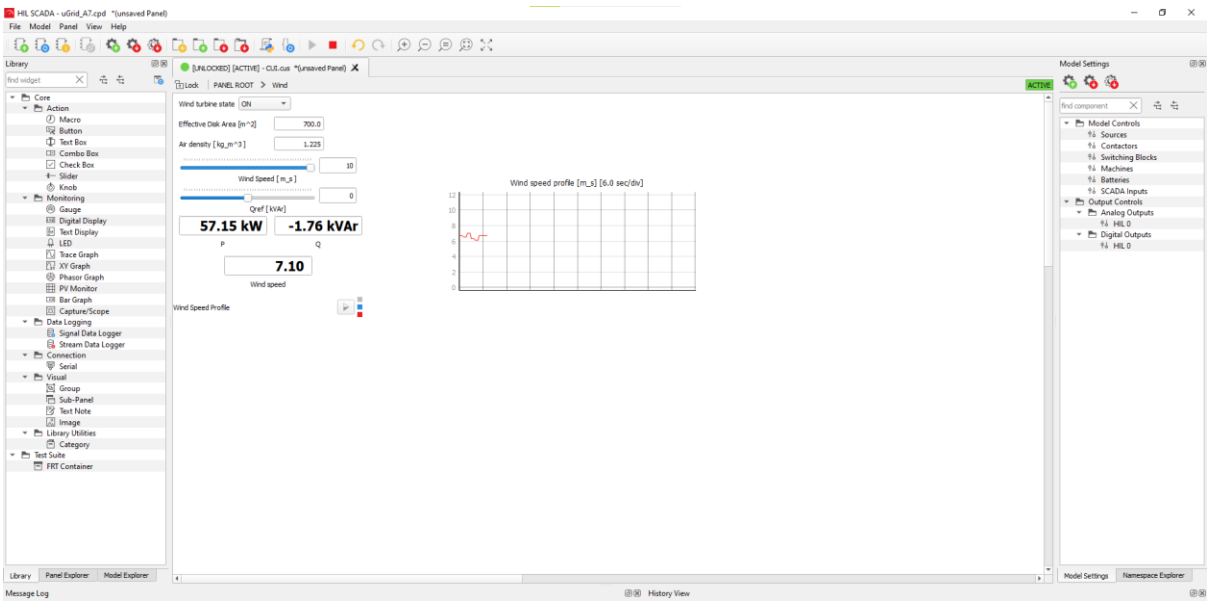

In SCADA WIND

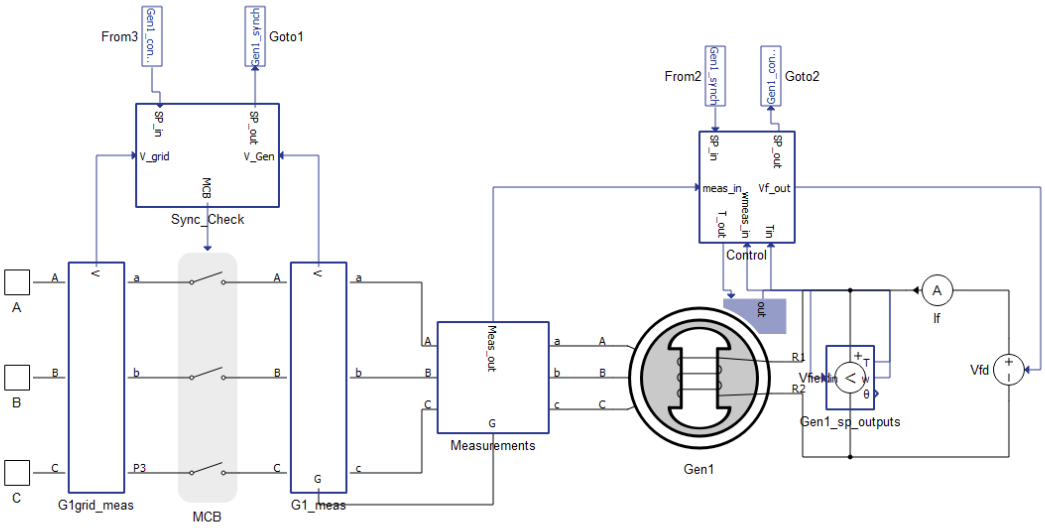

Generator

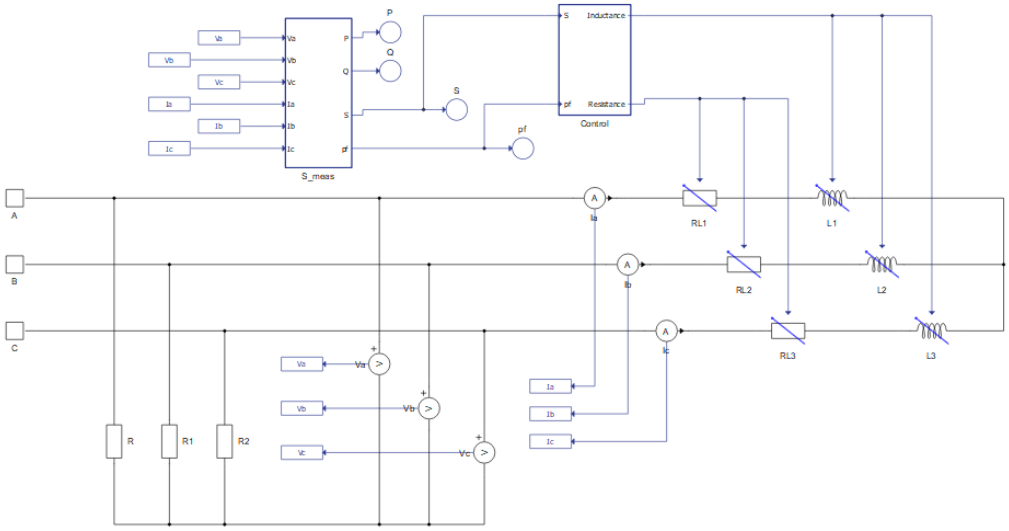

Load circuit

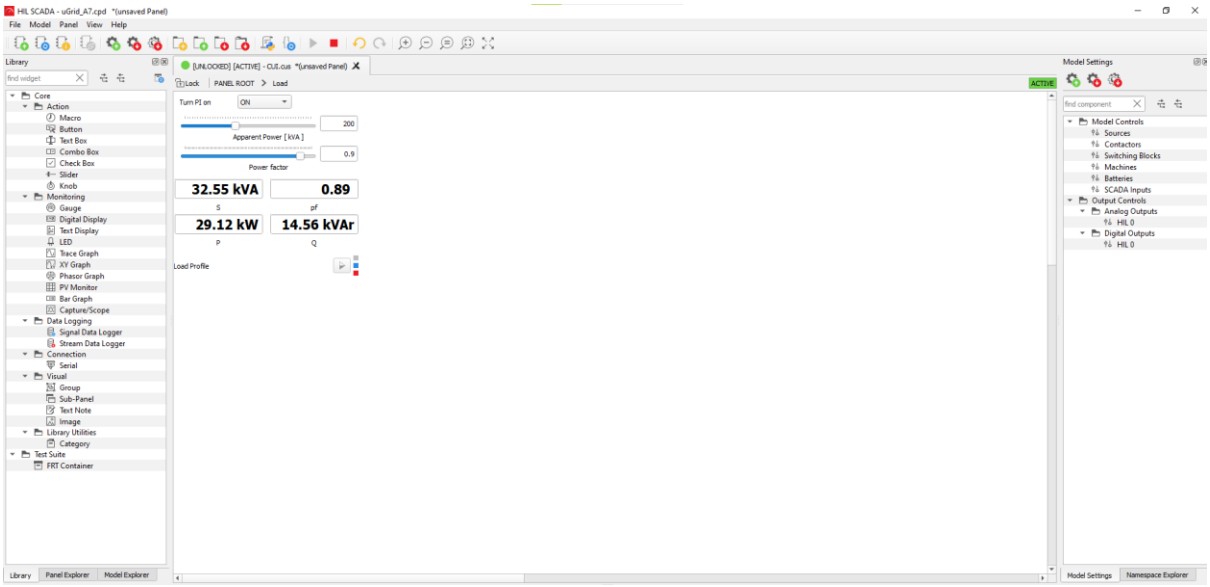

In SCADA Load

Numpy module is imported as 'np'

 # Scipy module is imported as 'sp'

 # Ts for ARM

#Ts = 20e-6

 # Ts for uBlaze

Ts = 200e-6

 # Governor specs

K = 10 # gain K

T1 = 1.0E-4 # Time constant T1 of Electric Control Box

T2 = 0.0 # Time constant T2 of Electric Control Box

T3 = 0.5001 # Time constant T3 of Electric Control Box

T4 = 0.025 # Time constant T4 of Actuator

T5 = 0.0009 # Time constant T5 of Actuator

T6 = 0.00574 # Time constant T6 of Actuator

Pm0 = 0.0 #0.0005 # Initial value of Mechanic Power

Tmax = 10 #1.1 # Max torque limit

Tmin = -0.1 # Min torque limit

```
Td = 0.024  # Engine time delay

dummy = 1.0 + 2.0*T5/Ts
coeff1 = (1.0 + 2.0*T4/Ts)/dummy
coeff2 = (1.0 - 2.0*T4/Ts)/dummy
coeff3 = 1.0
coeff4 = (1.0 - 2.0*T5/Ts)/dummy
numTF4d = [coeff1, coeff2]
denTF4d = [coeff3, coeff4]

dummy = 1.0 + 2.0*T6/Ts
coeff1 = (1.0)/dummy
coeff2 = (1.0)/dummy
coeff3 = 1.0
coeff4 = (1.0 - 2.0*T6/Ts)/dummy
numTF3d = [coeff1, coeff2]
denTF3d = [coeff3, coeff4]

numTF1d = [(1.0+2.0*T3/Ts),2.0,(1.0-2.0*T3/Ts)]
denTF1d = [(1.0+2.0*T1/Ts+4.0*T1*T2/(Ts**2)),(2.0-8.0*T1*T2/(Ts**2)),(4.0*T1*T2/(Ts**2)-2.0*T1/Ts+1)]

# Synchronous machine specs from Simulink's 4 MVA machine in PU

f = 50.0  # Synchronous speed
pms = 2.0  # Number of mechanical pole pairs
Sb_gen1 = 1.075e6  # Nominal/base power of machine in VA
Vn_gen1 = 460.0  # Machine terminal line to line rms voltage
Rs_pu_gen1 = 0.01524  # Stator resistance per phase in pu
Lls_pu_gen1 = 0.08  # Stator leakage inductance in pu
Lmd_pu_gen1 = 2.81  # Direct-axis magnetizing inductance in pu
Lmq_pu_gen1 = 1.64  # Quadrature-axis magnetizing inductance in pu
Rf_pu_gen1 = 0.004319  # Field resistance in pu
Llfd_pu_gen1 = 0.531  # Field leakage inductance in pu
Rkd_pu_gen1 = 0.2343  # D-axis resistance in pu
Rkq_pu_gen1 = 0.03365  # Q-axis resistance in pu
Llkd_pu_gen1 = 2.655  # D-axis leakage inductance in pu
```

```
Llkq_pu_gen1 = 0.2408  # Q-axis leakage inductance in pu
Ns_fd_gen1 = 1.0  # Turn ratio between the stator and the field windings
Ns_kd_gen1 = 1.0  # Turn ratio between stator and d-axis damper windings
Ns_kq_gen1 = 1.0  # Turn ratio between stator and q-axis damper windings
H_gen1 = 0.3222  # Inertia coefficient in seconds
Fpu_gen1 = 0.01322  # Friction factor in pu

# Base calculation

Vb_gen1 = Vn_gen1*((2.0/3.0)**0.5)  # Nominal/base voltage of machine terminal in V (Peak line to neutral voltage)
wb_gen1 = 2.0*np.pi*f  # Electrical angular speed base
wmb_gen1 = wb_gen1/pms  # Mechanical angular speed base
Zb_gen1 = (Vn_gen1*Vn_gen1)/Sb_gen1  # Impedance base
Trq_b_gen1 = Sb_gen1/wmb_gen1  # Torque base
Fb_gen1 = Trq_b_gen1/wmb_gen1  # Friction Factor base
Lb_gen1 = Zb_gen1/wb_gen1  # Inductance base

# Stator data in SI

Rs_gen1 = Rs_pu_gen1*Zb_gen1
Lls_gen1 = Lls_pu_gen1*Lb_gen1
Lmd_gen1 = Lmd_pu_gen1*Lb_gen1
Lmq_gen1 = Lmq_pu_gen1*Lb_gen1
Rkd_gen1 = Rkd_pu_gen1*Zb_gen1
Rkq_gen1 = Rkq_pu_gen1*Zb_gen1
Llkd_gen1 = Llkd_pu_gen1*Lb_gen1
Llkq_gen1 = Llkq_pu_gen1*Lb_gen1

# Mechanical data in SI

F_gen1 = Fpu_gen1*Fb_gen1  # Friction Factor in Nm.s
J_gen1 = 2*H_gen1*Sb_gen1/(wmb_gen1*wmb_gen1)  # Inertia in kg.m2

# Field base calculation
```

```
Lsfd_gen1 = (2.0/3.0)*Lmd_gen1*(1.0/Ns_fd_gen1)  # Mutual inductance between stator and field
ifn_gen1 = Vb_gen1/(Lsfd_gen1*wb_gen1)  # Nominal field current
ifb_gen1 = ifn_gen1*Lmd_pu_gen1  # Field current base
Vfb_gen1 = Sb_gen1/ifb_gen1  # Field voltage base
Zfb_gen1 = Vfb_gen1/ifb_gen1  # Field impedance base
Lfb_gen1 = Zfb_gen1/wb_gen1  # Field inductance base

# Field data in SI

Rf_gen1 = Rf_pu_gen1*Zfb_gen1  # Field resistance (Field side)
Llfd_gen1 = Llfd_pu_gen1*Lfb_gen1  # Field inductance (Field side)
Rf_prime_gen1 = Rf_gen1*(3.0/2.0)*(Ns_fd_gen1*Ns_fd_gen1)  # Field resistance referred to the stator side
Llfd_prime_gen1 = Llfd_gen1*(3.0/2.0)*(Ns_fd_gen1*Ns_fd_gen1)  # Field inductance referred to the stator side

# Exciter initialization

Tr_gen1 = 20e-4  # Low pass filter time constant
Ka_gen1 = 200.0  # Regulator gain
Ta_gen1 = 2e-3  # Regulator time constant
Ke_gen1 = 1.0  # Exciter constant
Te_gen1 = 1e-8 #Exciter time constant
Tb_gen1 = 1e-12  # Transient gain reduction time constant b
Tc_gen1 = 1e-12  # Transient gain reduction time constant c
Kf_gen1 = 0  # Damping filter gain
Tf_gen1 = 1e-12  # Damping filter time constant
Efmin_gen1 = -0.1 # Regulator output lower limit
Efmax_gen1 = 5.0 #5.0  # Regulator output upper limit
Vt0_gen1 = 0.0  # Initial terminal voltage
Vf0_gen1 = 0.0  # Initial field voltage
Const_gen1 = Vf0_gen1/Ka_gen1
```